# Forces Inferred from macroscopic Loading and grain Motions (FILM)

Mathias Tolomeo

Communauté
UNIVERSITÉ Grenoble Alpes

# THÈSE

Pour obtenir le grade de

**DOCTEUR DE LA COMMUNAUTE UNIVERSITE GRENOBLE ALPES**

Spécialité : 2MGE : Matériaux, Mécanique, Génie civil, Electrochimie

Arrêté ministériel : 25 mai 2016

Présentée par


## Mathias TOLOMEO

Thèse dirigée par **Vincent RICHEFEU, Maitre de Conférences, Communauté Université Grenoble Alpes**

préparée au sein du **Laboratoire Sols, Solides, Structures et Risques**
dans **l'École Doctorale I-MEP2 - Ingénierie - Matériaux, Mécanique, Environnement, Energétique, Procédés, Production**


# Estimation des forces de contact intergranulaires par mesures de champs cinématiques

# Forces Inferred from macroscopic Loading and grain Motions (FILM)

Thèse soutenue publiquement le **22 octobre 2018**,
devant le jury composé de :

**Monsieur Fahrang Radjai**
Directeur de Recherche, Université Montpellier 2, President du jury
**Monsieur José E. Andrade**
Professeur, California Institute of Technology, Rapporteur
**Monsieur Jin Ooi**
Professeur, University of Edinburgh, Rapporteur
**Monsieur Vincent Richefeu**
Maître de Conférences, Communauté Université Grenoble Alpes, Directeur de thèse
**Monsieur Gaël Combe**
Professeur, Communauté Université Grenoble Alpes, Invité
**Monsieur Gioacchino Viggiani**
Professeur, Communauté Université Grenoble Alpes, Invité
**Monsieur Jean-Noël Roux**
Ingénieur General des Ponts et Chaussées, Université Paris-Est, Invité
**Madame Vanessa Magnanimo**
Associate Professor, University of Twente, Invitée

# Abstract

In the experimental study of the micro-mechanics of granular materials, measuring inter-particle contact forces is still a challenging task, if compared to the well-established tools and techniques for the kinematic characterisation at particle scale. This doctoral thesis addresses this problem. The proposed approach consists of two parts: an experimental characterisation of the granular network geometry and of particle-scale kinematics, which can be carried out with common imaging techniques such as Digital Image Correlation; a numerical approach aiming to exploit these measurements for the estimation of forces.

One imposed constraint was to only make use of the rigid motions of particles, together with the knowledge of the contact network, to infer contact forces. Three different numerical techniques have been proposed to this purpose, referred to as Contact Elasticity Method (CEM), Contact Dynamics-based Method (CDM) and Quasi-Static Method (QSM). Each of these techniques is based on the formulation of common approaches in the family of Discrete Element Methods, respectively the classical Cundall-like DEM, the Non Smooth Contact Dynamics and a quasi-static approach accounting for both contact elasticity and plasticity. It is shown that memory of the history of the packing is the main concern with all the chosen techniques.

The three methods are first presented and validated by applying them to the estimation of forces in 2D granular systems generated by means of explicit-time DEM simulations. We refer to these simulations as "ideal" experiments since they are meant to provide the same information that can be extracted from experiments, but without any measurement error. An obvious benefit of this strategy is to get reference force sets that are taken as ground truth. Based on this, the main aspects that affect the determination of forces can be investigated. In particular, the crucial role of history is emphasised here, and some solutions to take it into account in the force inference have been investigated. An assessment of the influence of measurement error has also been carried out, to predict the applicability of each method to real experiments. A short analysis of the variability of the solutions is also provided.

Finally, some attempts have been made to infer forces from experiments carried out in the $1\gamma2\varepsilon$ device. Particle kinematics and connectivity have been assessed by means of the Digital Image Correlation technique. The benefits and drawbacks of the three methods have been demonstrated. They conduct us to envision a combined usage of the three methods. In the future, studying the stability of equilibrium might help reducing the variability of the solutions.

# Résumé

Dans les études expérimentales de la micromécanique des matériaux granulaires, la mesure des forces de contact entre particules est de nos jours toujours un challenge en comparaison avec les outils et techniques bien mieux établis pour la caractérisation cinématique à l'échelle des particules. Cette thèse de doctorat s'attaque à cet ambitieux problème. L'approche proposée implique deux aspects: (i) la caractérisation expérimentale du réseau de contact et de la cinématique à l'échelle des particules, qui peut être réalisée avec des techniques d'imagerie standards ; (ii) une approche numérique capable d'exploiter ces mesures afin de déduire les forces de contact.

L'une des contraintes qu'on s'était imposée était de ne s'appuyer que sur la connaissance de la géométrie des particules ainsi que du réseau de contacts pour réaliser la déduction des forces de contact. Trois techniques numériques différentes ont été proposées à cet effet : une méthode basée sur l'élasticité des contacts (CEM), une méthode basée sur la dynamique de contact (CDM) et une méthode basée sur l'équilibre élastoplastique de l'assemblage granulaire (QSM). Chacune de ces techniques repose sur une approche de la famille des méthodes en éléments discrets; il s'agit respectivement de le DEM de type Cundall, la dynamique des contacts non régulière, et une approche de calcul statique élastoplastique. La non-unicité de la solution est le principal problème avec les techniques choisies, et elles sont étroitement liées à l'indétermination des forces dans le système.

Les trois méthodes sont d'abord présentées et validées en les appliquant à l'estimation des forces dans les systèmes granulaires 2D générés au moyen de simulations DEM explicites. Nous prenons ces simulations comme des expériences "idéales" dans le sens où elles fournissent des données similaires à celles extraites des expériences, mais dépourvues d'erreurs de mesure. Un avantage évident de cette stratégie est d'obtenir des ensembles de forces faisant office de référence faisant foi. Sur cette base, les principaux aspects affectant la détermination des forces peuvent être étudiés. En particulier, le rôle crucial de l'histoire du chargement est mis en évidence et certaines solutions pour les prendre en compte dans la détermination des forces ont été prospectées. Une évaluation de l'influence de l'erreur de mesure a également été réalisée pour prédire l'applicabilité de chaque méthode à des expériences réelles. Une brève analyse de la variabilité des solutions est également fournie.

Finalement, des tentatives ont été faites pour déduire des forces issues d'expériences effectuées dans le dispositif $1\gamma2\varepsilon$. La cinématique des particules et la connectivité ont été évaluées au moyen de la technique de corrélation d'image numérique. Les avantages

et inconvénients des trois méthodes ont été éclaircis. Ils nous conduisent à envisager une utilisation combinée des trois méthodes pour tirer parti de leurs atouts respectifs. À l'avenir, il conviendra de réfléchir à la prise en compte de la stabilité de la solution – dans l'algorithme de convergence vers une solution – avec l'espoir de limiter la variabilité des solutions.

# Contents

**Introduction** **7**

**1 Linking the micro-scale with the macro-scale in granular materials** **12**
1.1 Motivations . . . . . 12
1.2 The missing link: measuring intergranular forces from experiments . . . . 14
1.2.1 Carbon paper technique . . . . . 14
1.2.2 Photoelasticity . . . . . 16
1.2.3 Contact forces estimated from grain geometry . . . . . 17
1.2.4 Contact forces from full field measurements . . . . . 18
1.3 Limitations and future challenges . . . . . 20

**2 Numerical methods for contact force estimation** **22**
2.1 Mathematical formulation of the methods . . . . . 25
2.1.1 Contact Elasticity Method (CEM) . . . . . 25
2.1.2 Contact Dynamics-based Method (CDM) . . . . . 28
2.1.2.1 Contact (and/or impact) laws . . . . . 30
2.1.2.2 Single-contact (local) problem . . . . . 32
2.1.2.3 Multi-contact (global) problem . . . . . 37
2.1.3 Quasi-Static Method (QSM) . . . . . 38
2.1.3.1 Overview of the method . . . . . 39
2.1.3.2 Matrix form of the problem . . . . . 39
2.1.3.3 Global projection: static admissibility . . . . . 42
2.1.3.4 Local projection: plastic admissibility . . . . . 43
2.1.3.5 Iterative procedure . . . . . 44
2.1.4 Comparison of the three methods and discussion . . . . . 45
2.2 Numerical application to a simple system . . . . . 49
2.2.1 Contact Elasticity Method . . . . . 51
2.2.2 Contact Dynamics-based Method . . . . . 54

2.2.2.1 Step-by-step procedure . . . 54
2.2.2.2 Characterisation of admissible solutions . . . 57
2.2.2.3 Analysis of the convergence . . . 59
2.2.3 Quasi-Static Method . . . 62
2.2.3.1 Step-by-step procedure . . . 62
2.2.3.2 Characterisation of admissible solutions . . . 65
2.2.3.3 Analysis of the convergence . . . 68
2.2.4 Conclusions . . . 72

**3 Contact force estimation from DEM simulations 75**
3.1 DEM simulations as "ideal" experiments . . . 76
3.2 Preliminary observations . . . 79
3.3 Contact Elasticity Method . . . 84
3.3.1 Estimation of tangential forces . . . 88
3.3.2 Estimation of normal forces . . . 90
3.4 Quasi-Static Method . . . 94
3.4.1 Convergence of the iterative procedure . . . 98
3.4.2 Assessment of the influence of measurement error . . . 100
3.5 Contact Dynamics-based Method . . . 104
3.5.1 Estimation of normal and tangential forces . . . 106
3.5.2 Estimation of only normal or tangential forces . . . 110
3.5.3 Exploiting contact elasticity . . . 111
3.5.4 Convergence of the iterative procedure . . . 112
3.5.5 Assessment of the influence of measurement error . . . 114
3.5.6 Force variability . . . 118
3.6 Concluding remarks . . . 124

**4 Contact force estimation from experiments 130**
4.1 Experimental campaign . . . 130
4.1.1 Granular material . . . 131
4.1.1.1 Normal compression on two particles . . . 132
4.1.2 The $1\gamma 2\varepsilon$ device . . . 135
4.1.3 Tests . . . 138
4.1.3.1 Isotropic compression . . . 138
4.1.3.2 Biaxial vertical compression . . . 139
4.1.3.3 Biaxial horizontal compression . . . 142
4.1.3.4 Simple shear . . . 142

4.1.3.5 Oedometer compression . . . 144
4.1.4 Measurement of particle kinematics . . . 146
4.1.4.1 Contact detection . . . 147
4.1.4.2 Particle Image Tracking . . . 148
4.1.4.3 Measurement accuracy . . . 149
4.1.5 Preliminary results . . . 151
4.1.5.1 Contact orientation . . . 152
4.1.5.2 Preferential orientations of contact deflection evolution . . . 154
4.2 Estimation of contact forces . . . 155
4.2.1 Contact Elasticity Method . . . 156
4.2.1.1 Assessment of measurement error . . . 157
4.2.1.2 Oedometer compression . . . 159
4.2.1.3 Isotropic compression . . . 160
4.2.1.4 Biaxial compression . . . 161
4.2.2 Quasi-Static Method . . . 163
4.2.2.1 Oedometer compression . . . 164
4.2.2.2 Other tests . . . 167
4.2.3 Contact Dynamics-based Method . . . 170
4.2.3.1 Oedometer compression . . . 172
4.2.3.2 Isotropic compression . . . 175
4.2.3.3 Biaxial vertical compression . . . 175
4.2.3.4 Biaxial horizontal compression . . . 178
4.2.4 Comparison between the three methods . . . 178

**5 Conclusions** **182**
5.1 Summary and conclusions . . . 182
5.2 Future work and perspectives . . . 187

**Bibliography** **190**

**List of Figures** **196**

**List of Tables** **205**

**Appendices** **206**
A Matrix form of the single-contact problem in the CDM . . . 207
B Determination of the interparticle friction coefficient . . . 210

# Introduction

Granular matter refers to a very heterogeneous class of materials, characterised by the fact that they are composed of distinct particles interacting at their contact points. These materials are ubiquitous in the world around us: after water, they are the second-most handled material on Earth. They represent an extremely vast category, spanning a wide range of particle size (from very small size particles, constituting powders, to grains); they include natural materials, such as sand and snow, but they can be of great commercial importance, particularly for applications in the pharmaceutical industry, agriculture and energy production. They can occur in nature in different states, assuming characteristics typical of solids, liquids or gases. Because of all these features, their study represents a multidisciplinary task, that involves physics and geomechanics among others.

In the field of geomechanics and geotechnical applications, research interest on granular materials has been increasing in the last decades. Historically, most engineering problems have been tackled with the tools of continuum mechanics, mainly based on phenomenological observations. Latest research has been focusing on how the discrete nature of granular materials affects their macroscopic behaviour, making continuum mechanics unsuitable for a complete description of such materials. Discrete Element Methods (DEM, see Cundall and Strack (1979)) have opened the way for a characterisation of the micromechanics of granular materials, giving full access to the particle scale.

Despite having proved an extremely powerful tool for the understanding of some typical features of these materials, numerical simulations still cannot replace experimental testing on real materials, particularly in terms of particle shape. Thus, the experimental characterisation of micromechanics remains fundamental for physically understanding the material behaviour. Calvetti et al. (1997) divided this challenging problem in three separate tasks: the description of the structure (*i.e.*, positions of grains and contact points); their evolution in time, *i.e.*, grain-scale kinematics (particle displacements and rotation); the description of inter-granular contact forces.

Among the three tasks for experimental characterisation of micromechanics, the first

two have been more accessible. Several techniques have been used to describe the geometrical arrangement and to perform full-field measurements, giving access to the particle scale of granular materials, first in 2D and then in 3D. Nowadays, grain-scale measurements can benefit from the technological advances in imaging techniques, both in 2D (high-resolution photographs) and in 3D, with X-ray computed tomography and 3D X-ray diffraction allowing a full characterisation of the granular geometry. The determination of the grain-scale kinematics is based on Digital Image Correlation and Digital Volume Correlation, respectively in 2D and in 3D.

The effort to experimentally characterise the micromechanics of granular materials has also involved the design of specific experimental equipments. One of these is the $1\gamma 2\varepsilon$ device, a shearing machine that allows 2D tests on Schneebeli material (a 2D analogue of a granular material, *i.e.*, an assembly of cylinders with a fixed length), with independent control on the three components of the macroscopic strain tensor ($\varepsilon_{xx}$, $\varepsilon_{yy}$ and $\gamma$, hence the name). Digital Image Correlation (DIC) can be applied to photographs of the assembly in order to obtain full-field measurements and characterise the geometry of the granular structure, commonly referred to as fabric. A variation of DIC, referred to as Particle Image Tracking, has been proposed by Combe and Richefeu (2013) as an adaptation to the discrete nature of this category of materials. This technique allows the measurement of the rigid-body kinematics of each individual particle.

What is lacking, from the point of view of the experimental micromechanical characterisation, is the measurement of interparticle forces, that still remains very challenging. In attempting to measure contact forces, directly or indirectly, the rich information that can be obtained in terms of geometrical arrangement and grain-scale kinematics represents an extremely powerful tool to be exploited. At the moment, a complete description of contact forces in a granular material requires a full characterisation of the micro-scale.

The measurement of contact forces is essential for understanding the mechanics of granular materials. First, it can help link the micro-scale (contact scale) with the macro-scale (sample-scale) behaviour of such materials, which is fundamental for building physics-based constitutive models. The investigation of force chains and their evolution, and in particular the phenomenon of force chain buckling, has been shown to be related to the onset of instability, and so to failure, in several works by Tordesillas (Tordesillas and Muthuswamy, 2009; Tordesillas et al., 2009). The understanding of other typical features of granular materials can benefit from the knowledge of contact forces: *e.g.*, it is the case of jamming, for which the apparition of force chains is a signature. At the same time, force transmission is relevant to several phenomena of engineering interest, *e.g.*, grain breakage and crushing (Stasiak et al., 2017; Karatza et al., 2018), that plays

a main role, for example, at the soil-pile interface (Doreau-Malioche et al., 2018). Intergranular force estimation is also crucial to understand the physics behind dynamic phenomena, such as projectile impact on granular materials (Ciamarra et al., 2004), for the study of both the drag force on the projectile and the distribution of normal contact forces between particles.

Important results in the field of contact force measurement have been obtained with some methods that will be briefly presented in Chapter 1. First experimental observations showed the heterogeneous character of force transmission in a granular packing (Dantu, 1957); more recently, new techniques have opened the way first for a statistical characterisation of normal forces, and then for a more accurate estimation of individual normal and tangential contact forces, both in 2D and 3D.

All these methods have their advantages and limitations; due to this, no method has really taken hold so far as a systematic method for force inference in non-ideal granular materials. For this reason, the research interest on this topic has not dampened.

The objective of this doctoral work is to discuss new possible approaches, being in general less demanding in terms of required experimental measurements, and suitable for application to any kind of material. To this purpose, three different approaches will be proposed for the estimation of interparticle forces in a 2D granular packing, in the philosophy of combining experimental measurements with numerical tools.

The experimental campaign was performed in Grenoble by means of the $1\gamma2\varepsilon$ device; the performed tests will be described in Chapter 4, together with the methodology for data acquisition, including high-resolution photography and Digital Image Correlation, with a focus on the adopted technique (Particle Image Tracking).

The information extracted from experiments consists of boundary conditions (external loading applied on the boundary), geometrical arrangement (grain position, contact network) and particle rigid-body motion (displacements, rotation). We aim to estimate contact forces from this data. Three different methods used with this purpose are presented in Chapter 2, with a focus on the required experimental measurements and the implemented equations and algorithms. A first method, referred to as *Contact Elasticity Method* (Sec. 2.1.1), estimates contact forces directly from contact relative displacements, exploiting the local elasticity at the contact scale but without imposing any condition to the resulting forces (*e.g.*, particle equilibrium for quasi-static loading conditions). The *Contact Dynamics-based Method* (Section 2.1.2) is inspired from Non-Smooth Contact Dynamics; it neglects contact elasticity, assuming grains to be rigid, and it determines contact forces through the application of the Gauss-Seidel iterative method for the solution of the resulting non-linear problem for a given contact network. A third method,

called *Quasi-Static Method* (Section 2.1.3), consists in alternatively projecting a guess set of forces onto the subspaces of statically admissible and plastically admissible forces, until both criteria are satisfied. It makes use of contact elasticity, but, in addition to the first method, it also accounts for equilibrium criteria; in addition, it neglects inertia, treating the evolution of a granular assembly as a succession of equilibrium states.

Before attempting an application to real experimental data, a number of 2D DEM simulations were performed, and the same data coming from experimental measurements (*i.e.*, fabric and particle kinematics) were extracted from these simulations in order to estimate the contact forces, with the clear advantage that in this case we get rid of any measurement error. Since the simulations were performed in quasi-static conditions, the actual values of contact forces were known at any stage of the simulations, and this allowed a comparison between the estimated forces and the true forces (*i.e.*, those obtained from the DEM simulations). In this way, by using simulations as a benchmark, the validation of the three approaches was carried out. These results are presented in Chapter 3. This section also includes an assessment of the influence of some experimental conditions, such as the frequency of measurements and their accuracy (measurement error). In particular, the latter was carried out by artificially perturbing the input data and measuring how this affected the estimation of forces, in order to reproduce experimental conditions and predict the reliability of each method.

Chapter 4 presents results from an application of the three methods to an experimental case, involving a number of different tests (oedometer compression, isotropic compression, biaxial vertical and horizontal compression) performed in the $1\gamma2\varepsilon$ device. Several criteria are adopted to evaluate the reliability of the solution, including the computation of a homogenised stress tensor from contact forces and of the distance from static equilibrium for each particle (having loaded the assembly in quasi-static conditions).

Finally, the main results are summarised in Chapter 5, in which future challenges and perspectives for incoming work are discussed.

# Chapter 1

# Linking the micro-scale with the macro-scale in granular materials

## 1.1 Motivations

In geomechanics, the study of granular materials has been typically carried out with the tools of continuum mechanics.

However, the discrete nature of these materials should not be neglected, as it is responsible for many aspects of their macroscopic behaviour. Almost one hundred years ago, this was brilliantly pointed out by Terzaghi (1920): "(...) Coulomb (...) purposely ignored the fact that [soils] consist of individual grains. Coulomb's idea proved very useful as a working hypothesis (...) but it developed into an obstacle against further progress. (...) [let's start] again from the elementary fact that [soils] consist of individual grains".

Accessing the particle scale is thus necessary for a complete description of granular materials, that should emerge from a link between the microstructure and the macroscopic scale. Moreover, constitutive models are often based on phenomenological observations, and consequently built on variables that might not have a clear physical meaning. Hence, linking the two relevant scales in granular materials is also fundamental for developing models that are more physics-based, by describing grain-scale phenomena and how they affect the mechanics at a larger scale.

With the aim of building multiscale approaches, the study of granular microstructure has been of interest to the scientific community for decades (see, *e.g.*, , the state-of-art work by Radjai et al. (2017)), first by means of experiments, and then also of numerical simulations. The way forces are transmitted through contacting particles under external

load is a main ingredient of micromechanics, and it is a clear evidence of the discrete nature of such materials. A perfectly uniform load sharing between particles is only possible in a crystal of identical spheres; in real materials, the slightest inhomogeneity of the packing results in a very heterogeneous distribution of forces. Geometrical exclusions and disorder are thus controlling the mechanism of force transmission in a granular assembly; in particular, forces tend to self-organise in chain-like structures, as Dantu (1957) first showed from photoelastic experiments. This qualitative observation was later corroborated by several studies, both experimental (Liu et al., 1995; Mueth et al., 1998; Majmudar and Behringer, 2005) and numerical (Radjai et al., 1996b, 1999). More recently, it has been possible to statistically characterise granular microstructure, both in terms of contact forces (Radjai et al., 1996b; Mueth et al., 1998) and of particle kinematics, for which non-affine particle displacements represent a typical proof of the divergence from a continuum-like behaviour (Radjai and Roux, 2002; Richefeu et al., 2012; Combe et al., 2015) and are currently being studied to highlight possible relations with the bulk material properties.

Important advances in the study of granular microstructure can be ascribed to the development of numerical techniques. Discrete Element Methods (DEM) first provided full access to the grain-scale of granular materials, by directly describing the dynamics of grains through integration of the Newton's law, and modeling intergranular contacts with appropriate laws accounting for friction. Numerical DEM simulations allow a complete characterisation of the micromechanics of an assembly, in terms of both particle motion and interparticle forces; on the other hand, grain-scale characterisation in experiments did not advance likewise in the last decades. Advances have been made from the point of view of kinematics, with the development of imaging techniques such as Digital Image Correlation and the improvements in measurement resolution, that made it possible to measure particle motion and deformations (Andò et al., 2012; Hasan and Alshibli, 2012; Combe and Richefeu, 2013), opened the way for a more complete characterisation of granular fabric in 3D (Wiebicke et al., 2017) and allowed building multiscale approaches (Andrade et al., 2011); on the other hand, measuring interparticle forces – either directly or indirectly – still remains a challenge to researchers, despite progresses in describing their statistics and spatial distributions. Several methods have been proposed in the last decades, combining experimental measurements with numerical techniques for force inference, but a systematic method for non-idealised, stiff particles has not emerged yet. In the following sections, some of these methods will be briefly presented, to show their advantages and limitations.

## 1.2 The missing link: measuring intergranular forces from experiments

In the context of experimental grain-scale characterisation, measurement of normal and tangential contact forces represents the missing part for a complete description of the micromechanics of granular materials.

To this purpose, a general method, applicable to all kinds of materials, has not emerged yet. Nevertheless, valuable results were obtained with different techniques, some of which are fully experimental, some others combining experimental measurements with numerical approaches. Important properties of force distributions, such as the exponential tail of normal force distributions for above-average (strong) values, were found to be characterising features of granular materials by means of these experimental techniques.

The main existing methods will be briefly introduced in the following sections, and their main features highlighted, also to anticipate common points and differences with the approach we propose. Among these techniques, carbon paper (Liu et al., 1995; Mueth et al., 1998; Blair et al., 2001; Mueggenburg et al., 2002) showed the heterogeneity of the distribution of forces at the bottom of a specimen, allowing a statistical study of such forces. Photoelasticity, first introduced by Dantu (1957) and then further developed by Allersma (1982) and by Majmudar and Behringer (2005), has been one of the most popular methods of force inference, giving access to a full characterisation (also quantitative) of contact forces in 2D packings − with attempts in 3D (Muir Wood and Leśniewska, 2011) −, though limited to a specific category of materials, and by necessary hypotheses on the constitutive behaviour. A first attempt to estimate normal forces from grain geometry in a packing of soft elastic spheres was performed by Saadatfar et al. (2012). More recently, approaches such as the Granular Element Method (Andrade and Avila, 2012) have been aiming to infer forces by trying at the same time to satisfy particle equilibrium and fit an average grain stress tensor obtained, through constitutive assumptions, from particle deformation, which can be measured, *e.g.*, by means of a combination of X-ray diffraction and X-ray tomography.

### 1.2.1 Carbon paper technique

The carbon paper method allows indirect measurements of the normal forces applied by the beads of a confined granular assembly on the walls. It makes use of a layer of carbon paper, placed on the constraining surfaces, that covers a blank sheet of paper.

By pressing the carbon paper onto the blank one, beads leave a mark whose darkness and area depend on the exerted force (Figure 1.1); through an appropriate calibration of the (monotonic) relationship between either mark's descriptor and the applied force, a quantitative assessment of forces over a range covering two orders of magnitude can be obtained, with an error of less than 15%. This degree of accuracy, together with the possibility of spanning such a wide range of values, was the key to studying the distribution of normal forces, and whether this is affected by changes in the spatial ordering or in boundary conditions.

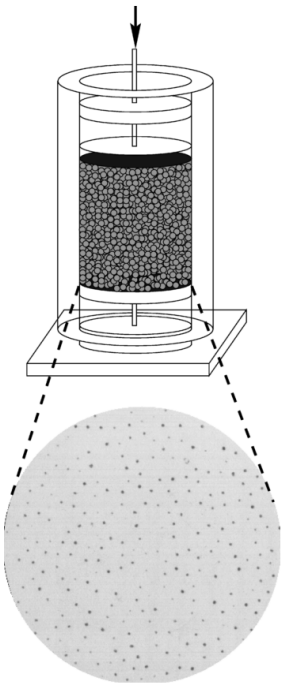

Figure 1.1 – Sketch of the experimental apparatus used by Mueth et al. (1998). A load is applied to the upper piston and the beads press the carbon paper into white paper, leaving marks from which contact forces can be determined, as shown by the detail of the marks left at the bottom boundary.

In particular, Mueth et al. (1998) showed that neither lateral boundary conditions nor spatial correlations in the arrangement of beads have a significant influence on the spatial probability distribution of forces, which is found to follow an exponential decay for the above-average normal forces, consistently with results from numerical simulations (Radjai et al., 1996b). As to the distribution of forces below average, more contrasting results were obtained, as the power laws predicted by Coppersmith et al. (1996) and Liu et al. (1995) were not confirmed with the improvement in sensitivity when measuring low forces.

However, this method shows some major limitations: it gives no information on

tangential forces, and it can only measure normal forces at the boundary of a specimen, without any insight on how forces are transmitted between grains, involving the majority of contacts; moreover, although the range of measurable forces was enhanced in the more recent applications, it is still not possible to capture very low forces, which also prevents from having a direct measure of the number of contacts.

### 1.2.2 Photoelasticity

As previously mentioned, photoelastic experiments by Dantu (1957) opened the way for revealing the highly inhomogeneous nature of force transmission in granular materials; more recent developments of the method have provided a better characterisation of forces from a quantitative point of view (Majmudar and Behringer, 2005; Daniels et al., 2017) – also in combination with other techniques such as the previously mentioned carbon paper one (Liu et al., 1995).

This technique exploits stress-induced birefringence, that is an optical property of a category of materials; based on this property, stress paths can be highlighted in this so-called photoelastic material (Figure 1.2).

Photoelastic experiments are typically performed on 2D systems (3D analogue of a 2D material). Force components are inferred by fitting the observed photoelastic pattern inside each disk based on the plane elasticity solution, assuming a perfect line contact between 3D grains.

Following results obtained with the carbon paper method, experiments on photoelastic disks by Majmudar and Behringer (2005) contributed to the statistical characterisation of contact forces, showing different behaviours between sheared and isotropically compressed systems; at the same time, by accessing the whole contact network, it showed the existence of spatial correlations of forces that were not observed before, providing a possible quantification for the concept of force chain. Though mainly applied to model materials, photoelasticity's governing equations can be adapted for application to arbitrarily-shaped grains.

The main limitation of this method is that its applicability remains constrained to a very specific category of materials; for real geologic materials, photoelasticity cannot provide an estimation of forces. Moreover, the method requires strong constitutive hypotheses on the material: assuming a plane elastic behaviour, as it is done in most applications of photoelasticity to infer forces, sets another significant limitation to the applicability. Finally, as for the carbon paper technique, the measure of very low forces remains dependent on the experimental resolution.

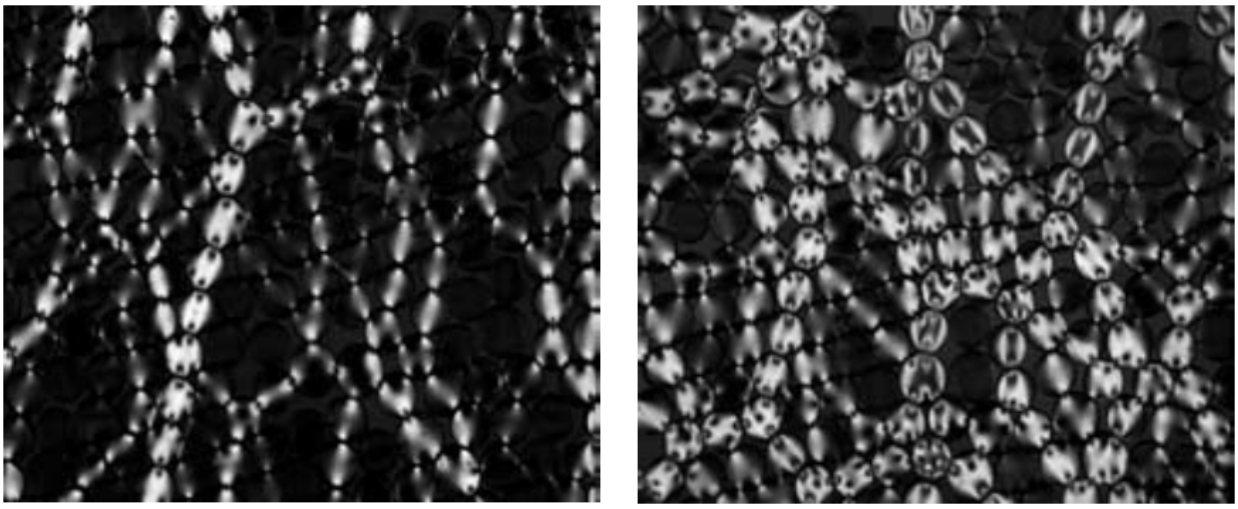

Figure 1.2 – Typical stress paths highlighted with photoelasticity: on the left, for a low-force sheared state; on the right, for a high-force isotropically compressed one (Majmudar and Behringer, 2005).

### 1.2.3 Contact forces estimated from grain geometry

Saadatfar et al. (2012) proposed a method that aims to infer contact forces from the simple grain geometry, based on the assumption of an appropriate contact law, in a packing of soft elastic spheres (rubber). By applying imaging techniques to X-ray computed tomography 3D images, the grain-scale kinematics of a granular assembly can be quantified. Local quantities can be defined in order to establish a relation with the estimated force. In particular, a particle interpenetration (overlap) is introduced to describe the contact compliance. Two possible definitions are taken into account: either to estimate the overlap from the distance between grain centres, or to derive it from the measured contact area, that is related with the number of voxels in common between two grains. Based on the latter definition of overlap (being less sensitive to measurement accuracy), the nonlinear Hertz-Mindlin model is assumed as a contact law to link the measured overlap with the estimated normal force. For the adopted material, the applicability of such a law is confirmed by the investigation of the mechanical response when compressing individual grains.

This alternative approach confirmed some well-established results, especially in terms of normal forces distributions, which was found to be exponential for large forces, as widely documented in previous literature and summed-up beforehand. Moreover, being based on simple contact laws, this method of force estimation turns out to be generally applicable to arbitrarily-shaped grains.

Apart from the lack of information on tangential forces, for which a measurement of particle rotation is required, the method's main limitation lies in the high sensitivity to the measurement accuracy and resolution, that limits its applicability to a narrow range of particle stiffness and applied load. This is particularly problematic for the evaluation of low forces, that are the most sensitive to this issue.

### 1.2.4 Contact forces from full field measurements

Based on advances in measuring average strain in sand particles, a method, also referred to as Granular Element Method (GEM), was proposed by Andrade and Avila (2012), aiming to link measured intra-particle strain fields with inter-particle contact forces.

The first step of the method consists in a full grain-scale description based on experimental imaging techniques. Image processing and Digital Image Correlation are used, respectively, to quantify geometrical arrangement and assess grain kinematics, including displacements and rotation, as well as particle deformation. Full-field grain strains are necessary to obtain volume-averaged grain stresses, and they can be found by using Digital Image Correlation on high-resolution photographs in 2D or Digital Volume Correlation for volumetric 3D images, that can be obtained as a combination of 3D X-ray diffraction and X-ray computed tomography (Hall et al., 2011) or from confocal microscopy (Mac Donald and Ravichandran, 2018).

By using grains as "strain gauges", GEM aims to use such measurements for inferring interparticle forces through the assumption of an appropriate constitutive law (*e.g.*, elasticity) that may link the measured average grain strain with an average grain stress. Then, the combination of basic Newtonian mechanics (that, for quasi-static loading conditions, translates into balance of linear momentum) with the fitting of the grain stress provides a system of equations in which contact forces appear as unknowns.

This general formulation also applies to grains of arbitrary shape, texture and opacity; applications have been made to both 2D and 3D granular packings.

Figure 1.3 shows contact forces inferred in a 2D assembly by Marteau and Andrade (2017). The obtained forces appear to be organised in the chain-like structures that are typical of granular materials. In addition, they show a good agreement with patterns of principal stress difference that emerge from the stress field measurements.

Force inference in a 3D material in quasi-static loading conditions was performed by Hurley et al. (2016a), by solving a multi-objective optimisation problem, that consists in finding the set of contact forces that best fits the measured data, in terms of stress (expressed by the stress-force relation) and momentum balance. A result from this work

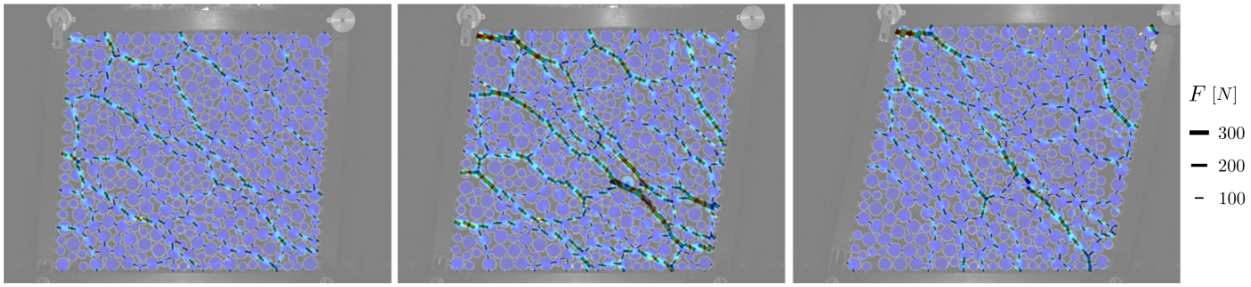


Figure 1.3 – Contact forces inferred with GEM superimposed on difference of principal stresses $\sigma_1 - \sigma_2$ for a simple shear test (Marteau and Andrade, 2017), at $\gamma = 0.075$ (left), 0.15 (center) and 0.275 (right).

is shown in Figure 1.4. Large magnitudes of the contact force vectors are found in correspondence of highly strained grains. Two force chains are isolated by drawing only those forces carrying at least twice the mean normal force (and the corresponding grains). The estimation of contact forces also allowed analyses on some of the main characteristics of force networks: in particular, force heterogeneity was quantified, showing a surprising inverse relationship with macroscopic load. In addition to this work, the multiobjective optimisation algorithm was also adopted for applications to the dynamic regime (Hurley et al., 2016b; Karanjgaokar, 2017), for impact tests on 2D granular assemblies.

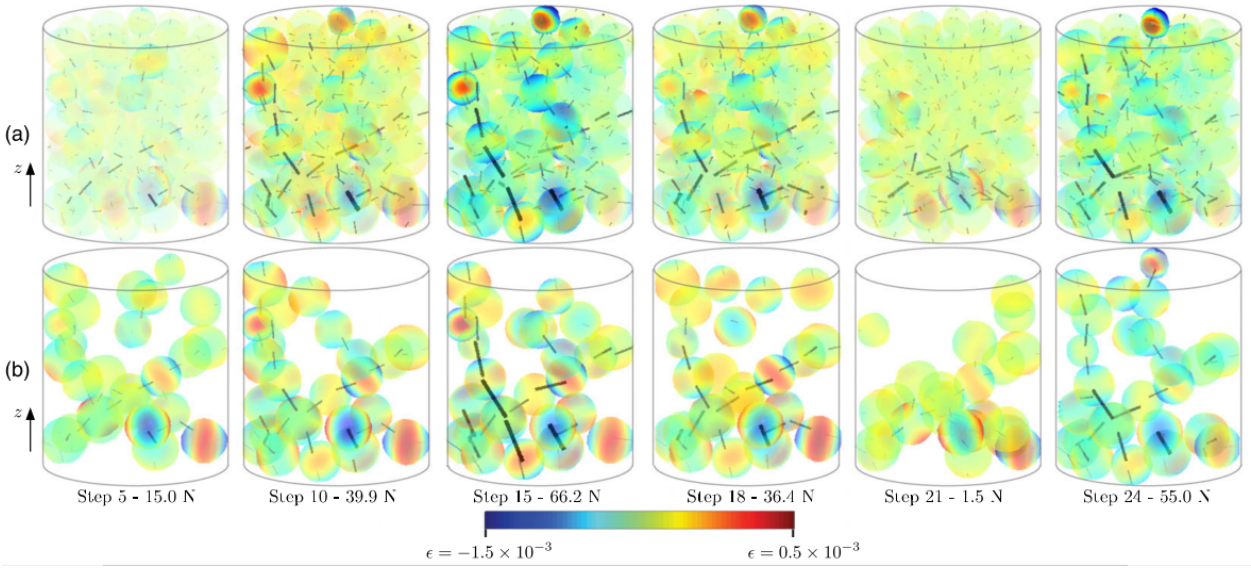


Figure 1.4 – Contact forces obtained in a 3D, frictional, stiff material by Hurley et al. (2016a), for a uniaxial compression test on quartz grains. (a) Force inference results at six load steps on a translucent rendering of grains coloured by strain ellipsoids. (b) Force chains found by plotting only forces whose normal magnitude exceeds twice the mean. Corresponding grains are also plotted with 30% opacity.

The general framework of this method makes it suitable for force inference in real materials. However, the method requires that grain deformation be measurable with a sufficient accuracy; hence, its applicability depends on a combination between the stiffness of the particles and the resolution of the measurements. This also sets a limitation to the scale of the system: even when working with non-idealised granular materials, the number of grains involved in the application of this method is rather small. The representativeness of such small systems can be questionable; some phenomena and typical observations, such as the apparition of shear bands, are difficult to reproduce when the number of grains is limited. In perspective, for the improvement of methods based on strain field measurements or for proposing different approaches, the size of the system will be a main concern, also to the purpose of enhancing the information on forces for a quantitative enrichment of their statistical study.

## 1.3 Limitations and future challenges

All the already existing methods have their own, specific features, with advantages and disadvantages, which have been mentioned in the previous sections. It is important, however, to focus on the main limitations, particularly those that are common to several approaches, in order to highlight the future challenges related to experimental force inference, and introduce the main motivations behind the approach proposed in this doctoral work.

Measurement accuracy is a primary issue for all the methods that have been discussed here. In particular, as previously explained, it sets limitation to several aspects of the experimental tests to which interparticle force estimation is applied. The stiffness of the particles is one of these: very stiff ones, for which intra-particle deformation or contact compliance cannot be easily determined with the current tools, are excluded from the range of applicability of some of the methods shown. There is also a scale problem: the number of grains in all these applications is generally limited, mainly to the purpose of providing a sufficient resolution for the grain-scale measurements. Even when forces are directly estimated, without any measurement of the grain-scale kinematics (Section 1.2.1), the information is quantitatively limited by the fact that only boundary contacts are accessible.

Measurement accuracy would certainly benefit from the desirable – and foreseeable – technological advancement in imaging resolution, in 2D (photography) and 3D (X-ray computed tomography, 3D X-ray diffraction), as well as in dynamic conditions (high-speed photography in 2D, which remains at the moment the only field of applicability).

However, it is advisable to proceed, in parallel, with building approaches that can be less sensitive to measurement accuracy. Such an approach should be able to estimate forces from simple measurements, possibly reducing the amount of required input information.

# Chapter 2

# Numerical methods for contact force estimation

Imaging techniques and technological advancements have given access, in experiments, to the micro-scale of granular materials, *i.e.*, the scale of the grain, from the point of view of grain-scale kinematics. On the other hand, a way for a direct measurement of inter-particle contact forces is yet to be found.

The aim of this doctoral work is to find the missing link between what is measurable at the grain-scale and what is not yet. This consists in proposing an approach that exploits the information obtained from direct measurements (geometrical arrangement, grain-scale kinematics) to perform an estimation of contact forces.

With this purpose, it is natural to think of the discrete approach for numerical modelling of granular materials, with its ability of giving a full description of the micromechanics in granular materials, as a tool to link these two classes of micro-scale variables.

The Discrete Element Method (DEM) was first introduced by Cundall and Strack (1979) for granular geomaterials as a method that describes particle interactions through two aspects: the unilateral character of contacts, that can only transmit compressive forces; the dissipation of energy, that comes from contact friction and inelastic collisions. This formulation was the first, and is still the most common one, to be applied to geomaterials; however, some alternative methods have emerged in the last decades, describing contact interactions in different ways. Hence, it is appropriate to consider the DEM as a family of methods, rather than a single one. From the DEM family, two more methods are suitable for application to dense systems, in which the granular assembly behaves as a solid. The Contact Dynamics (CD) method, proposed by J. J. Moreau and M. Jean (Moreau, 1977, 1983, 1988a,b, 1997, 2004; Jean and Moreau, 1992), describes contact frictional interactions assuming rigid particles with non-compliant contacts. When the

system can be described as a sequence of states of mechanical equilibrium, a quasi-static (QS) formulation can be adopted, replacing the dynamics that is used in the first two methods (Roux and Combe, 2011).

In order to distinguish between these three methods, we can refer to Cundall's formulation as MD-DEM, from the Molecular Dynamics (MD) formulation that is used for the simulation of molecular systems, and has a formal analogy with Cundall's application to granular systems; similarly, we refer to Moreau and Jean's formulation as CD-DEM, and to the quasi-static one as QS-DEM.

To summarise their main differences, we can refer to the modelling ingredients and parameters that are involved. The MD-DEM is the method that involves the most ingredients, *i.e.*, inertia, contact elasticity and friction. CD-DEM keeps inertia and friction, discarding contact elasticity through the assumption of rigid particles with non-compliant contacts. QS-DEM keeps contact elasticity and friction, while discarding inertia.

Another major difference between these approaches lies in the nature of their governing equations. In the MD-DEM, contact forces are explicitly defined as a function of contact relative displacements. In the other two methods, forces are not uniquely determined: there is a certain degree of indeterminacy that induces a variability of the solution.

Based on each of these methods, we aim to propose three approaches that, by taking the geometric (*i.e.*, contact network) and kinematic measurements as input, together with a loading that the sample can support, can make an estimation of the contact forces. As the three DEM are quite different from each other, the derived methods for force estimation will also differ; their working principles will be detailed in the following sections, but it is worth mentioning some of their main features.

The first proposed method stems from the MD-DEM and its force laws (assumed to be linear elastic for normal forces, and elasto-plastic for tangential ones); it makes a direct estimation of forces based only on the measured kinematics, relying on the evaluation of contact deflections and on contact elasticity. Hence, we refer to this force estimation technique as Contact Elasticity Method (CEM).

Based on the CD-DEM, we propose a method that, on the other hand, neglects the length scale associated with contact deformation, assuming perfectly rigid bodies and imposing that no particle interpenetration occurs. This will be referred to as Contact Dynamics-based Method (CDM).

Finally, we apply the quasi-static approach on single equilibrium states of a granular assembly; this consists of numerically resolving a problem in which contact forces, that appear as the unknowns of the problem, are required to satisfy two criteria at the same

time: the static equilibrium for all particles, and Coulomb's friction law for all contacts. We refer to this method as Quasi-Static Method (QSM).

In order to present the proposed numerical methods and their mathematical formulation, after the description of their main features and equations involved, an application is performed on a simple system composed of three disks; two of the disks are fixed in position, and the third one is in contact with both of them (Figure 2.11).

Before this, some remarks should be made on the nature of contact forces in granular packings, and on their determination with numerical methods. Based on the model adopted for the treatment of particle interactions, contact forces might not be uniquely determined. McNamara et al. (2005) have investigated this indeterminacy in detail for the case of a single disk in contact with two walls, equivalent to the one that we will study in Section 2.2. In the considered paper, the system is studied – both analytically and numerically – with two models for particle interaction: one assuming perfectly rigid particles with non-cohesive, frictional contacts, equivalent to the assumption in CD-DEM; the other one accounting for a contact compliance, in the same way as MD-DEM is defined. By testing both models, a duality is shown between indeterminacy, typical of the models with rigid particles, and memory, as the extra ingredient through which the model based on contact compliance obtains a unique solution for the contact forces. It is proved that when, with methods assuming rigid particles, the space of possible solutions is investigated, this is actually equivalent to searching over all the possible past histories of the packing.
With the aim of estimating forces in granular assemblies by means of numerical techniques, this link turns out to be crucial, as we will see in the description and application of the three methods.

A more accurate characterisation and quantification of the variability of forces due to non-uniqueness has also been attempted by several authors (McNamara and Herrmann, 2004; Unger and Kertesz, 2003; Unger et al., 2005); these works will be recalled later, when force variability will be quantified in the context of the application of the three methods to numerically-generated packings. For the purpose of the presentation and discussion of the methods, however, it can be sufficient to describe force indeterminacy on the basis of geometric quantities. The parameter that is typically invoked to this purpose is the *degree of force indeterminacy h* (also referred to as *degree of hyperstaticity*), which can be related to geometric properties of the assemblies through the following expression:

$$N_f + k = 2N_c + h \tag{2.1}$$

where $N_f$ is the number of equations of the problem – corresponding to the number of

degrees of freedom (DOFs): 3 per particle in 2D, plus the DOFs of the boundaries –, $2N_c$ is the number of unknown forces (normal and tangential component for each of the $N_c$ contacts) and $k$ (degree of hypostaticity) is the dimension of the space of *mechanisms*, *i.e.*, the sets of particle displacements that cause no relative displacements at contacts. Typically, the mechanisms in a granular assembly (without gravity) correspond to the DOFs of floating grains (*rattlers*) that are not in contact with other grains. The balance between these quantities returns the degree of force indeterminacy $h$, *i.e.*, the dimension of the space of independent sets of contact forces that are self-balanced.

## 2.1 Mathematical formulation of the methods

In this Section, the main parameters and governing equations are described for each of the three force estimation methods.

### 2.1.1 Contact Elasticity Method (CEM)

The first of the three methods to be presented is the Contact Elasticity Method (CEM), by which we aim to estimate contact forces through the assumption of contact elasticity, *i.e.*, by exploiting the deformation occurring at the contact between two particles, and typically affecting a small area around the contact. The aim is to measure appropriately defined contact-scale kinematic variables, and use them in combination with some force laws to assess forces.

Among the three proposed methods, it certainly is the most intuitive one. It consists in simply applying the Molecular Dynamics framework, by using the typical force laws that allows the determination of forces based on the evolution between two states, which is given. The only difference lies in the time resolution: rather than small time steps that allows a sufficient discretisation of the typical duration of a contact, we can only exploit coarse-grained relative displacements provided by experimental measurements.

Following the typical force laws of MD-DEM, it is decided to adopt a linear elastic law for normal compressive forces, and a linear elasto-plastic one for tangential forces, with implementation of Coulomb friction (Figure 2.1).

The only difference with respect to the common MD force laws is in the treatment of normal forces. In MD, they are commonly derived from the definition of a particle interpenetration (or overlap) $\delta_n = d_{ij} - R_i - R_j$ (where $d_{ij}$ is the distance between the mass centres, and $R_i$ and $R_j$ are the radii of the particles). In the perspective of the application

to experimental data, however, it is not possible to define a particle overlap of physical significance as in the model of contact compliance. On the contrary, measurements of particle displacements are very accurate and reliable. Therefore, it is advantageous to treat the law for normal forces as incremental (as it is already done in the MD for tangential forces), and compute normal force increments as a function of contact relative displacements. We assume that overlap increments $\Delta\delta_n$ can be fairly approximated by normal relative displacements $\Delta u_n$, as long as the normal at the contact does not rotate much between two states:

$$\Delta\delta_n = \int \mathrm{d}u_n \simeq \left(\vec{U}_j - \vec{U}_i\right) \cdot \vec{n} \tag{2.2}$$

where $\vec{U}_i$ and $\vec{U}_j$ are the $x$- and $y$-displacements of particles $i$ and $j$, and $\vec{n}$ is the normal unit vector oriented from grain $i$ to grain $j$. Similarly, tangential relative displacements can be determined as:

$$\Delta u_t = \int \mathrm{d}u_t \simeq \left(\vec{U}_j - \vec{U}_i\right) \cdot \vec{t} - R_i\theta_i - R_j\theta_j \tag{2.3}$$

where $\theta_i$ and $\theta_j$ are the rotations of particles with radii $R_i$ and $R_j$, and $\vec{t}$ is the tangent unit vector which forms an orthonormal basis with the normal and the unit vector perpendicular to the plane defined by $\vec{n}$ and $\vec{t}$ and going out of it.

Based on these displacements, the force laws, as in Figure 2.1, take the following expressions:

$$\Delta f_n = \begin{cases} -k_n\Delta\delta_n & \text{if } \delta_n < 0 \\ 0 & \text{otherwise} \end{cases} \quad \text{and} \quad \Delta f_t = \begin{cases} -k_t\Delta u_t & \text{if } |f_t + \Delta f_t| < \mu f_n \\ 0 & \text{otherwise} \end{cases} \tag{2.4}$$

where $\mu$ is the interparticle friction coefficient.

By adopting such force laws, the determination of the parameters that describe the behaviour at the contact scale becomes fundamental, as the estimation of forces directly depends on the choice of these parameters (as well as on the measurement of particle kinematics). For experimental applications, appropriate tests can be performed to estimate these contact parameters, as we will see in more detail. Alternatively to the measurement of $k_n$, this parameter (and $k_t$ consequently) can also be estimated by means of a re-scaling procedure. Contact forces can be determined from measured relative displacements with any initial value of $k_n$ and $k_t$; in a second stage, a homogenised stress tensor can be computed from these forces, and its components compared with the ap-

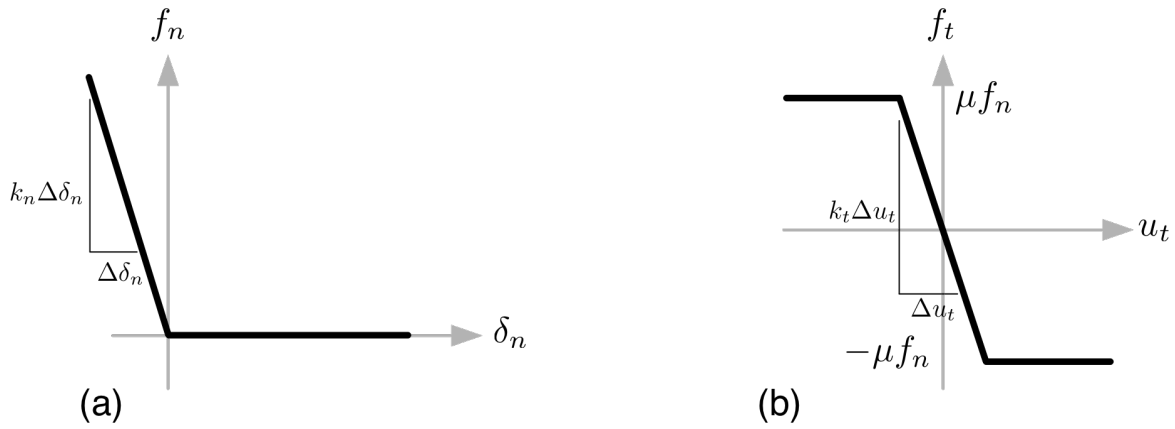


Figure 2.1 – Typical MD-DEM force laws adopted for the CEM: (left) linear elastic law for normal forces and (right) linear elasto-plastic law for tangential forces.

plied stress. The obtained ratio between the real and estimated stress components (or invariants) is then used to multiply – and, in doing so, re-scale – the contact stiffnesses.

However, some errors are intrinsic in the application of these incremental force laws to coarse-grained motions. If a non-zero normal force is already transmitted between two particles in contact in the initial state of the assembly, this model cannot recover this force. This will be discussed in more detail in Section 4.2.1. Another error is made whenever a contact is created between two consecutive states: in this case, the measured relative displacement between the two states would overestimate the increment of force, that is produced only by that part of relative displacement occurring after the two particles get into contact. To avoid this error, the initial force increment is neglected whenever a new contact is created, for both normal and tangential forces.

Some final considerations can be made on the expected quality of force estimation. Tangential forces can be expected to be more sensitive to error, with respect to normal forces. First, any error in the estimation of normal forces would also affect tangential forces, due to the condition $|f_t| \leq \mu f_n$ that introduces a dependency of the latter on the former. Moreover, an additional source of error can be found for tangential forces. Their estimation might become less accurate when the initial state is close to (or at) the yield surface, and measured displacements might not produce any force increment. Once more, this shows how the motion resolution of the problem is crucial to have a good quality of force estimation.

### 2.1.2 Contact Dynamics-based Method (CDM)

The CD-DEM, often referred to as Non-Smooth Contact Dynamics (NSCD), is a discrete element method for the simulation of granular materials that stems from a mathematical formulation of non-smooth dynamics by J. J. Moreau and M. Jean (Moreau, 1977, 1983, 1988a,b, 1997, 2004; Jean and Moreau, 1992).

A noticeable difference between this method and the common MD-DEM lies in how the small length and time scales associated with contact interactions are described. In MD-DEM, as shown in Section 2.1.1, particles are rigid, but their contacts are assumed to be compliant and the corresponding forces are expressed, through *force laws*, as a function of the current mechanical state. The discretisation of the equations of dynamics, for their numerical resolution, requires the time step to be small enough to guarantee a sufficiently fine discretization of the duration of a contact.

By contrast, in CD-DEM this small scale is not addressed and the contacts are not compliant (elasticity is removed). This makes the kinematics non smooth and, consequently, the force laws are replaced by *contact laws*, expressed as complementarity relations by means of inequalities that simply impose the conditions of non-interpenetration of particles (Signorini condition) and Coulomb's friction law. Forces and velocities are determined at the same time by crossing, at each contact, the contact laws with the equations of dynamics, that need to be expressed on a contact-base, rather than a particle one. Since the force at a single contact depends on all other contacts of the system, the global problem requires a numerical resolution that can be carried out by means of an iterative method. The most-commonly used method is the Gauss-Seidel one, which basically consists in solving the problem at a single contact, and then updating forces and velocities before solving it for another contact; once all contacts are solved, the whole procedure is iteratively repeated until a stopping criterion is fulfilled.

Due to this description of contact interactions, CD-DEM is mainly suitable for the study of granular flows in which contact elastic strains are irrelevant and the dynamics is explored at the scale of particle rearrangements. This makes it particularly appropriate for the modelling of very stiff particles. One main advantage associated with the use of CD-DEM, instead of the more common MD-DEM, lies in the choice of the time step and, consequently, in the numerical optimisation: since the small time scale related to contact deformations is neglected, larger time steps can be assumed. In addition to this, the main principles through which CD models the micromechanics of granular materials seems more realistic: the assumption of rigid contacts well suits the requirement of non-interpenetration between solid bodies.

Based on this formulation, several applications have been possible, ranging from the

investigation of granular materials to that, more generally, of any mechanical system composed of rigid bodies with frictional contact interactions.

Differently from more common applications, in this work the aim is to apply Contact Dynamics' framework to the estimation of contact forces in an assembly of grains for which the contact network and boundary conditions (external loading applied) are known. Since in this method forces and velocities are determined at the same time, one does not need to know velocities a priori to determine forces; the procedure of force estimation based on this method does not require the determination of the particle-scale kinematics, which makes Contact Dynamics particularly suitable for this application.

In order to carry out the estimation of forces, the Signorini-Coulomb problem is solved at each contact for a given state; the only difference with the typical applications of Contact Dynamics is that in the latter, once contact relative velocities are determined as a function of pre-collisional (known) and post-collisional (unknown) ones, one advances to a subsequent time step, in which pre-collisional velocities are those found in the previous time step.

Here, on the other hand, the aim is simply to determine forces at a given state, since we treat individual granular configurations, taken from photographs of the assembly, independently of the others.

The main limiting feature of this approach lies in the non-uniqueness of the solution. Since contact complementarity relations are expressed as inequalities rather than equations, there is a number of possible combinations of contact forces that fulfil these relations. The resulting indeterminacy can be studied analytically and described by a degree of force indeterminacy (Radjai et al., 1996a; McNamara et al., 2005); this parameter, however, does not describe directly the variability of forces: a high degree of force indeterminacy does not necessarily imply a large variability, since the solutions are limited by the complementarity relations. Hence, it can be useful to study the variability of the solution independently, as in Unger and Kertesz (2003); Unger et al. (2005); McNamara and Herrmann (2004).

On a mathematical point of view, CD-DEM deals with non-smooth motions: this means that the equations of dynamics cannot be resolved through discretisation. In 2D, these equations are then expressed in the form of the following balance of the momenta associated with static and impulsive actions over a finite time increment $\delta t$ (Radjai and Richefeu, 2009):

$$\left\{ \begin{array}{rcl} m_i \left( \vec{v}_i^{\,+} - \vec{v}_i^{\,-} \right) & = & \left( \sum_j \vec{f}_{j \to i} + \vec{f}_{i,\text{ext}} \right) \delta t = \vec{F}_i^{\text{ext}} \delta t \\ I_i \left( \omega_i^+ - \omega_i^- \right) & = & \left( \sum_j \Gamma_{j \to i} + \Gamma_{i,\text{ext}} \right) \delta t = \mathcal{M}_i^{\text{ext}} \delta t \end{array} \right. \tag{2.5}$$

where the subscript $i$ relates to the particle $i$, superscripts $-$ and $+$ refer respectively to the beginning and the end of a time increment; $m$ is the mass, $I$ is the inertia along the direction normal to the 2D plan, $\vec{v} = \dot{\vec{x}}$ is the velocity and $\omega = \dot{\theta}$ is the angular velocity; $\vec{f}_{j\to i}$ and $\Gamma_{j\to i}$ are respectively the contact force and torque due to an external particle $j$ acting on the particle $i$; and $\vec{f}_{i,\text{ext}}$ and $\Gamma_{i,\text{ext}}$ are any "external" force (or torque) possibly applied on the particle $i$ (these terms might be caused by bulk or boundary actions).

These relations can be seen as the classical equations of dynamics where (*i*) the accelerations have been replaced by velocity jumps, and (*ii*) the actions $\vec{f}$ and $\Gamma$ are only known as the mean of some "measures" $d\vec{f}'$ and $d\Gamma$ over $\delta t$. These measures may include *static* and/or *impulsive* actions.

In the context of a CD-DEM simulation, these equations of dynamics should be solved for an *entire system* and the motion of the particles may be performed, for instance, according to the leap-frog integration scheme, as proposed by Jean and Moreau (1992). However, in the present case, only contact actions need to be assessed. To do so, the NSCD approach requires that the Equations 2.5 be expressed at the contact level rather than at the particle level.

The mathematical formulation of the method is described in the following section. The contact laws governing the problem are defined in Section 2.1.2.1; then, the solution of the problem for a single contact, involving the definition of the equations of dynamics and of transfer equations to express them at the contact level, is given in Section 2.1.2.2. In these sections, equations are expressed for a single contact $c$; for sake of clarity, we omit $c$ in the notation of the following formulation. Finally, we present the multi-contact (global) problem, which requires a numerical resolution involving the Gauss-Seidel method.

#### 2.1.2.1 Contact (and/or impact) laws

Contact laws are defined by complementarity relations – the Signorini and Coulomb conditions – respectively enforcing particle impenetrability and ranging tangential forces within the Coulomb cone. Signorini's condition can be expressed by the set of following inequalities, based on the definition of an inter-particle distance $\delta_n$:

$$\begin{cases} \delta_n > 0 & \Longrightarrow \quad f_n = 0 \text{ (no contact)} \\ \delta_n \leq 0 & \Longrightarrow \quad \begin{cases} \dot{u}_n > 0 \implies f_n = 0 \text{ (opening contact)} \\ \dot{u}_n = 0 \implies f_n \geq 0 \text{ (contact)} \end{cases} \end{cases} \tag{2.6}$$

where $\dot{u}_n$ is the velocity of particle $j$ relative to particle $i$ at the contact point.

These inequalities correspond to three different cases: when there is a gap between two particles (no contact), no force can occur; when two particles are in contact, the condition of impenetrability is expressed by $\dot{u}_n \geq 0$ (the normal contact velocity has to be null or positive, *i.e.*, separating the particles); when $\dot{u}_n$ is strictly positive, no normal force is transmitted. Moreau (1994) summed up all these inequalities into only 3 cases that are more convenient for numerical implementation while being equivalent:

$$\begin{cases} \delta_n > 0 & \Longrightarrow \quad f_n = 0 \\ \delta_n \leq 0 & \Longrightarrow \quad \dot{u}_n \geq 0,\ f_n \geq 0 \\ \dot{u}_n > 0 & \Longrightarrow \quad f_n = 0 \end{cases} \tag{2.7}$$

In a nutshell, it is handy to represent these inequalities into the Signorini graph displayed in Figure 2.2a, where the horizontal axis carries the normal distance $\delta_n$ as well as the contact velocity $\dot{u}_n$.

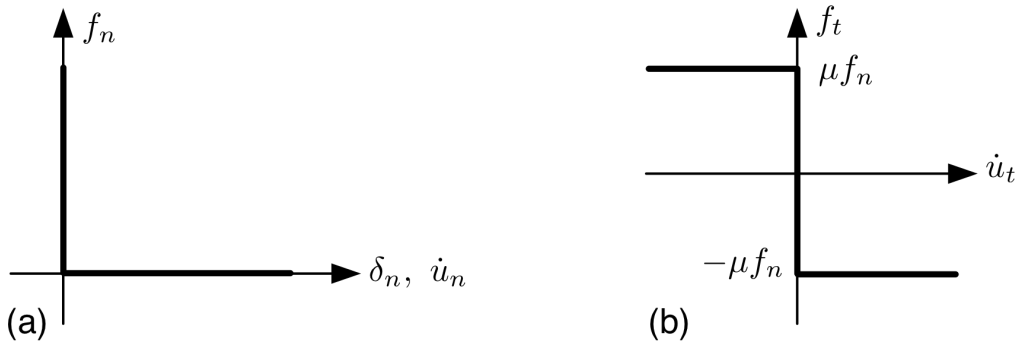


Figure 2.2 – Typical CD-DEM contact laws adopted for the CDM: (left) Signorini condition for normal forces that prevents particle interpenetration; (right) rigid-plastic law with implementation of Coulomb's friction law for tangential forces.

The contact velocity, however, is not clearly defined in the context of non-smooth motions. It can be the relative velocity at the beginning or at the end of a time increment. To deal with this problem, a *formal velocity*, still denoted by $\dot{u}_n$, has been introduced by assuming that it stands somewhere between its left-limit $\dot{u}_n^-$ and its right-limit $\dot{u}_n^+$:

$$\dot{u}_n = \eta \dot{u}_n^- + (1-\eta)\dot{u}_n^+ \tag{2.8}$$

where $\eta$ is a material parameter that characterises the contact. Choosing $\eta = 0$ implies $\dot{u}_n = \dot{u}_n^+$, and consequently a null formal velocity involves that the right-limit velocity remains also null; in other words, the contact is persistent. Since a non-zero force can only occur for $\dot{u}_n = 0$ according to the Signorini conditions, only persistent contacts can

carry a positive force. This is adequate for static situations, but it might be troublesome when some dynamic events are likely to occur. For $\eta > 0$, a binary shock implies that

$$e_n = \frac{-\dot{u}_n^+}{\dot{u}_n^-} = \frac{\eta}{1-\eta} \tag{2.9}$$

where $e_n$ is the normal restitution coefficient. Reintroducing $e_n$ in Equation 2.8, we get:

$$\dot{u}_n = \frac{\dot{u}_n^+ + e_n \dot{u}_n^-}{1+e_n} \tag{2.10}$$

This way, a normal dissipation can be accounted for through $e_n$, and using this formal velocity into the Signorini relations transforms it into a "*shock law*".

Similarly, Coulomb's friction law (Figure 2.2b) can be expressed as a complementarity relation between the tangential force $f_t$ and the sliding velocity $\dot{u}_t$ in the following way:

$$\begin{cases} \dot{u}_t > 0 \implies f_t = -\mu f_n & \text{(sliding)} \\ \dot{u}_t = 0 \implies -\mu f_n \leq f_t \leq \mu f_n & \text{(not sliding)} \\ \dot{u}_t < 0 \implies f_t = \mu f_n & \text{(sliding)} \end{cases} \tag{2.11}$$

where $\mu$ is the Coulomb friction coefficient. Once again, it is possible to introduce a tangential coefficient of restitution $e_t$ in the definition of the formal velocity $\dot{u}_t$. In practice, however, this coefficient is usually set to zero so that $\dot{u}_t = \dot{u}_t^+$, but if required it is defined as follows:

$$\dot{u}_t = \frac{\dot{u}_t^+ + e_t \dot{u}_t^-}{1+e_t} \tag{2.12}$$

#### 2.1.2.2 Single-contact (local) problem

Since the contact laws are expressed by inequalities, no explicit relation is given between the formal velocities $(\dot{u}_n, \dot{u}_t)$ and the contact actions $(f_n, f_t)$. To solve the problem for a given contact, it is required that the equations of dynamics defined at the particle levels (Equation 2.5) are transferred at the contact level, *i.e.*, by using contact-based quantities (formal velocities and contact actions). It is possible to group the different parameters of the whole system into appropriate large vectors and matrices in order to treat the global problem, but, in CD-DEM implementations, it is not usual to proceed that way. Instead, the contacts are considered and updated one by one as we will see in the next section. Here we focus on the solution of a single contact.

The derivation of the locally-transferred equation of dynamics can be a cumbersome

task, but it can finally be expressed in the following form for a given contact:

$$\underline{\underline{\boldsymbol{W}}} \cdot \begin{pmatrix} f_n \\ f_t \end{pmatrix} = \begin{pmatrix} \mathcal{W}_{nn} & \mathcal{W}_{nt} \\ \mathcal{W}_{tn} & \mathcal{W}_{tt} \end{pmatrix} \cdot \begin{pmatrix} f_n \\ f_t \end{pmatrix} = \frac{1}{\delta t} \begin{pmatrix} (1+e_n)\dot{u}_n \\ (1+e_t)\dot{u}_t \end{pmatrix} + \begin{pmatrix} a_n \\ a_t \end{pmatrix} \tag{2.13}$$

In this relation[1], the components of the matrix $\underline{\underline{\boldsymbol{W}}}$ (known as Delassus operator, having the dimension of an inverse mass) for a contact involving the particles $i$ and $j$ are expressed as follows:

$$\begin{aligned} \mathcal{W}_{nn} &= \frac{1}{m_i} + \frac{1}{m_j} + \frac{(\vec{c}_i \cdot \vec{t})^2}{I_i} + \frac{(\vec{c}_j \cdot \vec{t})^2}{I_j} \\ \mathcal{W}_{tt} &= \frac{1}{m_i} + \frac{1}{m_j} + \frac{(\vec{c}_i \cdot \vec{n})^2}{I_i} + \frac{(\vec{c}_j \cdot \vec{n})^2}{I_j} \\ \mathcal{W}_{nt} = \mathcal{W}_{tn} &= \frac{(\vec{c}_i \cdot \vec{n})(\vec{c}_i \cdot \vec{t})}{I_i} + \frac{(\vec{c}_j \cdot \vec{n})(\vec{c}_j \cdot \vec{t})}{I_j} \end{aligned} \tag{2.14}$$

where vectors $\vec{c}$ link the particle centres to the contact point, and $\vec{n}$ and $\vec{t}$ define the contact frame according to the conventions shown in Figure 2.3.

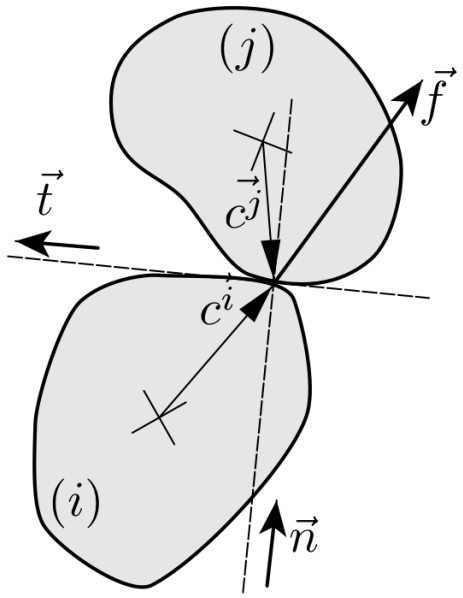


Figure 2.3 – Single contact parameters.

[1]This relation can actually be established using a matrix formalism as derived in Appendix A

Back to Equation 2.13, the offsets $a_n$ and $a_t$ can be expressed as:

$$a_n = a_n^{\text{free}} - (1+e_n)\frac{u_n^-}{\delta t} \tag{2.15}$$

$$a_t = a_t^{\text{free}} - (1+e_t)\frac{u_t^-}{\delta t} \tag{2.16}$$

where the terms $a_n^{\text{free}}$ and $a_t^{\text{free}}$ are the relative accelerations, respectively projected on $\vec{n}$ and $\vec{t}$, that would occur if the contact force was omitted. In the particular case of circular particles (disks), they write:

$$a_n^{\text{free}} = \frac{1}{m_j}(\vec{F}_j^{\text{ext}} \cdot \vec{n} - f_n) - \frac{1}{m_i}(\vec{F}_i^{\text{ext}} \cdot \vec{n} + f_n) \tag{2.17}$$

$$\begin{aligned} a_t^{\text{free}} &= \frac{1}{m_j}(\vec{F}_j^{\text{ext}} \cdot \vec{t} - f_t) - \frac{1}{m_i}(\vec{F}_i^{\text{ext}} \cdot \vec{t} + f_t) \\ &+ R_j\frac{\mathcal{M}_j^{\text{ext}}}{I_j} - R_i\frac{\mathcal{M}_i^{\text{ext}}}{I_i} \end{aligned} \tag{2.18}$$

where it should be recalled that the forces $f_n$ and $f_t$ act from particle $i$ to $j$, no resistive torque acts at the contacts, and the resultant actions $\vec{F}^{\text{ext}}$ and $\mathcal{M}^{\text{ext}}$ also include the bulk contributions together with the boundary (imposed) actions. Still for disks, Equations 2.14 simplify to:

$$\begin{aligned} \mathcal{W}_{nn} &= \frac{1}{m_i} + \frac{1}{m_j} \\ \mathcal{W}_{tt} &= \frac{1}{m_i} + \frac{1}{m_j} + \frac{R_i^2}{I_i} + \frac{R_j^2}{I_j} \\ \mathcal{W}_{nt} = \mathcal{W}_{tn} &= 0 \end{aligned} \tag{2.19}$$

and the relations of Equation 2.13, which correspond to local (contact) equations of dynamics, reduce to these two affine relations between formal velocities and contact forces:

$$\mathcal{W}_{nn} f_n = (1+e_n)\frac{u_n}{\delta t} + a_n \tag{2.20}$$

$$\mathcal{W}_{tt} f_t = (1+e_t)\frac{u_t}{\delta t} + a_t \tag{2.21}$$

where it is important to notice that the slopes are positive. The solution of a single contact problem consists of taking care of the contact laws in addition to these local dynamics. In other words, the intersection of the local equations of dynamics, expressed

in contact variables as a relation between forces $(f_n, f_t)$ and the formal velocities $(\dot{u}_n, \dot{u}_t)$, with the complementarity relations. This is illustrated in Figure 2.4

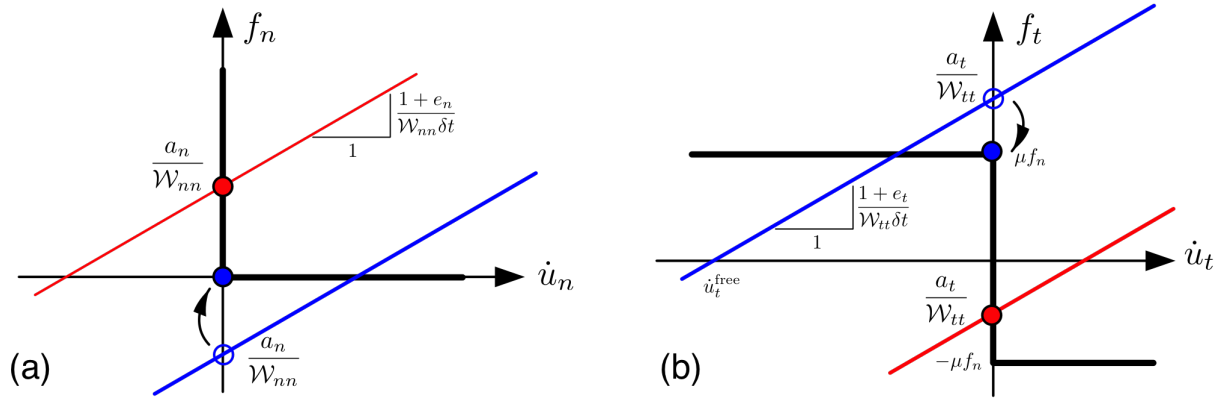


Figure 2.4 – Solution of the local single-contact problem, obtained from the intersection of the dynamics-transfer equations with the complementarity relations – Signorini (left) and Coulomb (right) conditions, provided that a contact exists ($\delta_n \leq 0$).

To proceed the intersection, the acceleration offsets $a_n$ and $a_t$ are first considered since they are proportional to the value at the intersection of the transfer equation with the vertical axis in the graphs. We will see hereafter that an equivalent reasoning can be done by considering first the intersections with the horizontal axis that are formal velocities. For the normal direction, it is clear that:

$$\begin{cases} a_n > 0 & \Longrightarrow \quad \dot{u}_n = 0 & \text{and} \quad f_n = \frac{a_n}{\mathcal{W}_{nn}} \\ a_n \leq 0 & \Longrightarrow \quad \dot{u}_n > 0,\ \dot{u}_n = \frac{-a_n}{1+e_n}\delta t & \text{and} \quad f_n = 0 \end{cases} \tag{2.22}$$

The tangential contact variable can subsequently be computed:

$$\begin{cases} -\mu f_n \leq \frac{a_t}{\mathcal{W}_{tt}} \leq \mu f_n & \Longrightarrow \quad \dot{u}_t = 0 & \text{and} \quad f_t = \frac{a_t}{\mathcal{W}_{tt}} \\ |a_t| > \mathcal{W}_{tt}\mu f_n & \Longrightarrow \quad \dot{u}_n = \frac{(a_t/|a_t|)\mathcal{W}_{tt}\mu f_n - a_t}{1+e_t}\delta t & \text{and} \quad f_t = \mu f_n \frac{a_t}{|a_t|} \end{cases} \tag{2.23}$$

If the particles are not circular, the term $\mathcal{W}_{nt}$ can be non null, which does not enable the simple affine form of the local equation of dynamics (Equations 2.20 and 2.21). In this case, the single-contact problem can be treated by considering the forces $(g_n, g_t)$ at the intersection with the vertical axis:

$$\begin{pmatrix} g_n \\ g_t \end{pmatrix} = \underline{\underline{\boldsymbol{W}}}^{-1} \cdot \begin{pmatrix} a_n \\ a_t \end{pmatrix} \tag{2.24}$$

where the inverse of $\underline{\underline{\boldsymbol{W}}}$ is guaranteed to be defined since $\det(\underline{\underline{\boldsymbol{W}}})$ is always positive.

The solution of the single contact problem as proposed in Equations 2.22 and 2.23 corresponds to what is proposed in Radjai and Richefeu (2009). In this approach the update of the formal velocities is actually not required because the offsets $a_n$ and $a_t$ depend only on the contact forces and on the left-limit relative velocities $\dot{u}_n^-$ and $\dot{u}_n^+$.

Indeed, the original approach, as it has been first expressed, rather exploits the formal velocities to solve a single-contact problem. Instead of determining a plausible formal velocity vector $\vec{\dot{u}}$ in the contact frame, the *free* one $\vec{\dot{u}}^{\text{ free}}$ is considered after having updated the resultant actions on particles and then the particle velocities ($\vec{v} = \vec{\mathcal{F}}/M$ and $\omega = \mathcal{M}/I$) :

$$\left\{\begin{array}{rcl} \dot{u}_n^+ &=& (\vec{v}_j - \vec{v}_i)\cdot\vec{n} \\ \dot{u}_t^+ &=& \left[(\vec{v}_j\cdot\vec{t} - r_j\omega_j) - (\vec{v}_i\cdot\vec{t} + r_i\omega_i)\right] \end{array}\right. \quad \text{and so} \quad \left\{\begin{array}{rcl} \dot{u}_n^{\text{free}} &=& \frac{\dot{u}_n^+ + e_n\dot{u}_n^-}{1+e_n} \\ \dot{u}_t^{\text{free}} &=& \frac{\dot{u}_t^+ + e_t\dot{u}_t^-}{1+e_t} \end{array}\right. \tag{2.25}$$

The corrections of formal velocities ($\Delta u_n$, $\Delta u_t$) and impulses ($\Delta f_n \delta t$, $\Delta f_t \delta t$) are derived from the transfer equations of dynamics (Equations 2.20 and 2.21 for disks):

$$\frac{\Delta f_n \delta t}{\Delta \dot{u}_n} = \frac{1+e_n}{\mathcal{W}_{nn}} \quad \text{and} \quad \frac{\Delta f_t \delta t}{\Delta \dot{u}_t} = \frac{1+e_t}{\mathcal{W}_{tt}} \tag{2.26}$$

But these corrections need to be done only if the complementary relations are *not* satisfied. To check this numerically, a graph thickness $\epsilon$ is used as a numerical tolerance. The Signorini conditions are first tested:

$$\left\{\begin{array}{l} \dot{u}_n^{\text{free}} < -\epsilon \\ \text{or} \\ \dot{u}_n^{\text{free}} > \epsilon \text{ and } f_n < 0 \end{array}\right. \implies \text{correction} \tag{2.27}$$

and then if a correction is still not required (*i.e.*, $f_n$ is necessarily positive), the Coulomb conditions are tested:

$$\left\{\begin{array}{l} |f_t| \geq \mu f_n \text{ and } |\dot{u}_t^{\text{free}}| < \epsilon \\ \text{or} \\ |f_t| < \mu f_n \text{ and } |\dot{u}_t^{\text{free}}| > \epsilon \end{array}\right. \implies \text{correction} \tag{2.28}$$

If requested, the correction is performed in the following way. First, the normal force correction $\Delta f_n$ is computed:

$$\Delta \dot{u}_n = -\dot{u}_n^{\text{free}} \implies \Delta f_n = -\frac{1+e_n}{\mathcal{W}_{nn}\delta t}\dot{u}_n^{\text{free}} \tag{2.29}$$

and the normal force is updated:

$$f_n \leftarrow \max(0,\ f_n + \Delta f_n) \tag{2.30}$$

Then, the tangential force correction $\Delta f_t$ is computed:

$$\Delta \dot{u}_t = -\dot{u}_t^{\text{free}} \implies f_t = -\frac{1+e_t}{\mathcal{W}_{tt}\delta t}\dot{u}_t^{\text{free}} \tag{2.31}$$

and the tangential force is updated based on the updated value of normal force ($f_n \geq 0$):

$$f_t \leftarrow \min\left(\mu f_n,\ \max(-\mu f_n, f_t + \Delta f_t)\right) \tag{2.32}$$

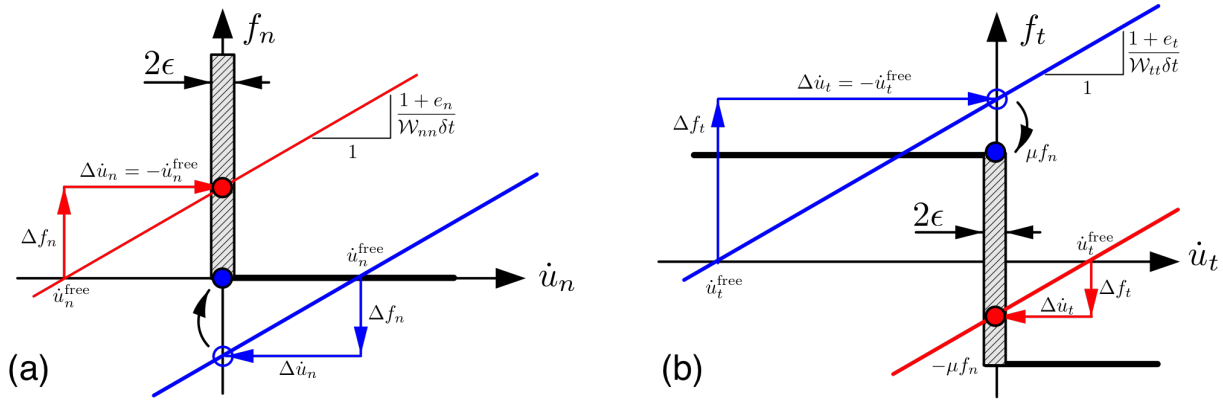


Figure 2.5 – Solution of the local single-contact problem, obtained from the intersection of the dynamics-transfer equations with the complementarity relations – Signorini (left) and Coulomb (right) conditions, provided that a contact exists ($\delta_n \leq 0$). A graph thickness $\epsilon$ is used as a numerical tolerance.

In this work, the second approach – said "à la Moreau" – is used. It has the benefit of being more intuitive to implement and, more importantly, the introduction of the "graph thickness" $\epsilon$ provides a tolerance which is a supplementary parameter that may absorb some possible noise in the input data.

#### 2.1.2.3 Multi-contact (global) problem

If a contact force, within the force network of a dense packing, is updated by considering a single-contact problem, it will subsequently involve an update of the "surrounding" forces (*i.e.*, those that imply one of the concerned particles). By doing so for each contact, a solution for the global problem should be reached. This procedure actually matches the strategy employed in the Gauss-Seidel method, which is an iterative method used

to solve a linear system of equations, also known as the *method of successive displacement*. The numerical procedure of the global problem becomes thus a *multi-contact* problem, which consists in updating one by one each force in the contact network as if it was a single-contact problem.

The procedure is repeated iteratively until a condition is satisfied with a chosen precision. Two criteria are used. The first is based on the number $n_{\text{verif}}$ of *consecutive* iterations without correction (*e.g.*, when $|\dot{u}_n| < \epsilon$). In general, 2 loops on all contacts without the need to update one of them are sufficient to obtain a satisfactory solution. So the iteration are stopped if:

$$n_{\text{verif}} > 2N_c \tag{2.33}$$

The second criterion is simply based on the total number of corrections, which should be limited in order to stop a computation in a reasonable time when convergence is too tedious.

### 2.1.3 Quasi-Static Method (QSM)

Quasi-static (QS) methods represent an important alternative, for the modelling of granular assemblies under quasi-static loading conditions, to the more typical MD-DEM and CD-DEM that account for inertial effects. Such methods aim to model systems composed of discrete elements, such as assemblies of granular materials, as networks of springs, plastic sliders and no-tension joints. They are based on the assumption that, when quasi-static motions are involved, the system, under a variable loading, can be treated as a sequence of equilibrium states; the stress increments between two consecutive states are treated in the hypothesis of small displacements, and the corresponding displacements and rotation of particles can be determined via an iterative procedure.

A full description of one quasi-static method is presented by Roux and Combe (2011), in which the method is presented as a way to determine, for a system subjected to small increments of applied loading, the equilibrium state – close to the initial state – to which it evolves.

In this doctoral work, a different formulation of this method is proposed, for application to the estimation of forces. Instead of small loading increments, only the final loading conditions are given, and the iterative procedure is used to reach a final solution (statically and plastically admissible) starting from any initial condition. This difference will be studied in more detail when applying the QSM to a simple system with only one free disk (Section 2.2.3).

The elasto-plastic formulation proposed in this work for the estimation of forces will

be the object of the rest of this Section 2.1.3, with the development of the problem in a matrix form. The iterative procedure for the numerical resolution of the problem will also be introduced.

#### 2.1.3.1 Overview of the method

For a given geometric configuration of a granular assembly, the Quasi-Static Method (QSM) is meant to find a set of contact forces that is, at the same time, *statically admissible* (*i.e.*, in equilibrium with the external loading) and *plastically admissible* (*i.e.*, fulfilling the adopted friction law). This is done by means of an iterative procedure of double projection, of an initial set of forces (guess solution), respectively on the subspace of statically admissible solutions and on that of plastically admissible solutions. In particular, since we assume Coulomb's friction law, the boundary of the subspace of plastically admissible solutions corresponds to the Coulomb cone.
Such a study of the quasi-static evolution of a granular system can be fully expressed in a matrix form, through the definition of a *rigidity matrix*, describing the structure of a contact network, and of a *stiffness matrix* (elastic or elasto-plastic), in which material properties (contact law parameters) also appear.

The matrix form of the problem stems from the linearisation of the contact laws from small increments, consisting in expressing small contact force increments as a function of small relative displacement increments.

Dealing with small motions, the *assumptions of small displacements* (ASD) can be adopted: this means that the displacement increments do not have any effect on the geometrical arrangement, which stays constant. In particular, this means that the contact local reference frames, defined at each contact to decompose forces along the normal and tangential direction to the contact point, are assumed to stay unchanged.

#### 2.1.3.2 Matrix form of the problem

The characterisation of the displacements in an assembly of particles can be done either at the particle level or at the contact one. The matrix formulation of the problem requires the definition of appropriate vectors and matrices grouping both particle-scale and contact-scale variables involved in the governing equations.

At the particle level, a displacement vector is defined:

$$\underline{\boldsymbol{U}} = \left( U_x^1 \; U_y^1 \; \theta^1 \; \dots \; U_x^{N_p} \; U_y^{N_p} \; \theta^{N_p} \quad \Delta^1 \; \dots \; \Delta^{N_b} \right)^T \tag{2.34}$$

which groups the displacements in correspondence of each *degree of freedom* (DOF) – usually 3 DOFs per particle in a 2D system; $\Delta^1 \dots \Delta^{N_b}$ are the $N_b$ possible DOFs of boundaries. The total DOFs is thus $N_f = 3N_p + N_b$, where $N_p$ is the number of free particles and $N_b$ is the number of DOFs associated with the boundaries of the system. At the contact level, a set of contact relative (normal and tangential) displacements is defined as follows:

$$\underline{\boldsymbol{u}} = \left( u_n^1 \; u_t^1 \; \dots \; u_n^{N_c} \; u_t^{N_c} \right)^T \tag{2.35}$$

where $N_c$ is the number of contacts and each contact – numbered $c$ in the following – is associated with a pair of particles; $c \equiv (i,\ j)$.

In order to build a system of equations composed of the contact laws, written as a function of particles DOFs, a transition is required from grain-based quantities (*e.g.*, grain displacements, body forces) and equations to contact-based ones (*i.e.*, contact relative displacements, contact forces). For an assembly of two-dimensional disks, contact relative displacements can be expressed as a function of the displacements of the two grains in contact through the following relations:

$$\begin{cases} u_n^c = (\vec{U}^i - \vec{U}^j) \cdot \vec{n}^c \\ u_t^c = (\vec{U}^i - \vec{U}^j) \cdot \vec{t}^c - R^i \theta^i - R^j \theta^j \end{cases} \tag{2.36}$$

that can be written in a local matrix form $\underline{\boldsymbol{u}}^c = \underline{\underline{\boldsymbol{G}}}^c \cdot \underline{\boldsymbol{U}}^c$ where

$$\begin{aligned} \underline{\boldsymbol{u}}^c &= (u_n^c \; u_t^c)^T \\ \underline{\underline{\boldsymbol{G}}}^c &= \begin{pmatrix} n_x^c & n_y^c & 0 & -n_x^c & -n_y^c & 0 \\ t_x^c & t_y^c & -R^i & -t_x^c & -t_y^c & -R^j \end{pmatrix} \\ \underline{\boldsymbol{U}}^c &= \left( U_x^i \; U_y^i \; \theta^i \; U_x^j \; U_y^j \; \theta^j \right)^T \end{aligned} \tag{2.37}$$

It should be noticed that a different sign convention for the definition of relative displacements $\underline{\boldsymbol{u}}$ in Equation 2.36 is adopted, with respect to the sign convention used in the CEM and CDM. This has a practical motivation, since, in this way, negative signs do not appear in the governing equations of the method.

By considering such relations for all contacts, a large matrix $\underline{\underline{\boldsymbol{G}}}$ can be assembled in order to express a single linear relation:

$$\underline{\boldsymbol{u}} = \underline{\underline{\boldsymbol{G}}} \cdot \underline{\boldsymbol{U}} \tag{2.38}$$

where the *rigidity matrix* $\underline{\underline{\boldsymbol{G}}}$ has size $2N_c \times N_f$.

In the same way, a linear relation can be established between the vector of external forces, grouping all external forces and body forces (*e.g.*, gravity) acting in correspondence of the DOFs of the system, and the set of contact forces. This relation, which actually expresses the condition of static admissibility as it verifies the equilibrium between external and internal forces, reads

$$\underline{\boldsymbol{F}}^{\text{ext}} = \underline{\underline{\boldsymbol{H}}} \cdot \underline{\boldsymbol{f}} \tag{2.39}$$

where $\underline{\boldsymbol{F}}^{\text{ext}}$ and $\underline{\boldsymbol{f}}$ are large vectors assembled similarly to $\underline{\boldsymbol{U}}$ and $\underline{\boldsymbol{u}}$, respectively. It can be easily proved that $\underline{\underline{\boldsymbol{H}}}$ is actually the transpose of $\underline{\underline{\boldsymbol{G}}}$. By equalising the external and internal work $\underline{\boldsymbol{F}}^{\text{ext}} \cdot \underline{\boldsymbol{U}} = \underline{\boldsymbol{f}} \cdot \underline{\boldsymbol{u}}$, and using the previous relations, we have

$$(\underline{\underline{\boldsymbol{H}}} \cdot \underline{\boldsymbol{f}}) \cdot \underline{\boldsymbol{U}} = \underline{\boldsymbol{f}} \cdot (\underline{\underline{\boldsymbol{G}}} \cdot \underline{\boldsymbol{U}}) \implies \underline{\underline{\boldsymbol{H}}} \cdot \underline{\boldsymbol{f}} = \underline{\underline{\boldsymbol{G}}} \cdot \underline{\boldsymbol{f}}$$

which is exactly the definition of the transpose of a matrix. So $\underline{\underline{\boldsymbol{H}}} = \underline{\underline{\boldsymbol{G}}}^T$ and

$$\underline{\boldsymbol{F}}^{\text{ext}} = \underline{\underline{\boldsymbol{G}}}^T \cdot \underline{\boldsymbol{f}} \tag{2.40}$$

Material properties are then injected into the problem through the contact laws describing the relation between forces and displacements, that are expressed in the following way:

$$\begin{cases} f_n^c = k_n^c \, u_n^c \\ f_t^c = k_t^c \, u_t^c \end{cases} \tag{2.41}$$

Grouping the set of equations in a matrix form leads to the equation

$$\underline{\boldsymbol{f}} = \underline{\underline{\boldsymbol{\mathcal{K}}}} \, \underline{\boldsymbol{u}} \tag{2.42}$$

where $\underline{\underline{\boldsymbol{\mathcal{K}}}}$ is a diagonal matrix, with size $2N_c \times 2N_c$, containing all contact normal and tangential stiffnesses:

$$\underline{\underline{\boldsymbol{\mathcal{K}}}} = \begin{pmatrix} k_n^1 & & & & & \\ & k_t^1 & & & & \\ & & \ddots & & & \\ & & & k_n^{N_c} & & \\ & & & & k_t^{N_c} \end{pmatrix} \tag{2.43}$$

At this point, the vector of external forces $\underline{\boldsymbol{F}}^{\text{ext}}$ can be easily expressed as a function

of the set of particle displacements $\underline{\boldsymbol{U}}$:

$$\begin{aligned} \underline{\boldsymbol{F}}^{\text{ext}} &= \underline{\underline{\boldsymbol{G}}}^T \cdot \underline{\boldsymbol{f}} \\ &= \underline{\underline{\boldsymbol{G}}}^T \cdot \underline{\underline{\boldsymbol{\mathcal{K}}}} \cdot \underline{\boldsymbol{u}} = \underline{\underline{\boldsymbol{G}}}^T \cdot \underline{\underline{\boldsymbol{\mathcal{K}}}} \cdot \underline{\underline{\boldsymbol{G}}} \cdot \underline{\boldsymbol{U}} \\ &= \underline{\underline{\mathbf{K}}} \cdot \underline{\boldsymbol{U}} \end{aligned} \tag{2.44}$$

where

$$\underline{\underline{\mathbf{K}}} = \underline{\underline{\boldsymbol{G}}}^T \cdot \underline{\underline{\boldsymbol{\mathcal{K}}}} \cdot \underline{\underline{\boldsymbol{G}}} \tag{2.45}$$

is a symmetric matrix referred to as *stiffness matrix* with dimension $N_f \times N_f$, grouping both material properties and geometrical ones.

Based on this matrix formulation, the elasto-plastic problem can now be solved. The solution consists in finding the set of particle (and wall) displacements $\underline{\boldsymbol{U}}$ that solves the equation $\underline{\boldsymbol{F}}^{\text{ext}} = \underline{\underline{\mathbf{K}}}\,\underline{\boldsymbol{U}}$, for a given set of external forces $\underline{\boldsymbol{F}}^{\text{ext}}$. The elasto-plastic problem is actually reduced to the solution of an elastic problem, for which an *elastic* stiffness matrix is used. Then, grains are subjected to additional correction forces to account for Coulomb friction.

This is performed through a numerical iterative procedure, which is detailed here. In a first stage, the set of contact forces is assigned an initial value $\underline{\boldsymbol{f}} = \underline{\boldsymbol{f}}_0$; any value can be given (it could be a guess solution, or even just a null vector). Then, the initial set of contact forces is submitted to a procedure of double, successive projection: it consists of an alternation of a global projection (involving all the contact forces at the same time) on the subspace of *statically admissible* solutions (hereafter also referred to as SA), and a local one (performed contact by contact) on the Coulomb cone, representing the (boundary of the) subspace of *plastically admissible* solutions (PA).

At the end of the iterative procedure, a solution is found if the intersection between the SA force set (an affine subspace) and the PA force set (a cone) is non-empty. In this case, the method will converge to the point of the intersection at the minimum distance from the starting point.

#### 2.1.3.3 Global projection: static admissibility

Given a set of contact forces $\underline{\boldsymbol{f}}$, and according to Equation 2.40, these forces are statically admissible when $\Delta\underline{\boldsymbol{F}} = \underline{\boldsymbol{F}}^{\text{ext}} - \underline{\underline{\boldsymbol{G}}}^T \cdot \underline{\boldsymbol{f}} = \underline{\mathbf{0}}$. If it is not the case, $\Delta\underline{\boldsymbol{F}} \neq \underline{\mathbf{0}}$, and we look for the motions $\Delta\underline{\boldsymbol{U}}$ able to produce this imbalance. According to Equation 2.44:

$$\Delta\underline{\boldsymbol{F}} = \underline{\underline{\mathbf{K}}} \cdot \Delta\underline{\boldsymbol{U}} \implies \Delta\underline{\boldsymbol{U}} = \underline{\underline{\mathbf{K}}}^{-1} \cdot (\underline{\boldsymbol{F}}^{\text{ext}} - \underline{\underline{\boldsymbol{G}}}^T \cdot \underline{\boldsymbol{f}}) \tag{2.46}$$

where it can be proven that the inverse $\underline{\underline{\mathbf{K}}}^{-1}$ exists, because $\underline{\underline{\mathbf{K}}}$ is positive, and positive definite unless $\underline{\underline{\boldsymbol{G}}}$ has a non-trivial kernel.

In practice, $\underline{\underline{\mathbf{K}}}^{-1}$ is not explicitly computed due to its large size ($N_f \times N_f$). An alternative method to compute $\Delta\underline{\boldsymbol{U}}$ is used instead, involving a Crout factorisation of matrix $\underline{\underline{\mathbf{K}}}$ that can be expressed as $\underline{\underline{\boldsymbol{L}\boldsymbol{D}\boldsymbol{L}}}^T$, $\underline{\underline{\boldsymbol{L}}}$ being a unit lower triangular matrix.

The corrective motions $\Delta\underline{\boldsymbol{U}}$ can be associated with force corrections $\Delta\underline{\boldsymbol{f}}$ based on Equations 2.38 and 2.42:

$$\Delta\underline{\boldsymbol{f}} = \underline{\underline{\boldsymbol{\mathcal{K}}}} \cdot \Delta\underline{\boldsymbol{u}} = \underline{\underline{\boldsymbol{\mathcal{K}}}} \cdot \underline{\underline{\boldsymbol{G}}} \cdot \Delta\underline{\boldsymbol{U}} \tag{2.47}$$

Finally, adding these corrective forces to the current set of forces, we obtain a new set of forces which is now statically admissible:

$$\underline{\boldsymbol{f}}^{SA} = \underline{\boldsymbol{f}} + \underline{\underline{\boldsymbol{\mathcal{K}}}} \cdot \underline{\underline{\boldsymbol{G}}} \cdot \Delta\underline{\boldsymbol{U}} \tag{2.48}$$

These operations realise a projection on a SA space. This projection is noted $\mathcal{Q}(\underline{\boldsymbol{f}})$. However, these forces can still be negative or not plastically admissible, *i.e.*, in general, they may stand outside the Coulomb cone.

#### 2.1.3.4 Local projection: plastic admissibility

Once a statically admissible solution is obtained through the projection just explained, the next step is the local projection on the Coulomb cone, to inject the condition of plastic admissibility. Differently from the global projection on the SA subspace, for which all the contacts have to be considered at the same time (since, for reasons of equilibrium, each contact force depends on the values of the others), in this case the projections are referred to as *local* as they are performed on single contacts independently of the others.

In order to have a plastic admissible solution, the condition that has to be satisfied is expressed through the two following inequalities:

$$\begin{cases} f_n^c & \geq 0 \\ |f_t^c| & \leq \mu\, f_n^c \end{cases} \tag{2.49}$$

The first inequality represents the condition for which no tensile normal force can be exerted between particles, which guarantees the unilaterality constraint; the second one defines the yield surface as the Coulomb cone, in which $\mu$ is the interparticle friction coefficient. It is interesting to notice that these relations are equivalent to the Signorini-Coulomb conditions, except that here the relative velocities are not considered because of the assumption of static equilibrium.

Some observations have to be done about how to carry out the local projection on the Coulomb cone. In plasticity, the choice of the projector $\mathcal{P}$ is said to define the flow rule, *i.e.*, the direction of plastic contact displacements. With respect to this, two options are possible. If the projection is performed orthogonally, this implies the choice of an *associated* flow rule. In this case, when sliding occurs at a contact (*i.e.*, the cone is reached), there is a local dilation defined by an angle equal to the angle of inter-particle friction. On the other hand, the usual treatment of Coulomb's friction implies a *non-associated* flow rule, typically with no dilation at sliding. In the frame of this doctoral work, we will only use the latter option, which is the best suited solution for granular materials.

This choice is reflected in the definition of the procedure adopted to apply the local projection. In the plane $(f_n, f_t)$ of each contact, such a projection can be represented as a vertical one (Figure 2.6); the corresponding procedure consists in simply bringing back the value of the tangential force to the sliding tangential force $f_t = \mu f_n$ (or $f_t = -\mu f_n$), while keeping constant the value of the normal force. On the contrary, if the violated condition is the first one in Equation 2.49, both contact force components are simply set to zero.

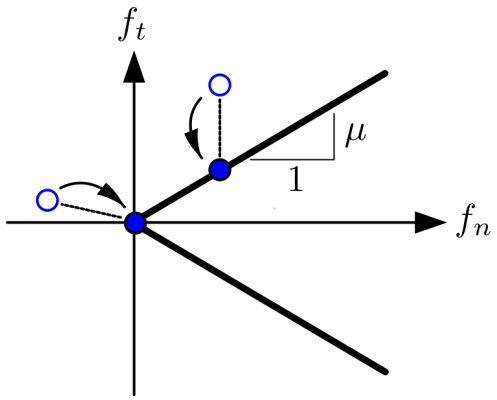


Figure 2.6 – Projector $\mathcal{P}$ onto the Coulomb cone, for the case of non-associated flow rule. The two open circles represent non-admissible situations linked to the two conditions in Equations 2.49.

#### 2.1.3.5 Iterative procedure

Having presented the two procedures of projection onto the two closed convex subsets defining the admissible solutions, the iterative algorithm to solve the problem can be presented in more detail.

At the beginning (iteration $k = 0$), the stiffness matrix $\underline{\underline{\mathbf{K}}}$ and the vector of external forces $\underline{\boldsymbol{F}}^{\text{ext}}$ are built according to the geometry and the loading. An initial set of forces $\underline{\boldsymbol{f}}^0$ is then considered.

Then, the iterative procedure consists in alternatively projecting the current set of forces on the PA and SA spaces:

$$\underline{\boldsymbol{f}}^{k+1} \leftarrow \mathcal{Q}\left(\mathcal{P}(\underline{\boldsymbol{f}}^k)\right) \tag{2.50}$$

until a stopping criterion is fulfilled. Several criteria are defined. The first criterion is based on the residual resultant actions $\Delta\underline{\boldsymbol{F}}$ on particles, as defined in Equation 2.46. It writes:

$$\max \Delta\underline{\boldsymbol{F}} < \epsilon^{SA} \tag{2.51}$$

A second criterion is based on a cumulated distance $\delta^{PA}$, over all contacts, from the Coulomb yield surface. This distance is defined according to the flow rule (and so to the projection described in Figure 2.6). It writes:

$$\frac{|\delta^{PA,k+1} - \delta^{PA,k}|}{\delta^{PA,k+1}} < \epsilon^{PA} \tag{2.52}$$

A third criterion is based on the same parameter $\delta^{PA}$, averaged over a certain quantum of iterations (typically 1000). It consists in checking that this parameter decreases in two consecutive quanta; if it does not, the iteration loop is stopped. Finally, a last, purely numerical criterion is introduced based on the total number of iterations. It allows the computation to be stopped in a finite time whenever the three previous criteria are not met.

### 2.1.4 Comparison of the three methods and discussion

In this Section, some observations are made by comparing the main features of the three methods, as described so far. In particular, we focus on a comparison between the CDM and the QSM, which have several common points; the CEM is only recalled to summarise the governing equations of the methods, as in the Table 2.1.

From a geometrical point of view, the transfer between particle-based quantities and contact-based quantities is similar between the three methods. As to the mechanics, both the CDM and the QSM treat it on a local level (contact-by-contact) and a global level; the CEM, on the contrary, only has a local treatment based on the force laws. Most importantly, it should be remarked that the CEM, differently from the other two

Governing equations of the 3 methods

| | CEM | CDM | QSM |
|---|---|---|---|
| | | **Geometry** | |
| | $\underline{\boldsymbol{u}} = \underline{\underline{\boldsymbol{G}}} \cdot \underline{\boldsymbol{U}}$ | $\underline{\dot{\boldsymbol{u}}} = \underline{\underline{\boldsymbol{G}}} \cdot \underline{\dot{\boldsymbol{U}}}$<br>$\underline{\boldsymbol{F}} = \underline{\underline{\boldsymbol{G}}}^T \cdot \underline{\boldsymbol{f}}$ | $\underline{\boldsymbol{u}} = \underline{\underline{\boldsymbol{G}}} \cdot \underline{\boldsymbol{U}}$<br>$\underline{\boldsymbol{F}} = \underline{\underline{\boldsymbol{G}}}^T \cdot \underline{\boldsymbol{f}}$ |
| | | **Mechanics** | |
| Local | $\underline{\boldsymbol{f}} = \underline{\underline{\boldsymbol{\mathcal{K}}}} \cdot \underline{\boldsymbol{u}}$ | $\Delta\underline{\dot{\boldsymbol{u}}}_n = \underline{\underline{\boldsymbol{W}}} \cdot \underline{\boldsymbol{f}}\delta t$<br>with $\underline{\underline{\boldsymbol{W}}} = \underline{\underline{\boldsymbol{G}}} \cdot \underline{\underline{\boldsymbol{M}}} \cdot \underline{\underline{\boldsymbol{G}}}^T$ | $\underline{\boldsymbol{f}} = \underline{\underline{\boldsymbol{\mathcal{K}}}} \cdot \underline{\boldsymbol{u}}$ |
| | $\oplus$ Unilaterality<br>$\oplus$ Coulomb | $\oplus$ Signorini<br>$\oplus$ Coulomb | $\oplus$ Unilaterality<br>$\oplus$ Coulomb |
| Global | $\varnothing$ | $\underline{\underline{\boldsymbol{M}}} \cdot \Delta\underline{\dot{\boldsymbol{U}}} = \underline{\boldsymbol{F}}\delta t$ | $\underline{\boldsymbol{F}} = \underline{\underline{\boldsymbol{K}}} \cdot \underline{\boldsymbol{U}}$<br>with $\underline{\underline{\boldsymbol{K}}} = \underline{\underline{\boldsymbol{G}}}^T \cdot \underline{\underline{\boldsymbol{\mathcal{K}}}} \cdot \underline{\underline{\boldsymbol{G}}}$ |

Table 2.1 – Summary and comparison of the main governing equations of the three methods (CEM, CDM, QSM). The main equations are expressed here in a matrix form; as regards the CDM, this formulation is described in the Appendix A.

methods, never accounts for mechanical equilibrium – neither on a global level, nor on a local level.

Among the points in common to the CDM and the QSM, the fact of employing a numerical iterative resolution is one of the most important. In the next section, the two algorithms will be detailed through the application to a problem with only one free disk, and the evolution of some quantities throughout the iterations will be investigated. However, some hints on how differently the two methods converge towards an admissible solution can already be given by looking at the values of normal forces at different steps of an application of the two methods.

A first comparison can be done by means of maps of normal forces; for the same system (around 100 particles, under isotropic loading conditions), the evolution of normal forces estimated with the two methods is shown (Figure 2.7 for the CDM; Figure 2.8 for the QSM). To allow a comparison, the same initial conditions are used in the two cases (null initial forces). It is clear that, in the CDM, forces gradually increase as the iterations go on. Due to the nature of the multi-contact problem, forces start increasing where the information is given (here, the applied load on the top and right wall). Then, as corrections are applied contact-by-contact and the resultant actions are updated for the particles involved, the information propagates throughout the packing, as perceivable in the four maps.

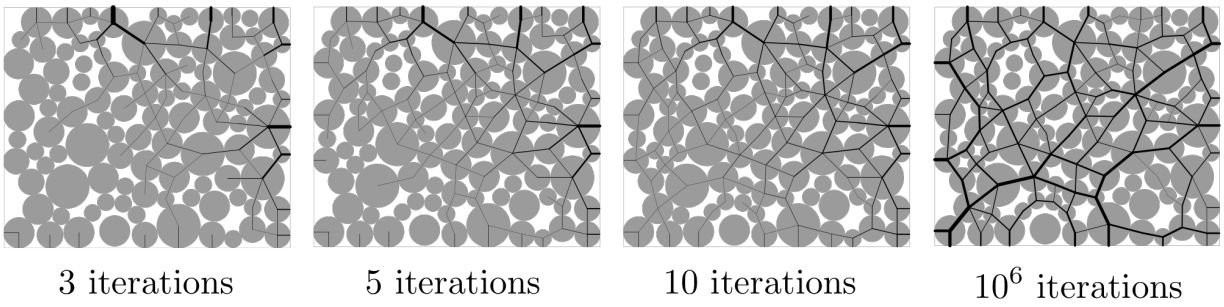


Figure 2.7 – Maps of normal contact forces in an isotropically-loaded packing of about 100 particles at different stages of the Gauss-Seidel iterative procedure. Only normal forces larger than $\langle f_n \rangle / 100$ are drawn.

On the other hand, the QSM applies a projection onto the subspace of SA solutions in a global way, by considering all contacts at once; due to this, a homogeneous distribution of non-null forces is already retrieved after only 1 iteration (Figure 2.8). Then, successive projections correct these forces and the distance from equilibrium is gradually reduced, until static admissibility is finally reached. Interestingly, static equilibrium seems to be approached more slowly for particles in contact with the walls.

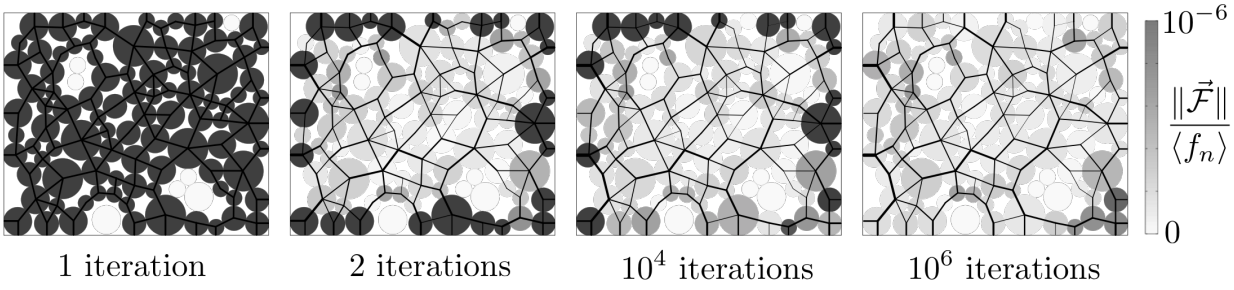


Figure 2.8 – Maps of normal contact forces in an isotropically-loaded packing of about 100 particles at different stages of the QSM double projection iterative procedure. Line thickness is proportional to the magnitude of the normal force. Distance from static equilibrium is expressed, for each grain, as the ratio between the magnitude of the resultant force on the grain and the average normal force at convergence.

Another comparison can be done in terms of the statistics of normal forces. A system with a larger number of particles ($\approx 1800$) is used, to have a sufficiently large dataset to perform a statistical analysis. For an isotropically loaded state, the Probability Distribution of normal forces estimated with the two methods is plotted (Figure 2.9), confirming the features already highlighted. In the CDM, low forces are predominant at the beginning, and their magnitude gradually increases. In the QSM, on the contrary, the distribution stays almost unchanged between the second iteration (at the first iteration the

same value is given to all contacts) and the converged case; only weak (below-average) normal forces are adjusted.

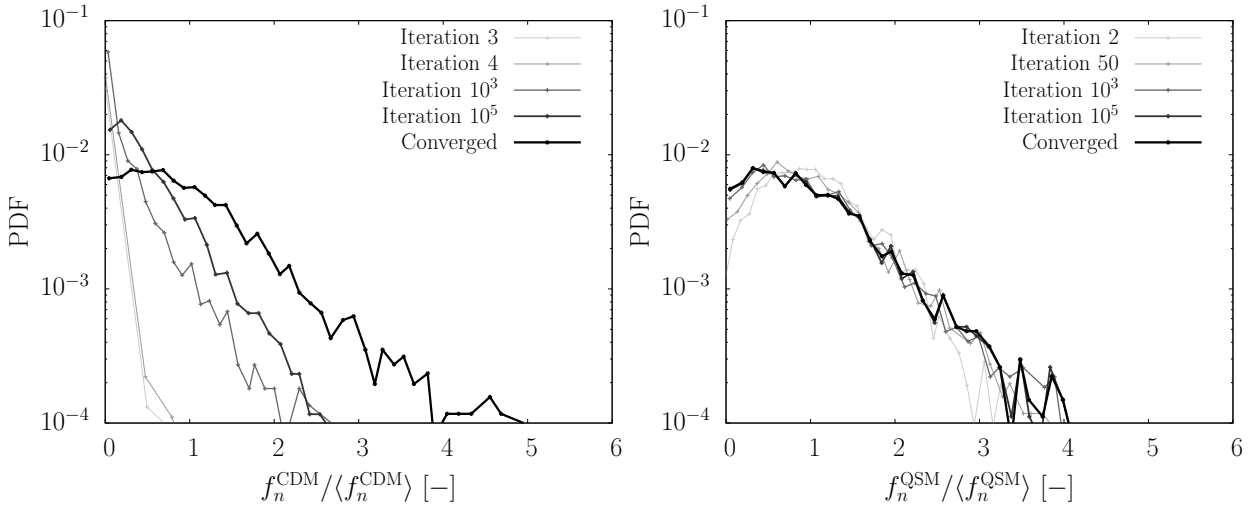


Figure 2.9 – Probability Distribution of normal forces estimated with the CDM (left) and QSM (right), for an isotropically loaded assembly of 1850 particles, during the iterations of the two methods. Normal forces are normalised with respect to their respective average value at convergence.

At convergence, the two Probability Distribution of normal forces – CDM and QSM – are very close to each other; in Figure 2.10, a comparison of the maps of normal forces confirms it, since a good correspondence is observed between the two force networks (at least for strong – above-average – forces that appear more clear).

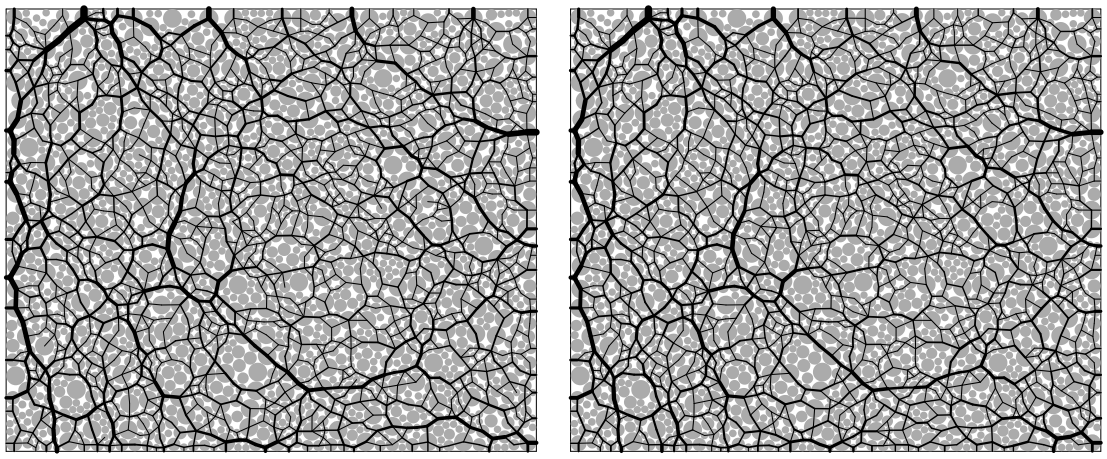

Figure 2.10 – Maps of normal contact forces estimated with the CDM (left) and QSM (right) on an isotropically-loaded system of $\approx$ 1800 particles. Line thickness is proportional to the magnitude of the normal force.

## 2.2 Numerical application to a simple system

In order to present some main features of these three different approaches, a numerical application is carried out for the determination of contact forces in a simple system as the one in Figure 2.11. For a similar case, McNamara et al. (2005) have shown the relation between force indeterminacy and memory of the packing. Here, the aim is mainly to present the three proposed methods and their governing equations with the aid of a simple, numerical example; however, at the same time, an attempt is made to characterise the variability of forces. Moreover, this application allows a further investigation and comparison of how the iterative procedures of the CDM and the QSM work.

The system is composed of three disks, two of which (1 and 2 in Figure 2.11) are fixed, while disk no. 3, in contact with both the other disks, has 3 rigid-body degrees of freedom (DOFs), *i.e.*, it can undergo displacements and rotation[2]. For the angle $\alpha$, a value of 45° is used. For a complete description of the geometry, a radius $R = 5.7$ mm is assigned to the disks.

A degree of force indeterminacy can be defined by means of Equation 2.1. Given the number of unknowns (4, *i.e.*, 2 per contact) and of DOFs, we have $h = 1$, since no mechanism is possible. At sliding, however, an additional relation is introduced ($f_t = \mu f_n$ or $f_t = -\mu f_n$), and the system becomes statically determined.

The system is loaded by a vertical downward force $P = 1530$ N applied on the free disk. Static equilibrium is guaranteed by the two contact forces $\vec{f}_{1\to3}$ and $\vec{f}_{2\to3}$. Due to the symmetry of the geometry and of the applied load, in order to reach equilibrium these forces are required to have the same $y$-components $f_y = P/2$, and opposite $x$-components $f_x$ that can vary in a given range as they are self-balanced (this is the consequence of the previously discussed force indeterminacy). The range of variation of $f_x$ can be defined from geometrical deductions, knowing that the resulting contact force has to fall within the Coulomb cone (Figure 2.12). The obtained range goes from $f_x^{\min}$ to $f_x^{\max}$, defined as follows:

$$f_x^{\min} = \frac{P(\sin\alpha - \mu\cos\alpha)}{2(\cos\alpha + \mu\sin\alpha)} \quad \text{and} \quad f_x^{\max} = \frac{P(\sin\alpha + \mu\cos\alpha)}{2(\cos\alpha - \mu\sin\alpha)} \tag{2.53}$$

In the $(f_n, f_t)$ space, the range of admissibility is given by the Coulomb yielding criterion $|f_t| \leq \mu f_n$; in addition, the static equilibrium of the system requires that all

[2]Given the symmetry of the system, only 1 degree of freedom – the displacement in the $y$-direction – is actually activated.

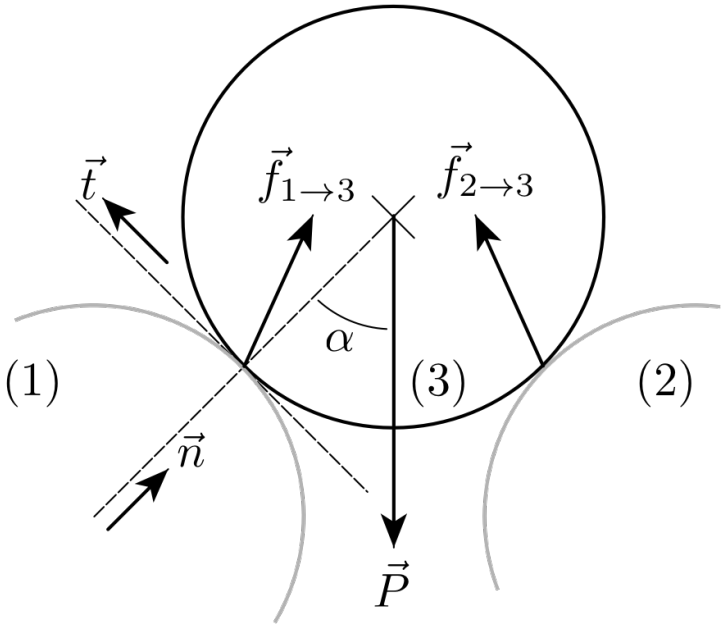


Figure 2.11 – Sketch of a simple system used to introduce the three numerical methods for force estimation. The system is composed of three bodies (disks), two of which (no. 1 and no. 2) are fixed (no degree of freedom). The only degrees of freedom of the system are the 3 DOFs of body no. 3, which is free to displace and rotate.

solutions lie on a line defined by the following affine relation:

$$f_t = \frac{P}{2\sin\alpha} - \frac{f_n}{\tan\alpha} \tag{2.54}$$

One way of characterising a single solution among all the possible solutions is to use a ratio of mobilised friction, ranging between $-1$ and $+1$:

$$\mathfrak{m} = \frac{f_t}{\mu f_n} \tag{2.55}$$

In the following sections, the three methods are applied to estimate forces in this simple system, and the solutions obtained are compared and discussed with respect to the range of admissibility determined by the geometry of the system and the requirement of static equilibrium.

Given the differences in their working principles, each of the methods gets to a solution in a different way. The Contact Elasticity Method estimates forces from the measured motion between an initial (unloaded) state and a final state in which the load is applied and static equilibrium has been reached. Contact Dynamics is used by applying the Gauss-Seidel iterator (numerical resolution method for a non-linear system) for

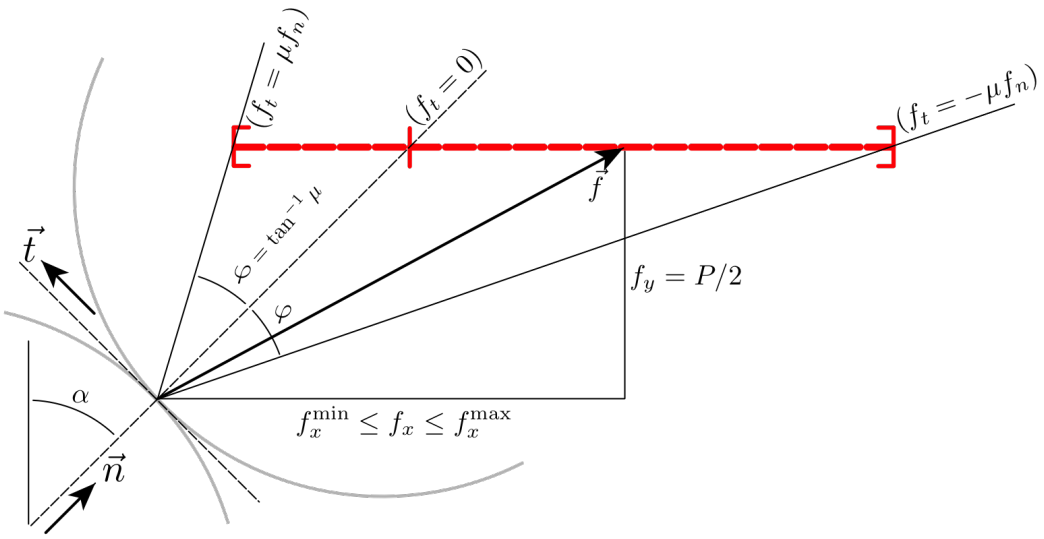


Figure 2.12 – Sketch of the contact $1 \rightarrow 3$, with indication of the range of admissibility of the force $\vec{f}_{1\rightarrow 3}$.

a given state (contact network, external loading); the final values of particle velocities, that express the dynamics of the system when Contact Dynamics is used to simulate the motion of a system – in which case the chosen time step has a physical meaning – are not used here, so we only focus on the obtained contact forces for the considered state. Moreover, since in our applications we are dealing with quasi-static loading conditions (for both experiments and MD-DEM simulations), final velocities are expected to be negligible. The Quasi-Static Method is applied exactly in the way it is meant, *i.e.*, by numerically finding a solution (set of unknown contact forces) for a granular system in static equilibrium, given a contact network and an applied external loading.

### 2.2.1 Contact Elasticity Method

With the Contact Elasticity Method, force estimation can only be performed for an evolution between two states. To create such an evolution in the simple problem previously explained, an MD simulation is performed. A time step $\delta t = \sqrt{\frac{m}{k_n}}\frac{1}{100}$ is adopted for the integration of the equation of motion (given the symmetry of the geometry and of the applied load, the system can be described by 1 DOF, *i.e.*, the $y$-displacement). Contact parameters need to be assigned: the same value is assumed for contact normal and tangential stiffnesses ($k_n = k_t = 5 \cdot 10^7$ N/m); the interparticle friction coefficient is $\mu = 0.5$. Viscous damping is implemented by defining a damping ratio $\zeta = 0.9$ and a viscosity coefficient $g_n = \zeta\sqrt{m_i k_n}$.

At the beginning, the vertical load is applied on the free disk, while the two contact forces start from zero. Iterations are stopped when static equilibrium is reached, *i.e.*, when the resultant force (only the $y$-component is considered) stays below a certain threshold for 200 consecutive time steps. In such conditions, the obtained solution is uniquely defined as $f_n = 721.5$ N and $f_t = 360.8$ N, and the mobilised friction is $\mathfrak{m} = 1$ (values are referred to the contact $1 \rightarrow 3$).

However, additional solutions can be generated by simply changing the initial conditions. A perturbation is introduced by imposing a vertical, upward velocity $\vec{v}_0$ to particle 3. This is equivalent to applying, only in the first time step, a force $\vec{F}_{\text{noise}} = m\vec{v}_0\delta t = (P\vec{v}_0\delta t)/g$ (having assumed $P = mg$); $\vec{v}_0$ can then be expressed as $(\vec{F}_{\text{noise}}/P)(g/\delta t)$. Hereafter, it is convenient to refer directly to the ratio $F_{\text{noise}}/P$, in the place of $\vec{v}_0$. By tuning the magnitude of $F_{\text{noise}}$, different equilibrium states are obtained, being characterised by different contact forces and different values of friction mobilisation $\mathfrak{m}$.

Figure 2.13 shows that the whole range of mobilised friction, from $\mathfrak{m} = -1$ to $\mathfrak{m} = 1$, can be retrieved by simply changing the initial conditions. For five relevant solutions ($\mathfrak{m} = -1, -0.5, 0, 0.5, 1$ respectively), we focus on the evolution of contact forces during the iterations. Figure 2.14 shows how different paths can lead to different final solutions, though always admissible (*i.e.*, falling within the limits of the Coulomb cone). Once the perturbation is applied and forces move away from $(f_n,\ f_t) = (0,\ 0)$, all paths follow the upper part of the Coulomb cone up to a given normal force, and then get back to static admissibility through perpendicular paths.

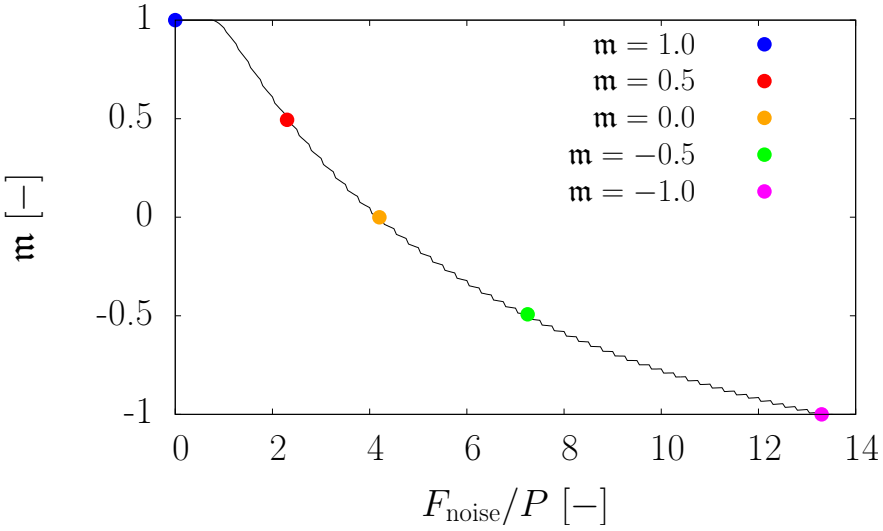


Figure 2.13 – Evolution of the mobilised friction $\mathfrak{m}$ in the MD simulation for different initial conditions, represented by the perturbation $F_{\text{noise}}$ applied at the first time step.

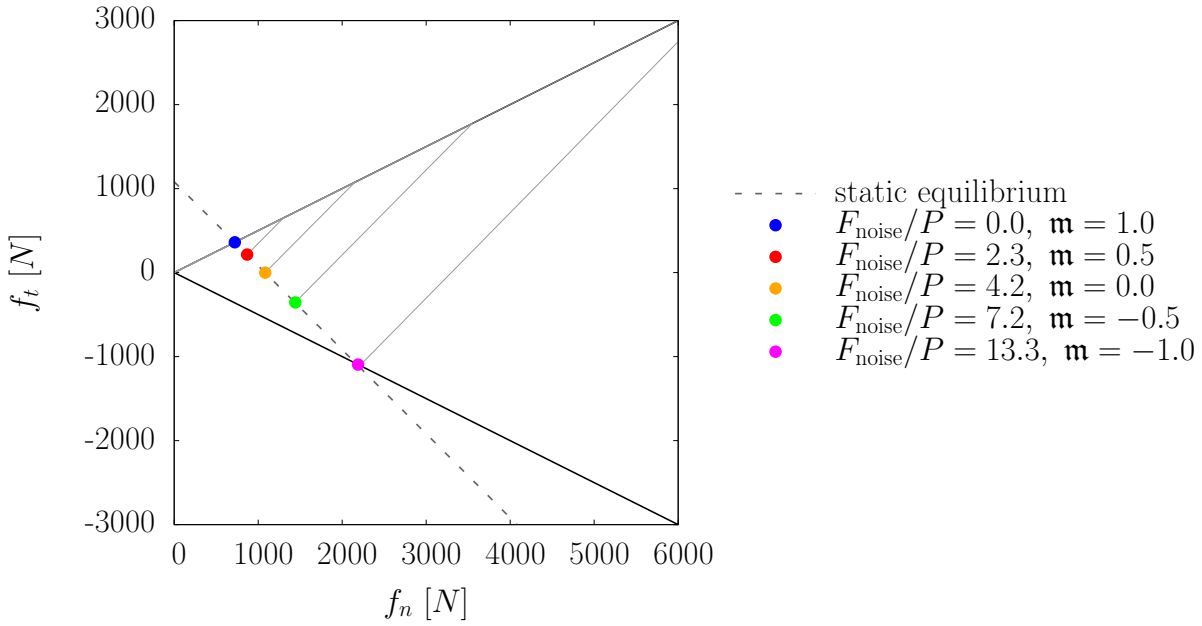


Figure 2.14 – Evolution of the normal and tangential components of the contact force $\vec{f}_{1\to3}$, during the MD-DEM simulation, for five different cases, each corresponding to a different initial condition and resulting in a different final solution, defined by the colour dots. The dashed gray line, corresponding to Equation 2.54, defines the range of admissible solutions with respect to static equilibrium.

The CEM is used to estimate forces for all the solutions obtained by imposing different initial conditions to the MD simulations. The application follows the force laws presented in Section 2.1.1 (Figure 2.1); as to the contact parameters $k_n$, $k_t$ and $\mu$, the same values as those adopted in the simulations are used here. Alternatively, $k_n$ and $k_t$ may be assessed through a re-scaling procedure, similarly to the one described in Section 2.1.1; in this case, the stiffness may be scaled such that the $y$-component of the obtained contact forces equals the applied vertical load.

The estimated force at contact $1 \to 3$ are studied with respect to the mobilised friction of the original solution (Figure 2.15). Despite the variability in the MD solution, which covers the whole range of mobilised friction $[-1 : 1]$, the solution estimated with the CEM always shows a full mobilisation of friction ($\mathfrak{m} = 1$). In terms of the values of single force components, the highest accuracy on the estimated normal force is retrieved for $\mathfrak{m} = 1$, *i.e.*, the only case in which the estimated $\mathfrak{m}$ corresponds to the actual one; in general, the resulting error on $f_n$ is limited (it stays below 0.2%). Also for the tangential force the best estimation is found at $\mathfrak{m} = 1$; however, for solutions with a lower (or opposite) mobilised friction the estimate of $f_t$ can be very far from the actual one. Once more, this shows that the loss of the history of the packing mainly affects the estimation

of tangential forces.

All these findings show that force indeterminacy, which is typically regarded as a peculiarity of methods that completely discard the history of the packing (such as the CDM and the QSM), can actually be retrieved also in the MD-DEM, by simply changing the initial conditions. Knowing the evolution of a system between two states – and not simply the initial and final state – is necessary for a complete description of its history: this affects the estimation of forces with the CEM, especially in terms of tangential forces (much less for normal forces).

### 2.2.2 Contact Dynamics-based Method

The application of the CDM for the solution of the system in Figure 2.11 is more direct than the application of the CEM. With the assumption of contact laws instead of force laws, the knowledge of the contact kinematics of the system is not required; hence, it is not necessary to simulate the motion of the system. Given the external loading and the contact network, a solution for the contact forces can be obtained by simply solving the multi-contact problem through the Gauss-Seidel iterator.

#### 2.2.2.1 Step-by-step procedure

The multi-contact problem is solved for the two contacts $1 \to 3$ and $2 \to 3$; the algorithm is described below only for one contact ($1 \to 3$), defined by the following local frame:

$$\vec{n}^{1,3} = \begin{pmatrix} \sin\alpha \\ \cos\alpha \end{pmatrix} \quad , \quad \vec{t}^{1,3} = \begin{pmatrix} -\cos\alpha \\ \sin\alpha \end{pmatrix} \tag{2.56}$$

Hereinafter, the indices referring to the contact are avoided for clarity, as all contact variables refer to the unique contact considered.

Assuming that the disks no. 1 and no. 2, being fixed in motion, have infinite mass, the only mass and inertial moment that appear in the expressions of the components of the Delassus operator $\mathcal{W}_{nn}$, $\mathcal{W}_{tt}$ and $\mathcal{W}_{nt}$ (Equations 2.19) are those of the disk no. 2. Hence the expression is simplified as:

$$\begin{cases} \mathcal{W}_{nn} &= \dfrac{1}{m} = \dfrac{g}{P} \\ \mathcal{W}_{tt} &= \dfrac{1}{m} + \dfrac{R^2}{I} = \dfrac{3g}{P} \\ \mathcal{W}_{nt} &= 0 \end{cases} \tag{2.57}$$

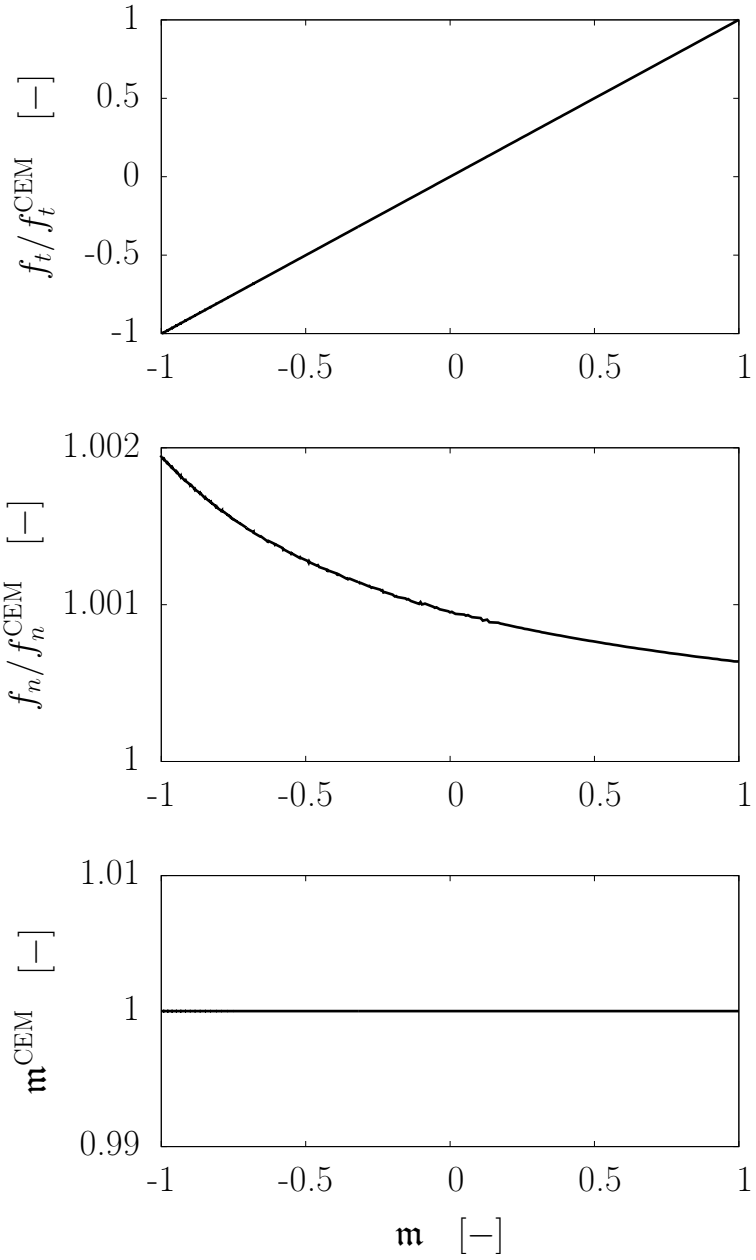


Figure 2.15 – Results of the force estimation at contact $1 \rightarrow 3$ with the CEM, for different solutions (different mobilised friction $\mathfrak{m}$): (top) ratio of the tangential force to the estimated one; (center) ratio of the normal force to the estimated one; (bottom) mobilised friction $\mathfrak{m}$ of the estimated solution.

considering $P = mg$.

Given the static character of the problem, contact laws can be treated without considering impacts by assuming $e_n = e_t = 0$. In this way, the expressions of the formal velocities ($\dot{u}_n^{\text{free}}$, $\dot{u}_t^{\text{free}}$ in Equations 2.25) are also simplified, as we have $\dot{u}_n^- = \dot{u}_t^- = 0$.

At the beginning of the iterator ($k = 0$), the resultant actions of disk no. 3 ($\vec{\mathcal{F}}^k$, $\mathcal{M}^k$) are computed, based on the loading and on a given set of initial forces ($f_n^0$, $f_t^0$), which can be any. Then, at each iteration the procedure described below is carried out.

↪ *Update the force at contact 1 → 3*

$\dot{u}_n^{\text{free}} = \dot{u}_n^+ = \frac{\vec{\mathcal{F}}^k \cdot \vec{n}\ \delta t}{m}$ (Equation 2.25)

**if** $\left(|\dot{u}_n^{\text{free}}| > \epsilon\right)$ **then**

  $f_n^{k+1} \leftarrow f_n^k - \frac{\dot{u}_n^{\text{free}}}{\mathcal{W}_{nn}\delta t}$ (Equation 2.29)

  **if** $\left(f_n^{k+1} > 0\right)$ **then**

    $\dot{u}_t^{\text{free}} = \dot{u}_t^+ = \frac{\vec{\mathcal{F}}^k \cdot \vec{t}\delta t}{m} - \frac{R\ \mathcal{M}^k\ \delta t}{I}$ (Equation 2.25)

    $f_t^{k+1} \leftarrow f_t^k - \frac{\dot{u}_t^{\text{free}}}{\mathcal{W}_{tt}\delta t}$ (Equation 2.31)

    **if** $\left(f_t^{k+1} > \mu f_n^{k+1}\right)$ **then**

      $f_t^{k+1} = \mu f_n^{k+1}$

    **else if** $\left(f_t^{k+1} < -\mu f_n^{k+1}\right)$ **then**

      $f_t^{k+1} = -\mu f_n^{k+1}$

    **end if**

  **else**

    $f_n = 0, f_t = 0$

  **end if**

**else**

  no correction required

**end if**

↪ *Update resultant actions of disk no. 3*

$\vec{\mathcal{F}}^{k+1} \leftarrow \vec{\mathcal{F}}^k + \left(f_n^{k+1} - f_n^k\right) \cdot \vec{n} + \left(f_t^{k+1} - f_t^k\right) \cdot \vec{t}$

$\mathcal{M}^{k+1} \leftarrow \mathcal{M}^k + R\left(f_t^{k+1} - f_t^k\right)$

This procedure is repeated for all contacts, until a criterion is reached.

Since the motion of the system is not integrated over time, any value can actually be chosen for the time step; we assume $\delta t = 1$, such that the contact force $\vec{f}$ appears the same as the impulse $\vec{f}\delta t$.

In the implementation of this algorithm for the problem in Figure 2.11, the symmetry of the system is imposed, and the degrees of freedom are consequently reduced from 3 to 1 (the $y$-component of the velocity of particle 3).

Two stopping criteria are used: one on the satisfaction of the contact laws, by setting a numerical tolerance $\epsilon$ for the graph thickness in Figure 2.5; a second criterion takes into account the static character of the problem, and sets a threshold for the vertical component $\mathcal{F}_y$ of the resultant force on disk no. 3:

$$\frac{|\mathcal{F}_y|}{P} < 10^{-15} \tag{2.58}$$

The graph thickness is set to a very low value ($\epsilon = 10^{-20}$) and this criterion is actually never met, so that the loop is stopped only when the second criterion is satisfied, *i.e.*, the solution is statically admissible.

#### 2.2.2.2 Characterisation of admissible solutions

The procedure described in the previous section takes into account the 3 DOFs of the system, *i.e.*, the $x$- and $y$-displacement and the rotation of particle 3. However, as previously mentioned, due to the symmetry of the geometry and of the load applied, only 1 DOF (along $y$) is actually relevant; the other two are removed by these constraints. The results shown for the following applications are obtained by simplifying the treatment of the problem, finally described by only 1 DOF. A specific code has been dedicated to this purpose. This simplification does not modify the force indeterminacy of the system: the number of unknowns (contact force components) and DOFs are equally reduced, and we still have $h = 1$.

A first application of the algorithm is carried out by only considering the applied loading $P$ at the first iteration, with no contact force ($f_n^0 = f_t^0 = 0$). Assuming $\mu = 0.5$, a final solution with $f_n = 811.40$ N and $f_t = 270.45$ N is obtained, corresponding to $\mathfrak{m} = 0.67$. It is interesting to notice that a different solution, with $\mathfrak{m} = 1$, would be obtained with a 3-DOF treatment.

Then, in order to characterise the space of admissible solutions, a set of initial conditions is given by imposing initial values for the normal and tangential contact forces. These values are randomly chosen in a range defined by the following conditions:

$$\begin{cases} 0 \leq f_n \leq f_n^{\mu=0} \\ |f_t| \leq \mu f_n^{\mu=0} \end{cases} \tag{2.59}$$

where $f_n^{\mu=0} = P\cos\alpha$ is the normal component of the unique solution obtained when $\mu = 0$. This set of initial conditions includes some values that are not plastically admissible, to check the behaviour of the method in such cases.

In a first stage, a number of solutions is generated, in this way, for different values of $\mu$, ranging from 0 to 1. The obtained solutions are characterised through the computation of the mobilised friction $\mathfrak{m}$. Figure 2.16a shows the evolution of this quantity as a function of $\mu$. For each value of $\mu$, several solutions are obtained, and the mean and standard deviation of $\mathfrak{m}$ over these solutions are computed, as well as the lowest and highest value it takes. It is observed that, as $\mu$ increases, friction can still be fully mobilised in the positive part of the cone ($f_t = \mu f_n$), while no solution with $f_t = -\mu f_n$ is obtained for $\mu > 0.075$. On average, however, $\mathfrak{m}$ remains close to 0 for the whole range of $\mu$, but it should be remarked that this does not mean that $\mathfrak{m} = 0$ is the most likely case, as one can infer from Figure 2.16b.

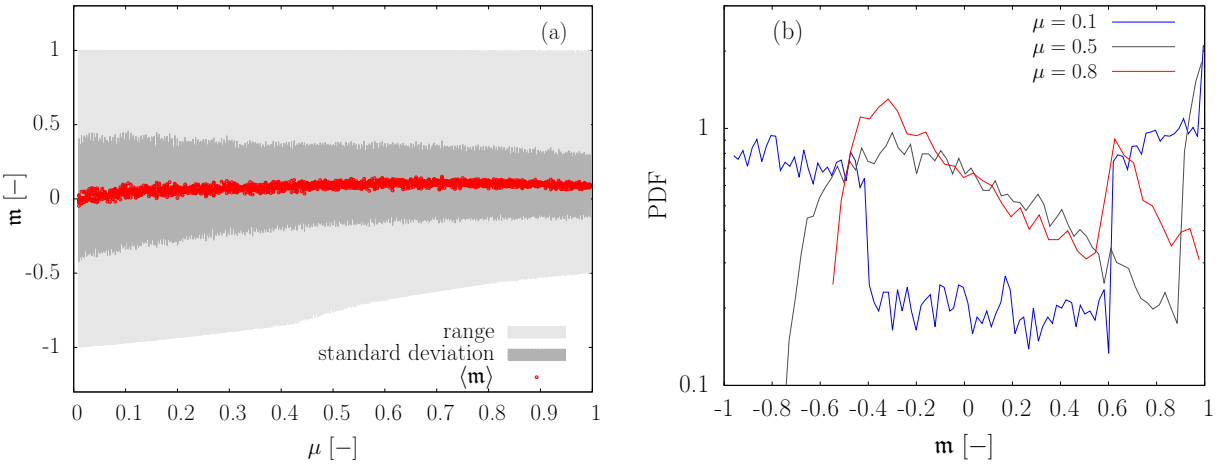


Figure 2.16 – Characterisation of the range of variability of the solutions found with the CDM for the system in Figure 2.11. (Left) range of admissibility, mean and standard deviation of the mobilised friction $\mathfrak{m}$ for different values of interparticle friction coefficient $\mu$. (Right) PDF of $\mathfrak{m}$ for given values of $\mu$.

These results become more clear by studying the evolution of the percentage of solutions at yielding, for each value of $\mu$ (Figure 2.17). For very low values of $\mu$, the whole friction is mobilised in almost all solutions; as $\mu$ increases, the number of solutions at yielding decreases: at $\mu = 0.5$, less than 10%; at $\mu = 1$, no solution has $\mathfrak{m} = \pm 1$.

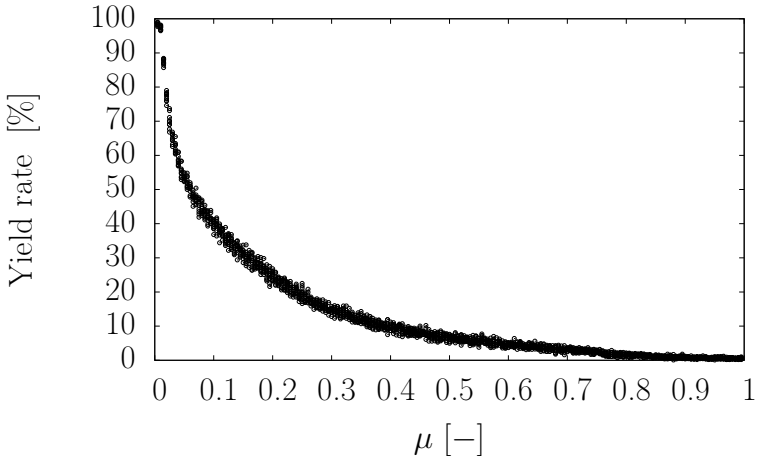


Figure 2.17 – Percentage of solutions that mobilise the whole friction ($\mathfrak{m} = \pm 1$), for different values of interparticle friction coefficient $\mu$, in the application of the CDM to the system in Figure 2.11. We assume that yielding is reached when $|\mathfrak{m}| \geq 0.99$.

#### 2.2.2.3 Analysis of the convergence

After having characterised the solutions obtained, it is interesting to focus on how the method gets from a given initial condition to a final, admissible solution. With this purpose, the evolution of several quantities during the iterative procedure of the CDM is studied in this Section; a unique value of $\mu = 0.5$ is assumed.

In a first stage, the path from the initial forces to the final solution is studied for few cases. Different initial conditions are given, including all possible cases: forces within the boundaries of the Coulomb cone, lying on the cone itself or outside its boundaries. Figure 2.18 shows these paths for a number of initial conditions. It can be immediately observed that the line of statically admissible (Equation 2.54) solutions is not reached with perpendicular paths, even when this would not contrast with the plastic admissibility; even for those paths that are basically linear, no common slope can be detected. As to solutions starting from outside the Coulomb cone, they tend to first reach the cone – though not via the shortest way – and then approach the static equilibrium line. As forces get closer to admissible solutions, some oscillations are observed.

The stopping criterion adopted (Equation 2.58) is based on the vertical component of the resultant force on grain 3. Its evolution throughout the iterative loop is shown in Figure 2.19 for three different solutions, obtained with different initial conditions. At iteration 0, the distance from static equilibrium can be very different; however, in all the cases $|\mathcal{F}_y|$ decays exponentially with the same slope, and the only difference is in the number of iterations required to reach convergence $n_{\text{iter}}$.

This suggests that there might be a correlation between the initial distance from

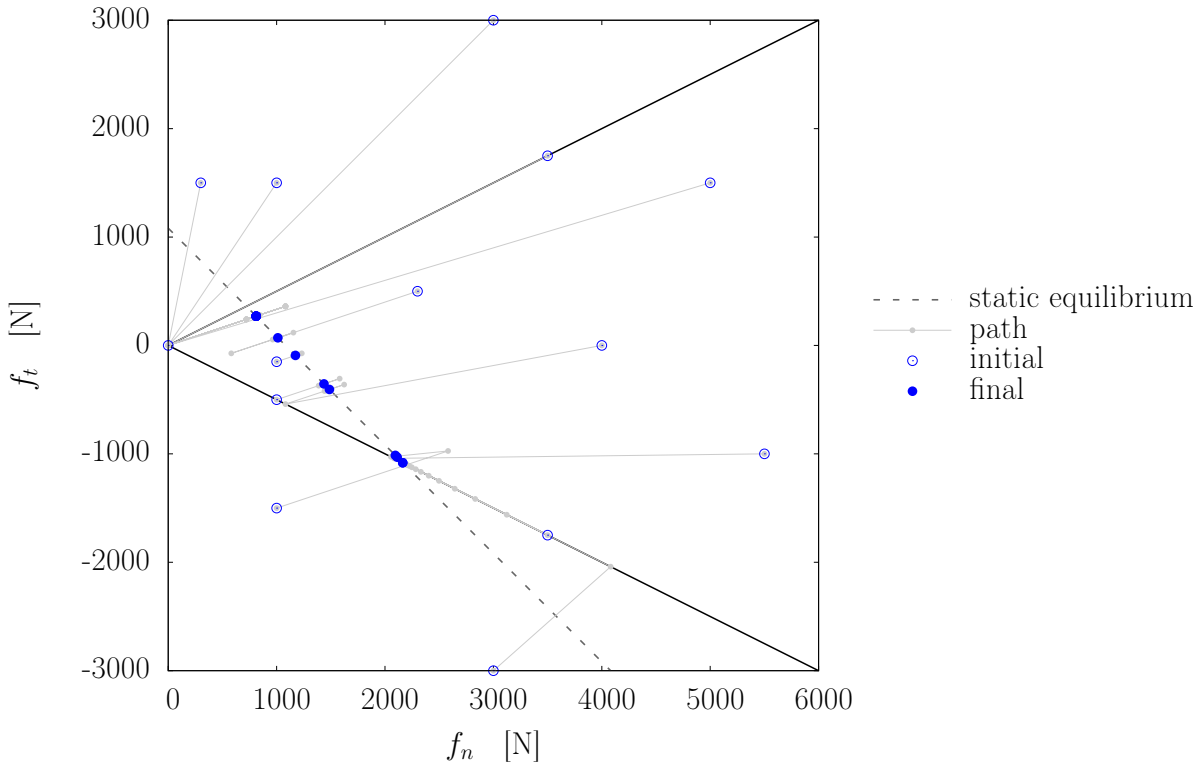


Figure 2.18 – Evolution of the normal and tangential components of the contact force $\vec{f}_{1\to3}$, in the CDM application, from the (randomly chosen) initial values of normal and tangential contact forces to the final values. The dashed gray line, corresponding to Equation 2.54, defines the range of admissible solutions with respect to static equilibrium.

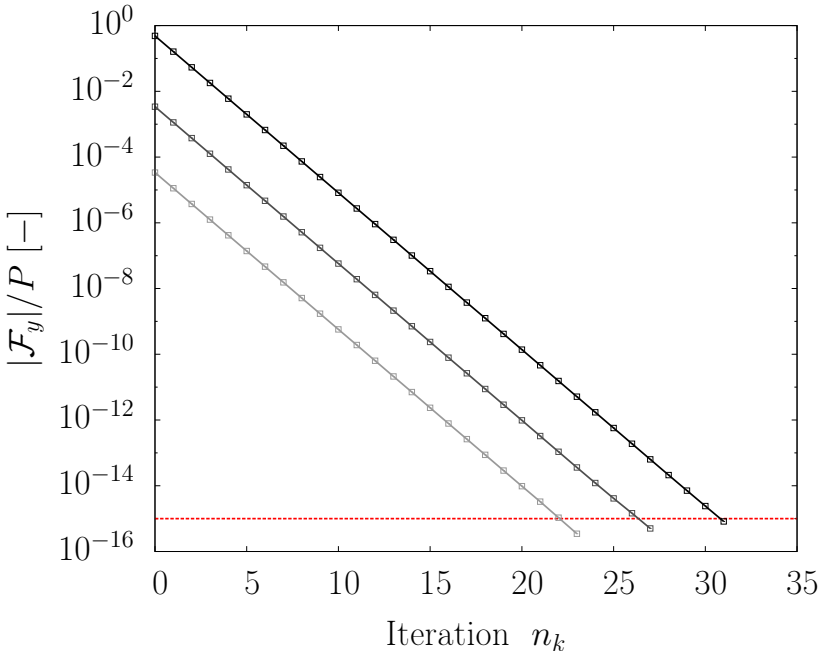


Figure 2.19 – Convergence towards admissible solutions obtained with the CDM when starting from three different initial conditions. The magnitude of the vertical component of the resultant force $\mathcal{F}$ on grain no. 3, normalised by the applied load $P$, is shown.

equilibrium and the number of iterations. To confirm this, the two quantities are plotted (Figure 2.20a). As expected, the highest number of required iterations is obtained for those cases in which the initial conditions are furthest from static equilibrium, in both direction ($\mathcal{F}_y^0$ oriented downward or upward).

Figure 2.20b shows the distance from static equilibrium at convergence $\mathcal{F}_y$, *i.e.*, once the criterion is fulfilled, as a function of the initial distance. Although the values of $\mathcal{F}_y$ can slightly differ between each other – while still being below the threshold –, no clear correlation is observed with their initial values. By plotting the distance from equilibrium without its absolute value, it is also observed that $\mathcal{F}_y$, at convergence but also throughout the whole iterative procedure, can take both positive and negative values, *i.e.*, the resultant force can be oriented both downward and upward. While its magnitude decreases monotonically, $\mathcal{F}_y$ rather oscillates around 0, changing orientation alternatively at each iteration.

Finally, with the aim of looking for a possible correlation with the initial conditions, a velocity of convergence is defined as the reduction of $|\mathcal{F}_y|$ through the whole iterative loop:

$$v_{\text{conv}} = \frac{|\mathcal{F}_y| - |\mathcal{F}_y^0|}{n_{\text{iter}}} \tag{2.60}$$

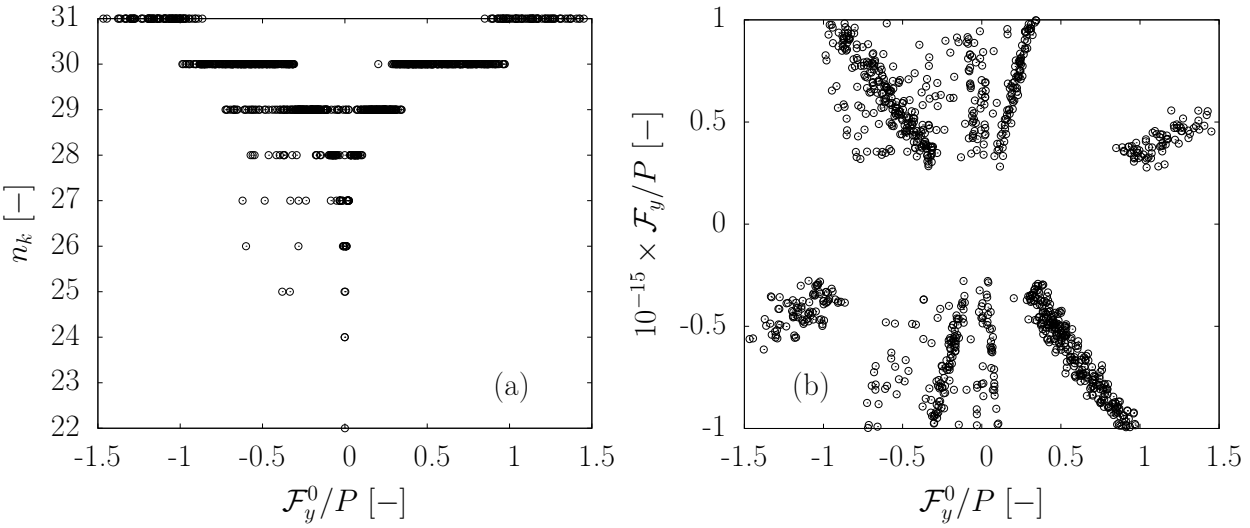


Figure 2.20 – Characterisation of the convergence for a set of 1000 solutions obtained with the CDM for different initial conditions.
(Left) Number of iterations required to reach convergence as a function of the initial distance from static equilibrium of grain no. 3.
(Right) Final distance from static equilibrium $\mathcal{F}_y/P$ as a function of the initial one $\mathcal{F}_y^0/P$.

Figure 2.21 shows that, despite a number of cases that show no relation, the velocity of convergence is mainly linear with the initial distance from equilibrium. In particular, this means that the CDM can apply larger *corrections*, at each time step, when its starting point is further from equilibrium.

### 2.2.3 Quasi-Static Method

Similarly to the CDM, also with the QSM the estimation of forces is simply based on the knowledge of the external loading and the contact network at a given state. The numerical procedure of double projection is described, for the simple case in Figure 2.11, in the next section. Then, the admissible solutions are characterised (Section 2.2.3.2) and the convergence of the method is studied (Section 2.2.3.3), as for the CDM.

#### 2.2.3.1 Step-by-step procedure

The small number of variables and equations involved in the problem in Figure 2.11 allows a step-by-step development and build-up of the matrix formulation of the method.

Such a formulation requires the definition of appropriate matrices to relate grain-based variables (corresponding to the DOFs of the system) with contact-based one (forces

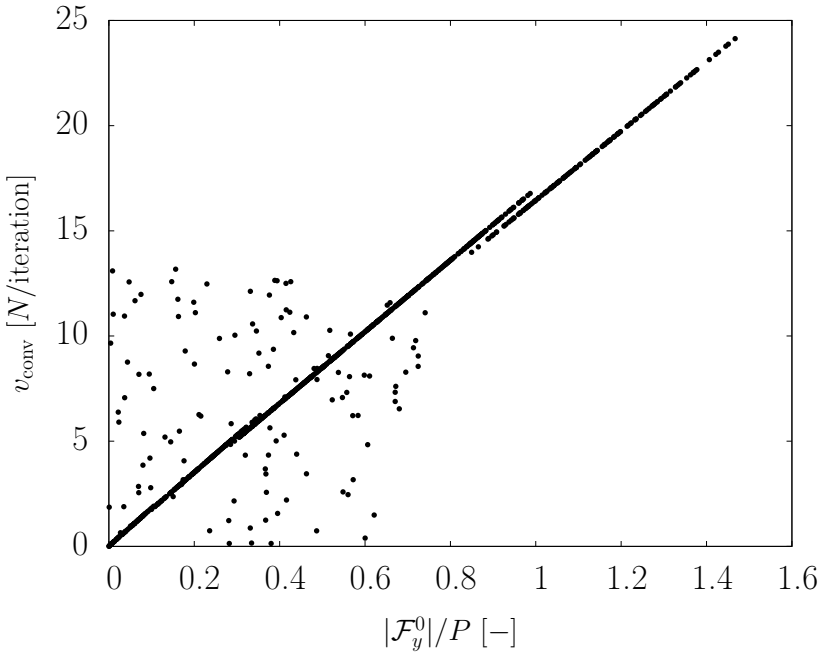


Figure 2.21 – Velocity of convergence for the same cases in Figure 2.20, expressed as the reduction of the distance from equilibrium over the number of iterations required, as a function of the initial distance from static equilibrium.

and relative displacements). With this purpose, a conventional local reference is introduced first, as defined in Figure 2.11. The normal and tangent vectors for the two contacts are defined as follows:

$$\vec{n}^{1,3} = \begin{pmatrix} \sin\alpha \\ \cos\alpha \end{pmatrix} \quad , \quad \vec{n}^{2,3} = \begin{pmatrix} -\sin\alpha \\ \cos\alpha \end{pmatrix} \quad , \quad \vec{t}^{i,j} = \begin{pmatrix} -n_y^{i,j} \\ n_x^{i,j} \end{pmatrix} \tag{2.61}$$

The set of variables can be written in a matrix form by grouping all the DOFs in the displacements vector $\underline{\boldsymbol{U}}$ (Equation 2.34); the same can be done for the contact relative displacements, defining the vector $\underline{\boldsymbol{u}}$ (Equation 2.35). The relation between these two vectors, in a matrix form, is $\underline{\boldsymbol{u}} = \underline{\underline{\boldsymbol{G}}}\,\underline{\boldsymbol{U}}$, where matrix $\underline{\underline{\boldsymbol{G}}}$ writes as follows:

$$\underline{\underline{\boldsymbol{G}}} = \begin{pmatrix} n_x^{1,3} & n_y^{1,3} & 0 \\ t_x^{1,3} & t_y^{1,3} & -R \\ n_x^{2,3} & n_y^{2,3} & 0 \\ t_x^{2,3} & t_y^{2,3} & -R \end{pmatrix} \tag{2.62}$$

The matrix of contact stiffnesses $\underline{\underline{\boldsymbol{\mathcal{K}}}}$, as defined in (2.43), is the following:

$$\underline{\underline{\boldsymbol{\mathcal{K}}}} = \begin{pmatrix} k_n^{1,3} & & & \\ & k_t^{1,3} & & \\ & & k_n^{2,3} & \\ & & & k_t^{2,3} \end{pmatrix} = k\,\mathbb{I} \tag{2.63}$$

having assumed the same stiffness $k = 5 \times 10^7$ N/m, for both contacts, in both normal and tangential directions.

It is now possible to build the global stiffness matrix $\underline{\underline{\mathbf{K}}} = \underline{\underline{\boldsymbol{G}}}^T \underline{\underline{\boldsymbol{\mathcal{K}}}}\,\underline{\underline{\boldsymbol{G}}}$, which groups all the material (*i.e.*, contact stiffnesses) and geometrical properties of the system:

$$\begin{cases} \mathrm{K}_{xx} = k_n^{1,3}\left(n_x^{1,3}\right)^2 + k_t^{1,3}\left(t_x^{1,3}\right)^2 + k_n^{2,3}\left(n_x^{2,3}\right)^2 + k_t^{2,3}\left(t_x^{2,3}\right)^2 \\ \mathrm{K}_{yy} = k_n^{1,3}\left(n_y^{1,3}\right)^2 + k_t^{1,3}\left(t_y^{1,3}\right)^2 + k_n^{2,3}\left(n_y^{2,3}\right)^2 + k_t^{2,3}\left(t_y^{2,3}\right)^2 \\ \mathrm{K}_{\theta\theta} = k_t^{1,3}\left(R\right)^2 + k_t^{2,3}\left(R\right)^2 \\ \mathrm{K}_{xy} = \mathrm{K}_{yx} = k_n^{1,3} n_x^{1,3} n_y^{1,3} + k_t^{1,3} t_x^{1,3} t_y^{1,3} + k_n^{2,3} n_x^{2,3} n_y^{2,3} + k_t^{2,3} t_x^{2,3} t_y^{2,3} \\ \mathrm{K}_{x\theta} = \mathrm{K}_{\theta x} = -k_t^{1,3} t_x^{1,3} R - k_t^{2,3} t_x^{2,3} R \\ \mathrm{K}_{y\theta} = \mathrm{K}_{\theta y} = -k_t^{1,3} t_y^{1,3} R - k_t^{2,3} t_y^{2,3} R \end{cases} \tag{2.64}$$

One last operation is required before the double projection procedure can be applied: the local projection $\mathcal{P}$ requires the inversion of matrix $\underline{\underline{\mathbf{K}}}$. Being $\underline{\underline{\mathbf{K}}}$ a $3 \times 3$ matrix, the inversion is quite easy, and many methods (*e.g.*, the one making use of the cofactor matrix) can be used. When $\alpha = 45°$, $\underline{\underline{\mathbf{K}}}^{-1}$ is obtained numerically:

$$\underline{\underline{\mathbf{K}}}^{-1} \simeq \begin{pmatrix} 2 \times 10^{-8} & 0 & 2.467 \times 10^{-6} \\ 0 & 10^{-8} & 0 \\ 2.467 \times 10^{-6} & 0 & 0.0006 \end{pmatrix} \tag{2.65}$$

The external loading $\underline{\boldsymbol{F}}^{\mathrm{ext}}$ consists of the following components:

$$\underline{\boldsymbol{F}}^{\mathrm{ext}} = \begin{pmatrix} 0 \\ -P \\ 0 \end{pmatrix} \tag{2.66}$$

At the beginning of the iterator ($k = 0$), the contact forces $\underline{\boldsymbol{f}} = \left(f_n^{1,3}\ f_t^{1,3}\ f_n^{2,3}\ f_t^{2,3}\right)^T$ are initialised to a guess solution $\underline{\boldsymbol{f}}_0$, which can be any. At each iteration, the double

projection is applied, following the procedure below.

↪ *Local PA projection* $\mathcal{Q}$ (Section 2.1.3.4)
**if** $\left(f_n^k < 0\right)$ **then**
  $f_n^k \leftarrow 0$
**end if**
**if** $\left(f_t^k > \mu f_n^k\right)$ **then**
  $f_t^k \leftarrow \mu f_n^k$
**else if** $\left(f_t^k < -\mu f_n^k\right)$ **then**
  $f_t^k \leftarrow -\mu f_n^k$
**end if**

↪ *Global SA projection* $\mathcal{P}$ (Section 2.1.3.3)
$\Delta \underline{U} = \underline{\underline{\mathbf{K}}}^{-1} \cdot \left(\underline{F^{\text{ext}}} - \underline{\underline{G}}^T \cdot \underline{f}\right)$
$\underline{f}^{k+1} \leftarrow \underline{f}^k + \underline{\underline{\mathcal{K}}} \cdot \Delta \underline{U}$

This iterative procedure is repeated until a criterion is met. Consistently with the CDM application (Section 2.2.2), the chosen criterion is based on the definition of a distance from static equilibrium:

$$\frac{|\mathcal{F}_y|}{P} < 10^{-15} \tag{2.67}$$

This criterion is actually part of the four criteria commonly used in the application of this method (Section 2.1.3.5).

#### 2.2.3.2 Characterisation of admissible solutions

A first solution for $\mu = 0.5$, obtained by using a null vector as the initial guess solution $\underline{f}_0$, is $\underline{f} = (721.25 \quad 360.62 \quad 721.25 \quad -360.62)^T$ with $\mathfrak{m} = 1$. This solution is different from the one obtained with the CDM when reducing the problem to 1 DOF; if the CDM is applied with a 3 DOF treatment, the same solution as the QSM is found.

Once again, in order to investigate the whole space of admissible solutions, a set of initial conditions is given. To allow a comparison with the solutions of the CDM, the same initial forces are used for both methods. In the same way as with the CDM, a range of interparticle friction coefficient $\mu$ is investigated.

A first comparison is made by looking at the percentage of solutions, for each value of $\mu$, that lie on the Coulomb cone ($f_t = \pm \mu f_n$). Figure 2.22 shows a tendency of the

QSM to find more yielding solutions, with respect to the CDM, for the whole range of $\mu$ considered. In particular, a certain amount of such solutions ($\approx 10\%$) is found even for large values of $\mu$, for which, on the contrary, all CDM solutions are strictly within the boundaries of the cone. Despite this,

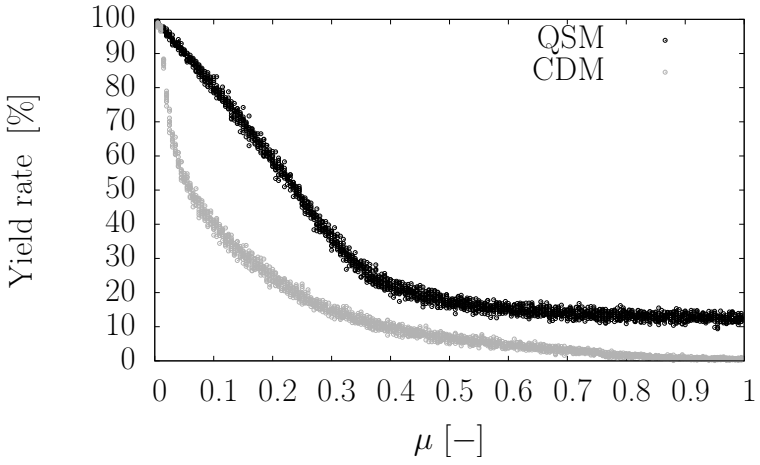


Figure 2.22 – Percentage of solutions that mobilise the whole friction, for different values of interparticle friction coefficient $\mu$, in the application of the QSM to the system in Figure 2.11. We assume that yield is reached when $|\mathfrak{m}| \geq 0.99$, as for the CDM. The values of the CDM application (Figure 2.17) are plotted for comparison.

This result already shows that, for the same initial conditions, the two methods do not get to the same solution; this is confirmed by a one-by-one comparison of the solutions provided by the two methods for each pair of $(f_n^0,\ f_t^0)$, for a given friction coefficient ($\mu = 0.5$). In Figure 2.23, the solutions are compared in terms of normal force, tangential force and mobilised friction. They appear to be quite dispersed around the line that indicates perfect matching. The difference can be quantified by computing its average and standard deviation; in absolute value, the difference is $7.2 \pm 165.5$ N for normal forces (the average normal force being $\approx 1080$ N for both the CDM and QSM solutions), and $0.03 \pm 0.3$ for the mobilised friction.

To complete the characterisation of the mobilised friction, its average, standard deviation and range of values are plotted in Figure 2.24a, as it was done for the CDM. Globally, $\mathfrak{m}$ shows the same features as in the CDM: while its deviation is reduced, its average remains close to 0 for all $\mu$, except for a very slight increase that is consistent with the observation – common to the two methods – that yielding is more likely on the positive side of the Coulomb cone. Although in average $\mathfrak{m}$ is close to 0, the case with no mobilisation ($\mathfrak{m} = 0$) still has a rather low probability (Figure 2.24b). However, in this case we observe that full *negative* mobilisation is still possible up to $\mu \approx 0.4$, while in the CDM it stops for much lower values.

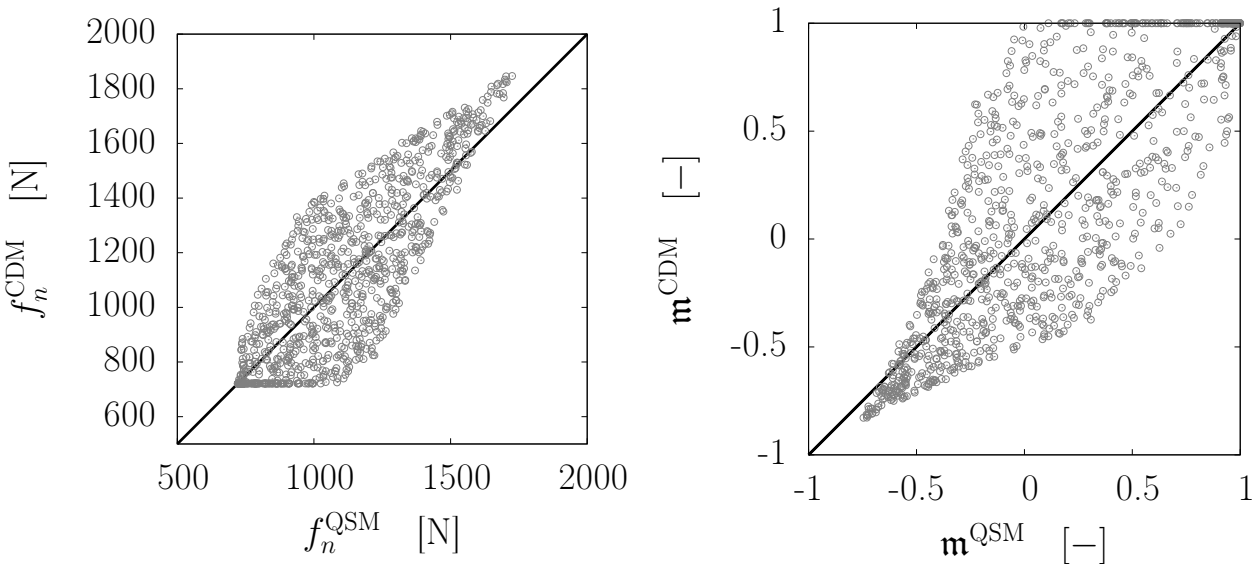


Figure 2.23 – Comparison of the solutions obtained, for the same initial conditions, with the CDM and the QSM: (left) normal forces; (right) mobilised friction. The black line indicates a perfect matching between the two solutions.

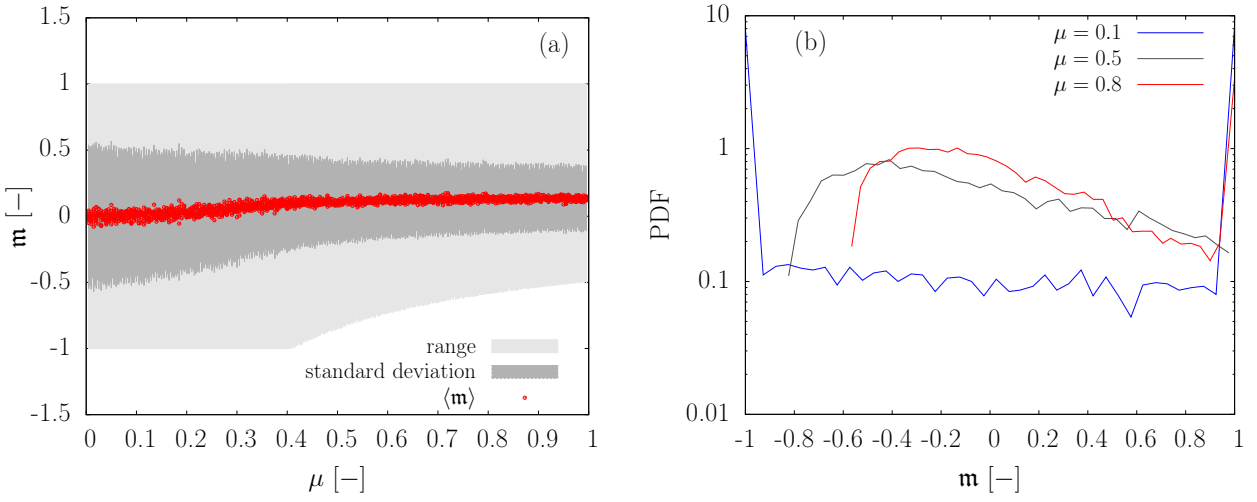


Figure 2.24 – Characterisation of the range of variability of the solutions found with the QSM for the system in Figure 2.11 (Left) Range of admissibility, mean and standard deviation of the mobilised friction $\mathfrak{m}$ for different values of interparticle friction coefficient $\mu$. (Right) PDF of $\mathfrak{m}$ for given values of $\mu$.

#### 2.2.3.3 Analysis of the convergence

A focus is made here on the convergence of the QSM towards an admissible solutions, as it was done for the CDM. In Figure 2.25, we analyse the evolution of normal and tangential forces, from $(f_n^0,\ f_t^0)$ to their final values, is studied for a number of initial conditions, including forces inside, on and outside the Coulomb cone. As in the CDM, the solutions are obtained by treating the problem with only 1 DOF, due to symmetry. For the same reason, the two contact forces composing vector $\underline{\boldsymbol{f}}$ are equal to each other, so hereafter we will only refer to one of them. A value of $\mu = 0.5$ is assumed for the following analyses.

It should be remarked that the algorithm explained in the previous section can actually be performed in two ways, by either starting with a $\mathcal{Q}$ projection on the SA subspace (as described) or with a $\mathcal{P}$ projection on the PA subspace. However, this choice might result in different final solutions, as the path in the $(f_n,\ f_t)$ space changes. In particular, if the initial condition (generally not statically admissible) is inside the subspace of plastically admissible solutions (*i.e.*, within or on the Coulomb cone), no projection is required on the PA subspace, so the first projection is always performed on the SA subspace, whether the algorithm is structured in one way or another. If the initial guess on forces lies outside the cone, two different paths can be taken based on which projection is performed first.

The alternative projection becomes particularly clear, in Figure 2.25, especially for the case starting from $(f_n^0,\ f_t^0) = (5500\ \text{N}\ ,-1000\ \text{N})$. Moreover, it can be observed that all projections on the SA subspace (here, the line of Equation 2.54) are performed orthogonally: at each step in which a projection is performed, the force point jumps directly onto the SA line through the shortest way. The orthogonality is the result of the choice of equal normal and tangential contact stiffnesses. The same paths, interestingly, were observed in the MD-DEM simulation (Figure 2.14). The main comparison, however, is with the CDM application: in that case, the evolution towards admissibility seems to involve longer paths (no perpendicularity) and more steps (due to oscillations around the final point).

This results might also explain the higher rate of solutions that mobilise the whole friction in the QSM, with respect to the CDM (Figure 2.22). Here, when the initial guess solution is such that its projection on the line of static admissibility falls outside of the space of plastic admissibility, the shortest possible path to an SA-PA solution leads to the intersection between the SA line and the Coulomb cone. Thus, in such cases the QSM is forced to reach a yielding solution. On the other hand, the CDM does not always reach a final solution at yielding.

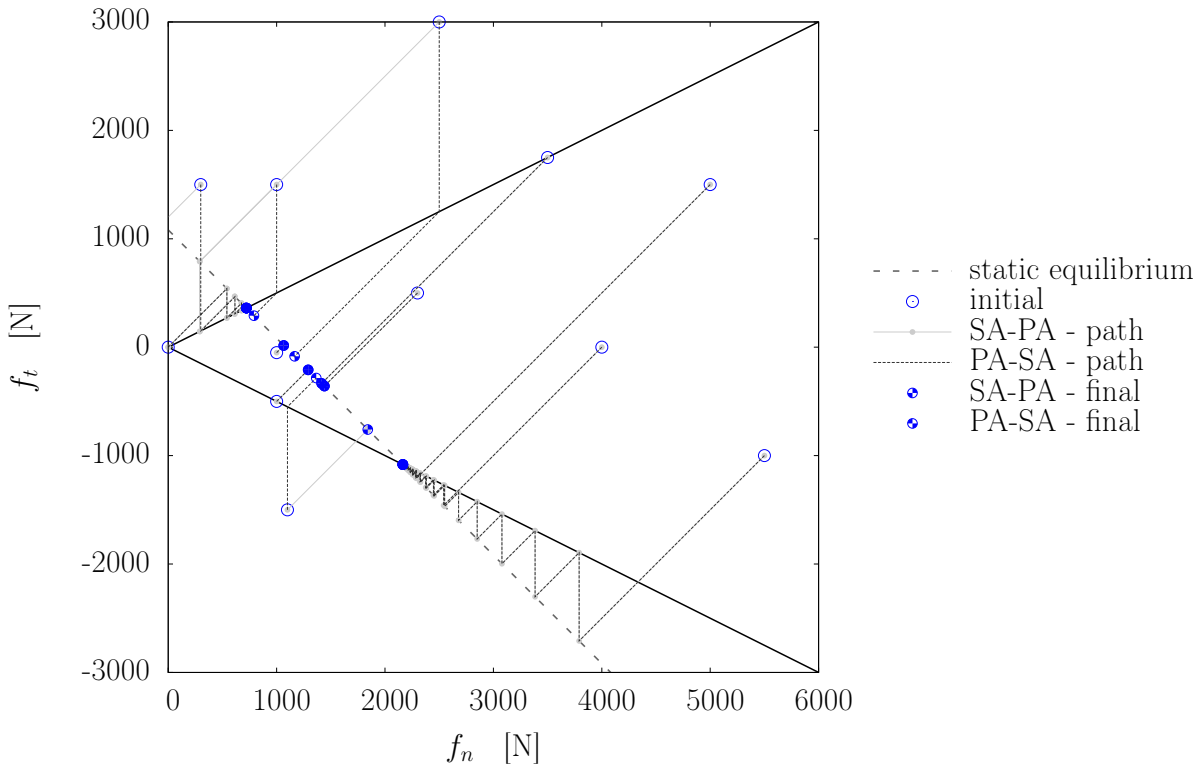


Figure 2.25 – Evolution of the normal and tangential components of the contact force $\vec{f}_{1\to3}$, in the QSM application, from the (randomly chosen) initial values of normal and tangential contact forces to the final values. The dashed gray line, corresponding to Equation 2.54, defines the range of admissible solutions with respect to static equilibrium. Different paths and final solutions, for a given initial condition, are shown according to the order in which the projections are performed.

It is interesting to compare the evolution towards convergence of the QSM, in the way it is applied in this work, with the standard formulation of this approach, which is meant to deal with small loading increments. To perform this step-wise application, some initial sets of forces are given, being plastically and statically admissible with the applied force $P_0 = 2P$. Then, loading increments $\Delta P = (P - P_0)/100$ are applied, and a solution equilibrating the current loading is determined for each step. In Figure 2.26, the result of this application is shown. The final solutions, for each of the three cases, corresponds very well with the solution obtained, for the same initial conditions, with the QSM formulation adopted in this work. For two of the three cases, *i.e.*, when the projection on the SA subspace falls within the Coulomb cone, also the paths correspond. This shows that interestingly, at least for this extremely simple problem, the two possible applications of the quasi-static approach reach the same result.

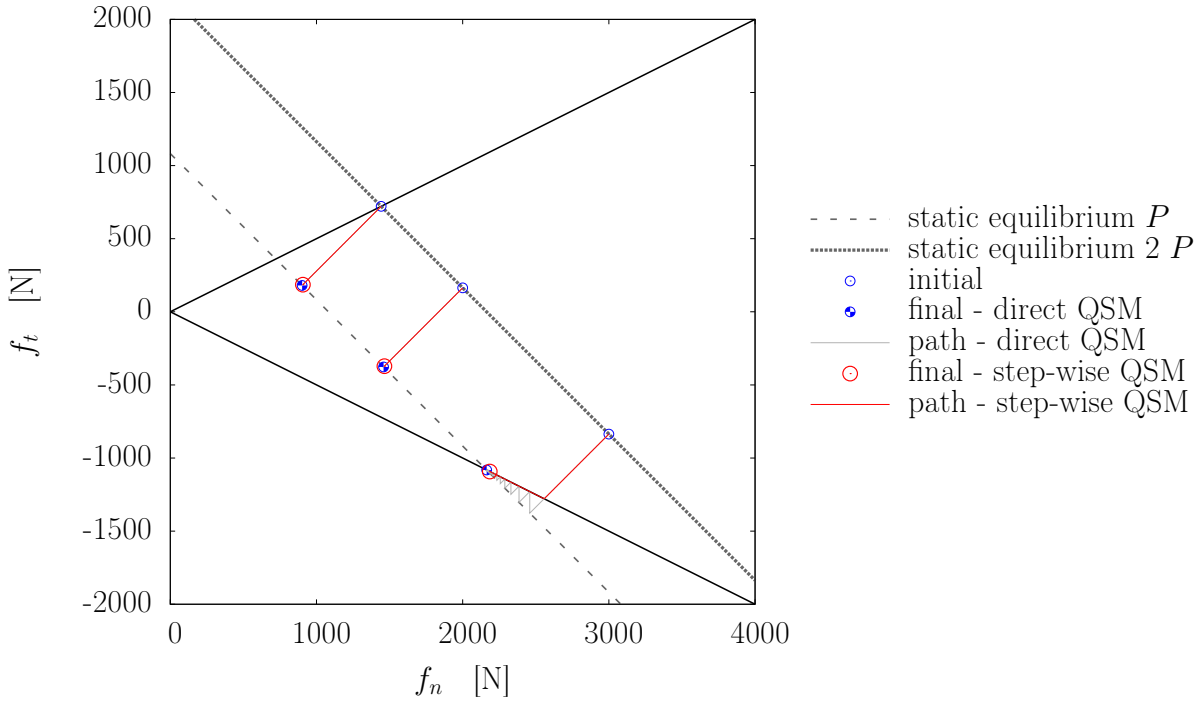


Figure 2.26 – Evolution of the normal and tangential components of the contact force $\vec{f}_{1\to3}$, in the application of the step-wise Quasi-Static approach, from the initial values of normal and tangential contact forces to the final values. The two dashed gray lines, corresponding to Equation 2.54, defines the range of admissible solutions with respect to static equilibrium when $P$ and $2P$ are applied. The final solution of the direct application of the QSM, for the same initial conditions, is shown for comparison.

Figure 2.27 shows the evolution of the distance from static equilibrium, *i.e.*, the parameter used as a stopping criterion (Equation 2.67), throughout the iterations of the QSM. An exponential decay is found here, as in the CDM; however, while in the CDM

a common slope is obtained, here two alternatives can be identified. Two of the three plotted curves has a similar slope (although one has a higher slope only in the first iteration); in the case of the third curve, convergence is reached with only one iteration, hence the much higher slope.

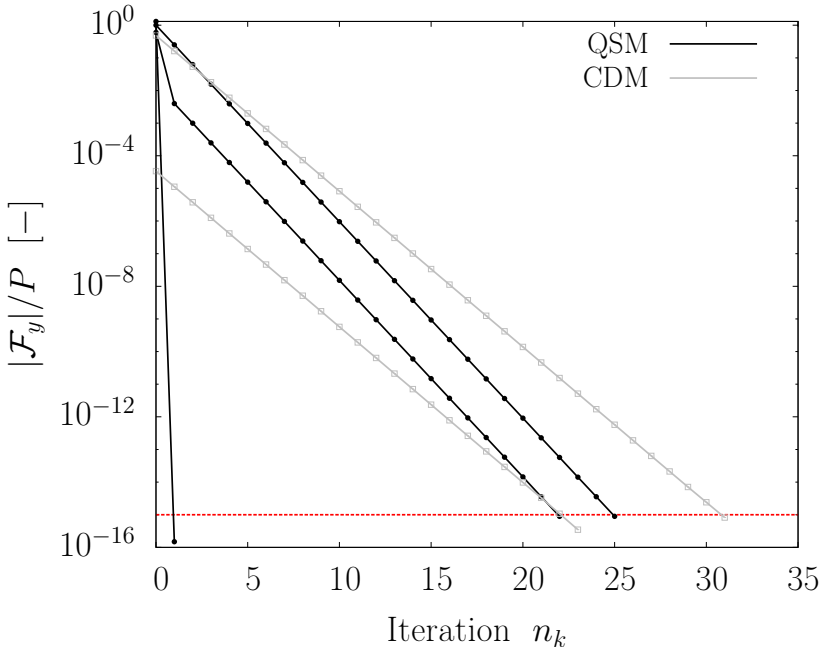


Figure 2.27 – Convergence towards admissible solutions obtained with the QSM when starting from different initial conditions. The magnitude of the vertical component of the resultant force $\mathcal{F}$ on grain no. 3, normalised by the applied load $P$, is shown. Two cases of the CDM application in Figure 2.19 are shown for comparison. The dashed red line shows the tolerance set for the stopping criterion.

This finding becomes more clear when looking at other important parameters for the characterisation of convergence. Figure 2.28a shows clearly shows the two possible responses of the QSM in terms of the number of iterations $n_k$ to reach convergence. While in some cases 1 iteration is sufficient to reach convergence, in other cases a number of iterations comparable with CDM is required. Such cases mainly correspond to initial conditions consisting in a negative resultant force (*i.e.*, directed downward). In the CDM, on the contrary, no correlation is observed between $n_k$ and the sign of the resultant force at $k = 0$. As to the cases in which QSM converges in 1 iteration, they are equally apt to occur for both negative and positive $\mathcal{F}_y^0$. Such cases can be clearly identified in Figure 2.25, in which they correspond to initial conditions within the Coulomb cone, whose projection on the SA line stays inside the cone.

Based on Figure 2.28b, no correlation can be found between the distance from equilibrium at convergence and the initial one, similarly to the CDM. However, it can be

noticed that QSM generally finds lower values than the CDM, *i.e.*, for the same threshold, QSM solutions are slightly closer to static equilibrium. This seems consistent with the nature of the method, which imposes static admissibility – while the CDM does not –; however, further conclusions cannot be taken as we do not investigate here how the methods would evolve with a more strict stopping criterion.

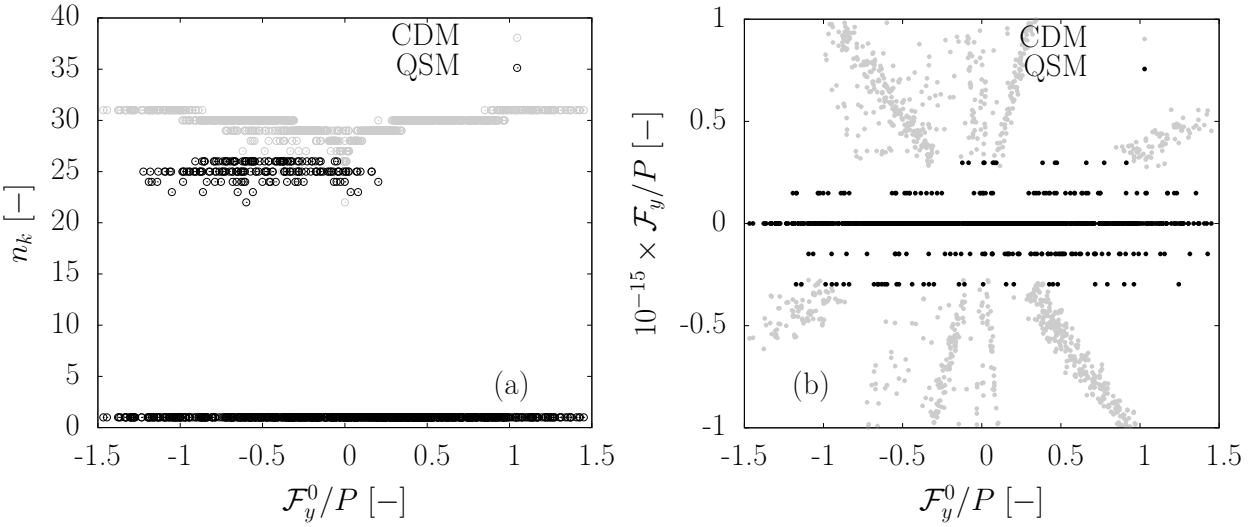


Figure 2.28 – Characterisation of the convergence for a set of 1000 solutions obtained with the QSM for different initial conditions.
(Left) Number of iterations required to reach convergence as a function of the initial distance from static equilibrium of grain no. 3.
(Right) Final distance from static equilibrium $\mathcal{F}_y/P$ as a function of the initial one $\mathcal{F}_y^0/P$.

Finally, the velocity of convergence $v_{\text{conv}}$ is defined in the same way as in Equation 2.60, and compared with the CDM application (Figure 2.29). The two possible responses are also observed here: a rather low velocity – although slightly higher than the average CDM velocity – corresponding to cases that require a certain number of iterations, and a set of much higher values when $n_k = 1$. In both cases, a clear linear correlation with the initial distance from static admissibility is observed.

### 2.2.4 Conclusions

Some final remarks can be made on the main differences between the three methods that have emerged during the description of their mathematical formulation and the application to a simple problem.

On the level of the mathematical formulation, major differences can already be highlighted, in particular with respect to the governing equations and the parameters in-

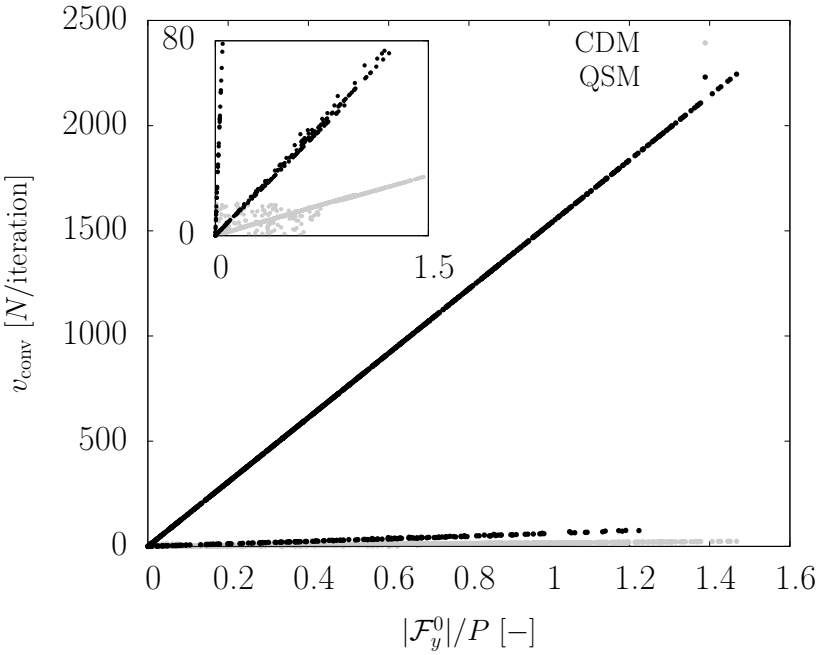


Figure 2.29 – Velocity of convergence for the same cases in Figure 2.28, expressed as the reduction of the distance from equilibrium over the number of iterations required, as a function of the initial distance from static equilibrium. The inset shows the same distribution for $v_{\text{conv}} < 80$ N/iteration.

volved: while the CEM involves several ingredients at the same time (*i.e.*, inertia, contact elasticity and friction), the CDM discards elasticity, and the QSM discards inertia.

In principle, based on their formulation, any of the proposed methods can produce sets of physically relevant solutions if suitably applied to a given load history (*e.g.*, with respect to the application presented here, by slowly increasing the imposed loading from zero to its current value). With the aim of proposing methods of force estimation that may be applicable to the most general cases, here we purposely test the three methods for rather extreme situations: the loading is not applied through small increments, and the history of the system is discarded. Forces are determined on the basis of an evolution between two conditions, in general far from each other.

Focusing on the way forces are actually estimated with the three techniques, some other differences have been shown. The CEM infers forces based on the motion between these states, although it loses some of the displacement history occurring between them. With the CDM and the QSM, forces can be determined without requiring a motion to occur; for a given state, they start from random initial conditions and attempt to reach an admissible solutions, which is not uniquely determined and depends on the starting point. These features have been directly observed by applying the three methods to a system with only one free disk (Section 2.2).

In general, it is expected that, for all the three methods, the finest possible discretisation of these evolutions can help the determination of forces: in the CEM, by enriching the information on displacement history; in the other two methods, by reducing the distance between the initial conditions – in which past history is encoded – and the admissible solutions.

Based on this idea, in the next chapter we will discuss and evaluate some strategies that can be adopted to facilitate the determination of forces; they are adapted to the method considered, but in general they all share the idea of exploiting the memory of the past history of the system.

The numerical application has also allowed, for the CDM and QSM, a study and comparison of the iterative procedures, helping to better understand the way they evolve from a given state to a state that is admissible with respect to some loading conditions. We have also shown that, for such a simple problem, the application of the QSM for a general evolution between two conditions, not discretised in small loading increments, leads to the same results as the step-wise application that is at the basis of the original formulation.

The one-disk system has been solved only for one geometrical configuration, fully described by the angle $\alpha = 45°$. In perspective, it might be of interest to investigate the range of solutions for different configurations; in particular, the range is expected to become infinite when the line of Equation 2.54 becomes parallel to (or less steep than) the lower part of the Coulomb cone. In terms of the parameters of the system, this situation is expressed by $\mu \tan \alpha \geq 1$.

# Chapter 3

# Contact force estimation from DEM simulations

In this Chapter, the three methods presented in Chapter 2 are applied to the estimation of forces in numerical, ideal packings subjected to Molecular Dynamics simulations, presented in Section 3.1. The input data extracted from these simulations has the advantage of being perfectly accurate: measurement error, that may represent a major issue in experimental applications, is completely avoided; as grains are perfectly circular, contacts are accurately detected, and grain position is known at any stage without all sort of uncertainties that are intrinsic to experimental measurements.

Moreover, an additional benefit lies in the fact that real contact forces are perfectly known – with a sufficiently high accuracy – at any stage of a DEM simulation, as long as the load is applied in quasi-static conditions; this means that these *ideal tests* can represent a benchmark for the force estimation methods, providing the solution (*i.e.*, the real values of contact forces) to the problem that we want to solve. Any estimated set of forces can be compared with the *reference* one, and, by using appropriate metrics for this comparison, the quality of the obtained solution can be assessed.

The reference set of forces may also be used to assess different possible strategies of accounting for the history of the packing, which, for the CDM and QSM, is contained in the initial conditions, *i.e.*, the initial set of forces assumed at the beginning of the respective iterative solvers. Some strategies will proposed, and their influence on force estimation assessed, in this chapter.

This approach also allows a prediction of the influence that measurement inaccuracy would have on the estimation of forces, in the perspective of the application to real experimental cases. Geometric and kinematic information from these simulations can be artificially spoiled by adding perturbations to reproduce the experimental conditions;

the extent of this perturbation can be controlled and the corresponding evolution of the accuracy of the estimated forces can be assessed. Therefore, it is possible to evaluate the sensitivity of each method with respect to possible measurement error, and its ability to provide a reliable and robust estimation of contact forces.

In conclusion, this approach allows a validation of the proposed numerical methods for force estimation, that is fundamental for identifying the relevant parameters involved in the problem before applying the methods to experimental data.

In the following sections, the simulations are presented (Section 3.1); then, some preliminary observations on the estimation of forces on a single state are made, with a focus on the two methods (CDM and QSM) that are characterised by force indeterminacy (Section 3.2). Finally, force estimation is performed on three complete MD-DEM simulations, with each of the proposed methods (Sections 3.3, 3.4 and 3.5).

## 3.1 DEM simulations as "ideal" experiments

MD-DEM simulations of biaxial vertical compression are carried out on a 2D granular assembly, the same as the one used in the tests in Chapter 4 in terms of number of particles and granulometry. The assembly consists of 1853 polydisperse disks, with four different diameter sizes: $8, 12, 14$ and $20$ mm.

As to the contact interaction, classic force laws are assumed: a linear elastic law for normal forces, and an elasto-plastic law for tangential forces, as those in Figure 2.1. An interparticle friction coefficient $\mu = 0.5$ is used; as to grain-wall contacts, it is assumed that $\mu = 0$.

After a first phase of isotropic compression until the desired confining pressure is attained, the simulations are performed by applying a constant strain rate $\dot{\varepsilon}_{yy}$, obtained by imposing a constant vertical downward velocity to the top wall, while the bottom one is kept fixed at its initial position; lateral walls are adjusted in order to ensure that the desired confining stress is kept constant. The imposed strain rate is chosen so that quasi-static loading conditions are ensured. In this regard, the typical criterion sets a limit to the inertial number, defined as the ratio between the inertial time $\tau_i = 1/\dot{\varepsilon}$ and the shear time $\tau_s = \sqrt{m/(p\, d^{D-2})}$, *i.e.*, the characteristic displacement time of a grain of mass $m$ and diameter $d$ under a pressure $p$ in $D$ dimensions. Therefore, we have $I = \dot{\varepsilon}\sqrt{m/(p\, d^{D-2})}$. The limit for quasi-static conditions is considered to be $I < 10^{-3}$ (Da Cruz et al., 2005). This limit is largely respected in laboratory experiments: for a typical triaxial test, $I \approx 10^{-7}$; for the $1\gamma 2\varepsilon$ tests described in Chapter 4, $I$ is in the same order. In the simulations, it is important to reproduce the quasi-static loading conditions

so that a whole simulation can be seen as a succession of equilibrium states, with a very low kinetic energy content. In order to reproduce such conditions, an inertial number $I = 10^{-5}$ is adopted for all the simulations, considerably lower than the limit of $10^{-3}$, although still larger than the value in typical experiments.

Together with the inertial number $I$, the stiffness level $\kappa$ is the second parameter that controls the physics of a smooth MD-DEM simulation. In the case of a linear force law, it is defined as in Roux and Chevoir (2011):

$$\kappa = \frac{k_n}{p\ d^{D-2}} \quad ; \tag{3.1}$$

with $D$ being the dimension of the system, the expression for a 2D case simply writes $\kappa = k_n/p$. The stiffness level is a dimensionless parameter that provides an estimation of the level of contact deformation attained in a certain simulation: as a matter of fact, it can be shown that $\kappa \approx d/\delta$, where $\delta$ is the average particle overlap. This deflection can be caused by increasing the pressure, or equivalently, by decreasing the contact stiffness.

For each of the three simulations described here, a different value of stiffness level is adopted, by tuning the initial confining stress, while the contact normal stiffness $k_n$ is kept unchanged. Given the definition of $\kappa$, this is perfectly equivalent to testing assemblies of particles with different compressibility but with the same stress level. In the tests described in Chapter 4, the level of stress that can be attained is fixed by the capacity of the force sensors – that allow measurements up to about 250 kPa –, hence the stress range is quite limited; therefore, tuning $\kappa$ basically corresponds to changing the compressibility of the particles. This way, it is possible to have a set of simulations that can reproduce the experimental behaviour of assemblies of particles with a different compressibility. At the same time, the numerical methods for force estimation can be assessed and validated in different experimental conditions, to show how their ability to retrieve contact forces changes with the stiffness of the particles.

As the stiffness level is changed, a set of other internal variables that describe the geometry of granular assemblies is affected consequently. In Table 3.1 some of these quantities are summarised for the initial states of the three simulations, which are relaxed in order to obtain a strictly static equilibrium. Among these variables, the degree of force indeterminacy $h$ (Equation 2.1) plays a fundamental role in the determination of contact forces when, in general, the history of the packing is discarded. This parameter has a clear inverse relation with the stiffness level $\kappa$; the choice of different $\kappa$ is indeed motivated by the possibility of exploring a range of $h$. Therefore, in the following, whenever we refer to $\kappa$, we will implicitly refer to $h$ as well. The influence of this

parameter on the estimation of forces will be studied in Section 3.5. Another important parameter, strongly related to $h$, is the coordination number, *i.e.*, the average number of contacts per particle. In the absence of gravity, $z$ is expressed as a function of the number of contacts $N_c$ and the number of particles $N_p$ by the following equation:

$$z = \frac{2N_c}{N_p} \tag{3.2}$$

Isotropically-loaded states

| $\kappa$ | $\phi$ | $z$ | $h$ | Rattlers [%] |
|---|---|---|---|---|
| 100 | 0.848 | 3.78 | 1601 | 4.2 |
| 1000 | 0.828 | 2.81 | 409 | 15.5 |
| 10000 | 0.825 | 2.56 | 196 | 19.7 |

Table 3.1 – Main characteristics of the initial states of MD simulations prepared with different stiffness level $\kappa$: packing fraction $\phi$, coordination number $z$, degree of hyperstaticity (as defined by Equation 2.1) and the ratio of *rattlers* (*i.e.*, "floating" grains not involved in any contact) to the total number of grains. There is a clear increase of the degree of hyperstaticity $h$ as the stiffness level $\kappa$ decreases.

Figure 3.1 shows the stress-strain curves for the three MD simulations, in which the stiffness level $\kappa$ is the only parameter that changes. As previously mentioned, $\kappa$ is tuned by setting a different pressure in the confining phase ($p = 5,\ 50,\ 500$ kPa, respectively), so that, with the given contact normal stiffness $k_n = 5 \times 10^7$ N/m, we have $\kappa = k_n/p = 10000,\ 1000,\ 100$, respectively.

The effect of $\kappa$ on the bulk mechanical behaviour of the assembly is mainly visible in the first part of the three curves, that is typically described as a phase in which the macroscopic deformation corresponds only to a change in the average particle interpenetration, without causing grain rearrangements. As $\kappa$ increases, we observe a reduction in the duration of this phase – the first grain rearrangements occur earlier for stiffer materials – as well as an increase in the slope of the curve.

Figure 3.2 shows the volumetric response of the assembly in the three different tests. All curves show the typical behaviour characterised by an initial phase of contractancy followed by a dilatant one. However, the duration of the contracting phase is much more significant for the low compressibility case ($\kappa = 100$); the same observation applies to the extent of the contracting deformations that are attained in the three cases. As the

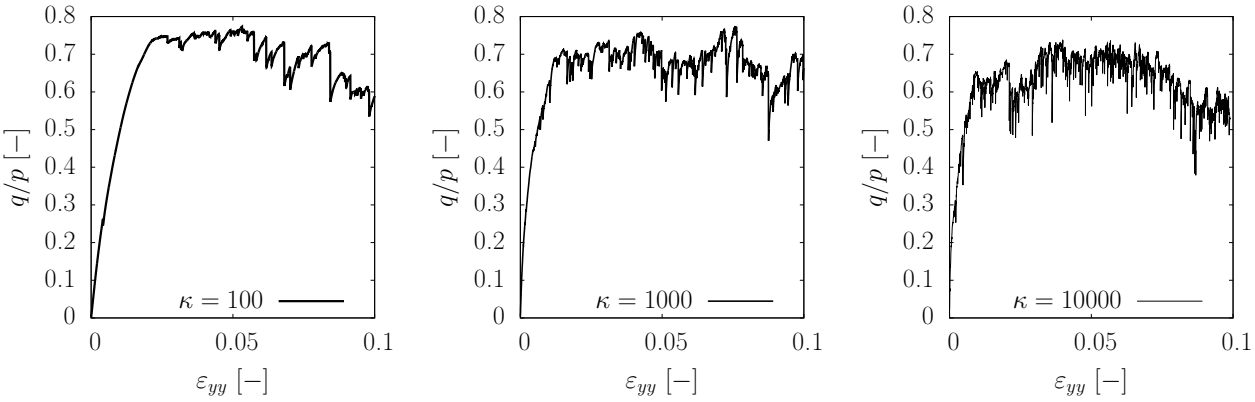


Figure 3.1 – Stress-strain curves for the three biaxial vertical MD simulations, for $\kappa = 100, 1000, 10000$ respectively, with the ratio between the deviatoric invariant $q$ and pressure $p$ on the $y$-axis.

rigid limit is approached, the contractant behaviour gets more and more limited, almost disappearing for $\kappa = 10000$.

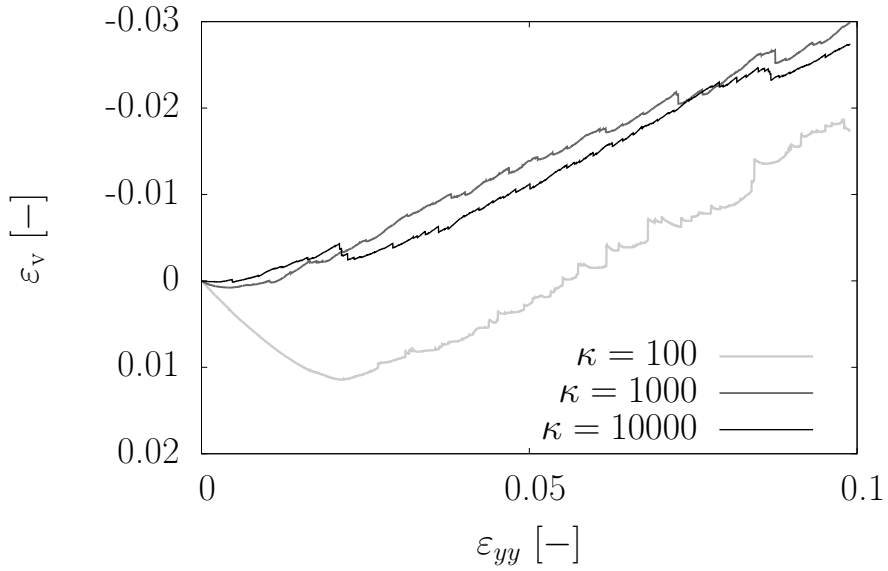


Figure 3.2 – Evolution of the volumetric deformation $\varepsilon_v$ for the three biaxial vertical MD simulations, for $\kappa = 100, 1000, 10000$ respectively.

## 3.2 Preliminary observations

In this section, some important features of the force estimation techniques are highlighted. In particular, we focus on the two methods that are characterised by force indeterminacy, *i.e.*, the CDM and QSM, and we study their behaviour in correspondence of

different initial conditions, since the history of the packing – that the two methods generally discard, causing indeterminacy of forces to appear – is basically contained in them. These observations are made here with reference to the initial, isotropically-loaded states of the three simulations just presented; however, they prove particularly important for the rest of this chapter, in which force estimation is carried out on a succession of states of biaxial simulations. In presenting these results, we also introduce the main metrics that are used in the rest of the chapter for comparing sets of forces.

In order to reproduce the typical experimental conditions, we aim to reconstruct the force network in the simulations by using the same information that one can get from the experiments, *i.e.*, boundary conditions, geometry of the packing and particle motion. Similarly to the experimental application, in which measurements are discrete-in-time as they come from pictures of the assembly that are generally shot every 5 $s$, we take this input data at distinct states of the assembly during the simulations.

An advantage of this approach is that, since the contact forces are known at any stage of the simulations, the success of the force inference methods can be tested by comparing the estimated forces with the reference forces.

Among the several ways of carrying out this comparison, two are adopted. The first one is a one-by-one comparison of contact forces. We define sets of all contact forces in a system for both the estimated solution $\left\{f^{1,\mathrm{M}}, ..., f^{N_c,\mathrm{M}}\right\}$ (M standing for the method considered) and the reference one $\left\{f^1, ..., f^{N_c}\right\}$. Typically, we treat normal and tangential forces separately. Then, we compute the correlation between two such datasets based on the expression of Pearson's correlation coefficient $r$, which writes:

$$r_M(f) = r(f, f^M) = \frac{\sum_{c=1}^{N_c}(f^{c,\mathrm{M}} - \langle f^{c,\mathrm{M}}\rangle)(f^c - \langle f^c\rangle)}{\sqrt{\sum_{c=1}^{N_c}(f^{c,\mathrm{M}} - \langle f^{c,\mathrm{M}}\rangle)^2}\sqrt{\sum_{c=1}^{N_c}(f^c - \langle f^c\rangle)^2}} \tag{3.3}$$

where $N_c$ is the sample size (number of contacts), $f^{c,\mathrm{M}}$ and $f^c$ are individual members of each sample (*i.e.*, values of single contact force components) and $\langle f^{c,\mathrm{M}}\rangle$, $\langle f^c\rangle$ are their respective mean values. $r$ lies in the range $[-1:1]$, where 1 means total positive linear correlation, 0 means no linear correlation, and $-1$ means total negative linear correlation.

Another way is to simply compute one-by-one differences of the forces between the two sets, and then describe the relation between the two sets through the definition of single parameters. For example, a *distance* between two sets of forces can be defined by computing the norm of the vectorial difference of forces at each contact, and averaging

it over the whole assembly:

$$\mathrm{dist}(\underline{\boldsymbol{f}}, \underline{\boldsymbol{f}}^{\mathrm{M}}) = \left\langle ||\vec{f}_c - \vec{f}_c^{\mathrm{M}}|| \right\rangle \tag{3.4}$$

In addition to the one-by-one comparison, that can be referred to as *local*, a second comparison (*global*) involves the definition of a homogenised stress tensor from contact forces. Different possible definitions are typically used; among these, we refer here mainly to the work by Weber (1966), whose expression of the homogenised stress is based on the sum, over all contacts $c$ included in the volume $V$, of the tensor product between the contact force $\vec{f}^c$ and the branch vector $\vec{\ell}^c$ joining the mass centres of the two particles:

$$\underline{\underline{\boldsymbol{\sigma}}} = \frac{1}{V} \sum_{c=1}^{N_c} \vec{f}^c \otimes \vec{\ell}^c \tag{3.5}$$

In presenting the results of the three methods, the homogenised stress is used for the comparison of sets of forces by computing $\underline{\underline{\boldsymbol{\sigma}}}$ for each set of forces, and comparing their components (or the stress invariants).

Before applying the three methods to the estimation of forces for a set of complete simulations of biaxial vertical compression, some preliminary remarks can be done by focusing on a single state. Similarly to what has been done for the system with only one free disk in the previous chapter, here we attempt to study the effect of memory of the past history of the packing for the two methods that generally discard it, *i.e.*, CDM and QSM. For such methods, history is encoded in the initial conditions assigned, *i.e.*, in the initial values of contact forces. In principle, both methods can reach any of the admissible solutions (for QSM, the intersection of the SA and PA subspaces; for CDM, all solutions that fulfil the Signorini-Coulomb conditions at all contacts). It is of interest to see if, by using appropriate initial conditions, we can address the solution towards the "good" one, *i.e.*, the reference (MD) set of forces.

To answer this, we test different initial solutions, generated by randomly perturbing, with increasing amplitude, the reference set of forces. In this way, history is accounted for, although with a variable amount of precision. A distance between this initial set $\underline{\boldsymbol{f}}^0$ and the reference one $\underline{\boldsymbol{f}}$ is determined, according with the definition in Equation 3.4. Then, force estimation can be performed with the two methods, and the obtained solution compared with the reference one by computing its distance in the same way.

This procedure has been implemented for a single state, isotropically-loaded, at the beginning of the three different simulations, in which $\kappa$ is varied – and the degree of force indeterminacy $h$ consequently –, to have a first idea of the influence of $h$.

In Figure 3.3, the final distance from the reference solution is plotted with the distance of the initial solution. Some general remarks, applicable to both methods, can be made. A correlation is observed between the two distances: as the initial set of forces gets closer to the "good" solution, the final set of forces does as well. This correlation is mainly observed for small initial distances; for very large ones, the final solutions tend to stabilise at a certain distance. The closer we are to the reference solution, the closer the estimated solution is to the reference solution. A clear influence of $\kappa$ is observed for both methods: for similar initial distances, the final solution is systematically closer to the solution taken as a reference for high $\kappa$. This is a clear sign of the influence of force indeterminacy, defined by $h$, on the estimation of forces for these two methods.

At the same time, the behaviour of the two methods shows some important differences. It is clearly observed that the QSM always provides a better estimation, for a given starting point. In particular, given an initial set, the QSM always gets closer to the expected solution; the CDM, on the other hand, is likely to find a solution which is further from the reference one than the starting point, although it may still be admissible (based on the CDM criteria).

In order to account for history when initialising contact forces, several strategies can be adopted; the one exposed so far is just one of the possible ways. In addition to this, we introduce some particular cases that need specific remarks. These specific cases (coloured points in Figure 3.3) include the following initial conditions:

- a vector of null forces $(f_n^0, f_t^0) = (0, 0)$
- normal forces initialised to their average value (computed from the reference force network), and null tangential forces: $(f_n^0, f_t^0) = (\langle f_n^{\mathrm{MD}} \rangle,\ 0)$
- normal forces initialised to their reference (MD) value, and null tangential forces: $(f_n^0, f_t^0) = (f_n^{\mathrm{MD}}, 0)$
- normal forces initialised to their reference (MD) value and forced not to change during the iterations of the two methods, and null tangential forces: $f_n = f_n^0 = f_n^{\mathrm{MD}}$, $f_t^0 = 0$

The first two strategies bring no significant improvement for both methods. In the CDM, at least for the two cases of $\kappa = 1000$ and $\kappa = 10000$, the obtained forces are as far from the reference one as those obtained for a similar initial distance. A slight improvement is only observed for $\kappa = 100$. In the QSM, on the other hand, these strategies seem to have an opposite effect on the determination of forces, which match

even less with the reference solution than those randomly-generated initial conditions with similar initial distances from the reference one.

Using the normal forces of the reference solution to provide a starting point $f_n^0$ has different effects in the two methods. The QSM, by this operation, can get very close to the expected solution, for all $\kappa$; the CDM, on the other hand, shows no improvement.

Finally, a particular application is carried out by modifying the iterative procedures: at the beginning, normal forces are assigned their reference values; then, at each iteration, they are forced not to be corrected. In such a case, the reference solution is perfectly retrieved, as it can be seen through the evaluation of tangential forces, which start from 0 and, at the end, reach their expected values. This is an important finding: it confirms that, for a granular system at equilibrium, the solution in tangential forces is unique if normal forces are known.

An additional case is considered, although not shown in the figure. It consists in starting both methods from the exact reference solution, for both normal and tangential forces; it is observed that, as expected, the reference solution is basically retrieved at the end of the iterative procedures, although little differences can be seen in the convergence of the two methods, related to their different formulation.

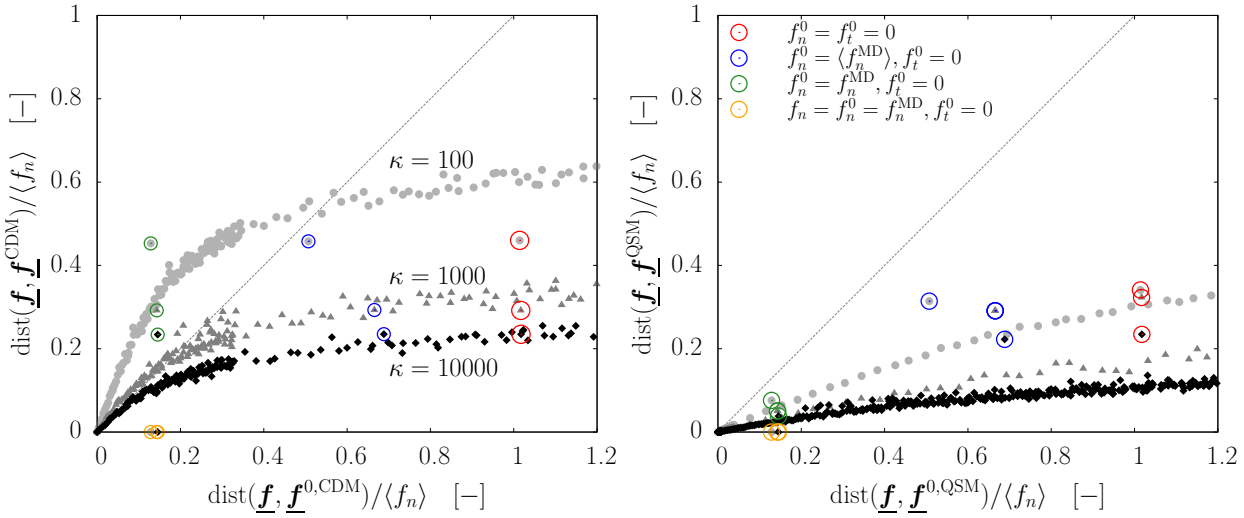


Figure 3.3 – Distance of CDM- (left) and QSM-estimated forces (right) from a reference one, plotted with the distance of randomly-assigned initial conditions they start from. One isotropically-loaded state for each of three different simulations ($\kappa = 100, 1000, 10000$) has been used. The distance is defined as in Equation 3.4. Coloured points correspond to cases with particular initial conditions.

From the analysis of these results, some conclusions can be deduced. The QSM has proven more prone to approach the reference solution by exploiting information on the history of the packing than the CDM, especially for high degrees of force indeterminacy

(low stiffness levels). On the contrary, when we impose these values throughout the whole iterative procedure, both methods end up with a solution which corresponds exactly to the reference one. In general, from a comparison of the two methods it can be deduced that the QSM is more suitable for working on equilibrium states, as expected.

A possible approach for a future improvement of these methods involves the use of the concept of stability of an equilibrium state. With the CDM, we have no direct access to measures of the stability of the system; we can only look at the distance from equilibrium, which can give some information although not being totally equivalent. A better way to express stability is based on the definition of a second-order work; this can be expressed, with the QSM notation, as $\Delta^2 W(\Delta \underline{\boldsymbol{U}}) = \Delta \underline{\boldsymbol{U}} \cdot \underline{\underline{\boldsymbol{K}}} \cdot \Delta \underline{\boldsymbol{U}}$ (Roux and Combe, 2011). An equilibrium state is said to be stable when $\Delta^2 W(\Delta \underline{\boldsymbol{U}})$ is positive (according to the QSM sign convention). By applying some displacements $\Delta \underline{\boldsymbol{U}}$, we can find a direction that improves stability. We expect that the solution following this path is closer to the reference one. The treatment of instabilities might in particular prove useful for those cases that are not perfectly at equilibrium. For such cases, the CDM is more suitable, since it can determine particle accelerations. The QSM, for its intrinsic nature, only deals with states at equilibrium, but it can provide important information on the nature of instabilities through the second-order work.

So far, the comparison of sets of forces has always been carried out in terms of the distance in Equation 3.4, due to the impossibility of defining a Pearson correlation coefficient for sets of forces with the same value at all contacts. However, it has been observed that this distance is anti-correlated with Pearson's $r$, which is why the two metrics can be used equivalently, and in the following we will always refer to Pearson's $r$.

In order to complement the definition of Pearson's $r$, in Figure 3.4 we show four examples of CDM-obtained force networks, for a generic state, with four different correlations with the reference solution. As $r$ decreases, the change in normal forces appears clearly, although it should also be remarked that the low-correlated networks still share some common aspects with the reference one. In particular, the strong network seems to be fairly retrieved even for $r \approx 0.5$.

## 3.3 Contact Elasticity Method

The estimation of forces by means of the Contact Elasticity Method (CEM) is presented in this section.

To mimic the experimental conditions, in which measurements are based on the determination of particle displacements and rotation between photographs of the specimen

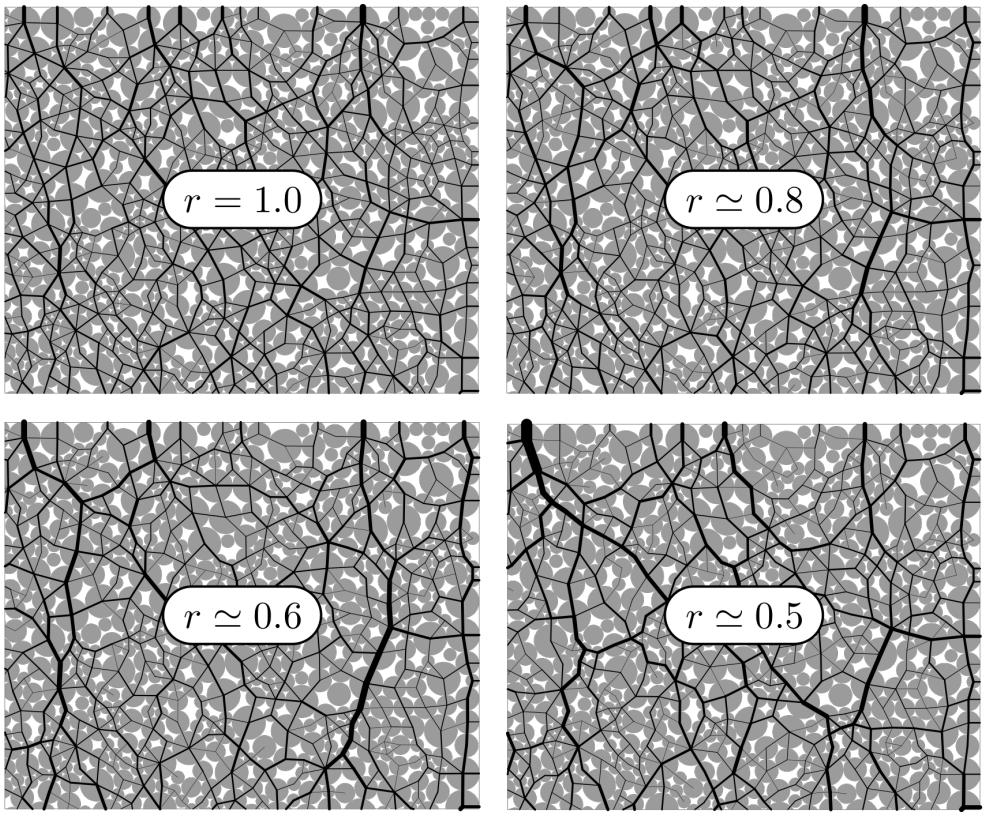


Figure 3.4 – Maps of normal forces for different solutions obtained with the CDM for a single state of one MD simulation ($\kappa = 100$). Each solution corresponds to a different correlation with the reference (MD) solution. Correlation is expressed as Pearson's $r$ of normal forces, $r = 1$ corresponding to total linear correlation.

that are taken at distinct times, in this application to numerical data we make use of geometrical configurations (particle position and orientation) that are extracted from the MD simulations with a constant frequency and, consequently, a corresponding constant strain window between two configurations $\Delta\varepsilon_{yy}^{\min} = 2 \times 10^{-5}$.

Particle displacements and rotation are obtained from the evolution of position and orientation between two of these configurations. Then, normal and tangential forces can be directly determined through the assumption of the typical MD-DEM force laws.

Force estimation is performed with the main goal of validating the method, with a view to its application to the experimental case. Hence, some aspects that can affect the estimation are reproduced and taken into account here.

Concerning the inference of normal forces, in the application to the reference simulations they can be directly retrieved from the simple measurement of particle overlaps, knowing that a linear elastic force law is assumed. Contact normal stiffness $k_n$, if not known, can be still estimated as a function of the mean particle overlap and the applied pressure, knowing that, in 2D, the order of magnitude of the mean normal forces is given by $\langle f_n \rangle \simeq k_n \langle \delta_n \rangle \simeq P \langle d \rangle$ (Combe and Roux, 2011). A more accurate estimate of $k_n$ can be derived from a re-scaling procedure based, for instance, on a scalar quantity issued from the calculation of a homogenised stress (*e.g.*, stress invariants, or stress projected on a plane), as described in Section 2.1.1.

Under these assumptions, normal forces are perfectly retrieved, and the problem is restricted to the determination of tangential forces. The latter is more challenging and some issues have to be taken into account. In particular, due to the assumption of an incremental elasto-plastic force law, tangential forces are a function of the amount of force that is already transmitted through the packing, and that cannot be determined with this method. It can be assumed that this has no relevant effect as long as the initial state is close to unloaded conditions; in this case, contact forces (both normal and tangential) are negligible, so it is expected that forces determined as the accumulation of force increments, based on the force laws in Figure 2.1, almost equal the actual forces.

However, an unloaded configuration is not representative of a real situation in which at least gravity is acting on particles. In addition, typical soil mechanics experiments are carried out with an initial phase of consolidation through the application of an isotropic compression. In such cases, the tangential forces already transmitted between particles cannot be determined with the method in question.

The error of estimated forces does not only depend on the amount of force already present in the system; it evolves with the restructuring of the force network, because as contacts open and new ones are created, the effect of the previous history is gradually

lost. This aspect is investigated by estimating tangential forces in two different situations. In the first case, initial forces are taken into account and force increments are added to these forces. In the second case, such initial forces are neglected and current forces are determined only as a sum of the measured force increments.

Since force increments are computed from measured displacements, another aspect to be considered is the frequency of data acquisition. Even if we consider "ideal" experiments here, it is recalled that the CEM is planned to be applied on data issued from quantitative image processing. With the given force law for tangential forces, a dependence is introduced on the history of particle motion. This means that the displacements and rotation of two particles in contact between two configurations are not sufficient for a correct determination of the force increment: for example, if a contact enters the *sliding* condition by violating Coulomb's friction law, the displacement that is accumulated after this point does not entail any increment of tangential force. As a consequence, the correctness of the estimated force is expected to depend on the amount of contact relative displacement occurring between two configurations.

This effect can be studied by modifying the width of the strain window between two consecutive states: in this way, the amount of displacement history that is lost can be reduced to a minimum (in the case of the smallest strain window) for a better approximation of force increments, or enlarged, with an expected decrease in the quality of force estimation. In this case, the smallest strain window corresponds to $\Delta\varepsilon_{yy,min} = 2 \times 10^{-5}$, as previously mentioned; then, displacements (and, consequently, force increments) are measured between configurations separated by a larger strain window (10, 50, 100 or 500 $\times \Delta\varepsilon_{yy}^{\min}$). This is equivalent to changing the frequency of data acquisition from experiments, *e.g.*, by changing the velocity of loading application or the frequency in shooting photographs. In experiments, similar strain windows between consecutive measurements can be obtained with photographs on 2D experiments, as those that are performed in this work (Chapter 4); on the other hand, 3D imaging techniques such as X-ray tomography are typically characterised by larger strain windows.

With a view to the application to experimental measurements, the determination of normal forces becomes more challenging, since the mechanisms of contact deformation cannot easily be reduced to the simple model of rigid bodies with a contact compliance, as in typical MD-DEM use. As we will see in Chapter 4, based on the measurable quantities, normal forces can be assessed from experiments only as force increments, on the basis of a normal relative displacement, with a force law similar to the one for tangential forces (but without plasticity). Therefore, we will also try to estimate normal forces in this way from numerical data, and see if this assumption has an influence on

the determination of normal forces.

In the following sections, these aspects are examined separately. First, tangential forces are estimated and the possible sources of error examined in Section 3.3.1, assuming that normal forces are perfectly known. In the second place, we will focus on normal forces in the case that no particle overlap can be measured, so that such forces need an estimation procedure (Section 3.3.2).

### 3.3.1 Estimation of tangential forces

The estimation of tangential forces is carried out under the assumption that normal forces are known, *i.e.*, they can be perfectly retrieved simply from the measurement of particle overlaps. Although this choice does not completely resembles the condition when dealing with experimental measurements, separating the assessment of the obtained forces – between normal and tangential – can prove useful for several reasons.

In the first place, the assumption of Coulomb's friction law introduces a dependence of tangential forces on normal ones, by implementing the condition $|f_t| \leq \mu f_n$. Therefore, the choice of using the correct values of normal forces is made in order not to introduce any additional error on Coulomb's law, that would affect the estimation of tangential forces. In this way, it is possible to draw attention to the error coming only from the estimation of $f_t$, and identify the main sources of such an error.

Moreover, the determination of normal forces has been typically considered to be less challenging than that of tangential forces: other methods, already summarised in Chapter 1 (*e.g.*, Saadatfar et al. (2012)), have shown the ability of assessing normal forces from the measurement of a contact deformation, provided that an appropriate measurement resolution and particle deformability are given.

The estimation of tangential forces from experiments, on the other hand, has always represented a major challenge. It is then fair to assume normal forces to be known, with a certain approximation, and work mainly on tangential ones.

The influence of the frequency of data acquisition is studied by changing the width of the strain window between two consecutive geometric configurations, from which particle displacements and rotation are computed. In Figure 3.5, the evolution of Pearson's $r$ between estimated and actual tangential forces is shown, for different sizes of the strain window, in two different cases: respectively, when initial tangential forces are taken into account, and when they are not. In both cases, it is clear how the increase in the amount of displacement history that is lost between two states has the effect of reducing the correlation of forces – and thus the quality of the force estimation –, partic-

ularly in the phase in which most granular rearrangements occur, and the macroscopic behaviour becomes strongly irreversible.

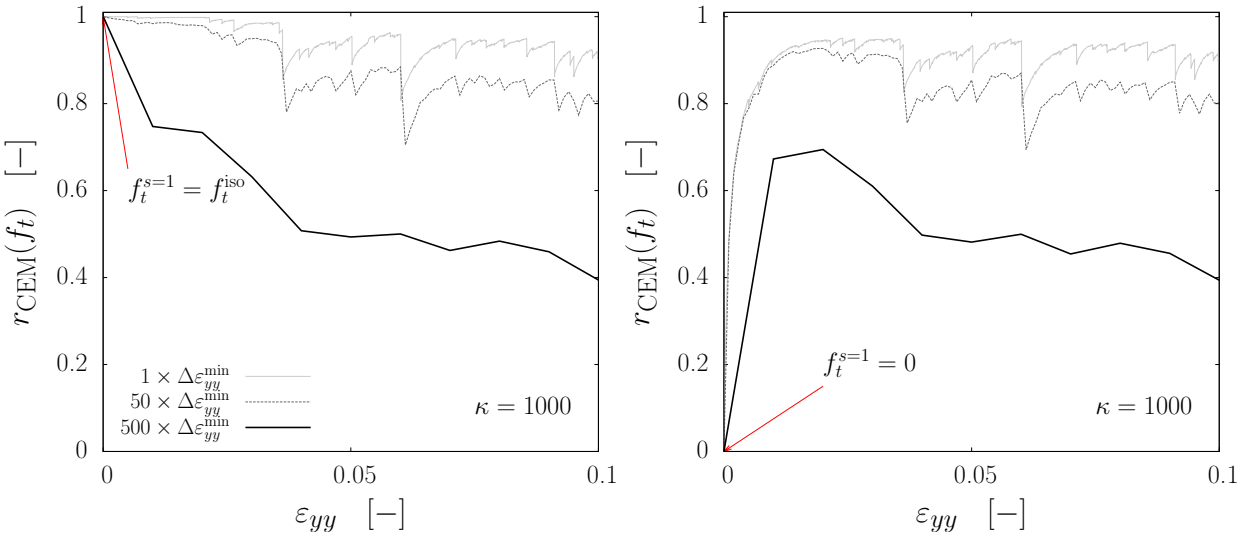


Figure 3.5 – Evolution of Pearson's $r$ of tangential forces, estimated with the CEM on numerical data (MD simulation with $\kappa = 1000$) for different frequencies of data acquisition, when previously accumulated tangential forces are taken into account (left) and when they are neglected (right). Normal forces are assumed to be perfectly retrieved.

In the second place, we focus here also on the influence of starting from a loaded configuration, for which forces that are already present in the system cannot be inferred with this approach. In Figure 3.6, we show the difference between the two light gray curves in Figure 3.5, corresponding to the estimation of forces with the same strain window (the smallest one), but respectively accounting for previously accumulated tangential forces, and neglecting them. It is observed that the difference between the two curves has a fast decrease in a first phase, but then it vanishes only after a large applied displacement ($\approx$ 10% of applied vertical deformation, corresponding to a displacement $\Delta H$ in the order of 4 times the mass median diameter $D_{50}$).

By treating tangential forces separately from normal ones, it is also possible to show the effect of a wrong estimation of $f_t$ on macroscopic quantities such as the homogenised stress. In particular, it is observed (Figure 3.7) that the estimation of tangential forces does not have a substantial effect on the global homogenised stress, for which a good estimation of normal forces is typically sufficient to reproduce the applied stress.

At the same time, the computation of a homogenised stress allows additional observations about the influence of the strain window. As $\Delta\varepsilon_{yy}$ increases, the evolution of the vertical normal stress $\sigma_{yy}$ still follows the overall evolution of the applied stress (gray curve in Figure 3.7); however, the typical drops due to stress relaxations occurring in cor-

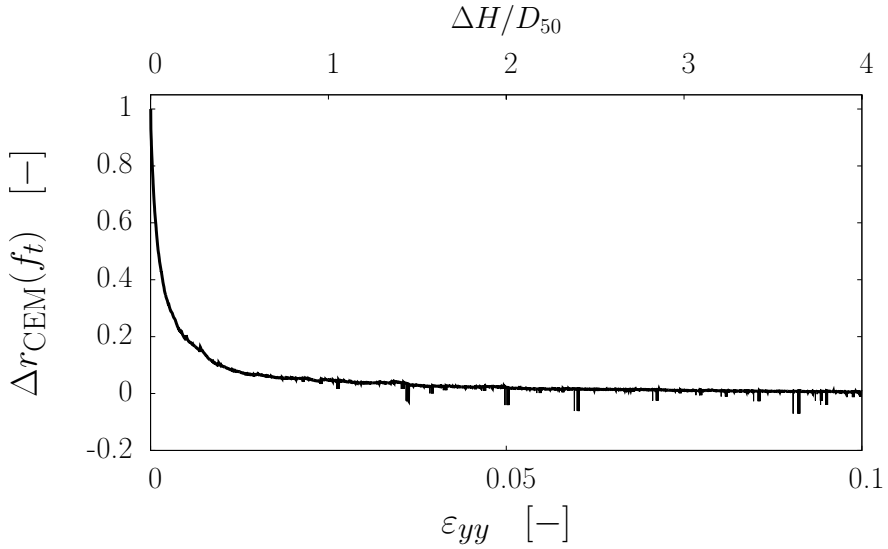


Figure 3.6 – Evolution of the difference, for Pearson's $r$ of tangential forces estimated with the CEM on numerical data (MD simulation with $\kappa = 100$), between the two cases in Figure 3.5: respectively, accounting for previously accumulated tangential forces, and neglecting them. The $x$-axis is also expressed in terms of applied vertical displacement, normalised by the mass median diameter $D_{50}$.

respondence of major granular rearrangements are not caught when the strain window is too large. It seems that the homogenised stress obtained with a large strain window is a running average of the one obtained with the smallest strain window.

### 3.3.2 Estimation of normal forces

So far, normal forces have been determined by simply measuring particle overlaps, based on the MD model of contact deformation that assumes rigid particles with compliant contacts. In the perspective of applying the CEM to force estimation in experiments, the applicability of such a simple model is questionable.

In order to apply this model on the typical experimental measurements that can be performed in granular materials, some appropriate contact-scale geometric (kinematic) quantities should be introduced, to describe contact deformation and reproduce the role of particle overlap in MD. Then, forces may be determined assuming MD-DEM force laws (linear elastic, or the Hertz-Mindlin model, as in Saadatfar et al. (2012)).

However, this approach requires an extreme accuracy in the determination of contact-scale mechanisms, which cannot always be guaranteed considering the given measurement resolution ($\Delta\varepsilon_{yy}$) and the sources of measurement inaccuracies. Therefore, when dealing with experimental data, the most reliable quantities seem to be particle dis-

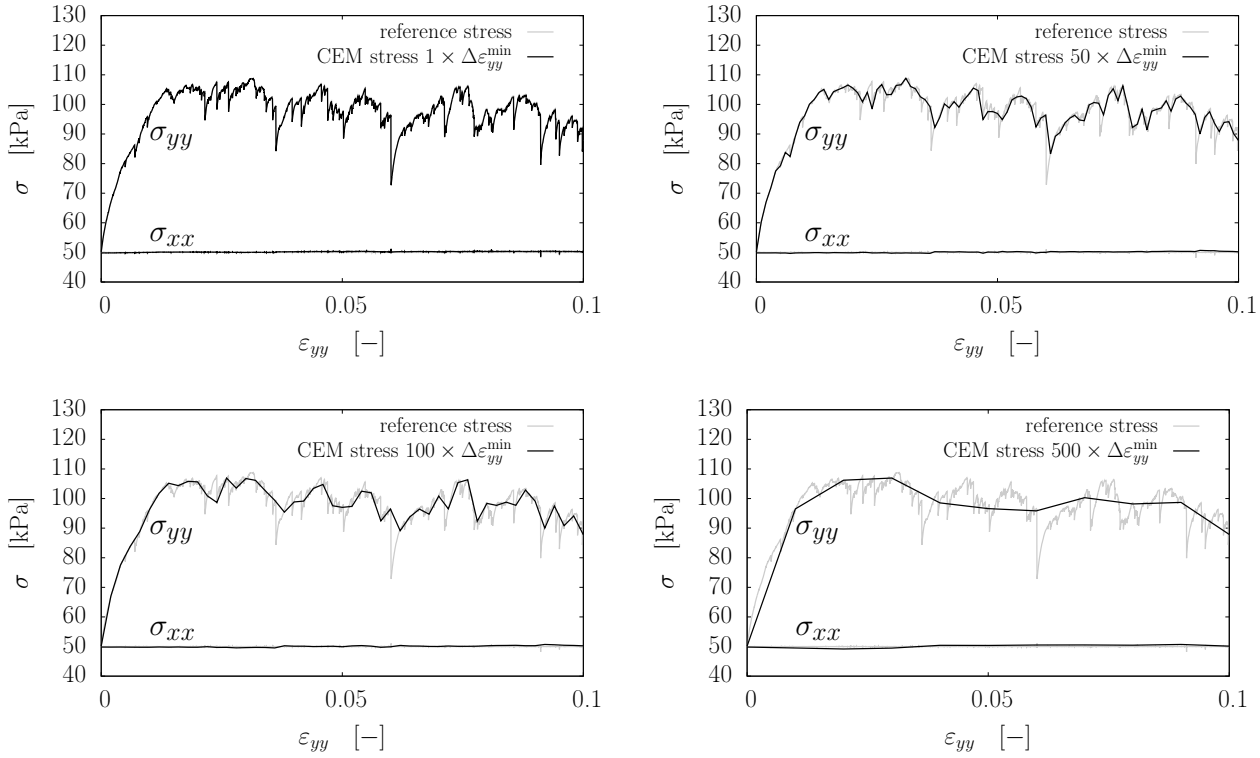


Figure 3.7 – Comparison between the homogenised stresses computed, respectively, from original contact forces and from CEM-estimated forces, with four different frequencies of data acquisition, for an MD simulation with $\kappa = 1000$. Only tangential forces are actually estimated, while normal forces are assumed to be known.

placements, which are raw outputs of DIC measurements. Normal forces can then be determined from force increments that are function of normal relative displacements. In order to check the effect of this assumption on the estimation of forces, we assess normal forces from simulations similarly to what has been done with tangential forces in the previous section.

In particular, we investigate here the effects, on the estimation of normal forces, of two main issues that are expected to characterise the application to experimental data: the loss of previous displacement history and the reduction of the frequency of data acquisition.

Figure 3.8 shows the effect of starting the estimation of normal forces from an already loaded configuration, for which no information is given about the existing forces acting between grains. A comparison is shown between the two different cases – normal forces initialised to zero, or to their current value – in terms of Pearson's correlation coefficient $r$ between the estimated normal forces and the actual ones. The difference between the two curves is shown to be decreasing as the deformation goes on, *i.e.*, as the restructuring of the force network makes the previously accumulated forces less and less relevant for the determination of the actual value.

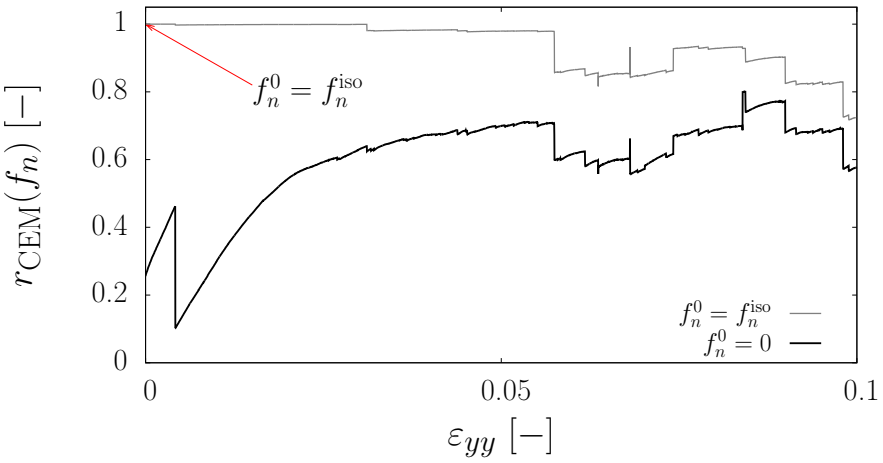


Figure 3.8 – Evolution of Pearson's $r$ of normal forces, as estimated with the CEM on numerical data (MD simulation with $\kappa = 100$), in two cases: when previously accumulated forces are taken into account (gray curve) and when they are not (black curve).

However, the same plot also shows a second, main point. Even when initial forces are taken into account, the correlation of normal forces does not remain perfect ($r = 1$) for the whole duration of the simulation. It only does in the first phase, in which no major rearrangement is typically occurring. Then, some drops are observed in the correlation curve, in correspondence with the main rearrangement events, and $r$ goes down to $\approx$

0.75.

This error comes from the assumption that, between two consecutive states $s$ and $s-1$, overlap increments $\Delta\delta_n = \delta_n^s - \delta_n^{s-1}$ can be approximated by normal relative displacements between the states $s$ and $s-1$, determined as $\Delta u_n = (\vec{u}_j - \vec{u}_i) \cdot \vec{n}^s$ (Figure 3.9). This is true when, in the hypothesis of small displacements, the local reference of a contact (normal and tangent unit vector) stays practically unchanged between consecutive states. However, when rearrangements occur, this assumption is no longer verified: touching grains can undergo considerable displacements and rotations, though still being in contact, as in the sketch of Figure 3.9. In such cases, the normal at the contact point can dramatically change its orientation. Therefore, the projection of contact relative displacements along the normal at the current state $s$ cannot reproduce the increment of overlap.

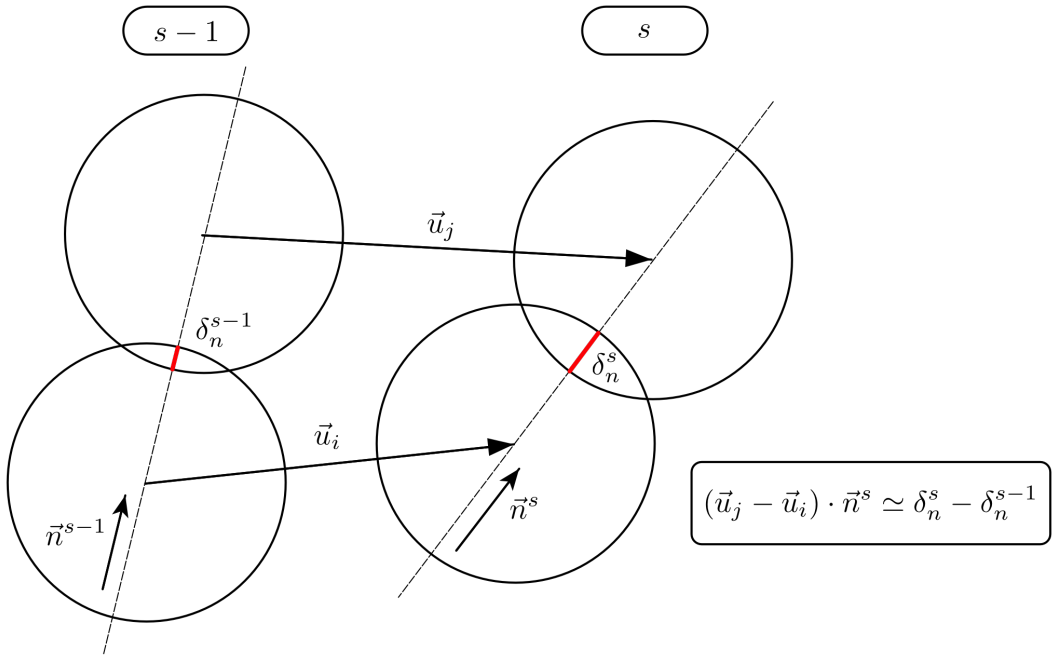


Figure 3.9 – Sketch of the evolution of a contact between two states $s-1$ and $s$, with indication of particle overlap and contact normal vector in both states.

This issue, and its resulting error, are analysed in Figure 3.10, that shows two different situations. In one case (red dots), the contact network does not change much between two consecutive states; normal vectors at contacts stay practically unchanged (the rotation of the normal vector $\Delta\alpha_n$ stays below $0.1°$) and, consequently, normal relative displacements match very well with overlap increments. As a result, very low errors ($< 1\%$) are obtained in the estimation of normal force increments, defined as the absolute difference between the value estimated with the CEM and the reference value

in the MD simulation, normalised by the latter to have a dimensionless definition. On the other hand, when major rearrangements occur and the change in the normal vector orientation can reach up to $\approx 100^\circ$ (black dots in Figure 3.10), normal relative displacements and overlap increments do not always match perfectly, and, especially for high rotations of the contact normal $\Delta\alpha_n$, $\Delta u_n$ can underestimate or overestimate $\Delta\delta_n$, even up to $10^2 \div 10^3$ times. As a consequence, the estimation of normal force increments globally returns a much higher error, that grows almost linearly with the change in orientation and can reach up to $\approx 100$ times the value of the correct force increment. This shows, once more, the importance of maximising the time resolution of measurements for the application of the CEM. If one can reduce the amount of global displacement occurring between two consecutive states, the local reference would not rotate much and, in such a case, normal relative displacements match very well the increments of overlap.

It is important to recall that, in case of intense rearrangement, all possible changes of the contact network have to be taken into account in the estimation of normal force increments. In addition to changes in the orientation of the normal unit vector for persisting contacts, two additional situations typically occur, *i.e.*, contact opening and closing. The first case does not add any complexity, since normal forces go to zero as the contact is lost. As to closing contacts, the determination of a normal relative displacement should account only for the motion occurred after the starting time of the contact, that can happen at any time between the considered states; for simplicity, one can simply neglect the first force increment and assume the two grains get into contact exactly at the time of the current state. The error coming from this assumption is found to be negligible.

The effect of the frequency of data acquisition is studied by estimating normal forces, with the previously accumulated forces taken into account, for three different amplitudes of the strain window between two consecutive configurations of the packing: the smallest strain window $\Delta\varepsilon_{yy}^{\min}$ is respectively taken as it is, and then multiplied by 10 and 50 (Figure 3.11). The influence on the estimation of normal forces seems not so relevant, if compared with the previously investigated effects.

## 3.4 Quasi-Static Method

As it has been presented in Section 2.1.3, the application of the QSM only requires the knowledge of the contact network and of the boundary conditions (applied external load). The contact network can be fully determined by knowing, for each disk of the assembly, its position ($x$- and $y$- coordinates of the centre) and radius. As to the boundaries, due to the applied conditions in the MD simulation, their motion is described by

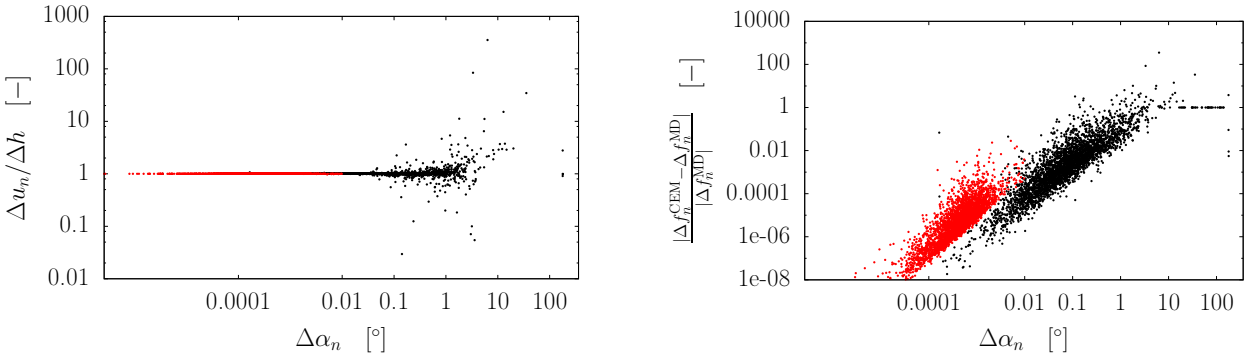


Figure 3.10 – (Left) Ratio of normal relative displacement $\Delta u_n$ with increment of overlap $\Delta\delta_n$, plotted with the unsigned change in orientation of the normal unit vector $\Delta\alpha_n$ for all persisting contacts, between two consecutive states of the MD simulation with $\kappa = 100$: (red) an evolution with no major rearrangement; (black) an evolution with intense grain rearrangement.
(Right) Corresponding error in the determination of normal force increments, defined as the absolute difference between the estimated normal force increment $\Delta f_n^{\mathrm{CEM}}$ and the real one $\Delta f_n^{\mathrm{MD}}$, normalised by $\Delta f_n^{\mathrm{MD}}$.

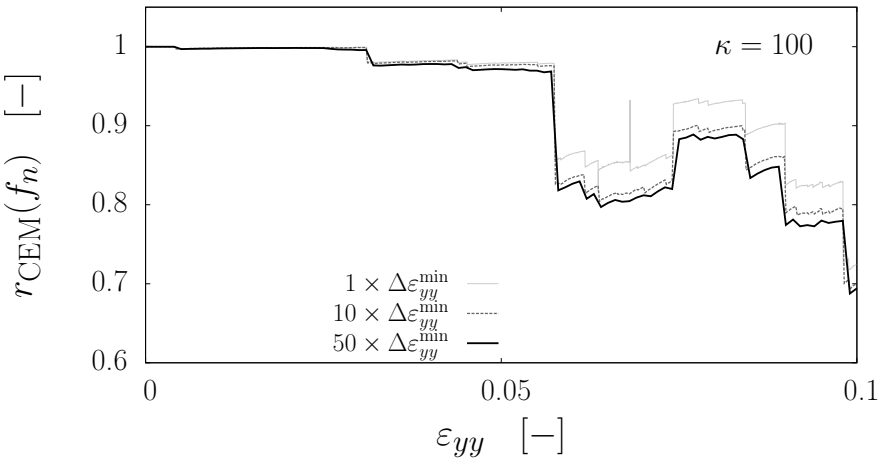


Figure 3.11 – Evolution of Pearson's $r$ of normal forces for different frequencies of data acquisition, as estimated with the CEM on numerical data (MD simulation with $\kappa = 100$).

only 2 degrees of freedom (the vertical displacement of the top wall – while the bottom one is fixed –, and the horizontal displacement of the lateral walls, equal and opposite to each other). The contributions of the boundaries to the vector $\underline{\boldsymbol{F}}^{\text{ext}}$ is composed of the two forces in correspondence of these DOFs.

Knowing the whole geometry of the assembly, not only contacts can be detected (and their location – assuming they are punctual – identified), but also a particle overlap can be determined, and used for a first approximation of normal forces, through the assumption of a simple linear elastic force law. Contact normal stiffness is not a given material parameter in this law: it is indirectly retrieved by imposing that the sum of normal forces at the grain-wall contacts be equal to the applied external load, similarly as it is done in the CEM.

Therefore, while the initial guess solution (*i.e.*, the set of contact forces to which the iterative procedure is initialised) consists of null values for tangential forces, for normal forces an approximation of the final solution is already used. Then, a solution is sought through the iterative double projection procedure that was exposed in Section 2.1.3.

The comparison between the reference MD-DEM contact forces and those estimated via the QSM is carried out by means of the Pearson correlation coefficient $r$. In Figure 3.12, it is shown that, for two simulations with different initial stiffness level ($\kappa = 100$ and 10000 respectively), the targeted solution is very well approached, being $r$ very close to 1 (*i.e.*, perfect linear correlation) in both cases, and both for normal as well as tangential forces.

The difference between the two simulations, despite relevant changes in the main geometrical properties of the assembly (coordination number, packing fraction and, in particular, degree of force indeterminacy), is rather limited, though a slightly lower correlation (especially for tangential forces) is observed for the simulation with a higher degree of force indeterminacy ($\kappa = 100$).

It is expected that this response is somehow affected by the fact of using the elastic estimation of forces as an initial guess, based on the findings of Section 3.2. To verify this, the method is also applied without making any assumption on the contact behaviour. In such a case, contact compliance is neglected and no approximation can be made on normal forces; therefore, any set of forces could be used as an initial guess for the iterative solver. If the starting point is chosen such that only null forces are used, the iterative procedure does not converge to a solution; however, it is sufficient to use sufficiently small (*e.g.*, $10^6$ smaller than the expected average normal force) values for all normal forces to retrieve a successful convergence.

Differently from the case in which contact elasticity is exploited, the obtained set of

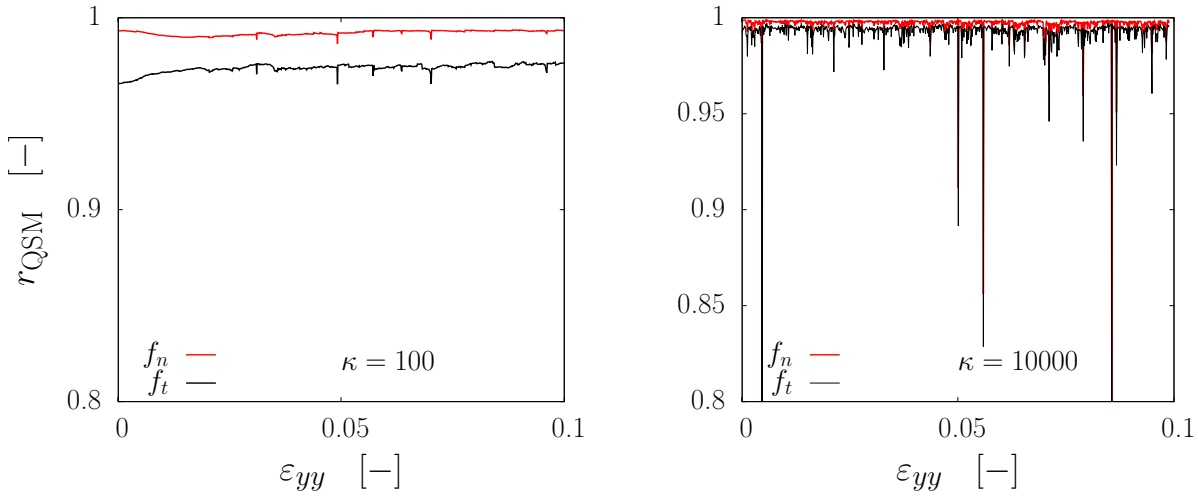


Figure 3.12 – Evolution of the correlation of normal and tangential forces, estimated via the QSM, for two different MD simulations ($\kappa = 100$ and 10000). Here, initial normal forces are estimated based on the measurement of a particle overlap.

forces depends now on the degree of force indeterminacy of the system, as it is clearly observed in Figure 3.13, in which force estimation is compared for the three MD simulations ($\kappa = 100, 1000$ and 10000 respectively). The effect is particularly obvious for the case with the highest degree of force indeterminacy, corresponding to the lowest $\kappa$, for which the correlation of forces goes from $r \approx 0.99$ down to $r \approx 0.7 \div 0.8$ for normal forces, and from $r \approx 0.97$ down to $r \approx 0.6 \div 0.7$ for tangential ones. The influence of force indeterminacy will be further investigated in the context of the application of the CDM, in which an attempt will be made for the characterisation of the variability of forces, that could help explain the observed differences in the estimation of forces.

Still dealing with different initial conditions, another way of accounting for the history of the assembly is to use the solution obtained at a state $s - 1$ as an initial guess for the state $s$. If the solution obtained in the previous state is close to the reference one, this operation is expected to help the QSM approach the "good" solution also at the current state, assuming the force network does not change dramatically between two consecutive states. We test this procedure for different cases, shown in Figure 3.14. First, both normal and tangential forces are initialised to their values at the previous state, and for the first state ($s = 1$) a solution is obtained by starting from null forces. This strategy may be applicable also to experimental cases in which no other estimation of forces is provided. In this case, since the solution is quite far from the desired one ($r(f_n) \approx 0.7$, $r(f_t \approx 0.55)$), the fact of re-using it for the next state does not help convergence towards the desired solution; the obtained curves of $r(f_n)$ and $r(f_t)$ are similar to those when null forces are used for all the states. An attempt is also made to use only tangential

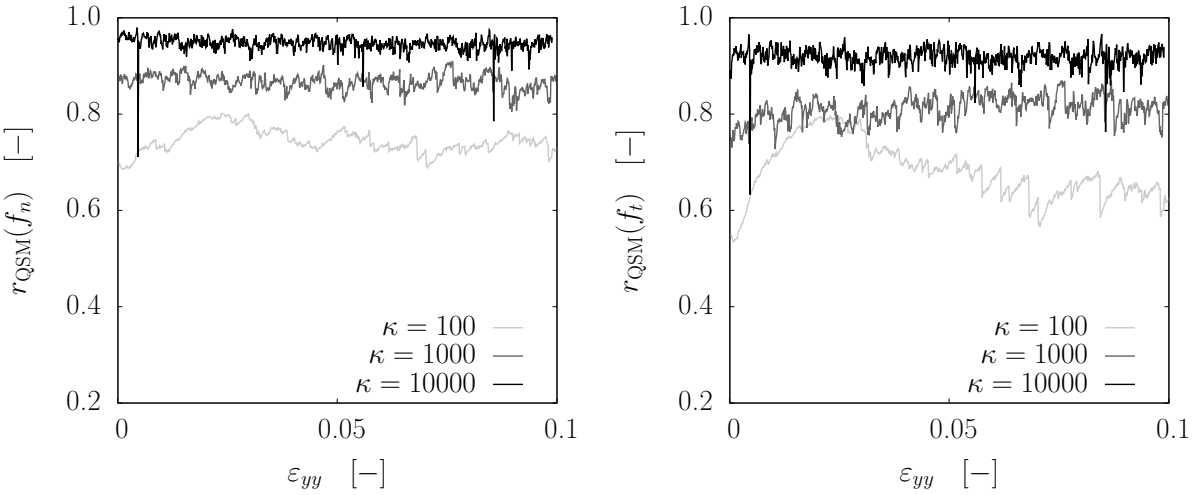


Figure 3.13 – Evolution of Pearson's $r$ for normal (left) and tangential (right) contact forces in the three MD simulations (for $\kappa = 100, 1000, 10000$ respectively), between the solution estimated via the QSM and the real one. Here, both normal and tangential forces start from null values.

forces from the previous state, while normal forces can be assessed, for example, based on a measured particle overlap. This is equivalent to another situation that may occur in experiments, when normal forces can be estimated (*e.g.*, by means of the CEM, or any equivalent method). It has already been shown that in this application to simulations, by simply providing a good estimation of normal forces, tangential forces are also retrieved very well with the QSM, although not perfectly ($r \approx 1$). If, in addition, the information on previous tangential forces – always available when working on successive states – is added, a further improvement is observed for both normal and tangential forces. In general, it can be deduced that providing an estimate of normal forces (*e.g.*, obtained with the CEM) represents a better help than using the forces from the previous state, which can be far from the desired one especially for highly hyperstatic systems.

### 3.4.1 Convergence of the iterative procedure

Some considerations should be made on the evolution of the iterative procedure towards a solution. Through this loop, the method seeks to fulfil two criteria: the static admissibility and plastic admissibility of the obtained forces. Even though the MD-DEM simulations for which we try to reconstruct the force network are carried out in quasi-static loading conditions, with a very low inertial number ($I = 10^{-5}$), dynamic events characterised by a high kinetic energy content and relevant rearrangements of the contact network still occur. When extracting geometrical configurations of an assembly at

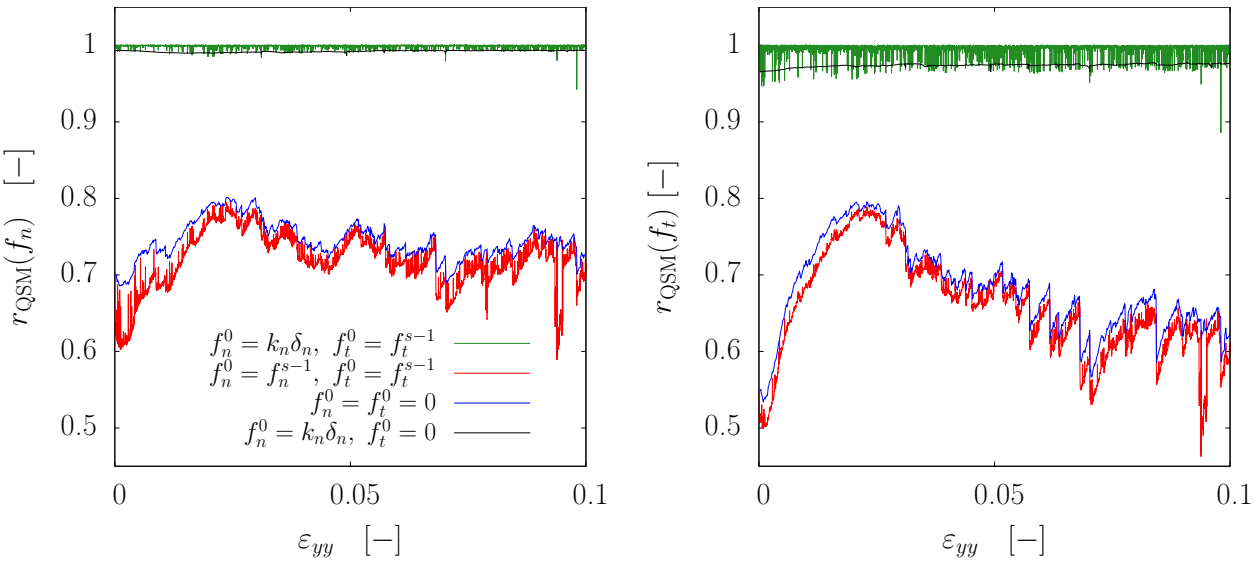


Figure 3.14 – Evolution of Pearson's $r$ for normal and tangential forces, between the original ones and those estimated via the QSM for an MD simulation with $\kappa = 100$, for different initial conditions.

distinct instants of these simulations, some configurations might correspond to such dynamic events. In these cases, a statically admissible solution does not exist; the iterations would then be interrupted by one of the two other stopping criteria (Section 2.1.3.5) that are introduced to break the loop.

It is of interest, in such cases, to focus on how this affects the estimation of forces. Despite not fulfilling one of the two main criteria of the method (static admissibility), the obtained set of contact forces is typically not far from the desired one. Figure 3.15 gives a confirmation of this: even for those states for which the iterative solver does not converge to an admissible solution, the estimation of forces is still very good, with a correlation which in general is not lower than the average one. Therefore, it seems that the satisfaction of the two criteria of the QSM does not affect much the estimation of forces.

The failure of the method to obtain an admissible solution can anyway be further reduced if all the non-equilibrium states of the reference simulation are let to relax under constant external load, until equilibrium is reached. Then, the application of the QSM to the *relaxed* states removes any possibility that the method does not converge towards a statically and plastically admissible set of contact forces. An example is shown in Figure 3.16, where the evolution of the QSM iterations towards a solution is compared between its applications to the same geometrical arrangement, but in two different conditions: when the original state is taken as it is, and when it is let to relax under constant stress.

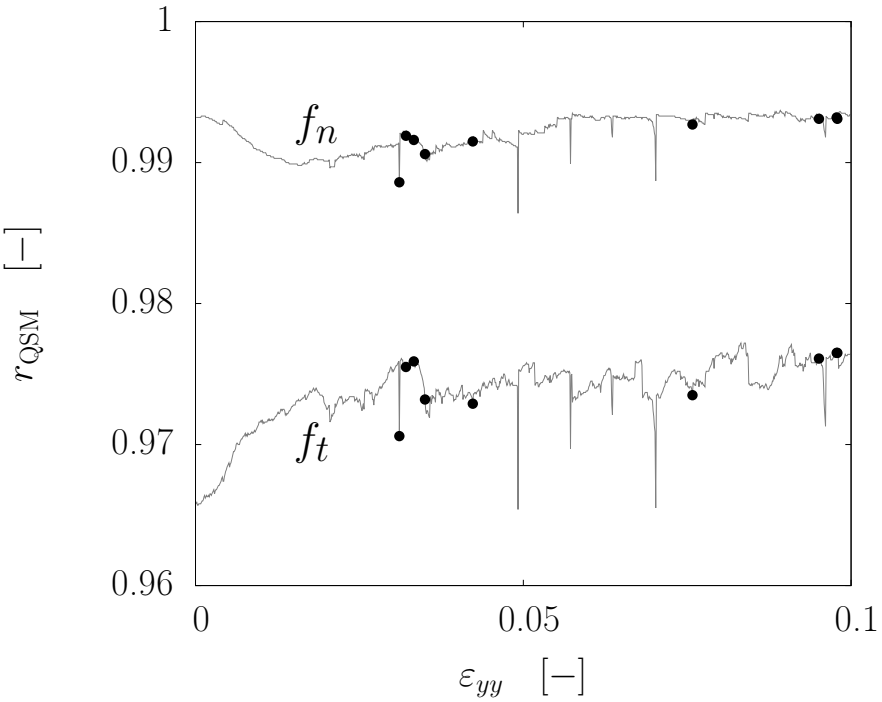


Figure 3.15 – Evolution of the correlation of normal and tangential forces, estimated via the QSM, for one MD simulation ($\kappa = 100$), with indication of states for which the method could not find a statically and plastically admissible solution (black dots).

The comparison is carried out by defining appropriate parameters that describe the distances from the satisfaction of the two criteria (static and plastic admissibility). For the first criterion, an error is defined as the maximum $x$- or $y$-component of unbalanced forces over all particles; for the latter, we take the distance from the Coulomb cone.

In the original state, the method does not converge, as the distances from the satisfaction of the two criteria stop decreasing after a certain number of iterations; on the other hand, when the original state is let to relax under constant stress, the distances from the satisfaction of the two criteria monotonically decrease, until a threshold is reached and a solution is assumed to be obtained.

A striking observation is that, although the obtained set of contact forces, in the first case, does not satisfy the requirements of the method, it is still very close to the original one, with a correlation with the original set $r = 0.999$ for both normal and tangential forces.

### 3.4.2 Assessment of the influence of measurement error

The estimation of forces from synthetic data (ideal material, no measurement inaccuracy) via the QSM has proven successful. However, to assess the applicability of the method

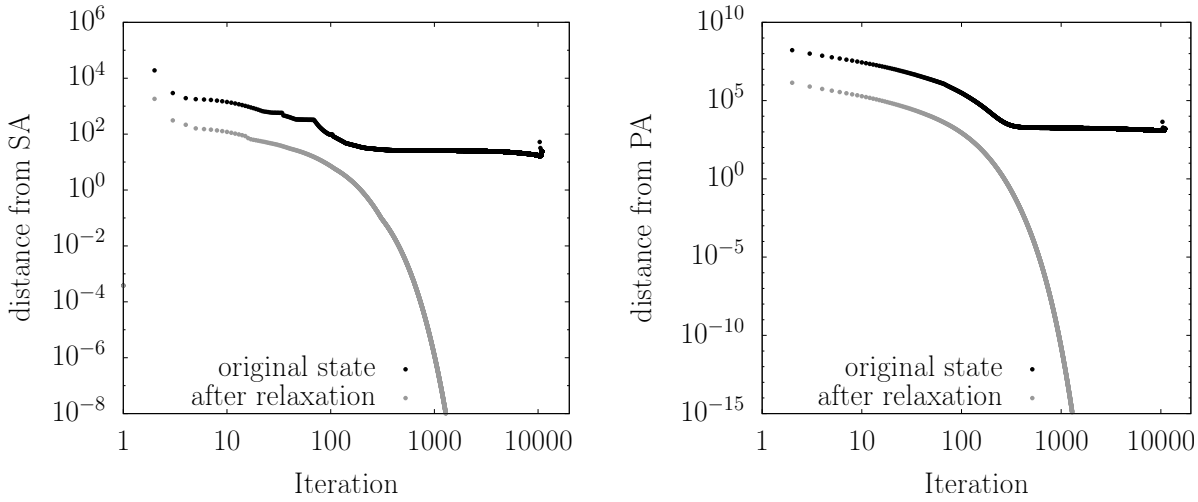


Figure 3.16 – Evolution of the error of the QSM during the iterative procedure, for a single state ($\varepsilon_{yy} = 3.1\%$) of an MD simulation with $\kappa = 100$, before and after the assembly is let to relax under constant stress. Only for the latter a statically and plastically admissible solution is found.
(Left) The error is a distance from static equilibrium, defined as the maximum $x$- or $y$-component of unbalanced forces over all particles and boundaries.
(Right) The error is a distance from plastic admissibility (Coulomb cone).

to real data, measurement error has to be taken into account. One way of doing so is to artificially introduce error in the synthetic data; then, the effect of this perturbation can be assessed by looking at how the estimation of forces is affected.

Several ways of perturbing geometrical data can be used. In this work, we focus on two methods, and we study the effect of these perturbations on the contact network and on the estimation of forces.

A first perturbation of the data is injected by modifying the radii of grains, thus affecting the contact network. In particular, a systematic error is introduced by applying a multiplying coefficient, slightly smaller or higher than 1, to have a global effect of, respectively, underestimation or overestimation of the number of contacts. This is indicative of a typical issue with experimental measurements, that is the definition of a gray-value threshold for the binarisation of images of the assembly, based on which contact detection is performed (as it will be explained in Section 4.1.4.1). By tuning this threshold, for which an exact value cannot be easily determined, the number of contacts can be modified.

This situation is reproduced for the application of the QSM to the three MD-DEM simulations. The two contact lists – the reference one, and the one used in the QSM after having perturbed the radii – are compared, and Pearson's $r$ is computed for the contacts

in common between the two lists (for normal and tangential forces, respectively).

Results are shown in Figure 3.17. Similar behaviours are observed for the three simulations: the decay of $r$, as the extent of perturbation increases, is similar, indicating that the degree of force indeterminacy has no, or rather limited, effect, from a qualitative point of view.

The perturbation seems to affect the estimation of forces more significantly for the case in which contacts are lost. However, it can be assumed that, as long as the extent of the perturbation is relatively small, the contacts that are lost are mainly those for which particle interpenetration was already small, and so they belong to the weak force network: in such cases, when the strong force network is preserved, a solution close to the real one can still be found.

When the number of lost contacts increases, the method proves unable to find a realistic estimation of forces: a loss of 5% of the contacts already entails a strong decay of $r$, for both normal and tangential forces.

On the other hand, a better response is observed when the number of contacts is overestimated. This information can prove useful for the application to experimental data, in which it might be advisable to intentionally overestimate the gray-value threshold for the determination of grain radii, rather than underestimate it. Indeed, a contact gain of 10% does not irremediably affect the estimation of forces.

In addition to looking at the evolution of Pearson's $r$, it is also useful to have a visual comparison of maps of contact forces. In Figure 3.18, the original force network (normal forces) in one state of an MD simulation is compared to the force network obtained, for the same state, through the QSM, with an underestimation of the number of contacts causing a total loss of $\approx 5\%$ of them. Despite this error, it is clear that the strong force network, including the main force chains, is correctly retrieved. In the same figure, such a comparison is carried out also for the case of overestimation of the number of contacts. Again, the strong force network seems not to be affected, and the additional contacts (here, $\approx 9\%$) can be assumed to be carrying mainly low forces.

In experiments, another source of measurement error that may cause bad contact detection lies in the determination of the position of grain mass centres. Typically, it is not a systematic error in one direction; therefore, to reproduce this inaccuracy in numerical data, a random deviation can be added on the $x$- and $y$-coordinates of all grains. The effect of such a perturbation on the building of the contact network is not unambiguous: it can cause, at the same time, the creation of new contacts as well as the opening of existing ones.

The evolution of Pearson's $r$ for normal and tangential forces in this case is shown

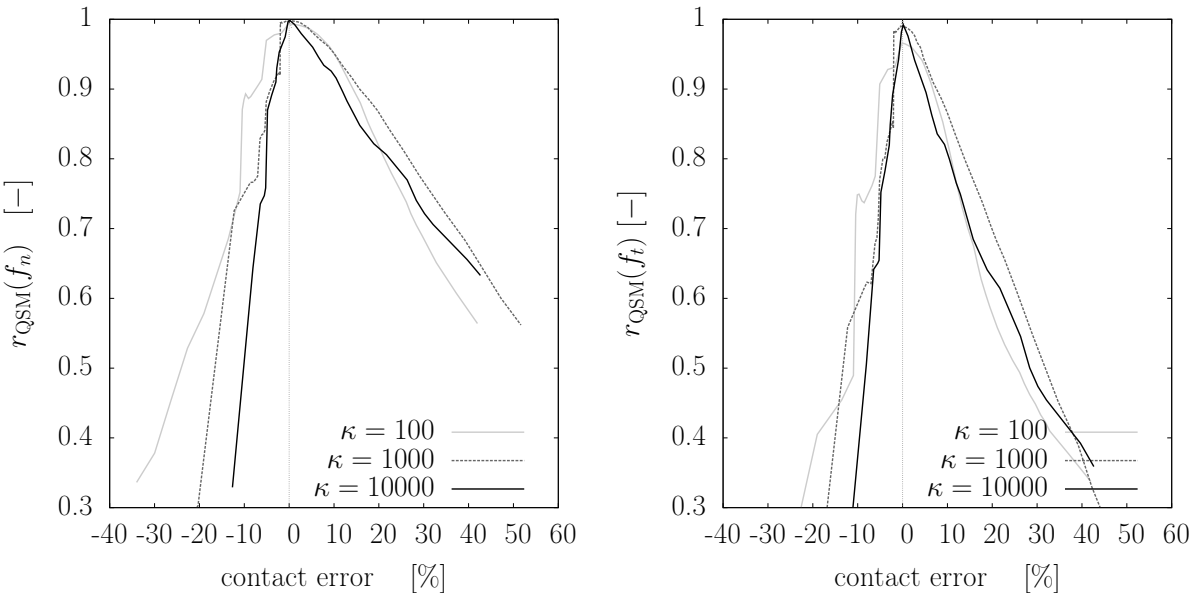


Figure 3.17 – Evolution of Pearson's $r$ for normal (left) and tangential (right) contact forces, between the real values and the ones estimated via the QSM, as the contact network is perturbed by artificially increasing or decreasing the radii of all grains proportionally to their value. All points in the curves correspond to a single granular state, at the beginning (*i.e.*, close to isotropic compression loading conditions) of the three simulations.

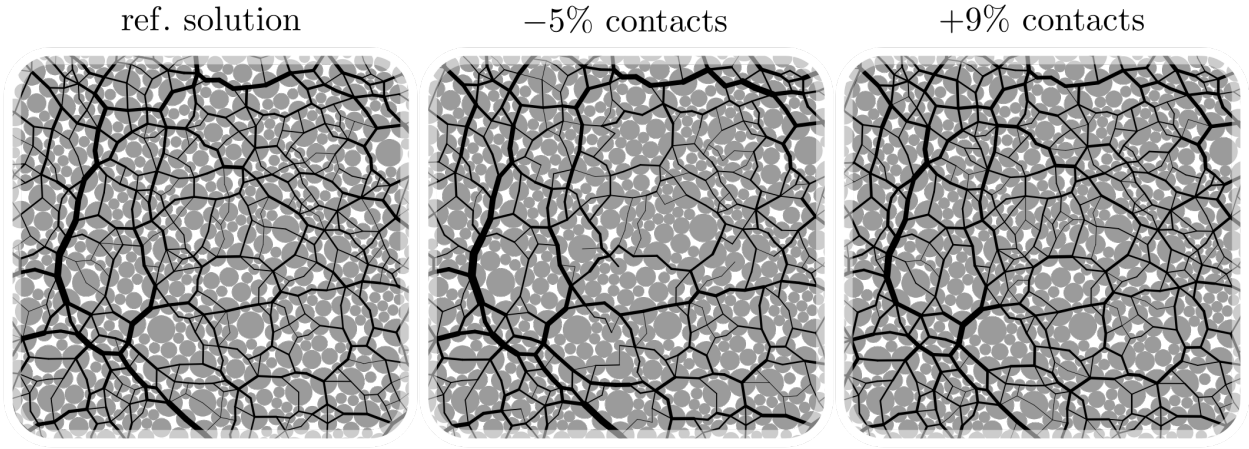


Figure 3.18 – (Left) Map of reference (MD) normal forces from an early state ($\varepsilon_{yy} \approx 0$) of a biaxial vertical compression with $\kappa = 10000$.
(Center) Map of normal forces obtained, for the same state, by applying the QSM with 5% fewer contacts with respect to the real contact network.
(Right) Map of normal forces obtained, for the same state, by applying the QSM with 9% more contacts with respect to the real contact network. All maps are zoomed in to show the differences in the weak network.

in Figure 3.19. The error is reported in terms of the difference between the contact lists that it entails; lost and gained contacts are considered at the same time and added up. However, it can be assumed that the main contribution to this error consists of contact loss: as the extent of the perturbation – which can be controlled through some scalar coefficient that tunes the magnitude of the applied displacement – increases, a clear predominance of contact loss is observed. In general, this type of error seems to have a higher impact on the estimation of forces: $r$ goes down to $\approx 0.8$ for normal forces and $\approx 0.7$ for tangential forces already with a contact error of 5%, in a similar way for all the three simulations. Maps of normal forces corresponding to a contact error of 4% ($r(f_n) \approx 0.9$) and 7% ($r(f_n) \approx 0.7$) respectively are shown in Figure 3.20, confirming anyway a good estimation of the strong force network even for relatively low $r$.

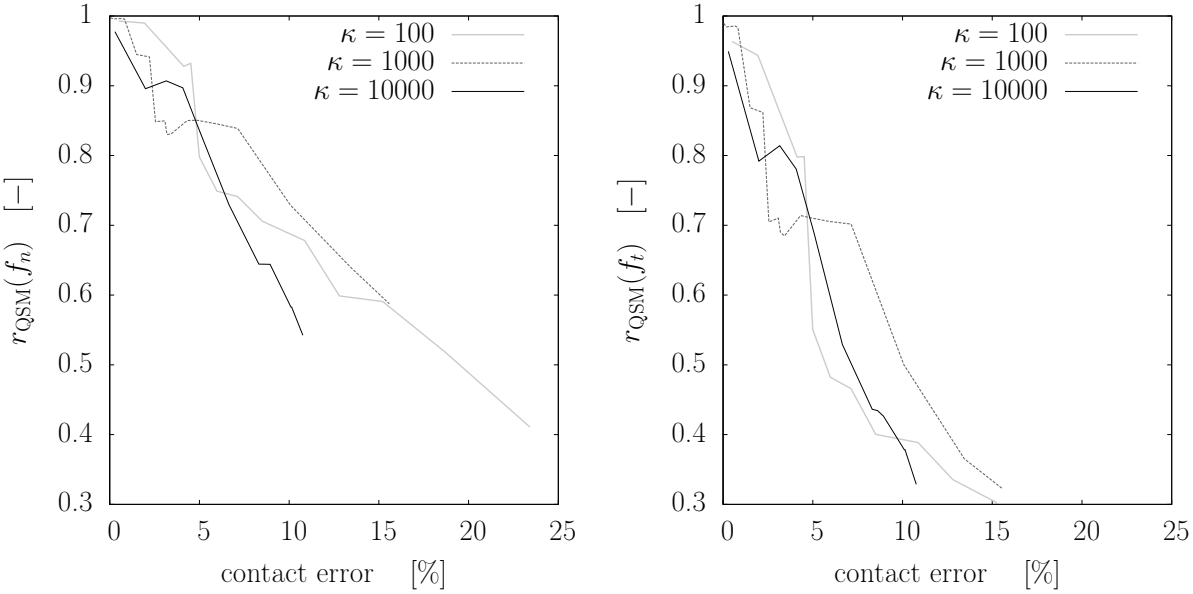


Figure 3.19 – Evolution of Pearson's $r$ for normal (left) and tangential (right) contact forces, between the real values and the ones estimated via the QSM, as the contact network is perturbed by adding random noise on the position ($x$- and $y$-coordinate) of grain mass centres. All points in the curves correspond to a single granular state, at the beginning (*i.e.*, close to isotropic compression loading conditions) of the three simulations.

## 3.5 Contact Dynamics-based Method

Similarly to the Quasi-Static Method, also Contact Dynamics can be applied to the estimation of forces by simply knowing the contact network and boundary conditions.

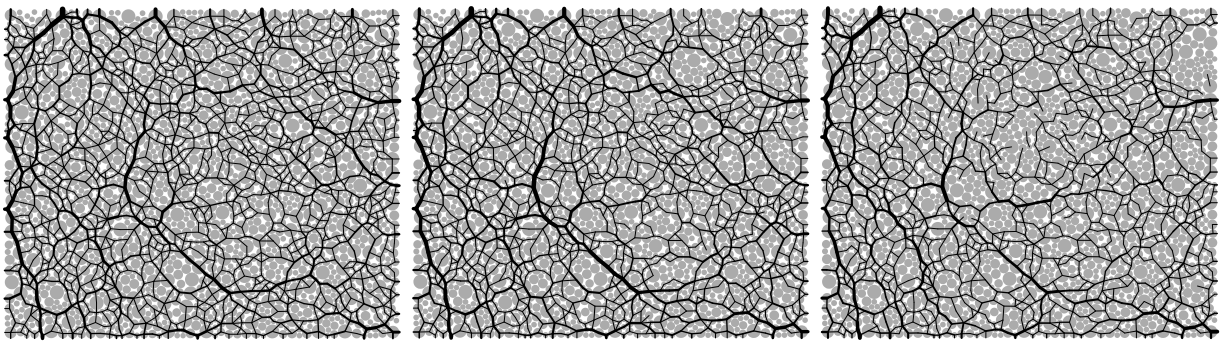

Figure 3.20 – (Left) Map of reference (MD) normal forces from an early state ($\varepsilon_{yy} \approx 0$) of a biaxial vertical compression with $\kappa = 10000$.
(Center) Map of normal forces obtained, for the same state, by applying the QSM with a 7% error on contacts with respect to the real contact network, due to perturbation on grain positions ($r(f_n) \approx 0.9$).
(Right) Map of normal forces obtained, for the same state, by applying the QSM with an error of 11% ($r(f_n) \approx 0.7$).

The main difference in the principles of the two methods is that in Contact Dynamics, with the assumption of rigid grains and no contact compliance, the length scale associated with contact deformation is completely neglected. Therefore, both normal and tangential forces are initialised to null values and their estimation does not exploit any additional information on their current state (Section 3.5.1).

A possible way of addressing the method towards the targeted (reference) solution consists in initialising the Gauss-Seidel iterator with the contact forces from the previous step. This is already common practice in CD simulations, for which it is shown that this is not simply a numerical trick to facilitate the convergence of the iterative solver, but, in helping account for the previous history of the assembly, it also reduces the indeterminacy of the solution in forces (McNamara et al., 2005).

One of the advantages of this validation approach is that the real MD forces are actually known; exploiting this information can help reduce force indeterminacy. An attempt is made (Section 3.5.2) to use the real values – normal or tangential forces, alternatively – and estimate only the remaining part of the force network. In particular, by fixing the values of normal forces to the real, MD values, that come from the assumption of contact elasticity, we try to re-inject this property in the method. Then we can investigate the effect of this operation on the estimation of forces, knowing that force indeterminacy of the system is a direct consequence of neglecting the contact deformation length scale.

Differently from simulations, in real experiments the values of (part of) the contact forces can only be estimated with a certain approximation; the approach of fixing part of the variables to these values might not be advisable. Nevertheless, estimated forces

can be used as an initial guess for the Gauss-Seidel iterator, again with the objective of reducing indeterminacy and improving the estimation of forces. This operation is tested in Section 3.5.3.

### 3.5.1 Estimation of normal and tangential forces

In the most basic application of the CDM, *i.e.*, when no initial guess is provided to the Gauss-Seidel iterator and no information on the history of the packing is exploited, force indeterminacy is expected to play a major role in the estimation of forces, as explained in Section 2.1.2.

This is confirmed by assessing the quality of the obtained forces through Pearson's $r$, for the three different MD simulations (Figure 3.21). A very good agreement with the real MD forces is obtained for the highest stiffness level ($\kappa = 10000$), also corresponding to the lowest degree of force indeterminacy (Table 3.1). As $\kappa$ decreases – and hyperstaticity increases simultaneously – the quality of force estimation considerably drops. In other words, as the space of possible solutions is expected to grow in size with the level of hyperstaticity, the variability of contact forces increases at the same time, and it is no surprise that the obtained forces are further from the desired ones. This will be studied in more detail in Section 3.5.6, in which an attempt will be made to build and explore the ensemble of possible solutions for a small system.

Another way of comparing the obtained contact network with the original one is to define an error on each contact force, and study its distribution. In Figure 3.22, the Cumulative Distribution Function of this quantity, defined for normal contact forces, is shown for the three MD simulations, confirming that higher errors are obtained for higher degrees of force indeterminacy.

It can be observed, at the same time, that the estimation of normal forces is slightly but constantly higher than that of tangential ones. This might be explained with reference to the rather high variability of tangential forces, for which the range of admissibility, defined by Coulomb's friction law, depends on the value that is assumed for the interparticle friction coefficient $\mu$. In this case, a relatively high value was adopted ($\mu = 0.5$); with a lower $\mu$, the range of possible tangential forces would shrink, and their estimation might be expected to improve at the same time.

As it was shown by McNamara et al. (2005), force indeterminacy in Contact Dynamics can be associated with the fact that the previous history of the packing is discarded by this method. The existence of a set of admissible solutions, rather than a single, uniquely determined one, comes from this: each of the possible solutions correspond to a different

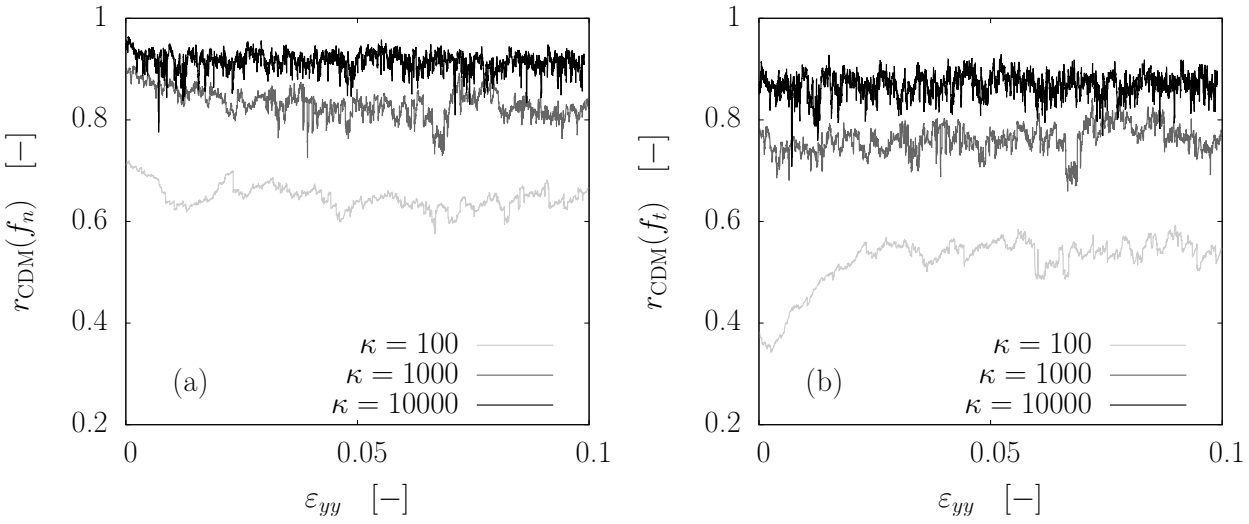


Figure 3.21 – Evolution of Pearson's $r$ for normal (left) and tangential (right) contact forces in the three MD simulations (for $\kappa = 100, 1000, 10000$ respectively), between the solution estimated via the CDM and the real one.

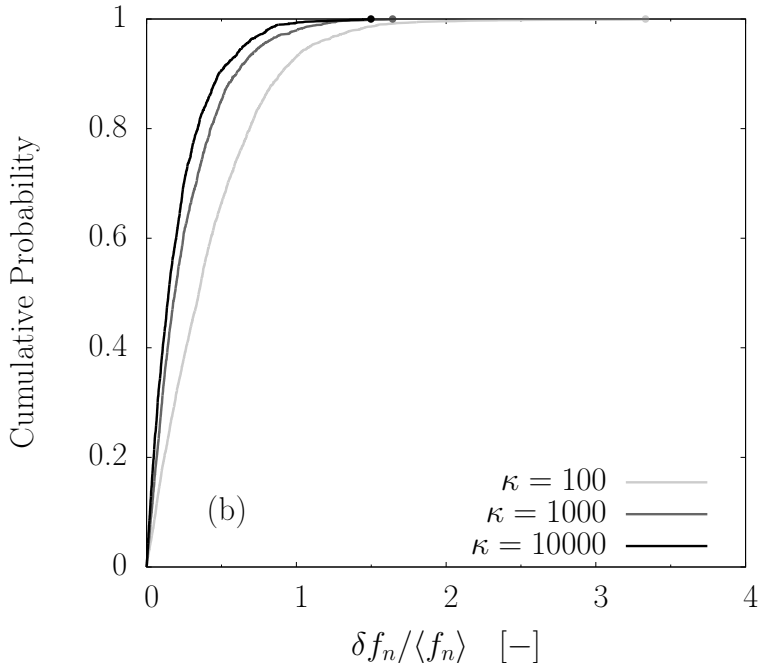


Figure 3.22 – Cumulative Distribution Function of normal force error – defined as the absolute normal force difference normalised by the average normal force – for all contacts in the application of CDM to a state at the early stage of the three MD simulations (close to isotropic compression conditions).

history of the packing. Because of this, the procedure of using forces from the previous time step as an initial guess for the CD iterative solver, that is common practice, is more than just a numerical trick: it has a physical meaning, as it compensates the absence of information on the history of the system.

This can be exploited also in the application of CD to the estimation of forces for given granular states, as in the aim of this work. The validation of the method, performed through application to MD simulations, makes it possible to assess the effect of this operation.

The CDM is applied in the two different ways – with forces starting from null values, and by exploiting forces from the previous state –, and the comparison between the two cases (Figure 3.23), for one of the MD simulations ($\kappa = 100$), shows that the estimation of both normal and tangential forces clearly benefits from retrieving previous forces. This result is confirmed by the comparison of homogenised stress tensor components, computed via the Weber formulation (Equation 3.5) from the reference (MD) contact forces, or for those estimated via the CDM (Figure 3.23). An almost perfect correspondence is observed when the CDM makes use of forces from the previous state, while the stress components slightly deviate from the good one in the other case (forces starting from zero).

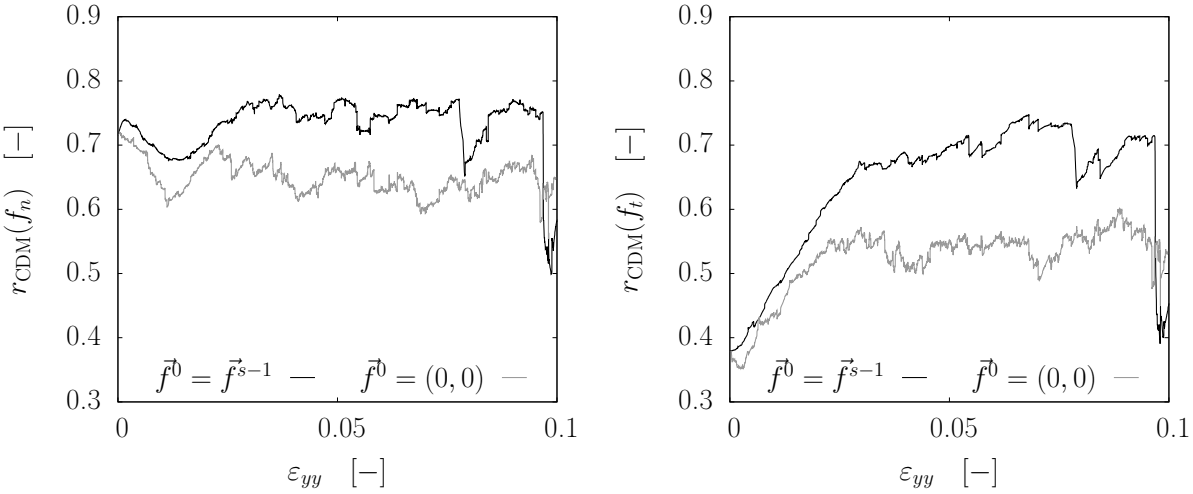


Figure 3.23 – Evolution of Pearson's $r$ for normal and tangential forces, between the original ones and those estimated via the CDM for an MD simulation with $\kappa = 100$, when forces are initialised to null values and when they are initialised to the values from the previous state.

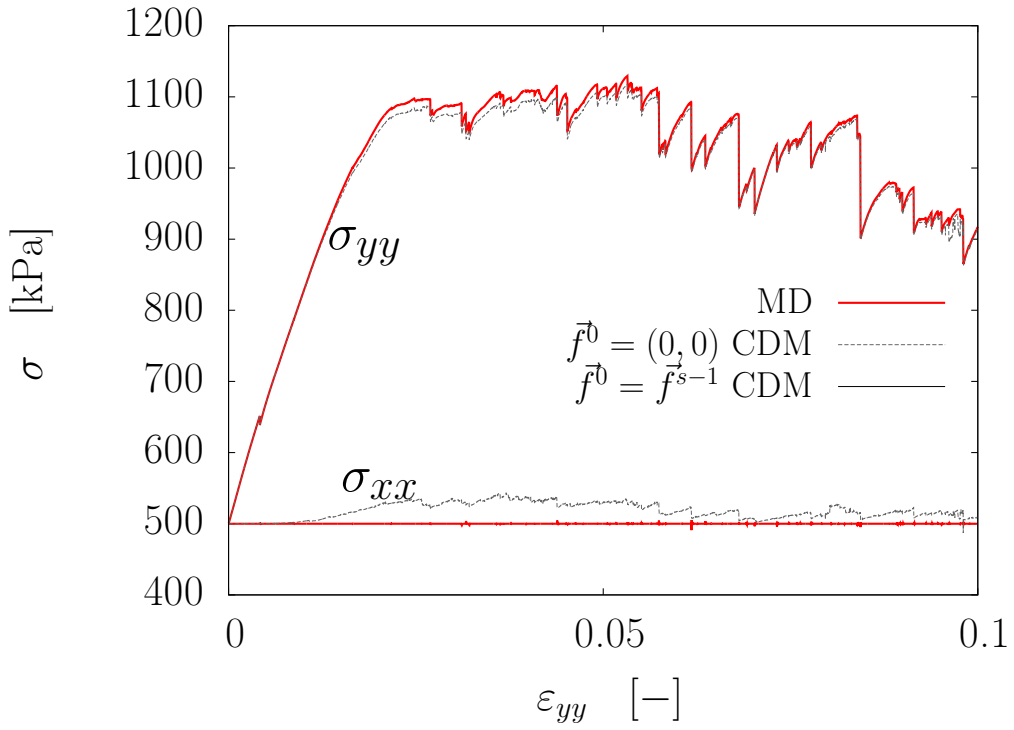


Figure 3.24 – Evolution of the homogenised stress tensor components from reference (MD) contact forces and forces estimated via the CDM, for a simulation with $\kappa = 100$, when forces are initialised to null values and when they are initialised to the values from the previous state.

### 3.5.2 Estimation of only normal or tangential forces

In Contact Dynamics, the treatment of particle interactions at contact consists in neglecting the length scale associated with contact deformation, so that contacts are assumed to be non-compliant. With respect to the contact model adopted for classic Molecular Dynamics, this model has more physical meaning, as it prevents particle interpenetration; it is also specifically suitable for the typical materials of interest in geomechanics, whose deformability is generally low, in particular if we compare their stiffness (*e.g.*, Young's modulus) with the level of loading that is generally attained in common geomechanical applications.

However, neglecting contact deformation comes with a drawback, *i.e.*, the non uniqueness of the solution in forces. It is of interest, in the context of an application to numerical data – in which actual contact forces are known and can be exploited – to reintroduce contact elasticity in the treatment of particle interactions of Contact Dynamics, and see how force indeterminacy and variability are affected.

This is done by fixing the values of normal forces, in the Gauss-Seidel iterator, to their original (MD) ones, which actually come from the assumption of contact elasticity. As the numerical solver proceeds in its iterations, tangential forces are constantly updated by crossing, as in regular applications, Coulomb's friction law – expressed through inequalities – and the equation of dynamics (in contact variables). Normal forces, on the other hand, are forced to maintain the value they were given at the beginning (*i.e.*, their original value in the MD simulation), even if this may cause a violation of the contact law.

In the end of the iterative procedure, the obtained tangential forces are compared with the reference (MD) ones. In Figure 3.25, this comparison is described through Pearson's $r$ for the application to one of the three MD simulations, with intermediate initial stiffness level. The correlation, that in the standard application (forces starting from zero) lies in a range between 0.7 and 0.8, jumps directly to $r > 0.995$ when normal forces are fixed.

This result is extremely important, as it means that force indeterminacy is practically overcome, and a unique solution is retrieved. This might prove particularly useful with a view to the estimation of forces from experiments: assuming that an established and reliable technique gives a realistic estimation of normal forces based on measurements of contact deformations, Contact Dynamics is expected to provide an accurate estimation of tangential forces, and, in doing so, complete the full characterisation of the loading state of individual particles.

In addition, an attempt is made to perform the inverse operation, *i.e.*, fixing tangential

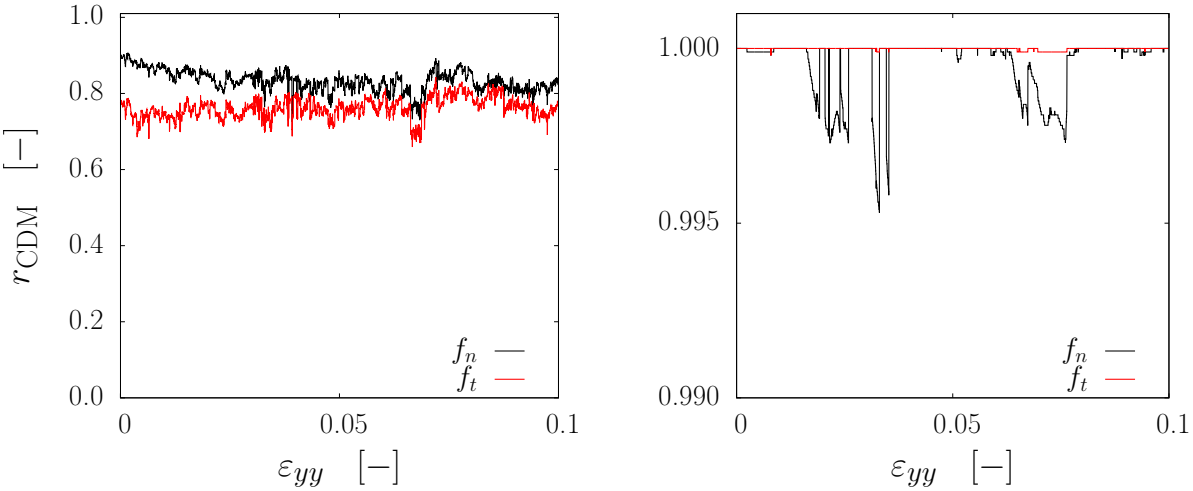


Figure 3.25 – (Left) Evolution of Pearson's $r$ for normal and tangential forces, between the CDM solution and the original set of forces. The stiffness level $\kappa$ is 1000. (Right) Evolution of Pearson's $r$, respectively for tangential forces $f_t$ when imposing normal forces to be constant and equal to their original values, and for normal forces $f_n$ when tangential ones are imposed, between the CDM solution and the original set of forces. The stiffness level $\kappa$ is 1000.

forces to their actual values and only determining normal ones. Though less suitable for an experimental application, for which an accurate approximation of tangential forces cannot easily be obtained, this attempt can still show interesting features: the estimation of only normal forces, when tangential ones are fixed, is considerably more accurate ($r > 0.995$) than it is in the standard application ($r = 0.8 \div 0.9$).

These findings can be explained with reference to the degree of force indeterminacy of the system, expressed by the parameter $h$ in Equation 2.1. This quantity describes the hyperstaticity of the system, *i.e.*, the excess of variables in the problem with respect to the number of equations to solve it; fixing the values of part of the variables can be considered equivalent to reducing their number, expecting that, in this way, isostaticity is approached and the uniqueness of the solution retrieved. The result in Figure 3.25 is indeed a confirmation of this.

### 3.5.3 Exploiting contact elasticity

Instead of imposing constant values, contact elasticity can also be exploited by simply using an estimation of normal forces as part of the initial guess of forces that represents the starting point of the Gauss-Seidel iterator. This is more suitable for experimental applications.

In this numerical application, we test this by using the original (MD) solution in

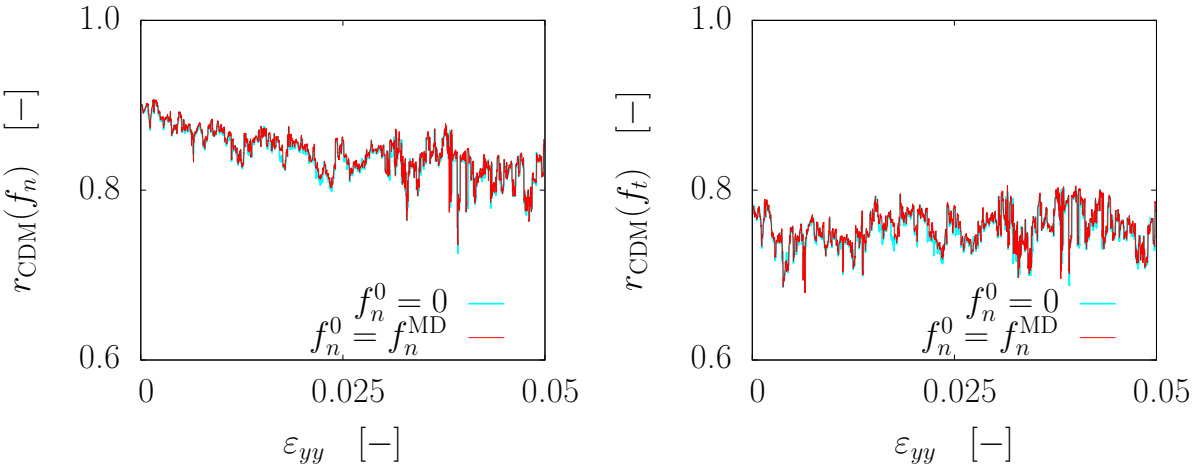


Figure 3.26 – Evolution of Pearson's $r$ for normal (left) and tangential (right) forces, between the CDM solution and the original set of forces, when normal forces are initialised to their original values and when they are not. The stiffness level $\kappa$ is 1000.

normal forces, that comes from the assumption of contact elasticity and measurement of a particle overlap, to initialise the values of normal forces, in the same way as it was done for the QSM in Section 3.4. It is also interesting, at this point, to compare the response of the two methods to the same procedure.

In Figure 3.26, the quality of force estimation (described by Pearson correlation) is compared, for the application of the CDM to an MD simulation with $\kappa = 1000$, between two different procedures, *i.e.*, when the original normal forces are used in the initial guess of the Gauss-Seidel iterator, and when null forces are used. The same quality of the solution is retrieved for all the states of the simulation, showing that the use of contact elasticity simply for the initial guess of the numerical solver is not sufficient to improve the estimation of forces in Contact Dynamics, while for the QSM this procedure is sufficient for the correlation of forces to directly jump to $r \approx 1$.

Thus, the CDM proves less sensitive to the introduction of contact elasticity, which can help overcome the non-uniqueness of the solution in forces only if part of them are imposed, provided that they are known with highest precision; using an approximation of normal forces, based on contact elasticity assumptions, does not improve force estimation as it does for the QSM.

### 3.5.4 Convergence of the iterative procedure

Differently from the Quasi-Static Method, Contact Dynamics is not meant to deal specifically with equilibrium states; hence, it does not set any requirement on the static equilibrium of particles. The only requirement is for the satisfaction of the two main conditions

expressed by the contact laws: the interpenetrability of particles (Signorini condition), and the constraint represented by Coulomb's law of friction for tangential forces.

However, the implementation of a numerical resolution (Gauss-Seidel's iterator) also requires the definition of appropriate stopping criteria. Typically, iterations are interrupted as soon as contact laws are fulfilled at all contacts in the system, but in some cases the iterative solver does not easily get to such a solution. For these situations, other criteria can be introduced in order to break the iteration loop and reduce the computational cost of the method.

Given the quasi-static character of the simulations, it can be assumed that most of the states extracted at distinct steps of the simulation are equilibrium states (or very close to equilibrium). Based on this, an additional rule to break the iteration loop is found in a limitation of the kinetic content of the system: iterations are stopped whenever the mean normal relative velocity (formal velocities are used) goes below a fixed threshold. The loop can also be stopped when no considerable change is observed in the solution between consecutive iterations. Finally, a limitations to the total number of iterations is set, as in the QSM.

All these additional criteria do not have a considerable influence on the estimation of forces. As it can be seen in Figure 3.27, the method converges to an admissible solution only in few states at the beginning of the simulation, still in the pseudo-elastic phase, in which few grain rearrangements occur and the macroscopic deformation practically results only in contact deformations; nevertheless, the estimation of forces remains very good for the following states, for which the Gauss-Seidel loop is prematurely terminated.

It is of interest to focus on how the solution evolves throughout the loop of the iterative solver. This can be seen in terms of the mean normal velocity that is used in one of the stopping criteria: in Figure 3.28, its evolution is shown for two different states – one state which was originally at equilibrium, and one which was not – and compared between two different applications: one in which forces are initialised to null values, and one in which they are initialised to their values in the previous state.

This comparison shows that, in terms of convergence of the iterator, retrieving previous forces does not make the procedure considerably faster; however, an admissible solution can be attained with fewer iterations simply because the initial state is closer to equilibrium. On the other hand, when forces start from zero, a higher kinetic content is observed in the beginning of the iterative procedure, *i.e.*, when the information is only stored at the boundaries and needs a certain amount of iterations to be transmitted through the whole assembly.

The comparison of a state at equilibrium with one which is not shows that, while for

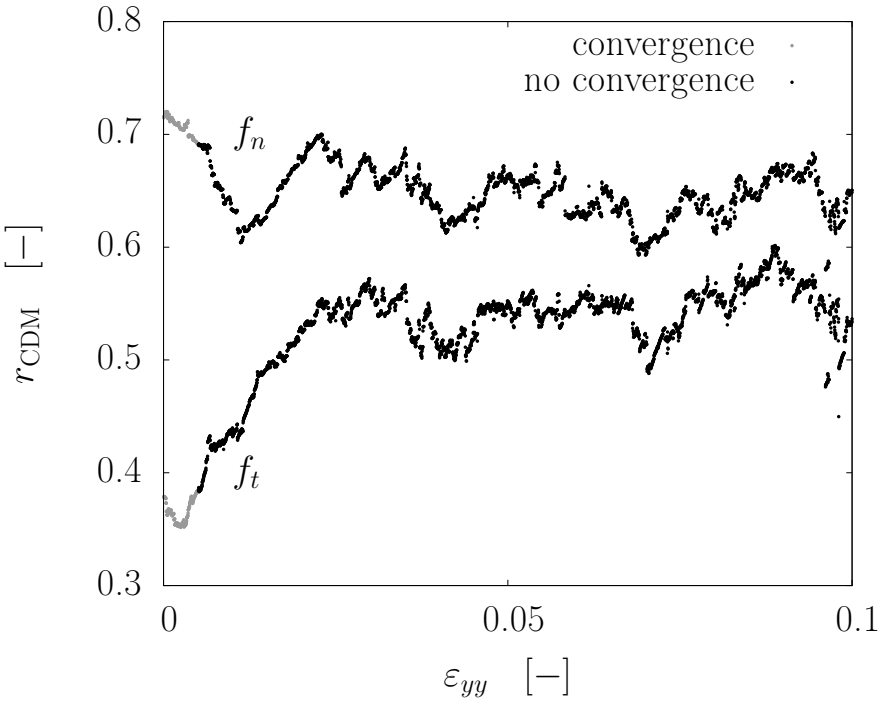


Figure 3.27 – Evolution of Pearson's $r$ for normal and tangential forces, between the original forces and those estimated via the CDM for an MD simulation with $\kappa = 100$, with indication of admissible and non-admissible solutions.

the first case the kinetic content monotonically decreases (until a threshold is reached), in the second case it seems to stabilise after a certain amount of iterations, clearly showing that the obtained solution does not imply static equilibrium.

### 3.5.5 Assessment of the influence of measurement error

Similarly to the Quasi-Static Method, also for this application of Contact Dynamics the main micromechanical information that is required for the estimation of forces is the contact network. Hence it is of the same importance, also for this method, to predict how errors in the input data would affect the final result of forces, with respect to the application to experiments.

In order to artificially add error in the geometric data, the same procedure as in Section 3.4.2 is adopted, consisting in introducing two different types of inaccuracy: a systematic error on grain radii, by multiplying them for a given coefficient $\lambda$, with the effect of a contact loss when $\lambda < 1$ and a contact gain when $\lambda > 1$; a random error on the $x$- and $y$-coordinate of grain mass centres, resulting in both contact loss and gain at the same time (though with a prevalence of the former). For both cases, the perturbation of the geometric data is carried out on a single state, close to isotropic compression

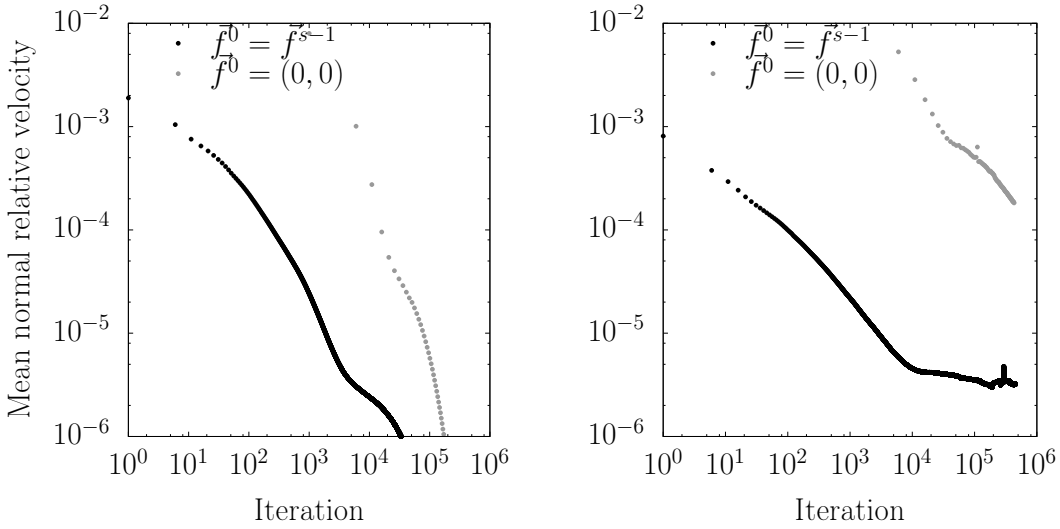


Figure 3.28 – Evolution of the mean normal relative velocity during the Gauss-Seidel iterations of an application of the CDM, to a single state of an MD simulation with $\kappa = 100$, when forces are initialised to zero and when they are retrieved from the previous step. (Left) A state originally at equilibrium. (Right) A state originally not at equilibrium.

conditions, of each of the three MD simulations; the estimation of forces is assessed as the extent of perturbation (number of contacts that are created or lost with respect to the correct network) is increased. The assessment is carried out with the common techniques that were previously used in this section.

As regards the systematic error on grain radii, Figure 3.29 shows the decay of Pearson's correlation of normal forces in common between the original network and the perturbed one, for both contact loss and gain. It can be observed that the decay of $r$ is limited; in particular, $r$ does not seem to drop for a contact gain – or loss – lower than 10% of contacts. This can have important outcomes in the perspective of an experimental application, for which such an error seems to overcome the expected accuracy in the detection of contacts: for the tests that are carried out during this work, an error of $\approx 10\%$ corresponds to around 300 misdetected contacts, which is very high if one assumes that a simple eye check can help locate most of the cases of wrong detection.

An important finding is that a similar response is observed for both contact loss and gain, differently from the QSM that proved to be more sensitive with respect to the former situation. This robustness of the CDM is a strong point for its application to experimental data, when it comes to a choice between these two methods.

More information can be extracted from the analysis of Figure 3.29. By comparing the results for the three different simulations, it is shown that force indeterminacy has no considerable effect on the decay of $r$, which is very similar in the three cases. Force inde-

terminacy, however, still has a strong influence on the starting point of the three curves, which is why they do not collapse in a single curve despite a comparable evolution.

To partially summarise, the main, general conclusion that can be inferred from this analysis is that the estimation of forces via Contact Dynamics is not significantly affected by errors in the grain radii. There are other ways to show and confirm this result. For example, one can compare maps of normal contact forces, to have a visual confirmation of how accurately forces, and particularly the chain-like structures in which they typically organise themselves in disordered systems, are retrieved. In Figure 3.30, the original force network of the analysed state (for $\kappa = 10000$) is compared with the force network provided by the CDM when the perturbation of grain radii results in a loss of $\approx 10\%$ of the original number of contacts. As a consequence of this error, the obtained set of forces is clearly not at equilibrium (while the original one is), as it can be inferred from the presence of particles with only one contact force acting on them (in the absence of gravity). Despite this, it is observed that the main force chains are retrieved with a good precision.

Figure 3.30 also shows the solution for the opposite case, when the error on radii entails a gain of $\approx 10\%$ contacts, for which similar results are obtained. While the weak force network is modified by the creation of new contacts, and static equilibrium is assumed not to be verified for all particles, the strong force network remains practically unchanged. For this situation, another confirmation is given by the analysis of only those contacts that come from wrong detections, in excess with respect to the correct network. It is observed (Figure 3.31) that these contacts, in the final CDM solution, mainly carry below average normal force (or no force at all), and they do not participate in the main process of force transmission, which still relies on the same force chains as in the original network.

There is another typical source of inaccuracy in experimental measurements that, similarly to the wrong estimation of particle radii, can spoil the detection of contacts between grains and, consequently, the identification of their location (assumed to be punctual), *i.e.*, the bad detection of grain centres.

In order to reproduce the effects of such an error in numerical applications, a perturbation of the original geometry of the packing is introduced by applying random displacements along the $x$- and $y$-direction to the position of grain mass centres, in the same way as it was done for the QSM (Section 3.4.2).

The estimation of forces is evaluated, as the amount of error increases, for the three MD simulations (Figure 3.32). The extent of perturbation is defined as the normalised difference of the number of contacts between the two contact lists (the correct one, and

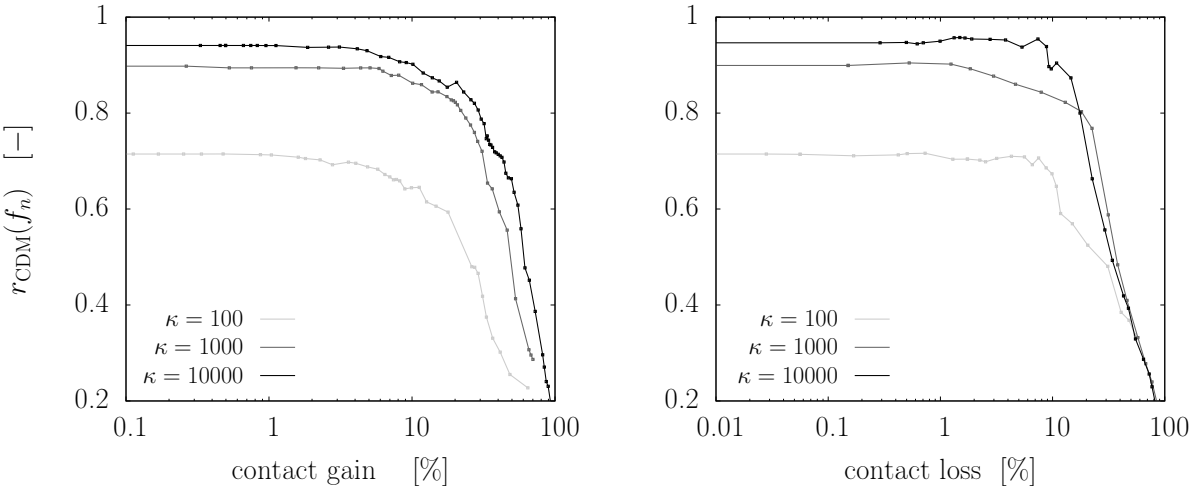


Figure 3.29 – Evolution of Pearson's $r$ of normal forces as the number of contacts is artificially increased (left) or decreased (right), for a state in the early stage of the simulations ($\varepsilon_{yy} \approx 0$, close to isotropic compression conditions), in the CDM solution. Contact gain (loss) is expressed as the increase (decrease) in the total number of contacts normalised by the initial value.

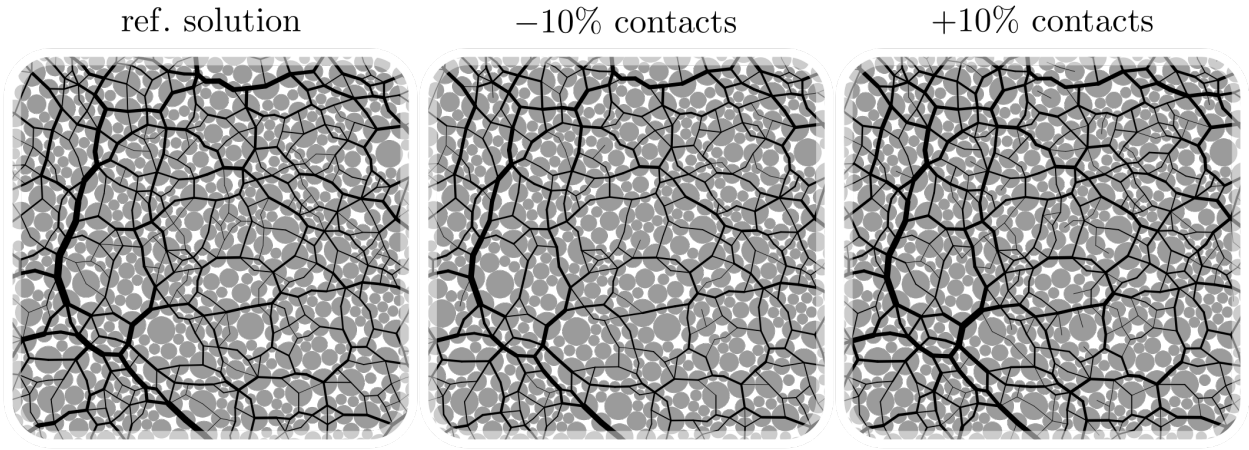


Figure 3.30 – (Left) Map of reference (MD) normal forces from an early state ($\varepsilon_{yy} \approx 0$) of a biaxial vertical compression with $\kappa = 10000$.
(Center) Map of normal forces obtained, for the same state, by applying the CDM with 10% fewer contacts with respect to the real contact network, due to error on grain radii.
(Right) Map of normal forces obtained, for the same state, by applying the CDM with an additional 10% of contacts with respect to the real contact network. All maps are zoomed in to show the differences in the weak network.

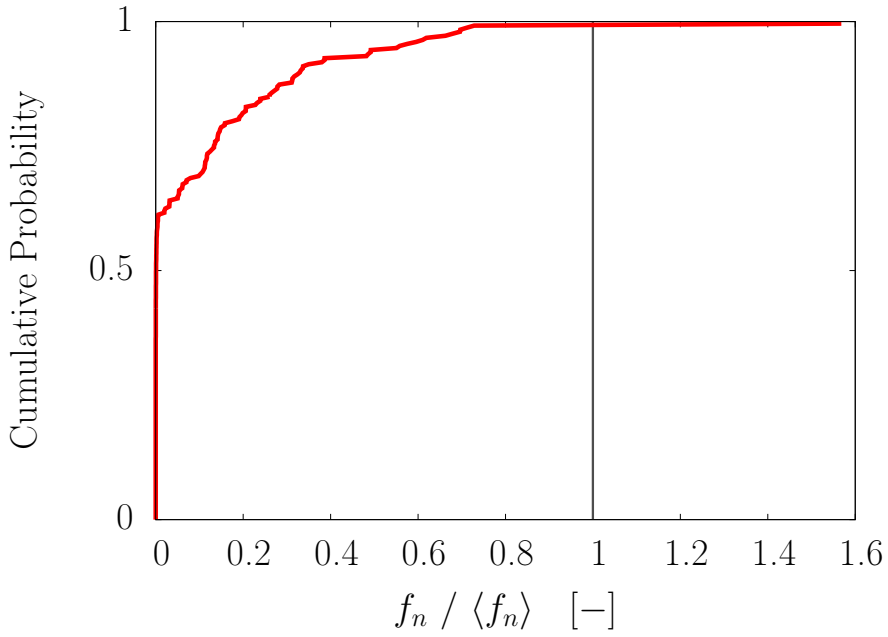


Figure 3.31 – Cumulative Distribution Function of normal forces carried by the additional 10% contacts for the same state as in Figure 3.30.

the one after perturbation), including lost and gained contacts at the same time; however, as it was already seen in Section 3.4.2, the lost contacts outnumber the gained ones.

The decay of correlation between estimated (normal and tangential) forces and real ones is comparable for the three values of $\kappa$; the main influence of the degree of force indeterminacy is in the starting point of the three curves, *i.e.*, when no perturbation is introduced yet. It is important to notice that the decay is higher for this type of perturbation, than for the error on radii: at 20% of error, Pearson's $r$ has already dropped down to very low values ($r < 0.5$) for both normal and tangential forces. This can be seen also in the maps of normal forces (Figure 3.33), which show that at 11% of error (corresponding to $r(f_n) \approx 0.7$) a change in the network is already observed, except for the main force chains close to the boundary which are still retrieved very well.

### 3.5.6 Force variability

Contact Dynamics has proven to be a powerful numerical tool for the study of frictional packings of rigid particles, characterised by force indeterminacy. Here, we use it to go a step beyond and try to quantify this indeterminacy and investigate its origin.

A first way of describing force indeterminacy is through the definition of a degree of hyperstaticity (force indeterminacy) $h$, as in Equation 2.1. It corresponds to the dimension of the null space of the contact matrix $\underline{\underline{\boldsymbol{H}}}$, as it was defined in Section 2.1.3.2. The

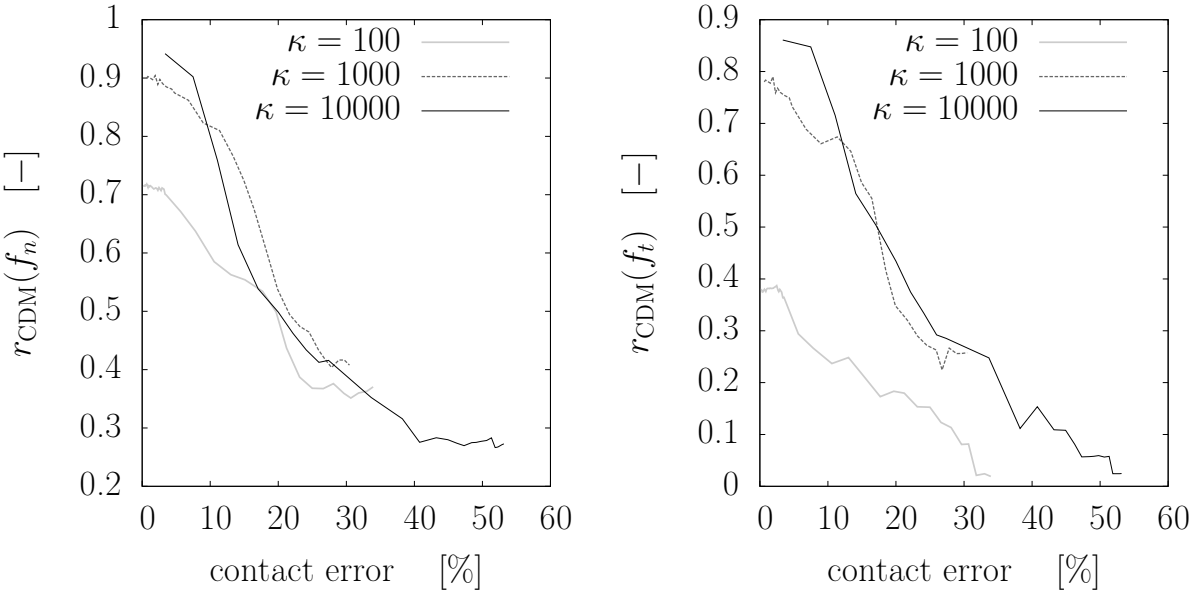


Figure 3.32 – Evolution of Pearson's $r$ for normal (left) and tangential (right) contact forces, between the real values and the ones estimated via the CDM, as the contact network is perturbed by adding random noise on the position ($x$- and $y$-coordinate) of grain mass centres.

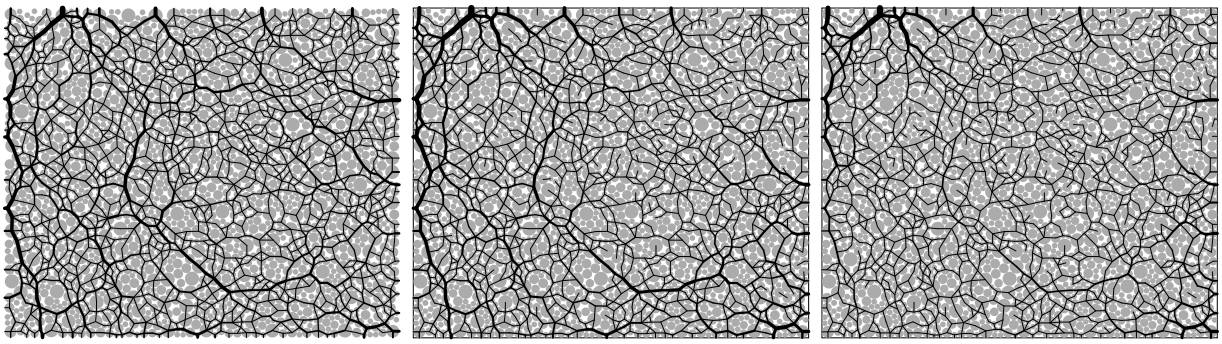

Figure 3.33 – (Left) Map of reference (MD) normal forces from an early state ($\varepsilon_{yy} \approx 0$) of a biaxial vertical compression with $\kappa = 10000$.
(Center) Map of normal forces obtained, for the same state, by applying the CDM with a 7% error on contacts with respect to the real contact network, due to perturbation on grain positions ($r(f_n) \approx 0.9$).
(Right) Map of normal forces obtained, for the same state, by applying the CDM with an error of 11% ($r(f_n) \approx 0.7$).

dimension of the kernel of $\underline{\underline{\boldsymbol{H}}}$) is the number of bases whose linear combination with an admissible contact state gives another admissible one; these bases constitute a space of self-balanced contact forces. In the limit of isostaticity, $(\dim \ker \underline{\underline{\boldsymbol{H}}}) = 0$ and the solution is unique.

An alternative and more advanced way consists in building and exploring the force ensemble $\mathcal{S}$, *i.e.*, all the possible *contact states* (sets of contact forces), and characterising it through the definition of appropriate parameters that quantify its size, and, therefore, the variability of forces.

Exploring this space can be a way of studying force indeterminacy, and its relation with the variability of contact forces. To this aim, an algorithm is required that is capable of generating a sufficient number of possible solutions. It is useful, in such a case, to work on a small system, with few contacts involved, so that this can be achieved without an excessive computational cost. Therefore, MD-DEM simulations of biaxial compression (up to a deformation $\varepsilon_{yy} = 20\%$) are carried out – with $\kappa = 100, 1000, 10000$ – on a specimen composed of 12 particles, which are simply extracted from the original specimen used in Section 3.1.

Different ways were proposed by other authors with the purpose of building the ensemble of possible contact forces. McNamara and Herrmann (2004) proposed an algorithm that locates points on the boundary of the contact state space, *i.e.*, where the number of sliding contacts equals $(\dim \ker \underline{\underline{\boldsymbol{H}}})$. Another method was adopted by Unger and Kertesz (2003); Unger et al. (2005). It consists in performing a *random walk* in the force space. The algorithm starts from a certain admissible contact state, which is then perturbed by adding random forces to the normal and tangential components; then, Contact Dynamics is applied by letting the Gauss-Seidel iterator solve the system to obtain a possibly new admissible contact state, re-fulfilling the consistency requirements (no particle interpenetration, no violation of the Coulomb condition) that are broken by the perturbation.

Among these two methods, the latter is adopted in this work. The chosen method is probably less rigorous than the one proposed by McNamara and Herrmann (2004); in particular, there is no guarantee that it weights appropriately the different regions of $\mathcal{S}$, or even that it explores all its parts (McNamara et al., 2005). However, the results obtained with the two methods are found to be similar and consistent. In particular, both methods confirmed that indeterminacy disappears in the limit of vanishing friction, as demonstrated by Roux (2000); moreover, they both get to the conclusion that the force network ensemble is a convex set. In addition to this, for a sufficiently small system it can be assumed that the random walk is capable of exploring the whole space $\mathcal{S}$, as

long as the number of generated solutions is sufficiently large; in fact, it is observed that, above a certain threshold, no new solution is generated.

Given an admissible contact state $\{f_n, f_t\}$, the random jump is performed as follows:

$$f_n^{\text{new}} = f_n + f_n^{\text{random}} \tag{3.6a}$$

$$f_t^{\text{new}} = f_t + f_t^{\text{random}} \tag{3.6b}$$

where $f_n^{\text{random}}$ and $f_t^{\text{random}}$ are chosen according to

$$f_n^{\text{random}}, f_t^{\text{random}} \in [-\lambda\langle f_n\rangle, \lambda\langle f_n\rangle] \tag{3.7}$$

The amplitude of the random walk is determined by the parameter $\lambda$. Several values have been adopted for $\lambda$, to assess its influence on the resulting force variability (based on the parameters defined in the following section); however, no significant effect is observed, so a final value of 1 is adopted for the following analyses, consistently with Unger and Kertesz (2003).

Unger and Kertesz (2003) proposed a set of parameters to characterise force variability once the space of possible forces has been built; these variables are typically defined for each contact, and then their average over all contacts (or the maximum) can be assumed as a global indicator of the variability of forces for a given granular state.

A first descriptor can be obtained by computing a variance, for a single contact $c$, of all the normal forces in the space of solution $\mathcal{S}$; this variance $\text{Var}(f_n^c)$ can then be averaged over all contacts, and normalised by the mean normal force of one solution (*e.g.*, the original MD one), in order to obtain a dimensionless parameter, that takes the following expression:

$$\mathcal{V}(f_n) = \frac{1}{N_c\langle f_n\rangle}\sum_{c=1}^{N_c}\text{Var}(f_n^c) \tag{3.8}$$

In a similar way, a range of existence can be defined, for each contact $c$, by identifying the maximum and minimum magnitude of normal forces, $f_n^{c,\max}$ and $f_n^{c,\min}$ respectively, over all the solutions in the force ensemble; then, by averaging and normalising in the same way as for the previous parameter, one gets the following expression:

$$\mathcal{R}(f_n) = \frac{1}{N_c\langle f_n\rangle}\sum_{c=1}^{N_c}(f_n^{c,\max} - f_n^{c,\min}) \tag{3.9}$$

In the same way, such parameters can be equivalently defined with respect to tan-

gential forces, for which the variability might be larger as it includes also the possibility of a change of direction, and, therefore, both positive and negative values, while normal forces are only compressive (and so positive). Other parameters can be defined with this purpose; here, however, we will only focus on the analysis of the presented ones.

It is expected that the variability of forces be somehow related with the accuracy of force estimation, as evaluated through the standard techniques (Pearson correlation above all). Therefore, forces are estimated via the CDM for the three MD-DEM simulations performed on an assembly of only 12 particles. To verify how indicative the above-mentioned parameters are for the description of the force ensemble and the quantification of its size, and confirm the expected correlations with the estimation of forces, their evolution is compared with that of Pearson's $r$ between estimated and reference normal forces for the simulation with $\kappa = 10000$.

In Figure 3.34, the amplitude of the force ensemble (*i.e.*, the variability of forces) is described through the mean normalised variance of normal and tangential forces ($\mathcal{V}(f_n)$ and $\mathcal{V}(f_t)$, respectively). Its evolution is compared to the quality of the estimated solution, and a correspondence is observed between the increase in the force variability and the decrease in the correctness of estimated forces, for both normal and tangential ones. In particular, sudden jumps in the curve describing the amplitude of $\mathcal{S}$ correspond to drops in the correlation of forces. At the same time, correlation increases when the mean normalised variances of forces decrease.

Similar results are obtained (Figure 3.35) for the mean normalised range of normal ($\mathcal{R}(f_n)$) and tangential ($\mathcal{R}(f_t)$) forces.

The usefulness of quantifying force variability has to be discussed in comparison with the information that a much more common – and easy to determine – parameter such as the degree of force indeterminacy $h$ can provide. From a qualitative point of view, a correlation between the estimation of forces (in terms of Pearson's $r$) and the indeterminacy of the system has already been observed for several applications of both the QSM and CDM; in Figures 3.36 and 3.37, this link is clearly shown, for both methods and for the estimation of both normal and tangential forces in a system with 1850 particles. In particular, the relation between $r$ and $h$ might be exponential, as suggested by the extrapolations in the figures. With the QSM, a correlation is observed both when forces are initialised to 0, as well as when the measured particle overlaps are used for a first estimation of normal forces: in this case, the final correlation of both $f_n$ and $f_t$ is $\approx 1$, but still a slight decay is observed for high values of $h$.

However, to observe a clear correlation between $r$ and $h$, a wide range of $h$ needs to be investigated; if we focus on a single simulation, for which $h$ oscillates in a smaller range,

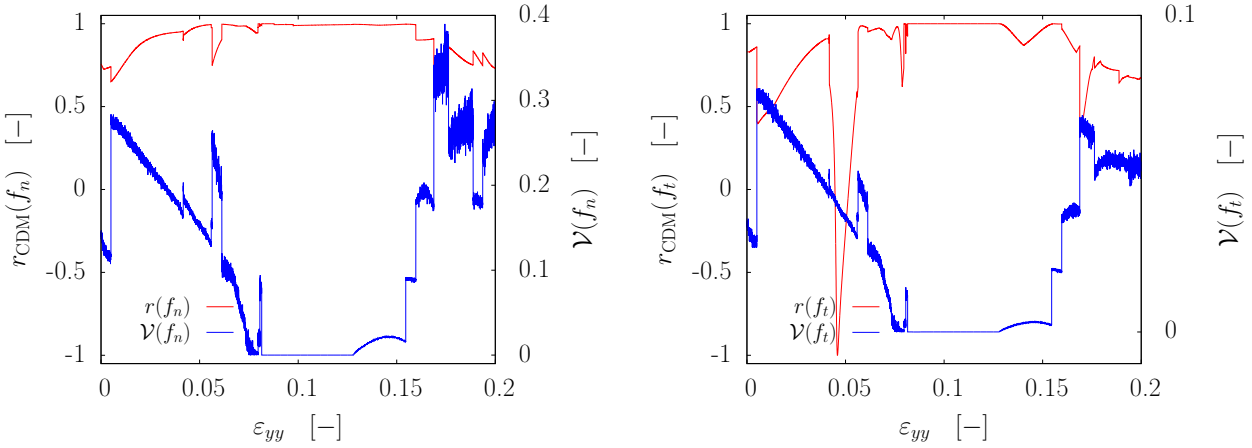


Figure 3.34 – Evolution of the mean normalised variance of normal (left) and tangential (right) forces, compared with the evolution of Pearson's $r$ between normal (left) and tangential (right) forces estimated through the CDM and reference ones, for an MD simulation of a small system (12 particles, $\kappa = 100$).

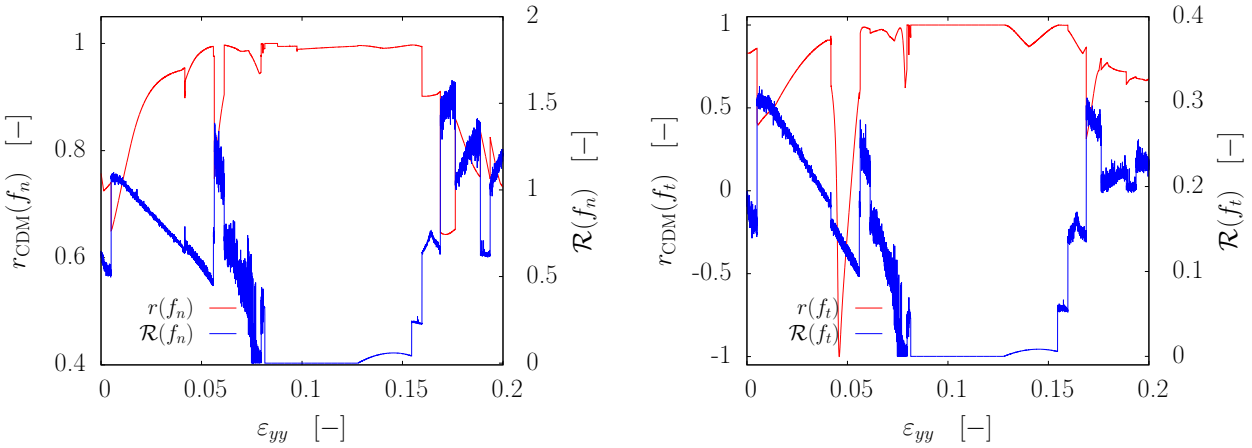


Figure 3.35 – Evolution of the mean normalised range of normal (left) and tangential (right) forces, compared with the evolution of Pearson's $r$ between normal (left) and tangential (right) forces estimated through the CDM and reference ones, for an MD simulation of a small system (12 particles, $\kappa = 100$).

we see that its evolution does not reflect the evolution of $r$ (Figure 3.38). Therefore, $h$ cannot properly describe – and predict – the correctness of the estimation of forces through the CDM, which is more directly related to the size of the force space and its quantification via the parameters previously proposed.

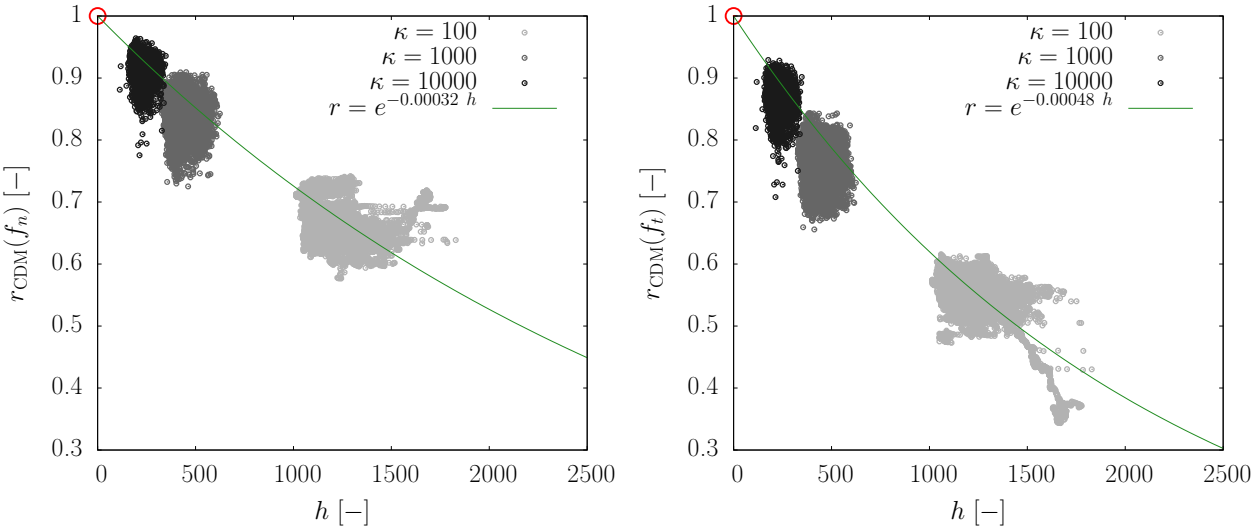


Figure 3.36 – Evolution of the degree of force indeterminacy $h$ with Pearson's $r$ on CDM-estimated normal and tangential forces, for the three MD simulations with 1850 particles. The curves suggest a possible exponential extrapolation.

Force variability, if properly quantified through appropriate parameters, can – better and more completely than the degree of force indeterminacy – explain the variation in the quality of force estimation. This is particularly clear for high values of $r$: having an $r$ that approaches 1 presupposes that the variability is relatively low.

## 3.6 Concluding remarks

Some partial conclusions can be outlined by comparing the main results of the application of the three force estimation methods to numerical data.

With the Contact Elasticity Method, a good estimation of forces proves to be dependent on two main aspects. Normal forces can be perfectly retrieved by simply measuring particle interpenetrations; with a view to the experimental application, however, this requires the definition of some appropriate microscale quantities that can suitably describe contact deflection. An estimation of normal forces based on an incremental law, exploiting measurements of contact relative displacements, seems to be less accurate, due to changes in the contact orientations when rearrangements occur. In this case, the frequency of data acquisition plays a crucial role, as it does for tangential forces: in both

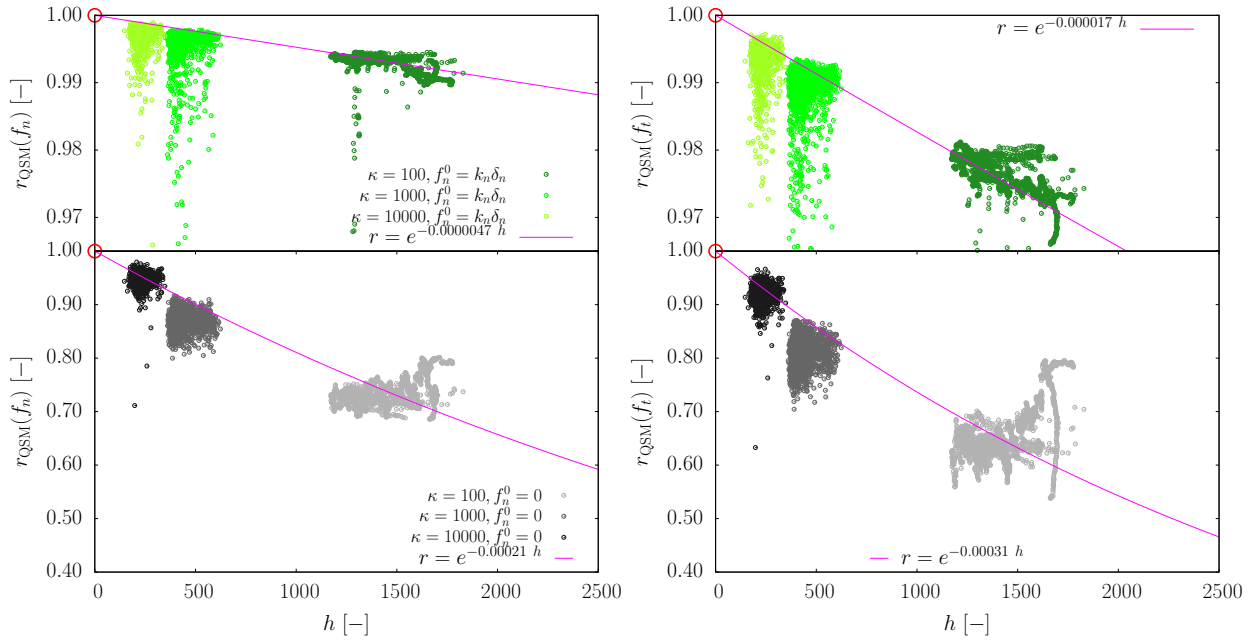


Figure 3.37 – Evolution of the degree of force indeterminacy $h$ with Pearson's $r$ on QSM-estimated normal and tangential forces, for the three MD simulations with 1850 particles. The curves suggest a possible exponential extrapolation.

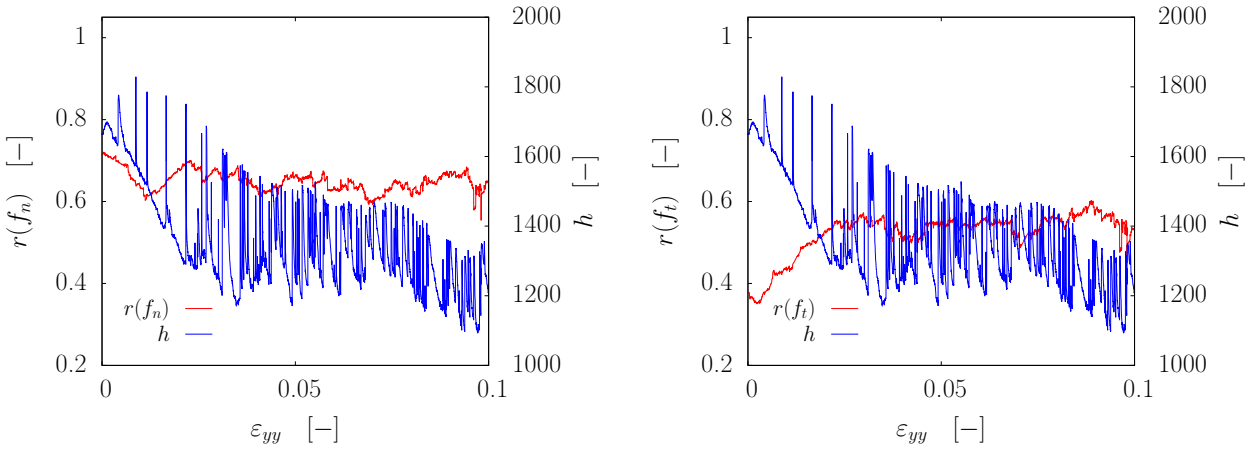


Figure 3.38 – Evolution of the degree of force indeterminacy $h$, compared with the evolution of Pearson's $r$ between normal (left) and tangential (right) forces estimated through the CDM and real ones, for an MD-DEM simulation with 1850 particles and $\kappa = 100$.

cases, by reducing the loss of displacement history between consecutive states, forces can be determined from normal and tangential relative displacements with a higher accuracy.

Unlike the other two methods, the estimation of forces through the CEM shows no considerable difference with respect to the main geometric properties of a granular packing, *e.g.*, density and coordination number. In particular, by taking into account the history of the packing, the CEM can provide a uniquely determined solution: force indeterminacy is not an issue for this method.

However, basing the determination of forces on the knowledge of the history of the system also results in one of the main weaknesses of the method. In the way it is built, the CEM cannot retrieve the initial forces in an equilibrium state of a packing if no information is given on the previous displacement history. This is a strong limitation, in particular from the point of view of the final aim of this force estimation method, *i.e.*, the experimental application: it can only provide an approximation of force increments from a given configuration, while all forces previously transmitted between particles are lost. In order to have a realistic estimation with the CEM (neglecting other possible sources of inaccuracy), the initial state should be as close to the unloaded state as possible.

As it was already shown in Chapter 2, the two other techniques – the Quasi-Static Method and the Contact Dynamics-based Method – have several common features. First, they both simply require the knowledge of the contact network and boundary conditions to provide an estimation of forces. Due to this, a solution can be determined also for an initial state, for which no previous displacement is known.

At the same time, the result of neglecting the history of the packing is that the obtained solution, while still admissible, may be far from the "correct" one. However, it is shown that the variability of forces can be reduced, and almost removed, if contact elasticity is re-introduced to provide a first estimation of normal forces. In particular, the QSM proves very prone to exploit a first approximation of normal forces as an initial guess: then, through the regular iterative procedure of double projection, it is expected to retrieve a very accurate set of forces, independently of the degree of force indeterminacy of the system (when no other source of inaccuracy, *i.e.*, measurement error, is considered).

For the CDM, the simple initialisation of forces to a guess solution in which normal forces are determined through the assumption of contact elasticity is not sufficient to retrieve the unique solution in terms of normal and tangential forces, among the set of possible ones, that corresponds to the original one. To do so, a part of the forces have to be fixed to constant values, while the remaining ones are determined by numerically

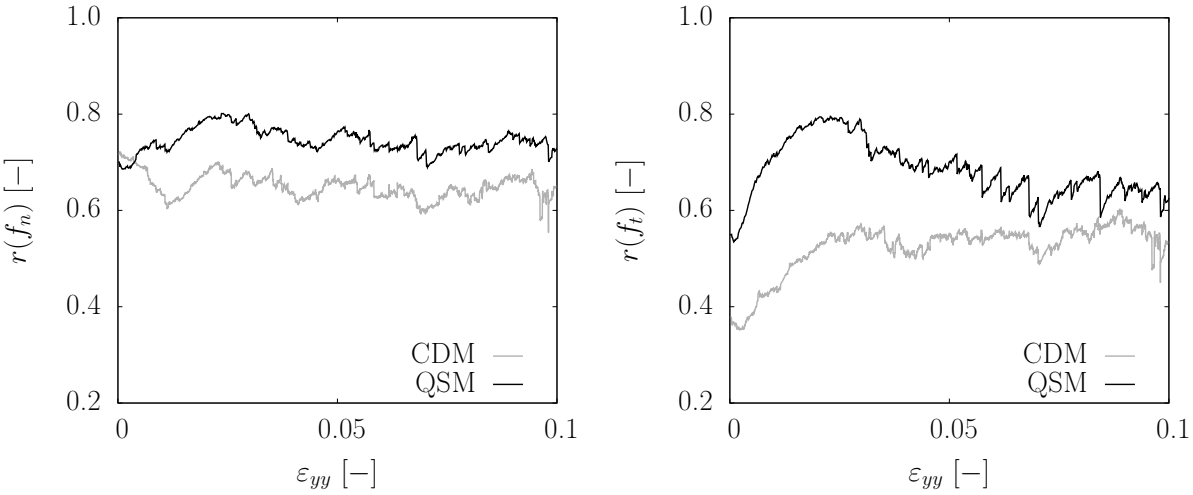


Figure 3.39 – Evolution of Pearson's $r$ for normal (left) and tangential (right) forces, between the reference set of forces (MD simulation, $\kappa = 100$) and, respectively, the CDM solution and the QSM one, when (almost) null normal forces are used as an initial guess for both methods.

solving the problem through the Gauss-Seidel iterator. However, this obviously requires the initial guess to be correct, in terms of normal forces; for the QSM, on the other hand, the initial guess can be obtained as a simple approximation, and then the iterative procedure of double projection is likely to provide a more realistic solution.

This might make the QSM preferable to the CDM; however, this potentiality of the method is strongly dependent on the capability of making a sufficiently realistic approximation of normal forces based on contact elasticity assumptions and measurements of contact-scale kinematic variables, which will be discussed in Chapter 4.

If a comparison is carried out between the results of the two methods when they both use a set of null (or almost null) normal and tangential forces for the initial guess, a comparable accuracy is retrieved for the estimated forces between the two methods (Figure 3.39). The QSM shows the same behaviour as the CDM, and also the dependence on the degree of force indeterminacy is retrieved. In conclusion, the QSM only works better when the correct normal forces are used as an initial guess; when the initial guess on normal forces is far from the original solution, it can still get closer to the reference solution than the CDM (as shown in Section 3.2), but in general it behaves similarly to the CDM, being its result strongly affected by $h$.

A deeper study conducted on force indeterminacy by building the force space and quantifying its size has allowed a characterisation of the variability of forces. This has shown a correspondence between the result of force estimation through the CDM and the amplitude of the force ensemble, that can prove very useful: in this way, the non-

uniqueness of Contact Dynamics solution can be characterised, and its influence on the estimation of forces predicted.

The QSM and CDM have also been assessed with respect to measurement inaccuracy, to reproduce a typical condition of experiments and try to predict the influence of such an error. This study completes the validation of the methods by testing their applicability to non-ideal data. In general, the solution they obtain is not much affected by this perturbation, as long as it stays relatively limited; the main error still seems to come from the variability of forces. The CDM shows a slightly higher robustness with respect to the introduced perturbation, specifically for the case in which the measurement error globally results in a loss of contacts, due to its capability of treating grain rearrangements by applying accelerations on particles.

In general, each of the methods has shown some strong and weak points. A combined use of them might represent a strategy to exploit their advantages and improve their results. For instance, the CEM is the approach that exploits the most information on past history, contained in the measured displacements. Provided that the measurements are made with a sufficiently high motion resolution, it can exploit contact elasticity to provide the most realistic estimation of normal forces. Tangential forces, on the other hand, are more difficult to estimate with the CEM. However, if a first estimate is available for normal forces, it can be used as an initial guess in the other two methods: in this way, history is re-injected, and both methods can benefit from this by approaching the correct solutions, among all the admissible solutions they can potentially reach. Moreover, the QSM and CDM can also be considered somehow complementary: despite some common points in their formulations and results, their different nature should not be forgotten. The QSM has proven very powerful for the treatment of static equilibrium states, for which it is built, but it cannot deal with dynamic events including intense grain rearrangements. The CDM, on the other hand, due to its formulation can treat both cases.

It should be recalled that an estimation of forces, to be relevant for experimental applications, should be as accurate as possible; often, even if a solution is admissible with respect to the particular criteria of either method, it might not be a good estimate. However, even in these cases some interesting features might be observed: typically, the strong network is systematically retrieved with a better accuracy than the weak network, as it is shown for a CDM application in Figure 3.40 (but the same result is observed with the QSM); more generally, global features such as force statistics can be deduced even if the single values might not be precise.

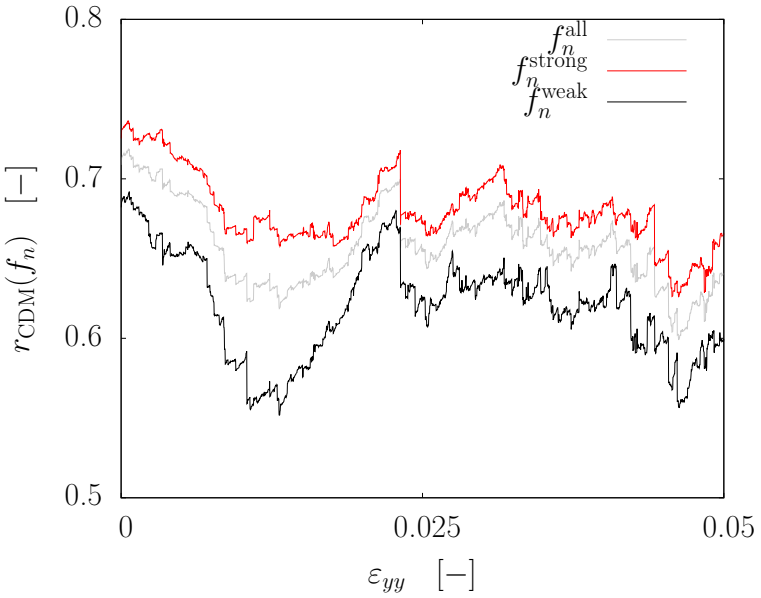


Figure 3.40 – Evolution of Pearson's $r$ of CDM-estimated normal forces for the MD-DEM simulation with $\kappa = 100$. $r$ is separately computed for the strong and weak force network.

# Chapter 4

# Contact force estimation from experiments

In this Chapter, the three methods presented in Chapter 2 are applied to the estimation of forces in real experiments. The experimental campaign is described in Section 4.1; then, force estimation is performed and its results are shown in Section 4.2.

## 4.1 Experimental campaign

The experimental campaign has been performed in Laboratoire 3SR, Grenoble. The granular material involved in the experiments is described in Section 4.1.1, and a focus on the behaviour under compression of a pair of grains in contact is made in Section 4.1.1.1. The experiments are carried out by means of the $1\gamma2\varepsilon$ shearing device (Section 4.1.2); they include several kinds of tests, such as isotropic compression (Section 4.1.3.1), biaxial vertical (Section 4.1.3.2) and horizontal (Section 4.1.3.3) compression, simple shear (Section 4.1.3.4) and oedometer compression (Section 4.1.3.5).

Section 4.1.4 focuses on the measurement of particle-scale kinematics performed during each test. The main features of image acquisition and image processing are given; some reference is made on the Digital Image Correlation algorithm that is adopted (which is detailed elsewhere), and the measurement accuracy it provides.

Some preliminary results from the analysis of measured kinematic fields are presented in Section 4.1.5; in particular, the focus is on contact orientation and kinematic quantities that are defined for the description of the contact-scale deformation.

### 4.1.1 Granular material

For this doctoral work, the experimental campaign is performed on an assembly of around 1850 cylindrical rods made of ash wood, having an elastic modulus $E = 12$ GPa and a Poisson ratio $\nu \approx 0.4$ (which can vary depending on the direction). Based on these material parameters, an estimation of the stiffness level $\kappa$ can be performed. This is particularly useful for comparison with the numerical simulations described in Section 3.1. For a mean pressure $p = 100$ kPa, $\kappa \approx 500$ is obtained.

As to the parameters describing particle interactions at contact, appropriate tests have been performed in this doctoral work. A simple test for the determination of the interparticle friction coefficient $\mu$ is described in Appendix B, while a first assessment of the contact normal stiffness $k_n$ is made by means of a compression test on a single contact between two rods in Section 4.1.1.1, although a re-scaling procedure can be alternatively used to determine it, as explained in Section 3.3. As to the tangential stiffness at the contact $k_t$, its determination is more challenging, and some assumptions can be done on its value with respect to $k_n$ (*e.g.*, it can be assumed that $k_t/k_n = 1$).

The assembly is polydisperse. The rods, all with a circular section and a length of 6 cm to match the depth of the machine, have four different diameters: 8, 12, 14 and 20 mm. The size distribution is reported in Table 4.1. With a mass per unit volume of approximately 730 kg/m$^3$, the average mass of a rod is 4.8 g.

Granular sample

| Diameter | | | | No. of rods |
|---|---|---|---|---|
| Nominal [mm] | Ratio | Mean [mm] | Std. deviation [mm] | |
| 8 | 0.4 | 7.926 | 0.106 | 798 |
| 12 | 0.6 | 11.998 | 0.127 | 426 |
| 14 | 0.7 | 14.027 | 0.102 | 406 |
| 20 | 1.0 | 19.978 | 0.256 | 220 |

Table 4.1 – Distribution of the number of rods for each category of grain diameter. Actual values have been measured by means of a calliper on around 20 rods for each of the four diameters, and their mean and standard deviation is reported.

The measurement of rods diameter for each of the four category shows that there is a certain variability in the size of rods. Diameters slightly deviate from the nominal ones, as reported in Table 4.1. However, this deviation does not represent an issue since the

resolution of photographs is sufficient to detect these oscillations, and diameters can be measured again directly from the images with a higher accuracy than that of manual measurements.

At the same time, the measurement of rods diameters has the purpose of verifying the circularity of rods sections. A maximum and a minimum diameter are detected, generally with a difference of around 0.1 mm (*i.e.*, $\approx$ 1% of the diameter). This may be related to manufacturing imperfections, as well as to the occurrence of small plastic deformations after having performed a number of tests on these rods. This imperfection is one of the main sources of inaccuracy in the measurements performed on images of the assembly; in particular, it affects the detection of contacts.

The procedure that is adopted for building the specimen consists in preparing sets of 26 grains, with a fixed number of grains for each size (3, 6, 6 and 11, respectively), and manually placing these sets one by one inside the frame, so that a rather homogeneous-in-space grading is obtained, to avoid zones with different density, as far as possible.

In order to correlate an internal subset of pixels for each grain between two pictures of the specimen (see Section 4.1.4.2), a unique black-and-white pattern is applied on their visible face (Figure 4.17). The procedure consists in lightly scratching a toothbrush on which black and white paint were alternatively applied. This generates small dots of the two colours. Differently from other tests involving softer materials (rubber), here the paint does not have to be particularly elastic, as very small deformations are expected for the given material stiffness and loading conditions.

#### 4.1.1.1 Normal compression on two particles

Since the objective of this work is the determination of contact forces, the main focus, when testing this granular material, is on the behaviour at the contact-scale. Therefore, in a first stage we study this response by carrying out a normal compression test on a pair of grains.

The test is performed by applying a vertical loading that is transmitted to the grains by means of two aluminium plates with a thickness of 12 mm (as in Figure 4.2). The two grains are placed on top of each other, so that the direction of load application corresponds to the branch vector linking the grain mass centres – and so to the normal at the contact. In this way, it can be assumed that no tangential force is applied, and the whole force applied by the loading system – measured by a force sensor – is a contact normal force. To guarantee the stability of the whole set-up, grains are cut along a horizontal plane – on the opposite side with respect to the grain-grain contact – so that they match with the aluminium plates, rather than having a line as a grain-plate contact.

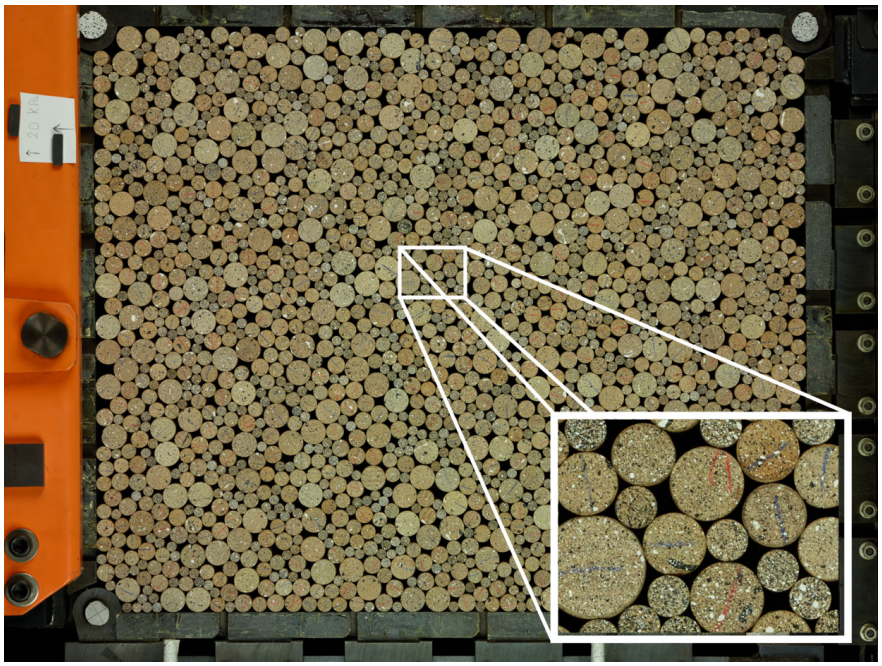

Figure 4.1 – Image of an isotropically compressed specimen in the $1\gamma 2\varepsilon$ device, with zoom on a small amount of grains to show the speckle pattern on their visible face. The frame measures 556 mm $\times$ 459 mm.

80 Mpixel photographs are taken throughout the application of the loading. Then, between consecutive photographs, the evolution of the length of the vector linking the two mass centres is determined by means of the software TRACKER (Combe and Richefeu, 2013), that applies Particle Image Tracking, a DIC-based technique to measure the rigid-body motion of grains. Assuming that the change in length of the branch vector perfectly corresponds to a contact relative displacement in the normal direction, the force-displacement response is determined (Figure 4.2), showing a rather bi-linear relationship.

After reaching the highest force measurable by the force sensor, the system is unloaded and then reloaded, and photographs are taken again. The non-correspondence of the loading and re-loading branches is the sign of an anelastic behaviour; it also means that different slopes are observed, for a same contact, in two consecutive loading phases. This situation is very common in experiments, since contacts may often undergo phases of alternate loading and unloading.

Considering this response, a unique value of $k_n$ cannot be easily determined. One predominant slope can be identified for forces above a certain threshold; we can define it as the mean between the slopes of the two loading curves. A value of $k_n = 1.09 \times 10^7$ N/m is obtained, given the m/pixel scale of the photograph.

The range of interest for the tests considered here, however, also include a part of the curve in which this slope does not apply: the average normal force is estimated, for a pressure $p = 100$ kPa, as $\approx 70$ N. Three force-displacement increment points estimated with the CEM for load steps $0-50$, $0-100$ and $0-200$ kPa of an oedometer test are shown in Figure 4.2, to show a typical range of values. Force increments and displacement increments are computed as the average of only positive values (those generating an increase in the force). Based on these considerations, the value of $k_n$ will be determined, for the use of CEM and QSM, through a re-scaling procedure equivalent to the one explained in Chapter 3, *i.e.*, by fitting the homogenised stress components to measured macroscopic stress components.

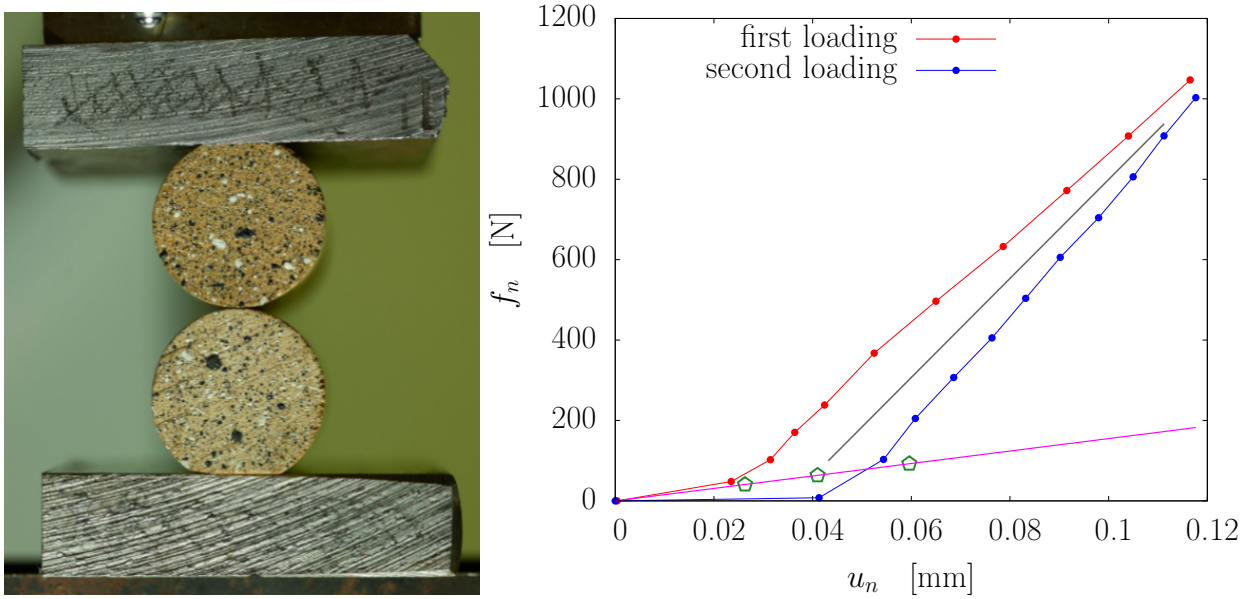


Figure 4.2 – Image of the loading system for the compression test on a pair of grains in contact (left), with plot of the normal force-displacement response (right) for two consecutive applications of the loading. The two lines represent possible approximations of a contact normal stiffness $k_n$ for different ranges of $f_n$. The three points fit by the magenta line represent three average normal force and displacement increments, determined with the CEM force law, for three different loading windows of an oedometer compression test.

Given the high resolution of the photographs, in particular with respect to the limited dimension of the system, an attempt is made to assess the strain level at the grain-scale. The software 7D (Vacher et al., 1999) is employed with this purpose. This software computes strains by means of a DIC technique. In the application to a 2D case, a grid of points is defined inside the body whose deformation is investigated; then, a pattern is determined around each point of the grid so that a mesh, whose deformation is assessed

by comparison of two pictures, is created. In this way, the Green-Lagrange strain tensor is fully determined.

In Figure 4.3, a map of the vertical strain $\varepsilon_{yy}$ is drawn. This strain component, which is the prevalent one given the loading conditions, appears to be clearly concentrated in a small area of the two grains around the contact point, leaving all the rest of the grain practically undeformed.

This corroborates two important assumptions of this work. Particle motion can be determined as a rigid-body motion, confirming the suitability of the software TRACKER for such measurements. In terms of force estimation, this confirms the description of particle interactions based on a rigid-body assumption, which characterises all the three methods proposed (despite differences in the treatment of contact behaviour).

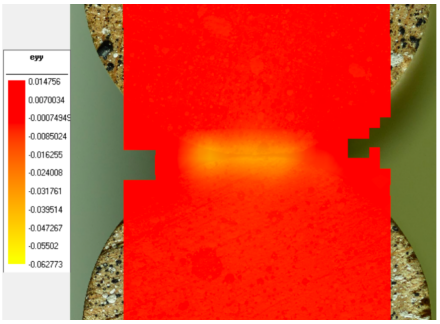


Figure 4.3 – Map of the vertical strain $\varepsilon_{yy}$ obtained from the software 7D (Vacher et al., 1999) for the compression test on a pair of grains.

### 4.1.2 The $1\gamma2\varepsilon$ device

The idea of creating a model of granular materials by using a 2D configuration dates back to the pioneering work by Schneebeli (1956, 1957). It is based on the recognition that most theoretical soil mechanics problems are approached in a 2D scheme. Experiments started to be performed on packings of cylindrical rods with a constant length, that was typically set to 6 cm, while the diameter variability controls the size distribution of the material. Polidispersity is introduced to try to reproduce realistic size distributions.

Based on this approach, a rather unique machine was built in Laboratoire 3SR, Grenoble, named $1\gamma2\varepsilon$, whose working principles are thoroughly described elsewhere (Joer et al., 1992; Calvetti et al., 1997). This device allows a roller stack to be subjected to general 2D loading conditions, by independently controlling the components of the macroscopic strain tensor, *i.e.*, deformations along vertical and horizontal axes ($\varepsilon_{yy}$ and $\varepsilon_{xx}$, respectively), and shear strain $\gamma$, hence the name of the machine.

The biaxial conditions are obtained as no loading is applied along the third direction (the one perpendicular to the plane in which the machine is built). Plane strain conditions are typically reproducible, as strains in the third direction can generally be neglected, especially for materials with a low compressibility.

The machine essentially operates in strain-controlled conditions; a system of 5 motors is adopted for the adjustment of the four wall lengths, that range between 560 mm and 670 mm, for the top and bottom one, and between 420 mm and 540 mm for the lateral ones (Figure 4.5). Velocities can be imposed on each motor independently of the others.

Strain-gauged hinges measure the forces in three of the four corners (O, B and C in Figure 4.4); the force in the last corner (A) can be deduced given the equilibrium of the frame. Only the position of point O is fixed during the frame deformation.

Stress at the boundary can be computed throughout the test from the measured forces in the corners. Based on this, the motor velocities can be imposed in order to satisfy any possible stress condition, thus allowing also stress-controlled tests.

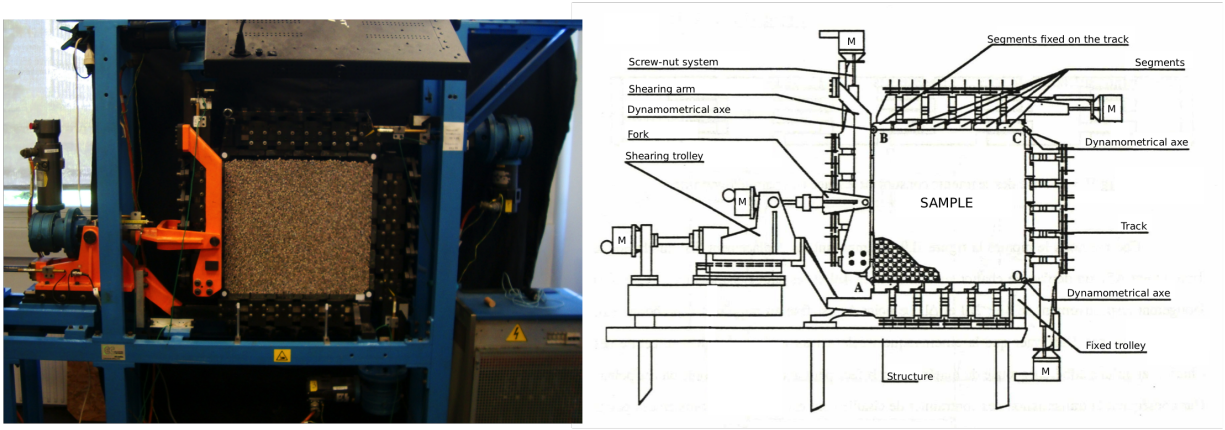


Figure 4.4 – Image of the $1\gamma 2\varepsilon$ device (left), with a sketch to illustrate the main components (right).

The machine is open on two sides, allowing photographs to be taken on one of these two sides (Figure 4.1).

By capturing the visible face of the specimen, the capability of accessing the particle scale depends on a combination between the resolution of the picture and the grain size (diameter of the cylindrical rods). For the granulometry described in Section 4.1.1, particles can be individually localised and tracked, and so a full grain-scale characterisation can be carried out, including the definition of granular fabric (particle positions, contact locations and orientations), based on which structural anisotropy can be described, and particle kinematics (displacements and rotation).

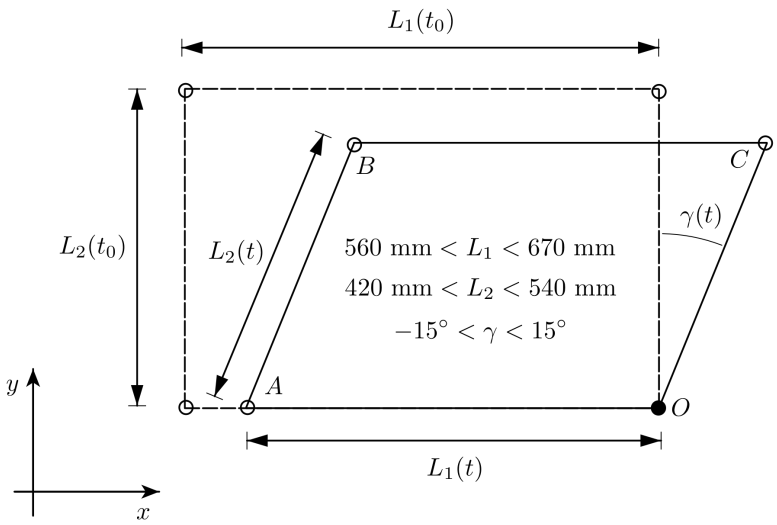


Figure 4.5 – Working principle of the apparatus with definition of the geometrical constraints.

### 4.1.3 Tests

In this Section, the tests that are carried out in the frame of this doctoral work are briefly presented, including isotropic compression, biaxial vertical and horizontal compression, simple shear and oedometer compression. Only few comments will be done on the grain-scale kinematics, since it is not the main objective of this work.

#### 4.1.3.1 Isotropic compression

A set of isotropic compression tests is performed on an assembly starting from an initial void ratio $e_0 = 0.257$. The procedure includes a first phase in which the assembly is confined with an isotropic stress state ($p = 20$ kPa) and a second phase in which stress increments of 20 kPa are applied for both $\sigma_{yy}$ (vertical normal stress) and $\sigma_{xx}$ (horizontal normal stress). The way a certain stress condition is approached by the machine, when both vertical and horizontal normal stress are controlled, consists in first reaching the desired vertical normal stress by imposing a constant velocity $v = 0.1$ mm/s to the top wall, and then keeping this stress constant while the horizontal normal stress is adjusted by applying the same velocity on the lateral walls. This explains why vertical deformations are generally higher than horizontal ones, along the test (Figure 4.7): the horizontal stress is already slightly increased when moving the top wall (while the lateral ones are fixed); then, lateral walls are moved in order to reach the same horizontal stress as the vertical one, but this requires a smaller deformation. However, this has no particular influence on the mechanical behaviour, as the load increments are relatively small. At the end of each increment, the load is kept constant as a photograph of the assembly is taken; in this way, it is possible to link a stress state with the corresponding granular arrangement.

Cyclic loading conditions are applied in all the isotropic tests (Figure 4.6). This has the objective of enhancing the data set, providing more geometrical configurations of the assembly for the analyses (micro-macro observations, force estimation), as the machine is rather limited in the range of applicable stresses – a maximum stress of $\approx 300$ kPa can be reached with the current force sensors.

Additional macromechanical observations can be made by analysing strain plots. It is observed (Figure 4.7) that part of the deformation is not recovered as the unloading phase is completed (from 200 kPa back to 20 kPa), especially concerning the first loading cycle; this indicates the apparition of some plastic behaviour that is probably related to rearrangements of grains. While in the following cycles this observation is not retrieved, by analysing the stress-strain curve for one of these cycles (Figure 4.7) we still observe

some hysteretic behaviour that is typical of dissipative phenomena (in this case, such a dissipation is linked to the friction between particles).

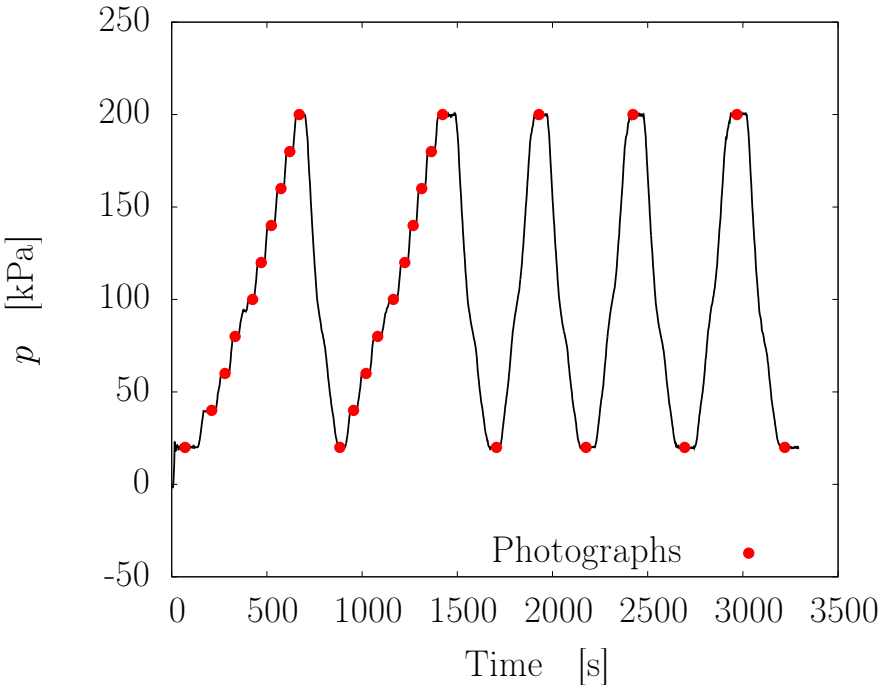


Figure 4.6 – Evolution with time of pressure, in one of the isotropic compression tests. The first two loading cycles are conducted by steps of 20 kPa, while the last three have no intermediate step. Each red dot corresponds to the shooting of a photograph.

#### 4.1.3.2 Biaxial vertical compression

A biaxial vertical compression test is carried out by imposing a downward motion to the top wall of the machine. The specimen is originally confined with a mean pressure $p = 100$ kPa; the corresponding void ratio obtained is For all the tests, the initial void ratio $e_0$ is around $e_0 = 0.220$. Then, a constant velocity $v = 0.01$ mm/s is applied to the top wall, while the movement of the lateral ones are adjusted so that the horizontal normal stress remains constant at the value of 100 kPa.

The mechanical response is shown in Figure 4.8. Two sudden drops in the vertical normal stress, probably due to large granular rearrangements, can be observed for vertical strains $\approx 0.1$ and $\approx 0.7$, as well as in the corresponding volumetric deformation curve. The material reaches a quite early plateau in the stress-strain curve; it appears to behave as a loose one, although the evolution of the volumetric deformation shows a clear distinction between a first contractant phase and a second dilatant one, typical of dense granular material behaviour. However, the rather small deformation attained

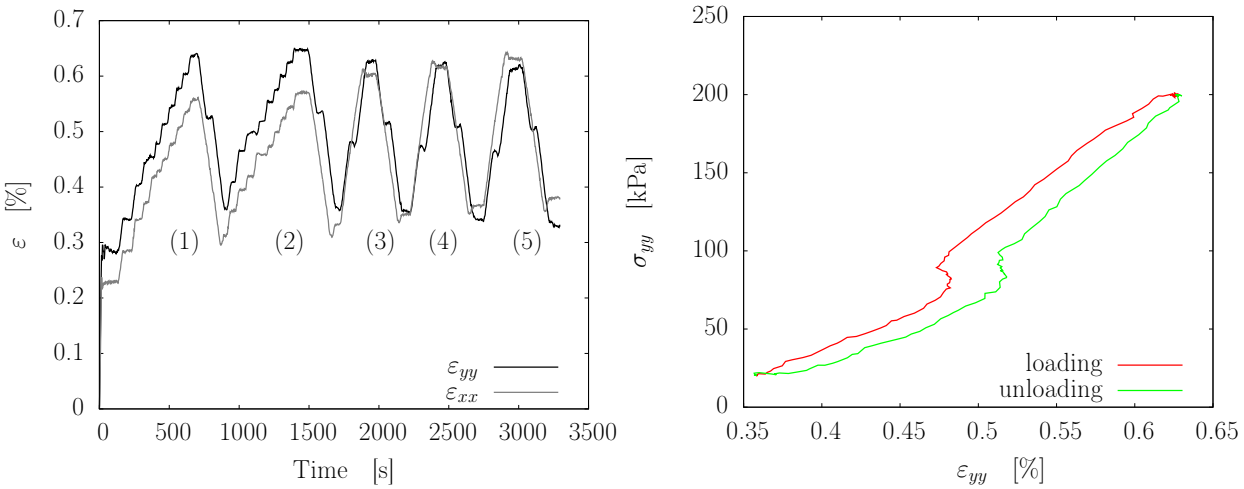


Figure 4.7 – (Left) Evolution with time of the vertical and horizontal strains ($\varepsilon_{yy}$ and $\varepsilon_{xx}$, respectively), in one of the isotropic compression tests. (Right) Stress-strain plot for the third cycle of the test.
Strain components are defined as $\varepsilon_{xx} = \Delta L_1(t)/L_1(t_0)$, $\varepsilon_{yy} = \Delta L_2(t)/L_2(t_0)$.

and the relatively low number of grains composing the assembly do not allow deeper reflections on the material response.

The main geometrical properties of the assembly are also determined, and shown in Figure 4.9. The volumetric response is defined through the void ratio $e = V_v/V_s$, as the ratio between the volume (surface) occupied by voids $V_v$ and the volume (surface) occupied by the rods $V_s$. The contact network is described by two geometric quantities: the degree of force indeterminacy – or degree of hyperstaticity – $h$, defined by Equation 2.1, and the coordination number $z$, as in Equation 3.2. More details on the detection of contacts will be given in Section 4.1.4.1.

Figure 4.9 shows that the evolution of such geometric quantities is related to the volumetric response: when the specimen contracts, there is a slight increase in the coordination of the assembly, and, consequently, in the degree of force indeterminacy. On the other hand, the dilatant phase that the specimen undergoes after $\varepsilon_{yy} \approx 0.005$ results in a loss of contacts, and so in a decrease of $z$ (and of $h$, consequently).

Differently from the isotropic compression test, pictures of the assembly are taken with a constant time step (5 $s$) during the whole test. The same time step is adopted also for the tests presented in the following sections (biaxial horizontal compression, simple shear, oedometer compression).

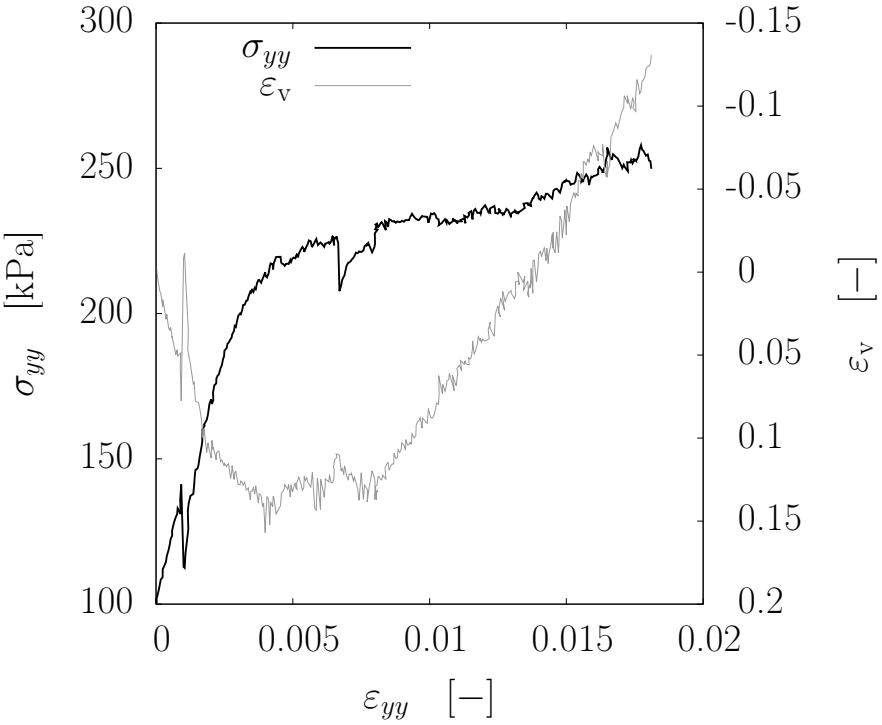


Figure 4.8 – Plot of the stress-strain curve (black) and evolution of the volumetric deformation (gray) for the biaxial vertical compression test.

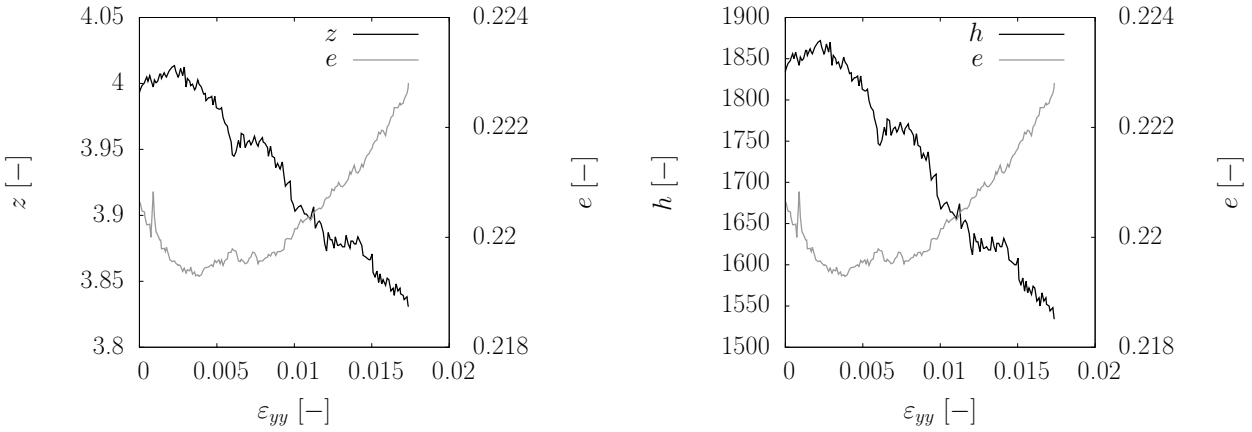


Figure 4.9 – Plot of the evolution of the main geometric properties during the biaxial vertical compression test: void ratio $e$, coordination number $z$ (left) and degree of force indeterminacy $h$ (right).

#### 4.1.3.3 Biaxial horizontal compression

After the end of the biaxial vertical compression test, a similar test is started with compression in the horizontal direction, using the same specimen, without any shaking or rearrangement of the assembly. Before starting the new test, the sample is brought back to an isotropic loading condition with $p = 100$ kPa, to start the test in the same conditions as the previous one, *i.e.*, with a distribution of contacts as homogeneous as possible. Then, the two lateral walls are moved inward, each with a constant velocity $v = 0.02$ mm/s.

Some mechanical feature can be inferred from the stress-strain and volumetric strain plot in Figure 4.10. Comparing the mechanical response with that of the vertical compression, it can be immediately noticed that the initial stiffness is lower in this case. Remarks can be made only with respect to the final stress reached during the test, slightly lower than the strength shown by the vertical compression test; however, the fact of not reaching a significant level of deformation prevents us from concluding on this, as the stress-strain curve does not show any plateau or softening branch for the attained deformation.

Similarly to the vertical compression test, the evolution of volumetric strain consists of two clearly distinct phases: a first one in which the material shows a contractant behaviour, and a second one in which the tendency is inverted as it becomes dilatant. In Figure 4.11, the same anti-correlation is shown between the void ratio and the coordination (force indeterminacy) of the assembly.

#### 4.1.3.4 Simple shear

The two biaxial compression tests are followed by a simple shear test (still on the same specimen). Similarly to the previous two tests, first an isotropic loading condition is reached, with $p = 100$ kPa, and then the specimen is sheared by forcing the top face to slide laterally, with a constant velocity $v = 0.02$ mm/s. The angle of deformation $\gamma$ between contiguous faces is measured and used as a reference for the macroscopic mechanical analysis.

In Figure 4.12, the stress-strain curve shows some peculiar features. A first branch, characterised by a relatively high stiffness, is followed by a small plateau for $\tau_{xy} \approx 22$ kPa, and then by a further hardening that brings the stress up to $\tau_{xy} \approx 34$ kPa; this value is finally maintained constant as the angle of deformation increases.

Differently from the biaxial vertical and horizontal compression, here the volumetric behaviour shows a tendency to dilate from the very beginning of the test. This cannot

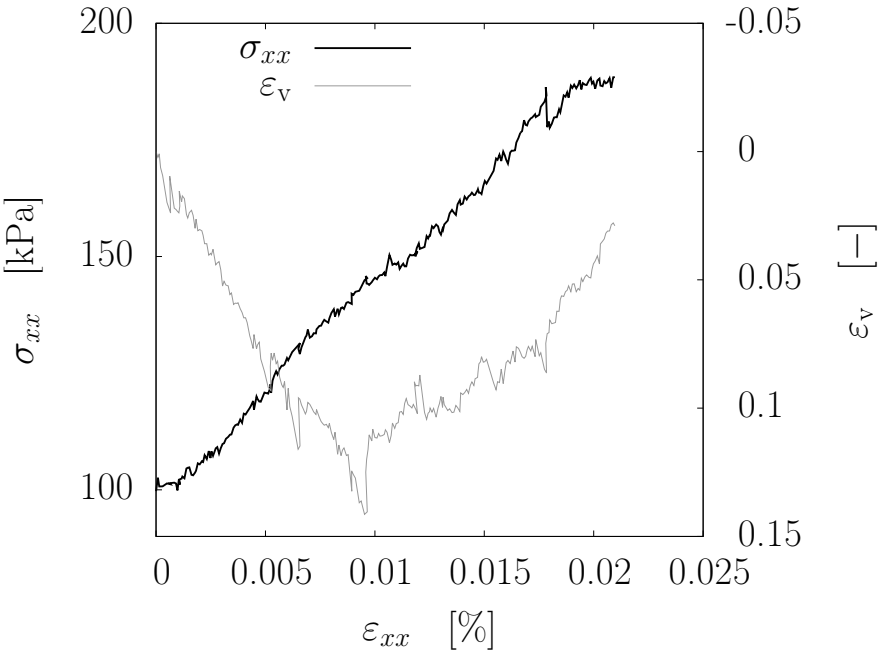


Figure 4.10 – Plot of the stress-strain curve (black) and evolution of the volumetric deformation (gray) for the biaxial horizontal compression test.

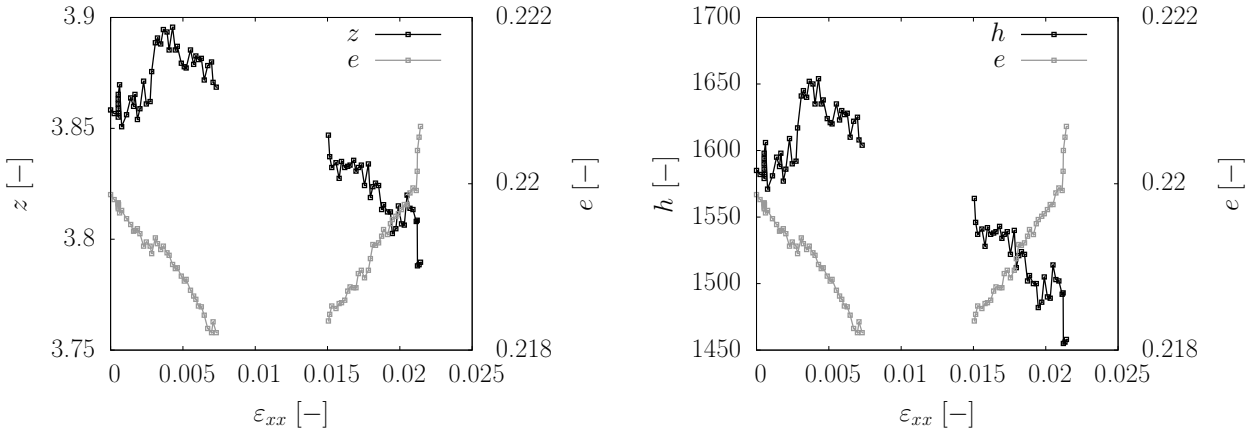


Figure 4.11 – Plot of the evolution of the main geometric properties during the biaxial horizontal compression test: void ratio $e$, coordination number $z$ (left) and degree of force indeterminacy $h$ (right). No photograph is available between $\varepsilon_{yy} = 0.007$ and $\varepsilon_{yy} = 0.015$.

be related to a clear difference in the initial density of the material, since the initial void ratio $e_0$ is practically the same in the three tests.

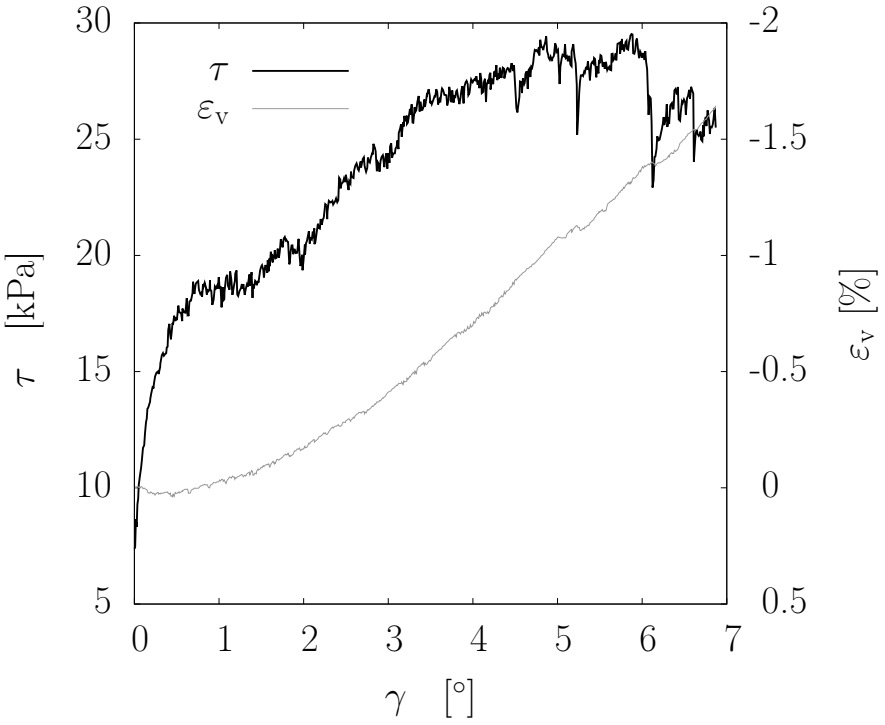


Figure 4.12 – Plot of the stress-strain curve (black) and evolution of the volumetric deformation (gray) for the simple shear test.

#### 4.1.3.5 Oedometer compression

A two-cycles oedometer compression test is carried out on an assembly with an initial void ratio $e_0 = 0.278$. The loading is applied by imposing a downward constant velocity $v = 0.005$ mm/s to the top face of the machine, while keeping the two lateral ones fixed, so that no lateral deformation can occur. The loading phase is stopped as the vertical normal stress $\sigma_{yy}$ reaches the value of 200 kPa, and followed by an unloading phase; two such loading cycles are performed.

Since the oedometer compression test recreates the lithostatic stress conditions in natural soils, with no lateral deformation occurring, this test is typically used to determine the coefficient of earth pressure at rest $k_0$, defined as the ratio between the horizontal and vertical normal stresses. For natural soils, this value is a function of the degree of overconsolidation of the material, and it typically ranges between 0.4 and 0.6. In this case, as it can be seen for the second loading cycle in Figure 4.14b, $k_0$ stays rather constant during the loading, and its value lies in the expected range.

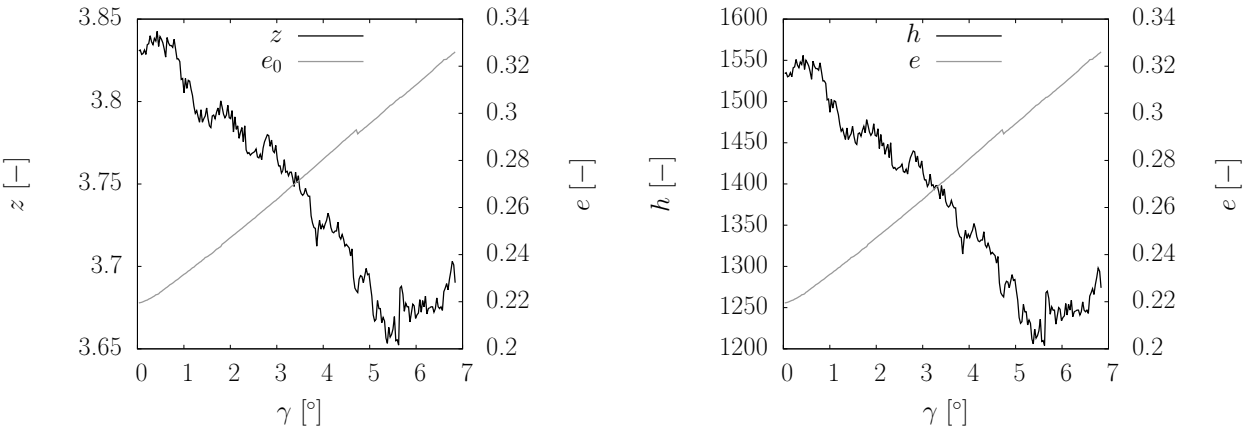


Figure 4.13 – Plot of the evolution of the main geometric properties during the simple shear test: void ratio $e$, coordination number $z$ (left) and degree of force indeterminacy $h$ (right).

It is worth mentioning that the two changes in steep that are observable in all the loading/unloading branches of the stress evolution are related to experimental issues (a sudden change in the velocity imposed by the engines on the walls), hence they have no significant mechanical meaning.

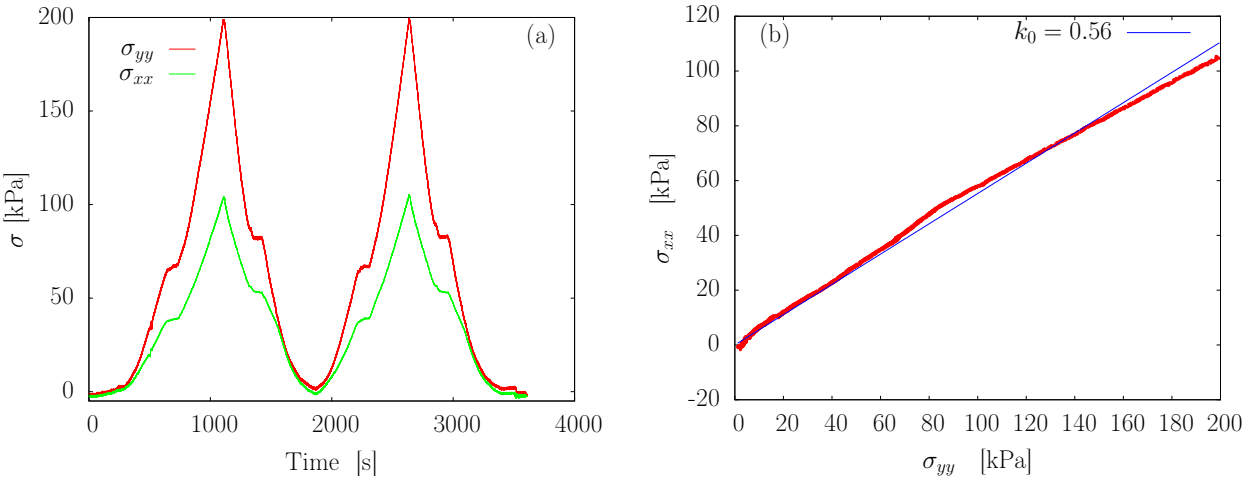


Figure 4.14 – (Left) Evolution with time of the vertical and horizontal normal stresses ($\sigma_{yy}$ and $\sigma_{xx}$, respectively), for the oedometer compression tests. (Right) Fit of the ratio between horizontal and vertical normal stress for the loading phase of the second cycle of the oedometer compression test.

One of the main uses of oedometer compression tests for the characterisation of soils is related to the material compressibility. The typical plot for this kind of result is the oedometric curve in Figure 4.15, linking the vertical normal stress $\sigma_v \equiv \sigma_{yy}$ with the void

ratio $e = V_v / V_s$, being $V_v$ the volume of voids and $V_s$ the volume of the solid part; given the two-dimensional character of the system, volumes here are meant as surfaces.

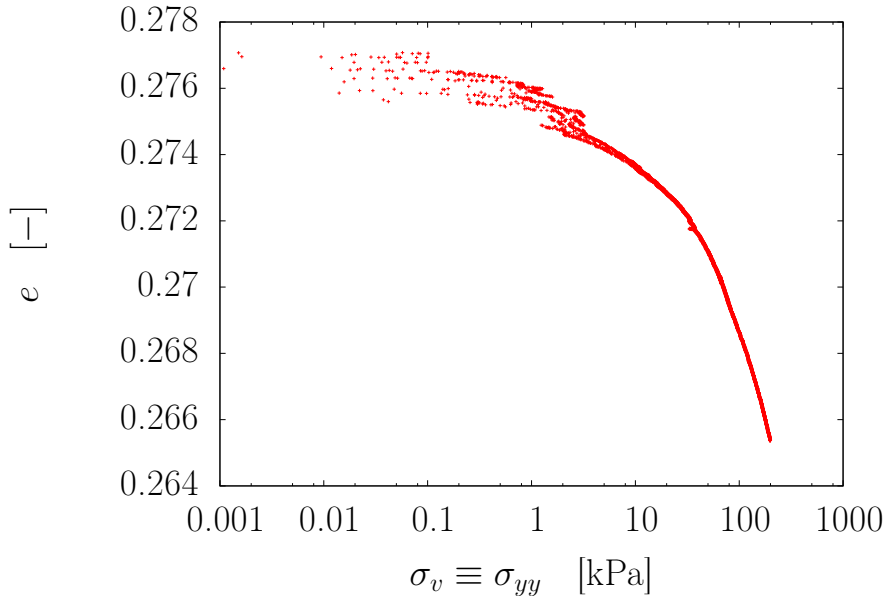


Figure 4.15 – Oedometric curve for the loading branch of the first cycle of the oedometer compression test.

### 4.1.4 Measurement of particle kinematics

By taking high-resolution (80 Mpixel) photographs of the granular assembly during the tests previously presented, its micro-scale can be fully characterised, through the determination of the granular fabric (grain position and size, contact point location and orientations) in single states and of the evolution of the packing (particle motion) between these states, based on a DIC-based technique, referred to as Particle Image Tracking (PIT) (Combe and Richefeu (2013)), which allows for tracking individual particles. This requires the definition of a subset of pixels inside each particle; this subset is searched for in consecutive photographs based on the gray-value associated with each pixel it is composed of.

For this case (circular grains), these subsets are defined as concentric circles internal to the particle. The radius of each subset is chosen as a fixed ratio (80%) of the particle one, so that a different radius is used for each particle: this aims to maximise the size of each subset, considering the fact that the accuracy of the correlation of a subset is found to increase with its size. Therefore, the definition of these subsets requires the determination, at least in one reference image (typically, the first one), of the mass centre position and the radius of each particle. The subsets are defined with respect to this

reference configuration; then, particle motion is determined by tracking each subset in the successive images.

For this specific case, in which we deal with a 2D image of rods with a circular section, the identification of a grain corresponds to the detection of a circle in an image. The algorithm adopted, referred to as FindGrains, provides a determination of grain position (centre of the circle) and radius with a sub-pixel precision. It works with Tiff 16-bit images – for which a gray-scale value ranging between 0 and 65535 ($= 2^{16} - 1$) is defined for each pixel – and it has been developed specifically for application to $1\gamma2\varepsilon$ images. In a first phase, a histogram of gray levels of the specimen's area is computed. A typical one, as in Figure 4.16, is characterised by a double bell-shaped curve: the first peak indicates high frequencies of blacks, corresponding to voids; the second part of the curve, much wider and with a lower peak, covers the whole gray level range inside grains. Based on this histogram, a threshold for the segmentation between grains and voids can be set as an approximation of the demarcation point between the two curves. Once all grains are identified by their position and radius, a subset of pixels to be searched for in all the successive images can be associated to each grain.

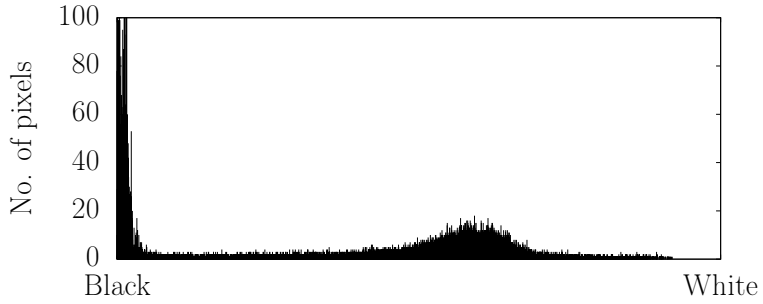


Figure 4.16 – Example of a gray level histogram from an image of a $1\gamma2\varepsilon$ specimen. The two peaks correspond to voids (left) and grains (right), respectively.

#### 4.1.4.1 Contact detection

An accurate detection of contacts between grains is a crucial part of the image processing operations that are prior to the final objective of this work, *i.e.*, the estimation of contact forces, as it will be shown in more detail in Chapter 3 and 4. Here, the procedure adopted for building the contact network is described; then, the main sources of error – and possible ways to contain their effects – are discussed.

A common approach for the definition of a contact list consists in simply going through all the possible pairs of grains, and verifying whether two grains are touching or not from the definition of a criterion based on the interparticle distance; since

grains are circular with a given radius, the distance from the centre to the boundary of a grain is independent of the direction. In this way, the contact criterion can be expressed as a function of the following parameter:

$$x_{ij} = R_i + R_j - d_{ij} \tag{4.1}$$

where $R_i$, $R_j$ are the radii of the two grains and $d_{ij}$ is the distance between their mass centres.

As it is discussed in other sections of this chapter, measurement accuracy is a major concern for this work. Among the possible sources of measurement error, the shape of grains can affect the detection of contacts: the presented algorithm assumes grains to be perfectly circular, while it has been shown (Table 4.1) that the actual shape is slightly elliptical, and a maximum and minimum radii can be measured for each grain. Moreover, the value of the radius itself can represent a source of error, since it depends on the gray-value threshold chosen for the detection of grains in the FindGrains algorithm: the choice of this threshold, based on the procedure explained in Section 4.1.4, is rather arbitrary as there is no steep delimitation between the range of gray values corresponding to grains and that corresponding to voids. Shape imperfections can also lead to cases in which two grains, that do not appear to be in contact in their visible surface, are actually touching along the 6 cm depth.

Taking into account all these problems, some further verification of the resulting contact network is necessary. To do so, the obtained contacts are visually checked, so that cases of clear misdetections could be revealed. In particular, taking into account the basic principle of static equilibrium for each particle, it is easy to identify those missed contacts that are actually necessary for the equilibrium of some grains: whenever a grain is found to be "floating" (with gravity and friction, it is necessary for equilibrium that each grain lie on at least one more grain), a missed contact is found.

However, even after this correction a perfect accuracy seems difficult to be obtained with the given resolution and scale of the system (in terms of size – and number – of particles): it is thus important to take into account that an error is made, and, when possible, try to assess its influence in the result of the numerical estimation of forces, as in Section 3.4.2 and 3.5.5.

#### 4.1.4.2 Particle Image Tracking

Once the granular fabric determined for a reference contact state, the missing part for a complete micro-scale description of the assembly is the measurement of kinematic fields.

Among several optical metrics that have been used for measurements of kinematics in experimental mechanics, Digital Image Correlation represents the most established and commonly used tool. After its first proposition in the 1980s as two-dimensional DIC (Chu et al., 1985), the method has been developing until an extension to the 3D case (*i.e.*, Digital Volume Correlation); 2D DIC still represents a very powerful tool when dealing with measurements of in-plane displacement and deformation fields of planar objects (Pan et al., 2009), such as in this work.

In order to take into account the discrete nature of granular materials, a specific image processing software named TRACKER was developed by Combe and Richefeu (2013), allowing the tracking of non-smooth trajectories of individual particles between digital images of a 2D granular packing. Given the relatively low compressibility of the chosen material with respect to the image resolution, deformations turn out to be rather low and mainly localised in a small area around the contact point; because of this, a rigid-body motion can be assessed for each grain by following the evolution of the position ($x$- and $y$-displacements and rotation) of a circular subset of pixels concentric to the grain. In this way, the relations between coordinates of any pixel in a subset of the first and second image can be simply expressed as the rigid displacements and rotation referred to the considered subset centre.

#### 4.1.4.3 Measurement accuracy

Several strategies have been adopted to minimise the error associated to the correlation process in TRACKER. First, it is important to recall that TRACKER, being optimised for application to discrete materials, has the advantage of not "losing" any grain during the tracking. Moreover, a very high accuracy is attained by means of a sub-pixel resolution of displacement and rotation measurements. This is achieved by the implementation of a bi-cubic interpolation.

One main operation to optimise the accuracy is to make each subset as unique and recognisable as possible, which is fundamental when searching for its new position in a successive image. To this purpose, a speckle black-and-white pattern is applied on the visible face of particles. The application of this pattern followed some recommendations by Lecompte et al. (2007), that studied the influence of the speckle pattern on the measurement accuracy, in particular through the variation of two features: the size of the dots and the focus, that was considered because of its influence on the transition between areas with different gray-scale intensities. The outcome of this study was that very large speckles are disadvantageous for the quality of correlation, and they should be avoided, as well as very steep gray-value transitions between speckles and background.

Following these findings, a pattern of black and white dots is laid on the visible surface of the ash wood rods used in this experimental campaign by lightly scratching a toothbrush on which black and white paint are alternatively applied (Figure 4.17). With this procedure, relatively small dots are obtained. As to the second point, a rather smooth transition between different gray intensities is achieved by keeping the natural rod surface as a background: in this way, an intermediate gray value between the two extreme ones (corresponding to black and white dots) is obtained.

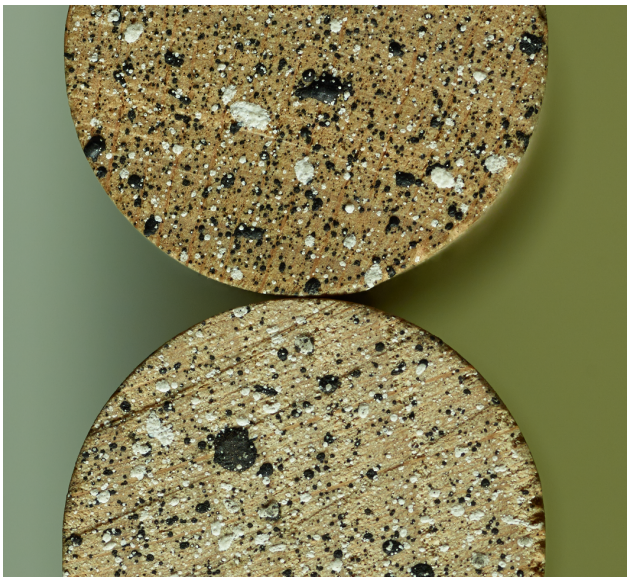

Figure 4.17 – Zoom on two grains ($d = 20$ mm) to show the black-and-white dots on their visible face. The speckles are obtained by spraying black and white paints with a toothbrush.

As previously mentioned, the size of the subset to be correlated also has an influence on the correlation. It has been observed that correlation is higher for larger subsets. This concerns in particular the determination of particle rotation, which can take advantage from the higher length of the subset circumference to obtain a more accurate pixel-level measurement of rotations.

Other sources of error that might affect these measurements can be found in the lens distortion error, as well as in possible undesired displacements of the camera itself. Appropriate procedures have been adopted to eliminate both errors. Distortion is assessed by taking six photographs of a wooden plate, which is rigidly displaced between each photograph. The amount of measured displacement that deviates from the rigid displacement applied is due to distortion, and can be corrected through the definition of an appropriate function and the computation of its eight parameters. Additional movements are corrected by using the measured displacements of a speckled paper rectangle,

applied on one side of the $1\gamma 2\varepsilon$ device which is fixed. This measured motion is assumed to come from possible displacements of the camera, and it is subtracted to all particle measured motions to correct this error.

Once all possible strategies to avoid other sources of inaccuracy have been adopted, the remaining error associated to the correlation process of TRACKER can be assessed; to this purpose, a procedure was developed by Combe and Richefeu (2013). It consisted in measuring possible changes in the length and orientation of two segments, perpendicular to each other, that were drawn on a number of particles, in an area sufficiently far from the particle boundary so that it could be assumed to stay undeformed throughout a test. As a result of this rigid motion, the two segments are expected to preserve their original length and perpendicularity; variations of length and orientation measured by TRACKER are regarded as a bias associated to the correlation technique.

A granular assembly of around 2000 grains was subjected to a quasi-static shearing during which 24.5 Mpixels pictures were taken. Once the distortion error was corrected, the bias (coming only from the correlation error) was described by a length variation $\Delta S = 0.01 \pm 0.05$ pixel and an angle variation $\Delta\alpha = 0.01 \pm 0.06°$. With the scale of that test, the length variation could be expressed as $1.1 \times 10^{-3} \pm 5.5 \times 10^{-3}$ mm; the higher resolution provided by the camera used in this doctoral work (80 Mpixels instead of 24.5 Mpixels) allowed for a smaller scale ($\approx 6 \times 10^{-5}$ m/pixel), so that the error can be quantified as $\approx 6.0 \times 10^{-4} \pm 3.0 \times 10^{-3}$ mm. In Table 4.2, the bias and random error are summarised, and the error on lengths is expressed as a function of the mean diameter $\langle d \rangle = 11$ mm of the granular material considered.

Accuracy of particle tracking

| | Bias | Random error |
|---|---|---|
| $\Delta S / \langle d \rangle$ | $10^{-4}$ | $5 \times 10^{-4}$ |
| $\Delta\alpha$ | $0.01°$ | $0.06°$ |

Table 4.2 – Bias and random error of changes of length $\Delta S$, normalised by the average grain diameter $\langle d \rangle = 11$ mm, and changes of angle $\Delta\alpha$.

### 4.1.5 Preliminary results

Before tackling the question of force estimation, some interesting observations can be inferred from the analysis of the data extracted from the experimental measurements

of geometrical and kinematic micro-scale quantities. In particular, based on grain mass centre, contact point positions and contact orientations, the fabric of the granular packing could be fully assessed from the result of image processing and DIC application, showing interesting results in terms of structural anisotropy.

All these analyses, described in the following sections, contribute to revealing strong links between the evolution of contact-scale quantities and the bulk behaviour of a granular assembly; moreover, their results represent a first corroboration of the choice of exploiting micro-scale kinematic measurements for the inference of contact forces, that characterises one of the force estimation methods proposed (Section 2.1.1).

#### 4.1.5.1 Contact orientation

The analysis of the evolution of contact orientations is an immediate tool to describe the effect of loading in the granular structure of the assembly. Although significant grain rearrangements are generally not occurring in the considered tests, due to the high initial density and the relatively low deformation attained at the end of each test, modifications in the granular network prove to be affected by the direction of the applied loading.

In order to highlight possible preferential directions in the granular arrangement, the contact network can be statistically characterised by building a histogram of contact orientations. In Figure 4.20, such a histogram is built by dividing the global range $2\pi$ in 36 10°-wide bins, and then assigning to each bin the number of contacts whose orientation lies within the bin limits.

The orientation is defined by a convention that consists in labelling all $N_p$ grains in an assembly with a number from 1 to $N_p$ and then directing the normal unit vector at each contact as pointing towards the grain that has the highest label in the pair (Figure 4.18).

Three different tests (biaxial vertical compression, biaxial horizontal compression, simple shear) are studied, comparing the initial histogram (under isotropic loading conditions, with $p = 100$ kPa in all cases) with the one at the end of each test. The initial histogram shows a quite uniform distribution of contacts in all directions. For the three tests, only a slight deviation from this condition is observed after the load has been applied, confirming that restructuring of the contact networks are somehow limited; however, it can be observed that contacts are generally gained along the direction of maximum compression for each test (defined by the sketch in Figure 4.19), showing a clear effect of loading conditions on structural anisotropy.

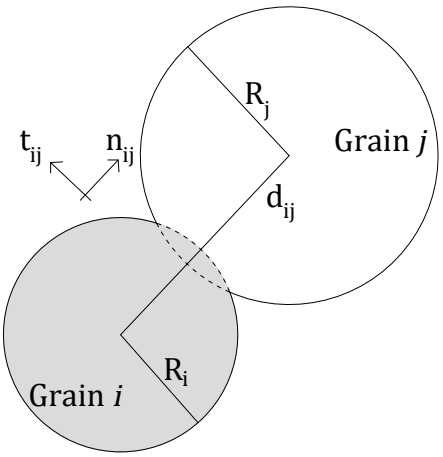


Figure 4.18 – Sketch of two grains in contact, with definition of the convention for the local reference (normal $\vec{n}^{i,j}$ and tangential $\vec{t}^{i,j}$ unit vectors at the contact).

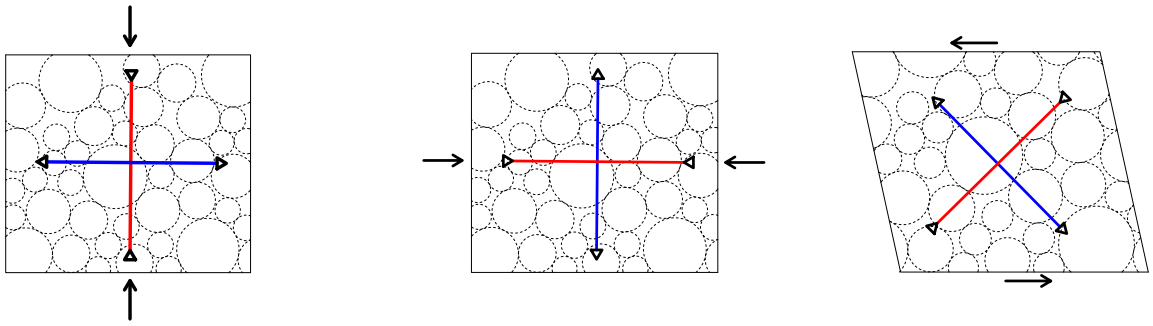

(a) Biaxial vertical compression

(b) Biaxial horizontal compression

(c) Simple shear

Figure 4.19 – Sketch of the applied loading conditions in three different tests. The direction of maximum compression and extension, for each test, are marked in red and blue, respectively. For the simple shear test, the maximum compression occurs along the short diagonal of the trapezoidal specimen area.

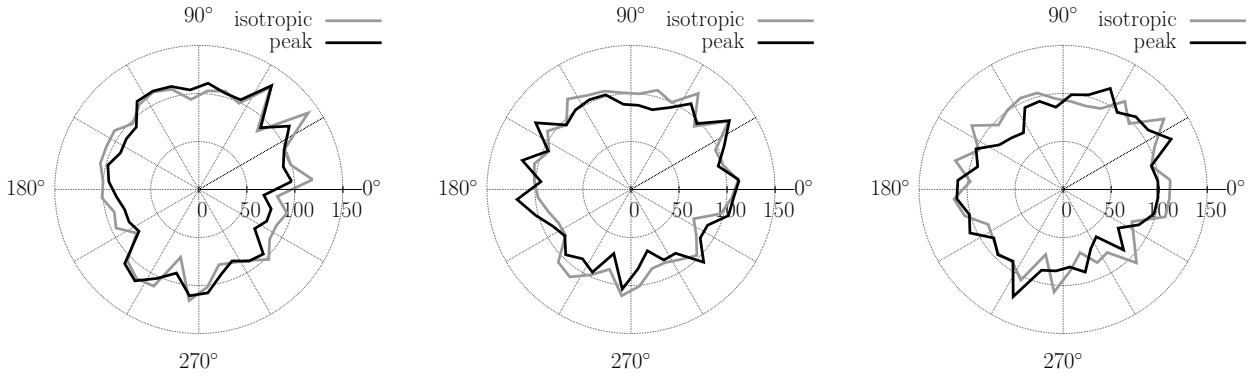


(a) Biaxial vertical compression

(b) Biaxial horizontal compression

(c) Simple shear

Figure 4.20 – Polar histogram of contact orientations for three different tests, respectively at the beginning of the test (under isotropic stress conditions) and at the end of the test (when structural anisotropy is enhanced by the anisotropic loading conditions). Contacts seem to be generally gained along the direction of maximum compression for each test, and lost along the direction of maximum extension, as they are defined in Figure 4.19.

#### 4.1.5.2 Preferential orientations of contact deflection evolution

The effect of load application on the structural anisotropy is a first signature of the relationship between micro-scale quantities and bulk behaviour in granular materials. In addition to geometrical quantities, kinematic micro-scale measurements represent a further method of describing the micromechanics of an assembly, and can be exploited to highlight possible links between the contact scale and the specimen one.

Based on this, a similar statistical analysis as in Section 4.1.5.1 is carried out. One micro-scale quantity that is assumed to be representative of the macroscopic behaviour is the normal relative displacement of two grains in a persistent contact, between two reference configurations. Here, the evolution is determined between the initial configuration (*i.e.*, isotropic loading conditions) and the end of each test.

By selecting only those contacts undergoing a negative normal relative displacement (*i.e.*, the grains in contact are getting "closer", more compressed), a statistical study of their orientation reveals the clear existence of preferential orientations that roughly follow the direction of maximum compression for each test, as in Figure 4.21.

Assuming that a relationship exists between this kinematic-based micro-scale descriptor and normal contact forces, this result seems to suggest that normal force increments, between two states of a test on a granular assembly, will possibly follow the direction in which the load is applied, that is also the direction in which force chains are expected to appear.

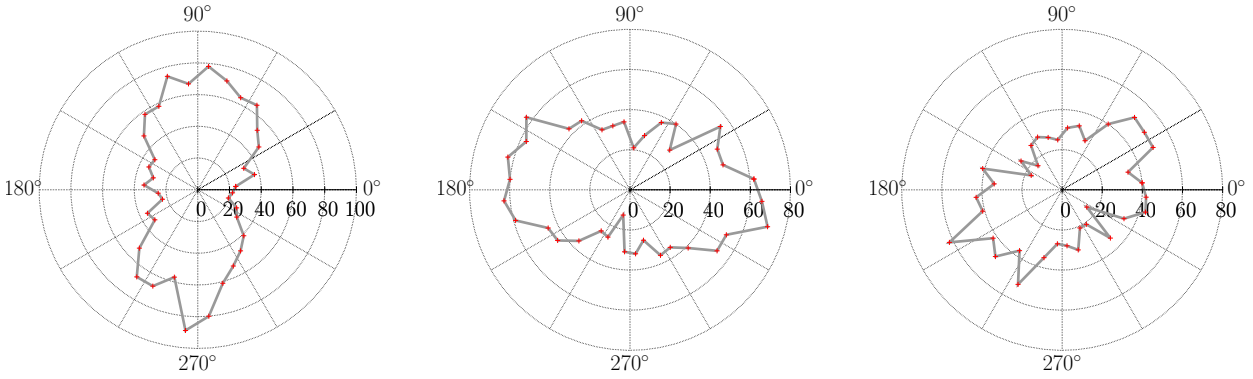


(a) Biaxial vertical compression

(b) Biaxial horizontal compression

(c) Simple shear

Figure 4.21 – Polar histogram of contact orientations for contacts undergoing negative relative displacement (*i.e.*, grains getting closer). It can be clearly seen that such contacts are mainly oriented along the direction of maximum compression for each of the three tests analysed, as in Figure 4.19.

## 4.2 Estimation of contact forces

In this section, the three methods presented in Chapter 2 are applied to the estimation of contact forces in real experiments. The tests considered are part of the experimental campaign, described in the previous sections of this chapter, that was carried out with the $1\gamma 2\varepsilon$ shearing device. From these tests, DIC-based measurements of the particle kinematics between quasi-equilibrium states of the granular system, caught by shooting high-resolution photographs of the whole specimen, are the basis for the application of the three force estimation techniques, that is equivalent to what was shown, as a validation phase, in Chapter 3.

The results of a single contact compression test (Sec. 4.1.1.1) corroborate one of the main assumptions common to the three techniques, *i.e.*, that particles are rigid and maintain their original shape. In the whole experimental campaign, particle deformation is constrained in a relatively small area around the contact point, and particle kinematics can be reduced to the simple rigid body motion (displacements and rotation). As for contact deformation, when we estimate forces with the three techniques proposed, we either neglect it (CDM) or model it as a particle overlap that does not modify the shape of particles (CEM, QSM), as in the typical MD-DEM model of contact interaction.

For each of the three applied techniques, contact forces are determined for all those states of the granular packing for which a photograph is available. The quality of the result is then evaluated mainly through comparison of the homogenised stress, computed from the estimated contact forces, with the stress applied and measured by the machine

throughout the whole test. In addition to this, maps of normal forces are analysed; the self-organisation of forces in typical structures such as chain-like ones will be deemed as a possible sign – although not sufficient – of the good quality of force estimation.

Further assessment of the quality of the obtained results might only be performed through comparison with other methods of force estimation; however, such an approach is not part of this work – it is a concrete perspective for the near future, though.

In the following sections (4.2.1, 4.2.2, 4.2.3), the applications of the three methods are developed separately, focusing in more detail on how they work (also with respect to possible necessary adjustments for the application to the experimental case) and showing the main results. Further comments and discussions conclude the chapter (Section 4.2.4).

### 4.2.1 Contact Elasticity Method

The application of the Contact Elasticity Method to the estimation of forces from 2D experiments in the $1\gamma2\varepsilon$ device follows the working principles of the method, as already presented in Section 2.1.1.

In particular, it is important to recall that one of the main characteristics of this technique is that it provides a direct and unique estimation of forces, by simply injecting the measured kinematics (particle displacements and rotation) into appropriate force laws, based on the MD-DEM.

Nevertheless, some observations are necessary about the application of this framework to the specific case of real tests, to highlight some major differences from the validation phase that only involve numerically-generated data. The main point concerns the definition of a force law for normal forces. As presented in Section 2.1.1, the typical approach of MD-DEM assumes that contact deformation can be described by a simple model in which particles are rigid while contacts are compliant, *i.e.*, they can deform under compression, and such a deformation is described through the definition of a particle overlap.

The application of this simple model to a real case, however, is not straightforward. When two disks are in contact, and a compressive force is transmitted, the deformation of the two particles, though possibly limited in a zone close to the contact point, might entail a slight change in the shape of the particle. In such a situation, the definition of a microscale geometric variable that can be equivalent to MD's overlap seems rather arbitrary. Moreover, such a parameter would turn out to be strongly affected by the chosen gray-value threshold for the detection of a particle's edge.

Based on this, an alternative approach is adopted in this study, which provides a

more reliable measurement, getting rid of the uncertainty on the initial state. As already discussed in Sec. 3.3 for the application to virtual experiments, this approach consists in simply measuring the change in contact deflection as a relative displacement between particles at contact, and assuming that any decrease (increase) of the interparticle distance of two touching particles is related to a proportional decrease (increase) of the normal force transmitted between the two particles. Therefore, normal forces can be determined as the accumulation of normal force increments, simply obtained by injecting measured normal relative displacements into the incremental contact law in Equation 2.4. With this approach, also non-persistent contacts can be easily dealt with, as already shown in Sec. 3.3.2.

Similarly, an incrementally linear force law is assumed for tangential forces, with implementation of Coulomb friction. In this law, tangential relative displacements, which are assumed to be linear with the force increment through the stiffness $k_t$, are function not just of particle displacements ($\vec{U}_i$, $\vec{U}_j$) but also of rotations ($\theta_i$, $\theta_j$).

While certainly more reliable than a model requiring the definition of a fictitious overlap, this approach comes with a major drawback: by definition, it cannot provide an estimation of any initial (*i.e.*, pre-existing) force in the system. This reduces its applicability to cases in which the initial state is as close as possible to an unloaded one.

Moreover, Equation 2.4 shows that the estimation of normal forces depends on the definition of an additional parameter, *i.e.*, the normal contact stiffness $k_n$. This parameter, together with the corresponding tangential stiffness for the second force law (and the interparticle friction coefficient $\mu$), requires itself an estimation, that can be based on an appropriate experimental procedure, derived from other material properties (namely Young modulus and Poisson ratio) through the assumption of a suitable relation, or yet estimated with a re-scaling procedure to fit some macroscopic measurements such as the applied stress. This introduces an additional uncertainty in the final determination of forces, in particular with respect to the CDM that, on the other hand, neglects contact elasticity. As to the estimation of the other two parameters, for $k_t$ we usually assume it can be expressed as a given ratio of $k_n$ (*e.g.*, $k_t/k_n = 1$). In Appendix B, a simple test for the determination of $\mu$ is described.

#### 4.2.1.1 Assessment of measurement error

Before showing the main results of the application of the CEM to the $1\gamma2\varepsilon$ experiments, it is important to discuss the reliability of the estimated forces by trying to assess, even in an approximate way, the extent of the expected measurement inaccuracy, and consequently predict the error associated with the obtained forces.

One type of error has already been discussed: it is the error related to the inability of the CEM to estimate forces in an initial state, *i.e.*, when no information is available about the previous history of the packing. However, this error can be limited by trying to guarantee that the initial state is as close as possible to an unloaded one. In the case of $1\gamma2\varepsilon$ tests, this condition corresponds to a state in which the only load consists of the particles own weight; the normal forces already transmitted in the system can be assumed to be sufficiently low if compared to the expected average normal force developed during the test, that can be estimated, for an assembly supporting a pressure $p$, as $\langle f_n \rangle \sim p \, \langle d \rangle^{D-1}$ (Combe and Roux, 2011). The system can be regarded as a two-dimensional one, but the length of rods $l$ should be included in the expression. With all these considerations, for a pressure $p = 100$ kPa, one can estimate $\langle f_n \rangle \sim p \, d \, l = 66$ N, *i.e.*, approximately $10^4$ the average weight of an ash wood rod with diameter $d = 0.011$ m and length $l = 0.06$ m.

In addition to this, the main sources of error consist in the inaccuracy associated with the measurement of the quantities that appear in the force laws, in particular particle (and consequently contact) displacements (Table 4.2).

Based on the adopted force law, normal forces are (incrementally) linear with measured displacements via the normal stiffness $k_n$. Therefore, the expected error can be roughly estimated by simply multiplying the measurement accuracy $\Delta S$ by the normal stiffness: the resulting error is $\approx 50$ N, *i.e.*, in the same order of magnitude of the expected average normal force.

Such a large error already indicates that the estimation of forces through the CEM, with the given measurement resolution and the deformability of the chosen material, cannot be considered reliable. In the following sections, we will see this in more detail by analysing the results of the application to the different $1\gamma2\varepsilon$ tests.

As further discussed at the end of this chapter and in the next one, this does not totally close the door to future applications, provided the measurement error is substantially reduced. This can be achieved in several ways: for example, by increasing the resolution of the measurements (*i.e.*, reducing the m/pixel scale), either zooming in a smaller part of the specimen, or by means of a higher resolution camera device. Measurement accuracy can also be improved by increasing the deformability of the particles, and so decreasing the normal stiffness $k_n$: in this way, contact deformation would be larger for the same level of applied stress, and the influence of the error $\Delta S$ on the measured displacement less relevant; or, equivalently, it can be observed that the error in force, estimated as $k_n \Delta S$, is linear with $k_n$, so a reduction of the stiffness would also result in a reduction of the error.

#### 4.2.1.2 Oedometer compression

The first test considered is an oedometer compression test with two cycles of loading, until a vertical normal stress $\sigma_{yy} = 200$ kPa.

Once the contact forces estimated for all the 629 granular states, each corresponding to one photograph of the assembly, on the basis of DIC-measured displacements and the force laws previously described, Weber's definition of homogenised stress (Equation 3.5) is used to compute the stress tensor components, in the whole volume $V$ of the specimen, from the obtained contact forces. This is compared with the stress applied by the device at the boundaries of the specimen.

Figure 4.22 shows the evolution of the normal components $\sigma_{yy}$ and $\sigma_{xx}$ of the measured and estimated stress tensors. Some observations can be made, in the first place, from a qualitative standpoint. The overall evolution, *i.e.*, the double cycle of loading and unloading, is fairly well retrieved, with the maxima and minima correctly placed along the $x$-axis. Moreover, it is interesting to notice that, during the application of the load, some errors were encountered in the regulation of the wall velocities, that led to a sudden change of slope in the stress curve, repeated in all the loading and unloading branches. These issues could be exploited as they define some new reference points for the qualitative comparison of stress components: in this case, it is observed that also these perturbations are retrieved in the CEM-based homogenised stress.

However, when the comparison moves to the quantitative level, the method proves unable of correctly reproducing the real stress. As it can be seen, a large error is found for the whole duration of the test, ranging between about 10% at the peak of the second loading cycle, and much larger values ($\approx 90\%$) close to the unloaded configuration.

In addition to this comparison, the assessment of the obtained solution in forces is carried out also through the computation, for each particle, of the distance from static equilibrium. This is based on the assumption that the tests were performed in quasi-static loading conditions, that is confirmed by the inertial number $I$ which was estimated to be in the same order of magnitude ($I \approx 10^{-7}$) as in typical triaxial tests – much lower than the threshold $I = 10^{-3}$ above which inertial effects cannot be neglected (Da Cruz et al., 2005).

In order to give a definition of the error as a distance from equilibrium, for each particle, the resultant of all forces acting on the particle – contact forces and own weight – is computed. Its norm $||\vec{\mathcal{F}}_i||$ – for a generic contact $i$ – can be taken as a measure of the error: in case of static equilibrium, $||\vec{\mathcal{F}}_i|| = 0$; as it increases, the distance from equilibrium does as well. The error is then obtained by normalising $||\vec{\mathcal{F}}_i||$ by the mean of all estimated normal forces in the system, so that a dimensionless quantity is obtained.

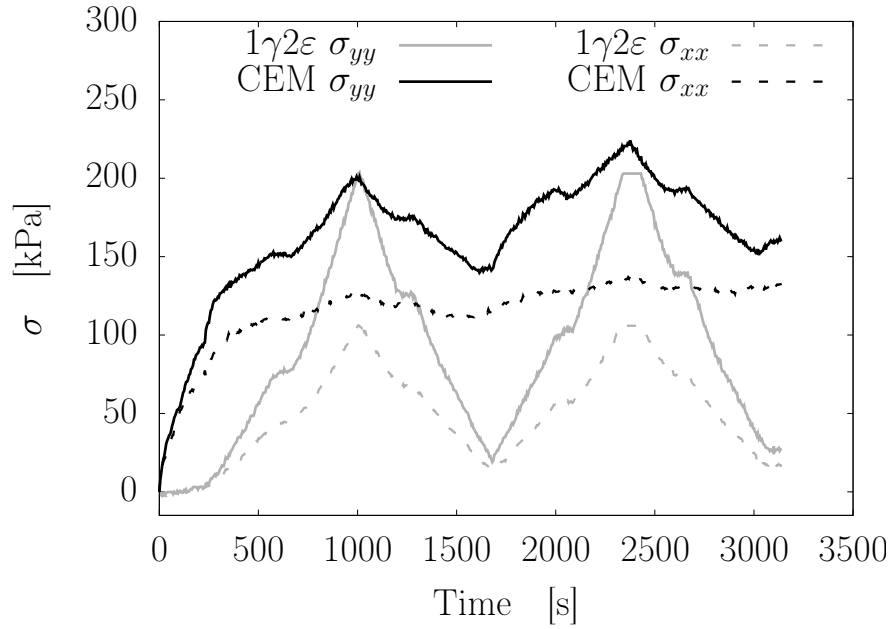


Figure 4.22 – Comparison between the $1\gamma 2\varepsilon$ macroscopic stress components and the Weber stress components computed from contact forces estimated via the CEM for an oedometer compression test.

For the oedometer test, a very large error is obtained, being quantified as $1.285 \pm 3.489$, *i.e.*, the average error is in the order of (even slightly higher than) the average normal force.

#### 4.2.1.3 Isotropic compression

The test is composed of five loading cycles, starting from a pressure $p = 20$ kPa up to $p = 200$ kPa; in the first two cycles, photographs are taken at loading steps of 20 kPa, so that each of the first two loading branches is described by ten different geometrical states. The third and fourth cycle are applied with no intermediate step.

The homogenised stress from CEM-computed contact forces is plotted in Figure 4.23, together with the stress actually applied. A value of 20 kPa is added to the whole curve, to take into account the initial state, for which the CEM cannot estimate the current loading state and the contact forces associated with it. Similarly to the case of oedometer compression, the two stress tensors compare well qualitatively, but not quantitatively. It is however interesting to notice that the main properties of the imposed stress, *i.e.*, symmetry ($\sigma_{xy} \approx \sigma_{yx}$) and isotropy ($\sigma_{xx} \approx \sigma_{yy}$ and $|\sigma_{xy}| \ll |\sigma_{xx}|$), are retrieved in the CEM stress tensor. From a quantitative point of view, the correspondence between the two stress tensors is not retrieved, as in the oedometer compression case. Here, the error reaches up to 60%, in correspondence of the load peaks.

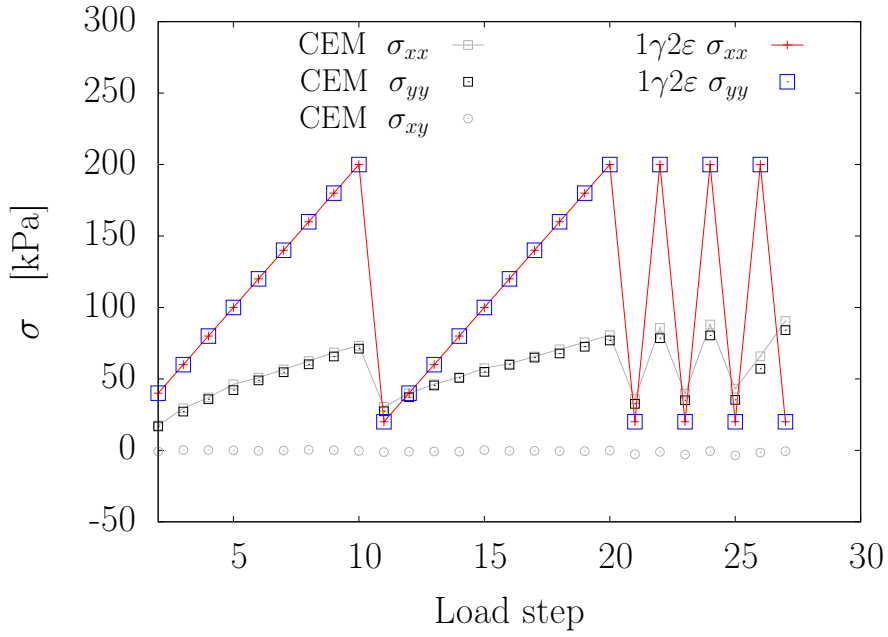


Figure 4.23 – Comparison between the $1\gamma2\varepsilon$ macroscopic stress components and the Weber stress components computed from contact forces estimated via the CEM for an isotropic compression test.

#### 4.2.1.4 Biaxial compression

For the two biaxial compression tests – one with load applied along the vertical direction, and one along the horizontal one –, the possibility of clearly identifying preferential directions of loading suggests the opportunity of looking for possible micro-macro relations, through the determination of appropriate quantities, expressed as function of the orientation, from micro-scale variables.

One way of doing this is to compute the magnitude of the normal stress $\sigma_\theta = \vec{n}_\theta \, \boldsymbol{\sigma} \, \vec{n}_\theta$ acting on a plane of given orientation $\theta$, defined by its normal unit vector $\vec{n}_\theta = (\cos\theta, \sin\theta)$. This can be expressed in micromechanical terms in the following way:

$$\sigma_\theta = \frac{1}{S} \sum_{c=1}^{N_c} f_\theta^c \ell_\theta^c \tag{4.2}$$

where $f_\theta^c$ and $\ell_\theta^c$ are the projections of, respectively, the force and the branch vector, at contact $c$, onto the normal $\vec{n}_\theta$ to the plane of orientation $\theta$, and $S$ is the surface of the whole specimen area, replacing the volume $V$ for the 2D case. Figure 4.24 shows the magnitude of normal stress for different orientations. Interestingly, for both tests the direction of maximum compression based on the imposed stress – almost vertical and horizontal, respectively – is very well reproduced by the distribution of normal stress

magnitudes, which have their maxima at 90° (and 270°) with respect to the horizontal direction for the vertical compression, and at 0° (and 180°) for the horizontal one. This might suggest that there is actually a link between measured micro-scale variables (here, contact forces derived from contact relative displacements) and macro-scale variables; however, the comparison between the real, macroscopic stress and the homogenised one computed from contact forces does not confirm this: similar results as for the previously described tests are found for the two biaxial compression tests – vertical (Figure 4.25a) and horizontal (Figure 4.25b).

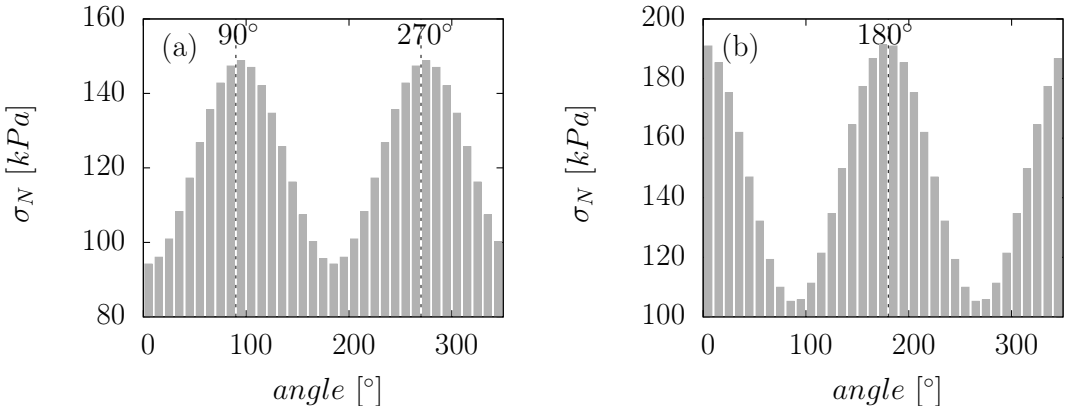


Figure 4.24 – Distribution of normal stress magnitude acting on planes with different orientations, from contact forces estimated via the CEM, at the end of the biaxial vertical (a) and horizontal (b) compression tests. Normal stress magnitude is determined with Equation 4.2.

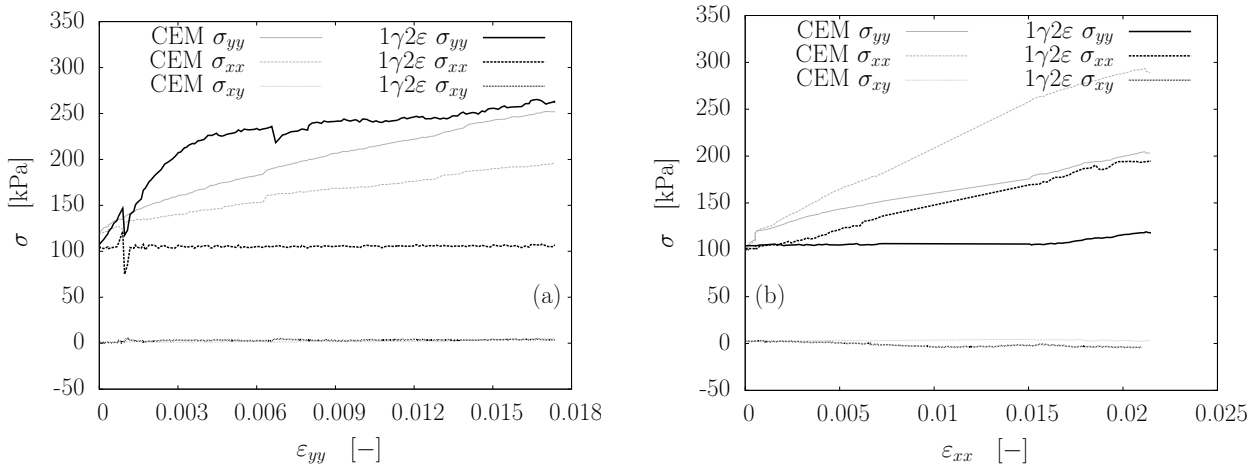


Figure 4.25 – Comparison between the $1\gamma 2\varepsilon$ macroscopic stress components and the Weber stress components computed from contact forces estimated via the CEM for a biaxial vertical compression test (left) and a biaxial horizontal compression test (right).

### 4.2.2 Quasi-Static Method

For the Quasi-Static Method (see Section2.1.3), the required input information consists of just the geometry of the granular assembly (*i.e.*, position and size of the disks, location of contact points) and the boundary conditions (stress applied on the walls). The geometry of the system is determined for single equilibrium states, from photographs of the specimen taken at distinct times, with a given time frequency, during the tests; in addition to this, the applied stress is continuously measured by the machine, and the values corresponding to the extracted equilibrium states are retrieved and injected into the problem.

The method results in the solution of a problem in which the number of variables and equations depends on the geometric properties of the packing. In particular, concerning the number of degrees of freedom of the system – *i.e.*, the number of equations –, one has 3 DOFs (2 translational and 1 rotational) for each particle. Regarding the walls, that have to be considered as bodies of the system, it is assumed that their motion can be described by means of just 2 DOFs, instead of 12: no rotation is allowed for any of the four walls of the system, and displacements are applied to only one direction for each wall. The remaining four displacements are not independent of each other, so two variables are sufficient to describe them by associating the four walls in couples: the motion of the top/bottom walls is defined by the (vertical) displacement of the top wall, as the bottom wall is never moved throughout all the tests; right and left walls are imposed the same (horizontal) displacement, only in opposite directions.

The vector of imposed external forces is built by following the definition of the DOFs of the system: gravity acts through a force along the $y$-direction (vertical) on each particle. In addition to this, forces applied by the machine are defined in correspondence of the two DOFs of the walls: a vertical force acting on the top/bottom couple, and a horizontal one acting on the left/right couple.

Before discussing in more detail the results in terms of obtained forces, some observations should be made concerning the evolution of the iterative procedure. For all the states for which contact forces are searched, the QSM fails to satisfy the two required criteria, *i.e.*, the static and plastic admissibility of the solution. The evolution throughout the iterations shows a rather early stabilisation of the error, defined as the distance from either criterion, which soon stops decreasing and never reaches the required threshold. The validation phase has shown that, even for simulations performed in quasi-static conditions, extracting a non-perfectly equilibrated state (*e.g.*, corresponding to dynamic events – particle rearrangements – occurring during the simulation) is sufficient to prevent the convergence of the method and the satisfaction of the required criteria; at the

same time, introducing little perturbations in the geometrical data (*e.g.*, loss of few contacts) has the same effect. In the same way, the geometry extracted from experiments, due to the measurement inaccuracy that was discussed in previous chapters, inevitably results in a partially wrong detection of contacts; the obtained contact network, in general, cannot be at equilibrium, thus it is no surprise that it is not possible to meet both criteria.

However, the failure in fulfilling such criteria does not necessarily imply a bad result in terms of force estimation: very high precision was obtained, for the numerical case, even for solutions that were considered inadmissible, on the basis of the previously mentioned criteria. A similar behaviour is observed in the experimental application. As it will be shown in more detail, for each of the $1\gamma2\varepsilon$ tests, in the next sections, the results of the application to experiments of the QSM are much more realistic than those obtained with the CEM: maps of normal forces show the typical structures in which forces are arranged in a granular medium, *i.e.*, chain-like and ring-like structures; moreover, a very accurate correspondence is found between the applied stress (measured during the test) and the homogenised stress determined from estimated contact forces.

#### 4.2.2.1 Oedometer compression

A first example of the use of the Quasi-Static Method is reported here, for the oedometer compression test. As usual, the evaluation of the obtained solution mainly relies on the building of a homogenised stress, from the estimated contact forces, and its comparison with the imposed stress (Figure 4.26). The difference with the application of the CEM (Figure 4.22) is clear. The two normal components of the applied stress ($\sigma_{xx}$ and $\sigma_{yy}$) are correctly retrieved for all the states extracted throughout the test, not only qualitatively, but also quantitatively.

Figure 4.27 shows a map of the normal forces obtained for a single state, at the end of the first loading cycle. Although a quantitative evaluation of the obtained result could not be performed, some interesting qualitative observations can be made. The heterogeneous organisation of forces shows the most typical properties of force distribution in granular media: forces tend to be organised in chain-like structures (sequences of grains in contact through which most of the applied load is transmitted through the assembly) and ring-like structures (closed groups of grains surrounding one or more grains that are weakly loaded). The observation of force chains allows additional qualitative remarks: such structures appear to be clearly organised along a preferential direction, *i.e.*, the vertical one, which is consistent with the applied stress ($\sigma_{yy} > \sigma_{xx}$).

It was already demonstrated, in previous chapters, that with the Quasi-Static Method,

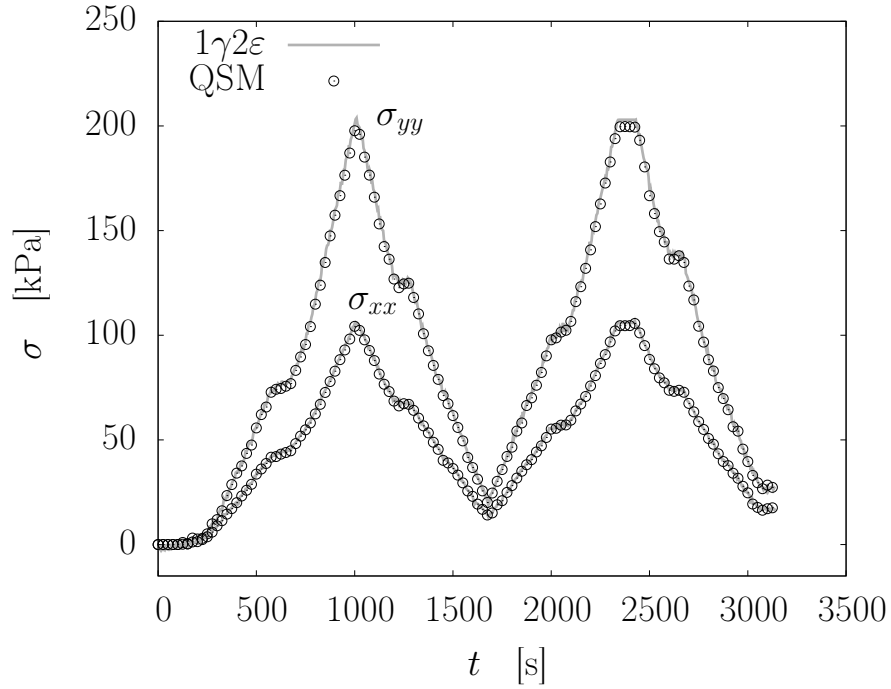


Figure 4.26 – Comparison between the $1\gamma 2\varepsilon$ macroscopic stress components and the Weber stress components computed from contact forces estimated via the QSM to an oedometer compression test. For clarity, only one every five CDM stress points are plotted.

as well as with Contact Dynamics, the solution obtained is only one among many possible solutions, especially when a realistic estimation of normal forces cannot be provided. It is interesting, at this point, to study the evolution of the force network: due to force variability, and to the fact that the history of the packing has been completely discarded, one can expect that force chains might dramatically change even between two consecutive states, when no large rearrangement of grains occurs and forces are expected to undergo only little variations. This is studied by comparing the set of forces (both normal and tangential) estimated, with the QSM, at one state of a test, with the forces estimated at the previous state. As usual, the comparison relies on the determination of the Pearson correlation coefficient, and it is shown in Figure 4.28. After a certain number of load steps (corresponding to the first half of the first loading cycle) in which forces tend to change significantly and evolve very fast, $r$ stabilises at very high values ($0.9 \div 1$) for both normal and tangential forces, and for the whole duration of the test. This result is obtained without exploiting any information on previous states, such as previously computed forces used as initial guess: it is a remarkable outcome, as it shows that force variability is, in the end, limited, and similar forces are retrieved for states with little or no difference in contact network and boundary conditions.

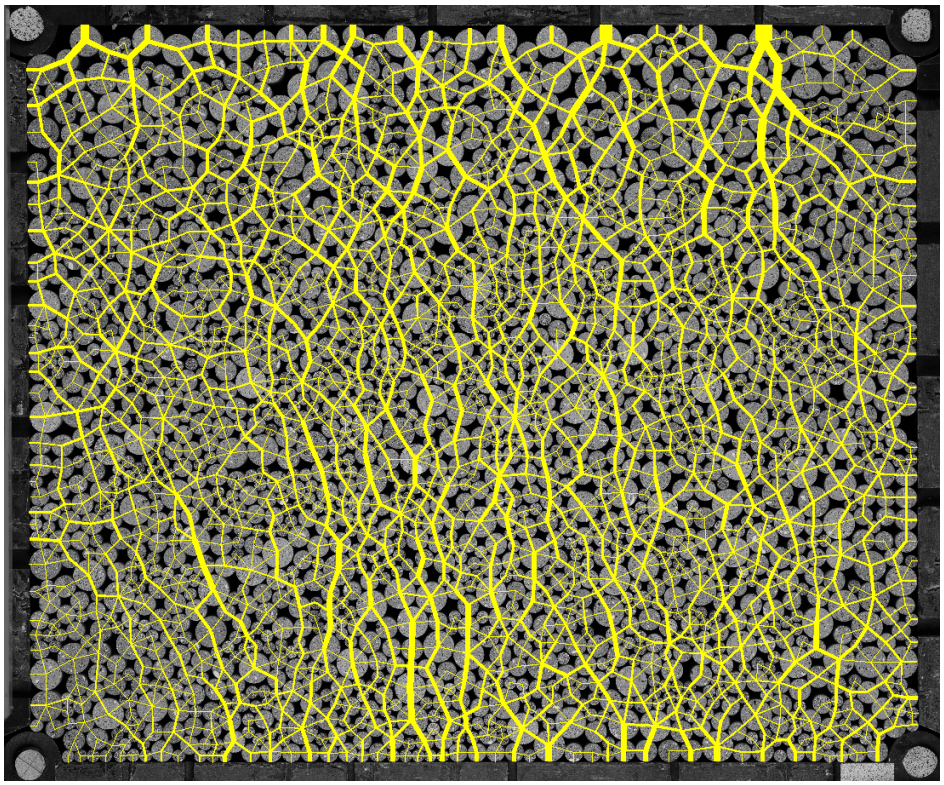

Figure 4.27 – Map of normal contact forces obtained via the QSM at the end of the first loading cycle of the oedometer compression test. The map is superimposed onto the photograph of the specimen in the corresponding state. Line thickness of the branch vectors is proportional to normal force intensity. The largest normal force is around 1000 N.

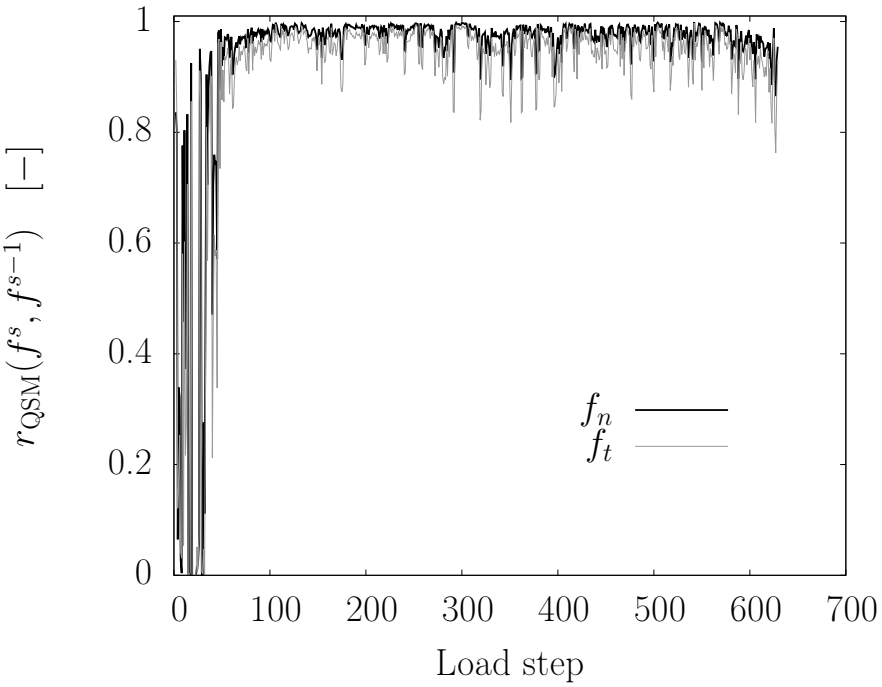


Figure 4.28 – Evolution of Pearson's $r$ for normal and tangential forces estimated via the QSM in consecutive states of an oedometer compression test.

A deeper quantitative assessment of the obtained solution is not possible at this stage. In the future, it might be useful to compare the solution with results from other similar methods, or simply with measurements of other quantities (*e.g.*, particle deformation), that could not be exploited in this particular case, given the measurement resolution and the relatively low deformability of the material.

When analysing contact forces in a granular packing, another typical result to be considered is the distribution of normal forces, that has been studied in many previous works, in which some common features of such a distribution have been highlighted; it is of interest, therefore, to see if the obtained solution is capable of reproducing such typical results. The probability distribution of normal forces is reported, again for the same state as before, in Figure 4.29. As expected, forces are found to cover a rather wide range, going from 0 to 5 times the average normal force. The typical exponential tail for strong (*i.e.*, above-average) forces is not clearly reproduced.

#### 4.2.2.2 Other tests

The main results of the application of the QSM to force estimation in experiments were shown and discussed in the previous section for the case of oedometer compression. Similar results were obtained for the other tests, and are briefly reported in this section.

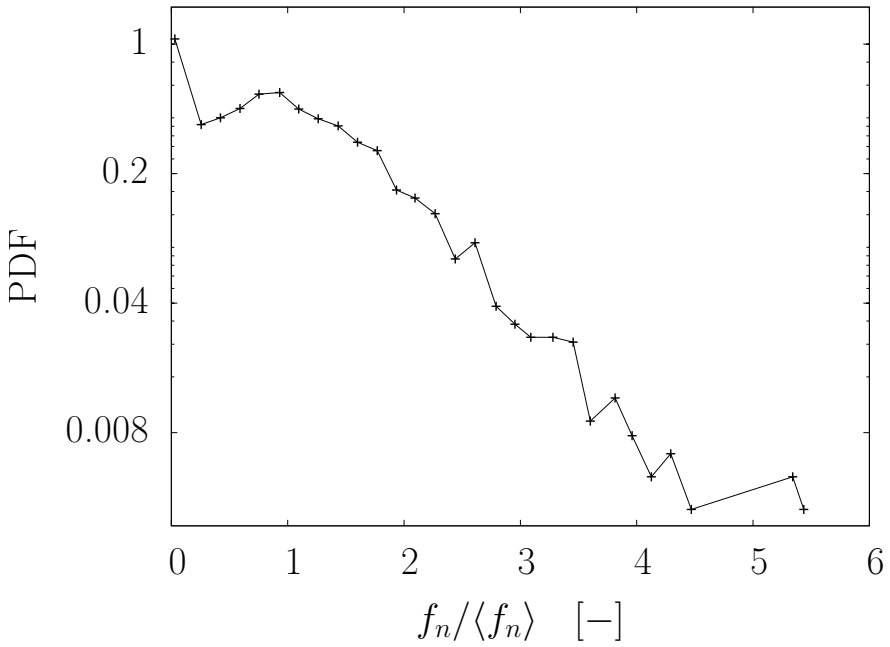


Figure 4.29 – Probability Density Function of normalised normal forces, estimated via the QSM at the end of the first loading cycle of an oedometer compression test.

Similarly to the oedometer compression test, the homogenised stress from QSM-estimated contact forces can reproduce very well the imposed stress for all the other tests. In particular, Figure 4.30 shows this plot for the case of isotropic compression, in which a pressure $p = 200$ kPa was applied, at first in two cycles with load steps of 20 kPa, and then for three more cycles with no intermediate step. In all points corresponding to the load steps, the original stress is retrieved with a very high precision.

Figure 4.31a and 4.31b show the homogenised stress obtained from contact forces for the biaxial vertical compression and biaxial horizontal compression, respectively. The normal stress components $\sigma_{xx}$ and $\sigma_{yy}$ are well reproduced for both tests. Also the tangential components $\sigma_{xy} \approx \sigma_{yx}$ are shown in the figures: it can be observed that, in both cases, such components stay very small with respect to the normal components, in agreement with the corresponding stress $\sigma_{xy}$ measured from the boundary forces acting on the sample.

Moreover, one of the main advantages of the application of this method, with respect to the CEM one, becomes clear: even when starting from a loading condition far away from the unloaded state (here, the initial state is at $p = 100$ kPa), with the QSM it is possible to retrieve an appropriate state (in terms of normal and tangential forces) without any information on the previous history of the packing, *i.e.*, by simply knowing the current boundary conditions.

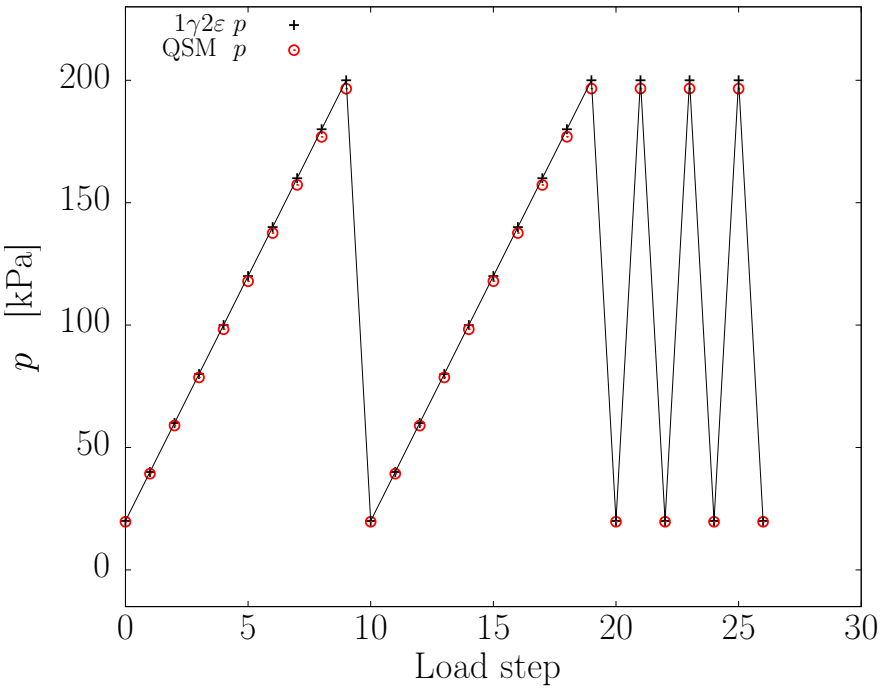


Figure 4.30 – Comparison between the $1\gamma2\varepsilon$ pressure $p$ and the Weber pressure computed from contact forces estimated via the QSM in an isotropic compression test. Please note that $1\gamma2\varepsilon$ pressure reported here is not a continuous measurement: it is just an interpolation of points corresponding to the load steps.

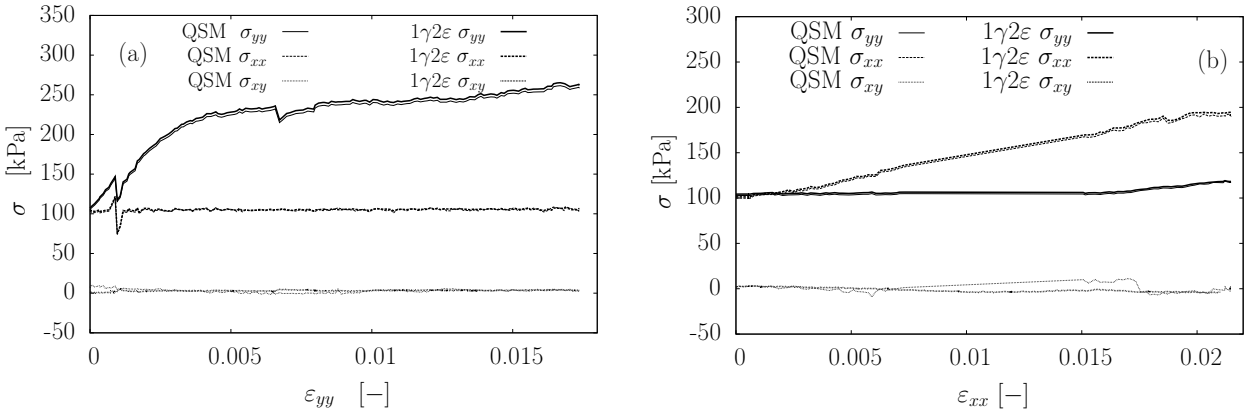


Figure 4.31 – Comparison between the $1\gamma2\varepsilon$ macroscopic stress components and the Weber stress components computed from contact forces estimated via the QSM in biaxial vertical (left) and horizontal (right) compression tests.

### 4.2.3 Contact Dynamics-based Method

A first attempt to estimate forces from experiments on 2D granular media through the use of Contact Dynamics was already performed by Richefeu et al. (2013), following the same approach of running the numerical resolution (Gauss-Seidel iterator) of the multi-contact problem – including the equations of dynamics and the contact laws – to retrieve a set of contact forces at each individual state, based on the imposed boundary conditions.

The outcome of this work was taken into account in this new attempt, in particular in terms of how to apply boundary conditions. However, before detailing the differences between the approach adopted in the present study and the one followed by Richefeu et al. (2013), some aspects about the modelling of the walls in this use of Contact Dynamics should be discussed.

The four walls that the frame of $1\gamma2\varepsilon$ consists of are treated as bodies of the granular assemblies, just in the same way as all other particles (disks). In particular, they are modelled as circles with very high radii, so that their higher mass is accounted for (a mass of 100 times the mean mass of a particle is assumed, for simplicity). As for the contacts between grains and walls, the definition of their (punctual) location and local reference is made separately: contact points are placed in their correct location (as it would come from simply considering the real shape of walls), and normal unit vectors are oriented perpendicularly to the walls – again, assumed as linear –, with tangent unit vectors defined accordingly.

The application of boundary conditions requires imposing constant values to either stresses (forces) or velocities to the edge bodies (*i.e.*, the four walls of the frame). To do this, two different ways had been tested by Richefeu et al. (2013): either imposing measured velocities for all boundaries, or constant stress on one boundary and imposed velocity on all other, so that the obtained solution in forces could also be scaled with the imposed stress.

With this approach, however, some limitations were underlined. The capability of obtaining a plausible (and consistent with the applied boundary conditions) solution, in general, required the use of forces from previous time steps as initial guess; otherwise, inconsistent and unrealistic solutions could be found when initialising forces to zero. This introduces a strong requirement on the frequency of data acquisition, since the use of previous forces can only be made when the two states are close enough, in terms of contact network (*i.e.*, contacts are mostly maintained) and values of forces.

In this doctoral work, a slightly different technique is adopted for the application of boundary conditions. A constant normal force is imposed on two walls (top and right);

its value comes from the force extracted, at the time corresponding to the considered state, from the measurement of the machine. These forces are generally split in two components, a vertical and a horizontal one, because the walls might not be perfectly vertical and horizontal, even in tests in which no tilting of the frame is imposed. This approach also allows an extension of the application of the CDM to the case of simple shear tests, in which the initially vertical walls rotate throughout the test, and tangential forces at the boundary are not negligible.

Similarly to Richefeu et al. (2013), the use of imposed forces as boundary conditions guarantee the good scaling of forces, as it is confirmed by the good quantitative agreement between the homogenised stress from CDM-estimated forces and the applied stress (as it will be shown in the following sections). In addition to this, the technique used herein proves more robust in the determination of a plausible solution: pathological cases that were found in the previous work are avoided here, and consistent solutions could always be found, even when no initial guess was provided for the contact forces. This is extremely important, as it allows the estimation of forces with no need for information on the previous history of the packing, and no requirement on the frequency of data acquisition: in principle, a realistic solution can always be obtained in this way, by simply knowing the boundary conditions and the current contact network.

In the modelling of contacts between particles and walls, a specific case must be taken into account for particles close to the four corners of the frame. As it can be seen from any photograph of the specimen (*e.g.*, Figure 4.1), in correspondence of each corner the walls have a curved connection. When particles are in contact with this part of the boundary, the local reference associated with the contact cannot be defined with respect to any of the walls, and a new reference should be defined. Therefore, it was decided to introduce four new bodies (disks) representing the four corners, with a radius defined by the curvature radius of the wall in the corner (easily measurable during the image processing phase), each of them being in contact, at the same time, with both walls converging into that corner. The local reference of contacts between particles and corners, on the other hand, was defined as for any other particle-particle contact, *i.e.*, with the normal unit vector along the branch vector connecting the two disks centres (and the tangent one defined accordingly).

Although a deeper quantitative assessment of the solution could not be performed at this stage, as for the QSM, these observations already show important improvements in the use of Contact Dynamics for the estimation of forces. A qualitative evaluation could be performed, with the same tools already used for the other two methods; its results are shown in the following sections.

#### 4.2.3.1 Oedometer compression

As usual, the evaluation of the obtained set of contact forces begins with the comparison between the applied stress, measured during the test, and the homogenised stress derived, via Weber's expression, from micromechanical quantities (contact forces and branch vectors). For the application of the CDM to the case of oedometer compression, this result is shown in Figure 4.32. As for the QSM, the evolution of both normal components of the stress tensor, $\sigma_{xx}$ and $\sigma_{yy}$, is correctly retrieved, not only from a qualitative point of view, but also from a quantitative one.

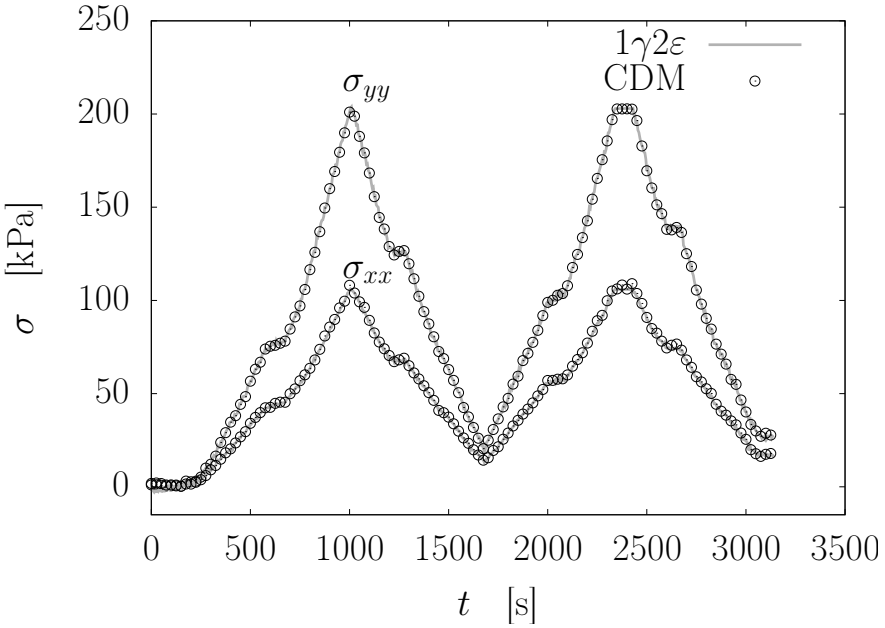


Figure 4.32 – Comparison between the $1\gamma2\varepsilon$ macroscopic stress components and the Weber stress components computed from contact forces estimated via the CDM to an oedometer compression test. For sake of clarity of the plot, one CDM stress point is drawn every 5 states.

In Figure 4.33, the map of normal forces in a single state (at the end of the first loading cycle) confirms, also at the contact-scale, that the obtained solution is plausible and realistic. Similarly to the QSM case, force chains are clearly appearing here, and mainly in the vertical direction, consistently with the applied loading conditions; ring-like structures emerge as well. Force chains also show continuity, *i.e.*, they are not interrupted, but they tend to cross the whole sample area (in particular from top to bottom).

As it has been done for the QSM solution, the distribution of normal forces for a given state is also analysed here, in order to look for common features of force distributions in granular media. Figure 4.34 shows the probability distribution of normal forces, for the same state as in the previous results analysed in this section. The distribution

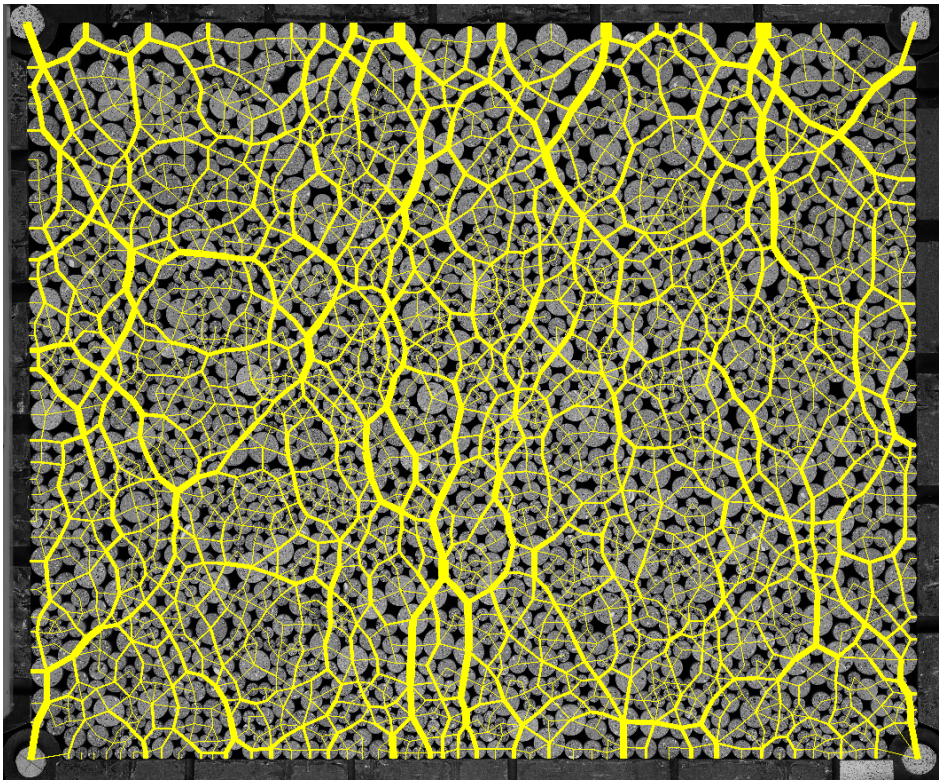

Figure 4.33 – Map of normal contact forces obtained via Contact Dynamics at the end of the first loading cycle of the oedometer compression test. Line thickness of the branch vectors is proportional to normal force intensity. The largest normal force is around 1000 N.

covers a relatively high range, going from 0 to 7 times the average normal force; the tail seems to indicate that above-average normal forces have an exponential decay (fair linear interpolation in a log-scale), although not clearly, as in the QSM. The PDF is also compared with the distribution of QSM-estimated normal forces; a similar behaviour is observed, although the solution of CDM covers a wider range than the QSM solution, reaching slightly higher values of normal forces.

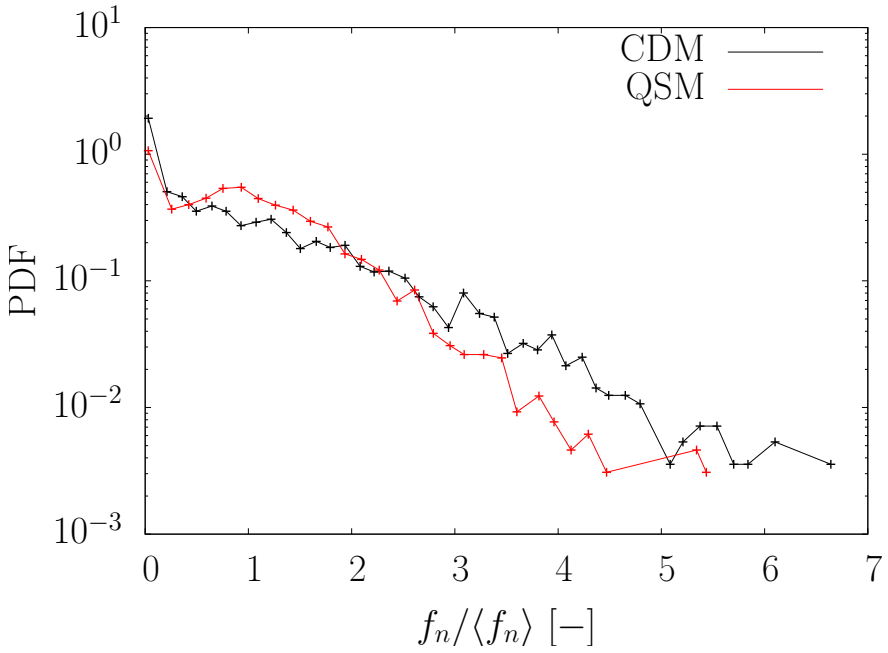


Figure 4.34 – Probability Density Function of normalised normal forces, estimated via the CDM at the end of the first loading cycle of an oedometer compression test. The PDF obtained with the QSM for the same state is shown for comparison.

As it was already discussed for the application of the QSM, a further quantitative evaluation of the obtained solution is not possible at this stage, and the estimated set of forces, although consistent with the macroscopic loading and capable of reproducing the applied stress, has to be regarded as only one of the possible solutions, due to the non-uniqueness issue discussed in the previous chapters.

The effect of non-uniqueness can be assessed by looking at how the solution evolves during the test, *i.e.*, how it changes between two consecutive states. Even if the force variability might be high (which is typically the case for dense specimens), the effect on the estimated solution can still be limited. To assess this effect, Pearson correlation coefficient is computed for normal (and tangential) forces estimated at consecutive states of the oedometer compression test, and its evolution is shown in Figure 4.35. It is observed that, after some load steps ($\approx$ 100, approximately corresponding to the middle

of the first loading cycle), the correlation becomes very high ($r \approx 1$), showing a good persistence of the obtained solution.

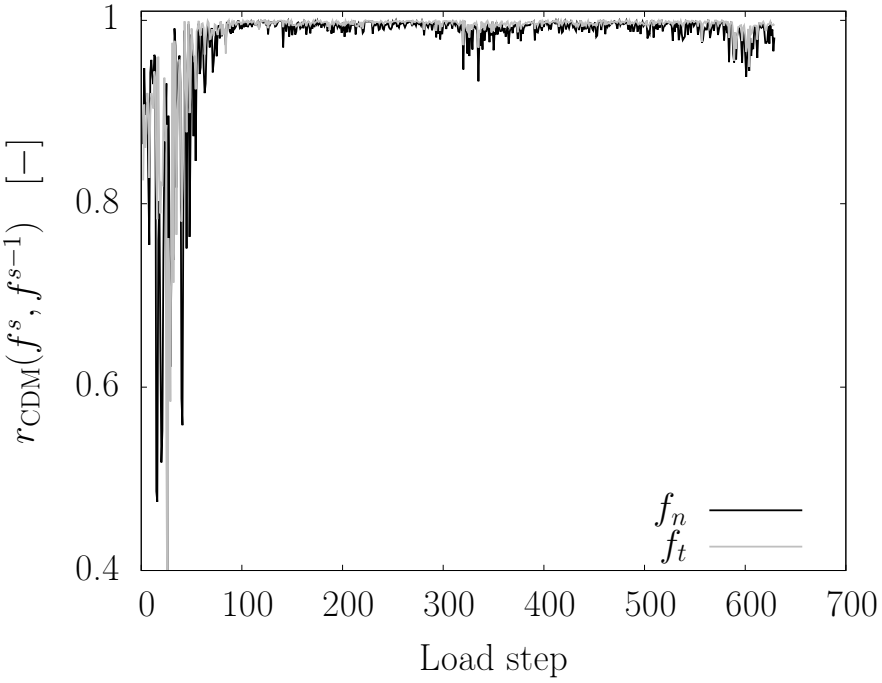


Figure 4.35 – Evolution of Pearson's $r$ for normal and tangential forces estimated via the CDM in consecutive states of an oedometer compression test.

#### 4.2.3.2 Isotropic compression

The test is the same already studied with the QSM in Section 4.2.2.2. It is composed of five consecutive loading cycles; however, for sake of brevity, only data from the first loading cycle is shown in the evolution of the homogenised stress components in Figure 4.36. The tangential stress component $\sigma_{xy} \approx \sigma_{yx}$ is also plotted here. The comparison of all stress components shows a very good agreement with the stress applied by the machine at each load step; it is also important to remark that the tangential components are correctly found to be much smaller (almost negligible) than the normal components $\sigma_{xx}$ and $\sigma_{yy}$.

#### 4.2.3.3 Biaxial vertical compression

The estimation of forces for the case of biaxial vertical compression returns an evolution of the homogenised stress that, once again, reproduces very well the real macroscopic stress from a qualitative point of view: tangential components are found to be negligible

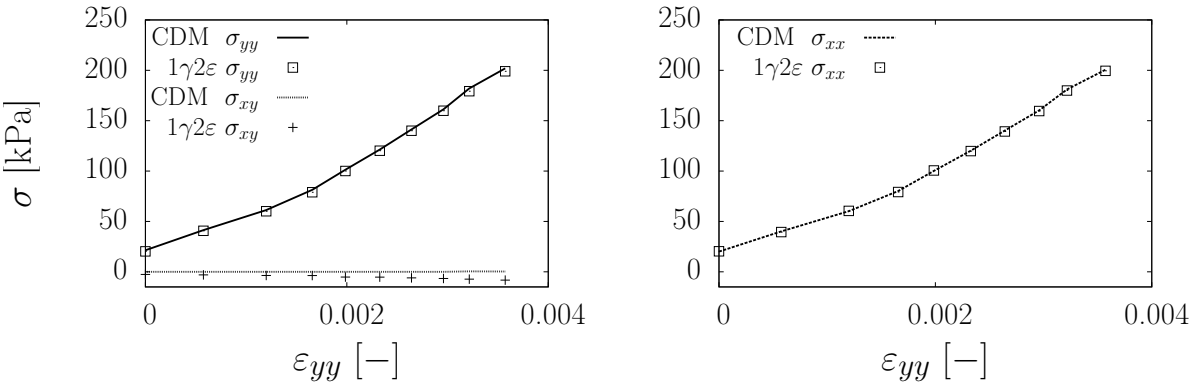


Figure 4.36 – Comparison between the $1\gamma 2\varepsilon$ macroscopic stress components and the Weber stress components computed from contact forces estimated via the CDM to the first loading cycle of the isotropic compression test. Please note that $1\gamma 2\varepsilon$ stress components reported here do not come from a continuous measurement: they are just linear interpolations of points corresponding to the load steps.

with respect to the normal components, and small drops in the stress evolution, generally due to grain rearrangements, are also retrieved. However, from a quantitative point of view a slightly worse agreement is found, with respect to the oedometer and isotropic compression tests, with errors up to 10% for the vertical normal stress $\sigma_{yy}$ and 20% for the horizontal stress $\sigma_{xx}$.

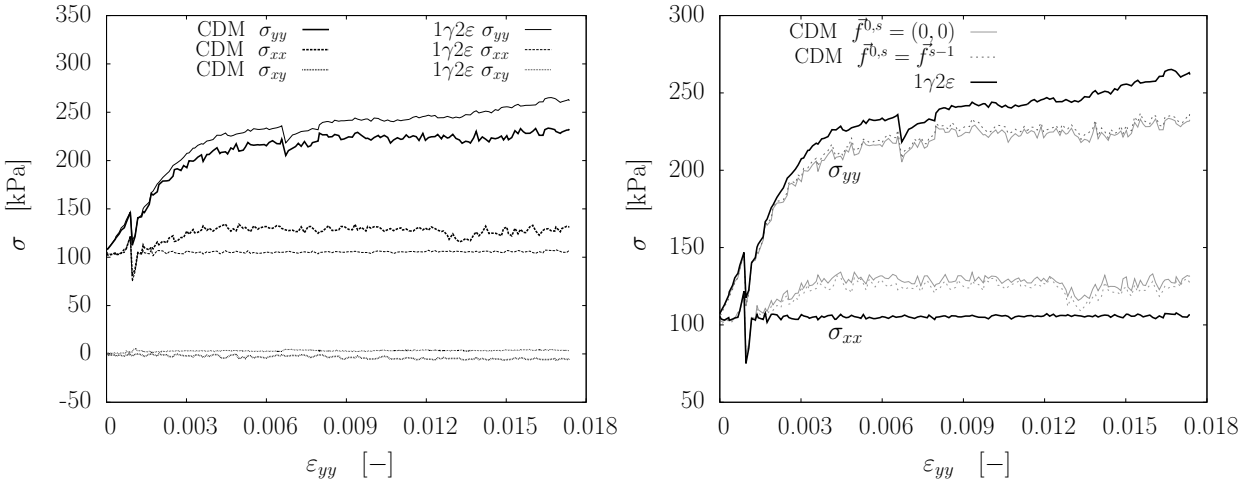


Figure 4.37 – (Left) Comparison between the $1\gamma 2\varepsilon$ macroscopic stress components and the Weber stress components computed from contact forces estimated via the CDM in a biaxial vertical compression test. (Right) Homogenised stress components when forces are initialised to null values and when they are initialised to the values from the previous state.

An attempt was made to assess the influence of using previously computed forces, which proved to be a useful tool in the CDM for the improvement of the quality of force

estimation in the application to numerical data. Figure 4.37 also shows the comparison between the homogenised stress components from forces computed in this way and the stress components obtained when forces are initialised to zero (always with the experimental stress components as reference): only a slight, almost negligible improvement in the agreement with the real stresses is obtained.

Due to the continuity of the data acquisition, with photographs taken at a relatively high frequency (every 5 s) with respect to the rate of the applied loading, just as in the oedometer compression case, it is possible to assess the persistence of the solution also for this test, by comparing the force network between consecutive states, through the computation of the Pearson correlation coefficient. For the biaxial vertical compression, this is done for both applications, *i.e.*, the standard one (when the Gauss-Seidel iterator starts with null forces) and the one in which forces estimated in the previous state are used as an initial guess for the iterative procedure in the new state. The evolution of $r$ for the two cases is compared in Figure 4.38. Similarly to the case of oedometer compression, a good persistence is obtained, in general, after a certain number of load steps. Moreover, as expected, the use of previous forces clearly improve the persistence: in this case, we have $r \approx 0.95$ for both normal and tangential forces, for the whole duration of the test (while $r(f_n) \approx 0.9$ and $r(f_t) \approx 0.8$ when forces are initialised to zero).

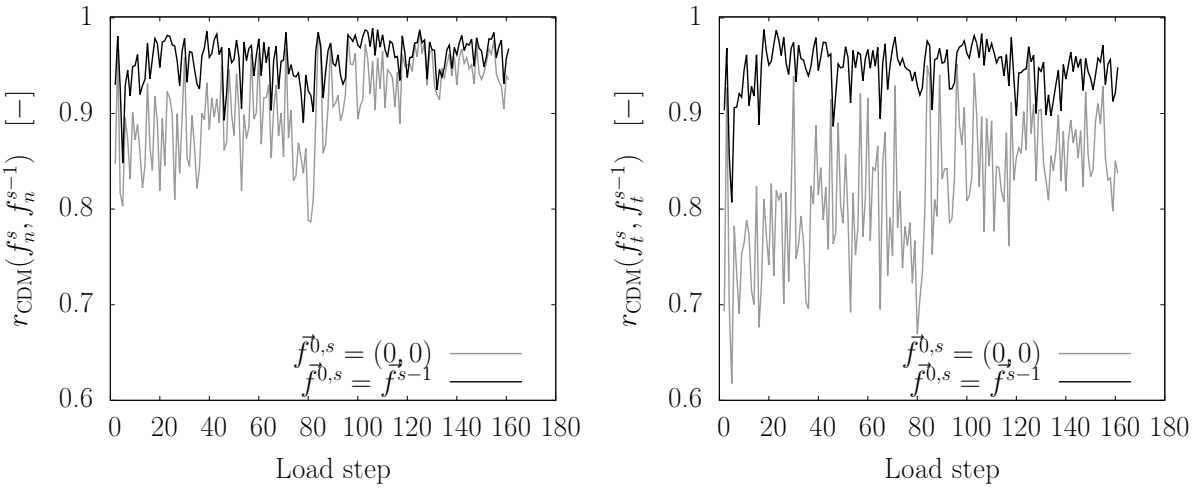


Figure 4.38 – Evolution of Pearson's $r$ for normal (left) and tangential (right) forces estimated via the CDM in consecutive states of a biaxial vertical compression test, with and without using previously computed forces as initial guess for the next state.

#### 4.2.3.4 Biaxial horizontal compression

The application of the CDM to force estimation in the case of biaxial horizontal compression yields similar results as for the biaxial vertical compression test. The homogenised stress determined from contact forces generally shows a good agreement with the experimental stress, although an error of approximately 10% is made in the estimation of the vertical normal stress $\sigma_{yy}$ towards the end of the test, while a better agreement is obtained for $\sigma_{xx}$. Tangential stress components, as expected, are found to be negligible with respect to the normal stress components.

As it has been done for vertical compression, contact forces are also estimated, in a second stage, using forces from the previous load step as initial guess for the current state (Figure 4.39b). Similarly to the previous test, this only results in a very little reduction of the error on $\sigma_{yy}$.

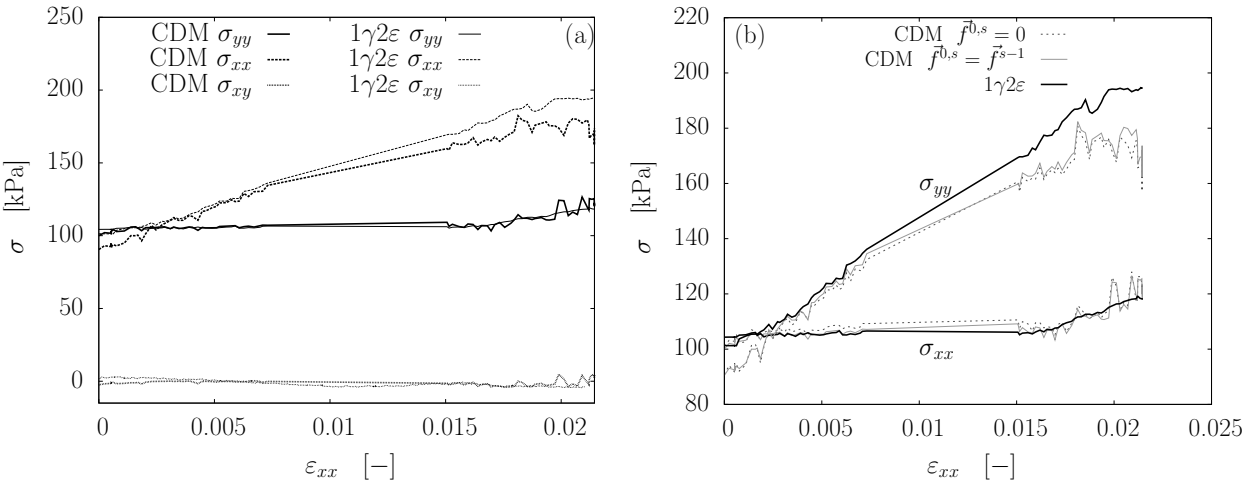


Figure 4.39 – (Left) Comparison between the $1\gamma2\varepsilon$ macroscopic stress components and the Weber stress components computed from contact forces estimated via the CDM in a biaxial horizontal compression test. (Right) Homogenised stress components when forces are initialised to null values and when they are initialised to the values from the previous state.

### 4.2.4 Comparison between the three methods

Some preliminary conclusions can be deduced by summing up the main outcomes of the application of the three methods (CEM, QSM and CDM) to the estimation of contact forces from experiments.

At this stage, the CEM cannot be considered as a reliable way of assessing forces from

experiments: the difficulty of describing contact deformation through a simple model as the one used in common MD-DEM (rigid particles with compliant contacts) imposes the use of different kinematic variables; with the assumed force law, the error on forces, essentially coming from measurement inaccuracy, is found to be far too high (in the order of the average normal force) to get a realistic solution. A third aspect that should discourage from the adoption of this technique lies in the impossibility of estimating forces in already loaded states: the method requires the knowledge of the evolution (*i.e.*, particle motion) between two states to compute force increments; any pre-existing contact force cannot be determined. The fact of recovering more or less a qualitative evolution of the stress can be explained by recalling that the anisotropy of the contacts is well captured, as well as the mean force can be fairly well estimated with the re-scaling procedure. These two ingredients may be sufficient to approximate the macroscopic response, as suggested by Rothenburg and Bathurst (1989), even if the forces themselves are far from the actual ones. It should also be recalled that another strong limitation of the method is that it never accounts for mechanical equilibrium.

In perspective, however, the method might still prove useful provided that the combination of measurement resolution (*i.e.*, scale of the photographs) and particle deformability (and, consequently, contact stiffness) results in a lower error: in this scenario, the estimation of forces – especially normal forces – on the basis of contact deformation measurements, even if not sufficiently realistic (*e.g.*, if the obtained solution is reputed non-plausible based on the common qualitative observations made in the previous sections), can still prove useful in combination with other methods, for example as an initial guess for the QSM.

A possible improvement could also be achieved through the choice of a more suitable force law, that may be capable of describing the observed force-displacement response at the contact-scale with a better precision.

As for the two other methods – QSM and CDM –, several qualitative – and, to some extent, quantitative – observations showed that they yield more plausible results. Estimated forces reproduce with a good accuracy the macroscoping loading conditions; the network of forces shows the typical structures of force organisation in granular media (force chains and ring-like structures, particularly evident for the CDM), as it is shown by a comparison of such maps for the three methods, in Figure 4.40.

It is also interesting to focus on the distance from static equilibrium of all particles in the assembly, and take it as a first, rough measure of the accuracy of the method, given the assumption that, the original test being performed in quasi-static conditions, the obtained solution should not be far from such a situation. This is particularly ap-

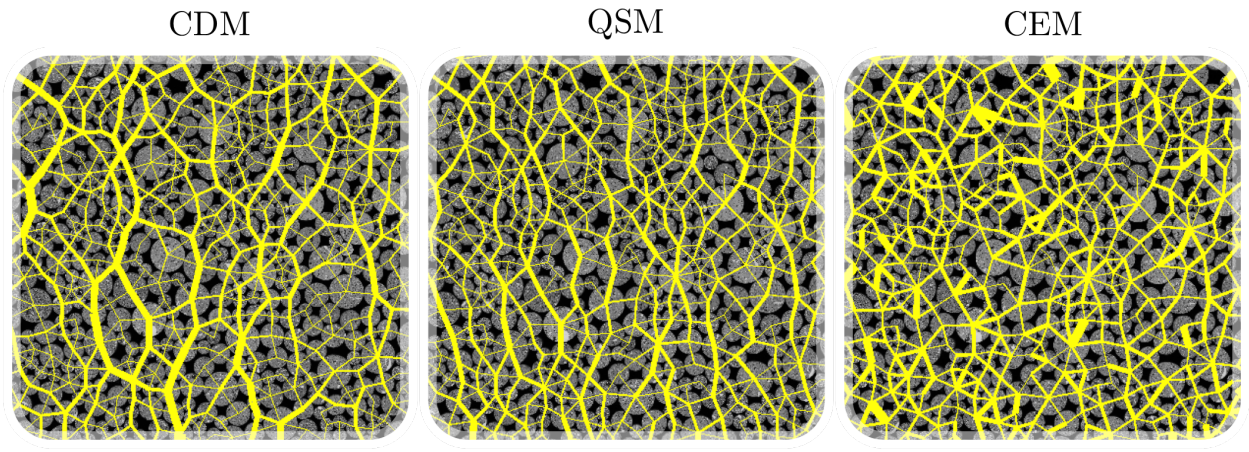


Figure 4.40 – Map of normal contact forces obtained with the three methods at the end of the first loading cycle of the oedometer compression test: zoom on a part of the specimen. Line thickness of the branch vectors is proportional to normal force intensity.

propriate for the QSM, in which static equilibrium is also a requirement of the method, *i.e.*, a criterion that, through the iterative procedure, we seek to fulfil. A distance from static equilibrium is then defined, as the magnitude of the unbalanced force normalised by the average normal force over all contacts. Figure 4.41 shows the distribution over all particles $i$ of such a distance, computed as the magnitude of the resultant force (normalised by the average normal force). It is confirmed by this result that the solutions obtained with the CDM and QSM are much more reliable: the highest "error" for both methods is around 10%, and for most particles ($\approx$ 90%) it stays below 1%. The CEM, on the contrary, gives an average error in the order of the average normal force.

The main issue associated with the QSM and CDM lies in the non-uniqueness of the solution. Although in the validation phase (Chapter 3) it has been proven that this can be limited by exploiting information on contact deformation, to have at least a first estimate of normal forces (QSM) or to fix their values and reduce the number of unknowns of the problem (CDM), in experiments this is more difficult, since a good, reliable estimation of normal forces based on contact deformation cannot be easily obtained. Therefore, force variability remains an issue that one has to consider: while a plausible solution can be obtained with both methods, this solution is only one among all the possible solutions. However, the effect of this indeterminacy is found to be limited when comparing force networks in consecutive states: for almost the whole duration of the considered tests, forces do not undergo dramatic changes, and similar solutions are obtained for states with little or no change in the contact network and in the boundary conditions. This outcome is even clearer when, for Contact Dynamics, forces from the previous state are

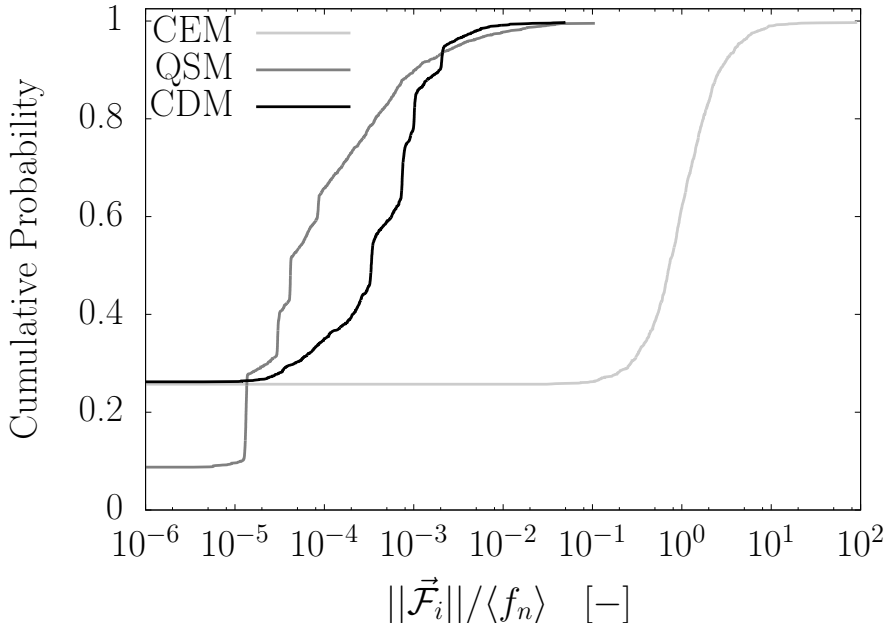


Figure 4.41 – Cumulative distribution function of the distance from equilibrium for all particles, at the end of the first loading cycle of the oedometer compression test, in the solutions obtained with the three methods.

re-used as an initial guess to the Gauss-Seidel iterator for the current step.

Comparing the QSM with the CDM, it can be concluded that the latter provides the most realistic solution, based on the assessment of the error, intended as the distance from static equilibrium (considering that the tests were performed in quasi-static conditions), and on the distribution of normal forces, that shows agreement with general features of force distribution in granular media mainly in CDM's application, and less for the QSM.

# Chapter 5

# Conclusions

## 5.1 Summary and conclusions

The objective of this doctoral work is to suggest possible methods to experimentally measure inter-particle forces in granular materials. The main objective is to discuss new approaches that, with respect to some of the methods proposed in the last years by other authors – listed in Chapter 1 –, would benefit from two main novelties: the limited amount of measurement required to provide an estimation of forces, and the applicability to a wider range of materials, in particular overcoming any constraint related to the stiffness of the particles.

As a result of this, the experimental data from which we aim to determine contact forces do not include measurements of a strain field inside each single particle. The only experimental measurements that are needed consist of boundary conditions, geometrical arrangement and particle rigid body motion.

Based on this input, three methods for contact force estimation are introduced and described in Chapter 2. Working with granular materials, it was natural to take inspiration from the DEM framework for building these methods. In particular, each of them is based on a different Discrete Elements approach, and its working principles depend on the main properties of the method that it is inspired to.

The first method, referred to as Contact Elasticity Method (CEM), comes from the Molecular Dynamics DEM, from which it takes the idea of determining contact forces directly from the micro-scale kinematics of the assembly (contact relative displacements that come from particle motion), assuming appropriate force laws (linear elasticity for normal forces and elasto-plasticity for tangential forces).

The second method, referred to as Quasi-Static Method (QSM), stems from the quasi-

static approach that aims to solve a granular system, in the sense of determining the contact forces transmitted between particles, by discretising the evolution of the system in a number of equilibrium states, in which contact forces can be determined, given a contact network and boundary conditions, through a numerical resolution that imposes the fulfilment of static equilibrium at all particles and plastic admissibility (Coulomb's friction law) at all contacts.

Finally, the Contact Dynamics-based Method (CDM) applies the framework of Contact Dynamics to single states, in which, given a contact network and some initial conditions (*e.g.*, boundary conditions), contact forces are determined by running the Gauss-Seidel iterator for the resolution of the multi-contact problem (equation of dynamics crossed with the adopted contact laws).

A major difference between these three methods lies in the way the history of the packing is treated, which has a direct outcome in the characterisation of the solution obtained. For the CEM, the knowledge of the current state (granular arrangement – *i.e.*, contact network – and boundary conditions) is not sufficient for the estimation of forces: it is also necessary to know how the system evolves before reaching the current configuration. This consists in defining particle motion during the whole evolution of the granular assembly: in this way, contact relative displacements can be determined and injected into appropriate force laws, which provide a unique value for contact forces. The other two methods do not require the knowledge of the history of the packing: for both of them, contact forces can be determined for single states, independently of how the granular system evolves between them. This is clearly a strong advantage, for an application to experiments; however, it comes with a drawback, *i.e.*, the non-uniqueness of the solution. This means that any solution estimated with one of these two methods is only one among the many possible solutions, and it was demonstrated by McNamara and Herrmann (2004) that this indeterminacy comes from neglecting the history of the packing.

The proposed methods have first been tested and validated by using synthetic data extracted from Molecular Dynamics two-dimensional simulations of biaxial vertical compression (Chapter 3). In a second stage (Chapter 4), the methods have been applied to actual measurements from experiments. The validation phase has helped highlighting the main features of the three methods, their weaknesses and advantages; it has also allowed an assessment of their ability to provide an estimate of forces, and a prediction of the relative accuracy and reliability.

Concerning the CEM, the dependence on the history of the packing might represent an issue when force estimation is based on non-continuous measurements: in particu-

lar, the loss of information on particle motion between two consecutive measurements is expected to affect the quality of force estimation. This issue has been assessed by evaluating the error as a function of the time interval (linear with the amount of applied displacement) between consecutive states; as expected, it is observed that the error increases as the loss of displacement history increases. Putting aside measurement inaccuracy – that is another main source of error –, a good estimation of forces with the CEM requires to minimise the amount of particle motion occurring between two distinct measurements, which can be attained by either slowing down the evolution of the system, or increasing the frequency of measurements.

As for the other two methods – QSM and CDM –, the non-uniqueness of the solution is a main issue. Force indeterminacy has been characterised through the parameter $h$, that can be associated with some geometric properties of the sample: for a given assembly, a higher number of contacts (or coordination number) generally results in a higher indeterminacy. For both methods, force estimation is found to be affected by this indeterminacy: in particular, a better agreement between the estimated solution and the reference one is obtained for assemblies with a lower degree of force indeterminacy.

However, it is not sufficient to be aware that the solution is not unique; it is also important to characterise and quantify its variability, so that the accuracy of force estimation can be somehow predicted. An attempt for this has been made, following the same approach as in Unger and Kertesz (2003), in the application of the CDM to a small system, for which it is possible to build a number of admissible solutions by imposing different initial conditions. Assuming that this is representative of the whole force space of the system, some parameters are introduced to describe the size of this space; crossing such quantities with the results of force estimation shows a correlation between the accuracy of estimated forces, obtained when zero initial forces are assigned, and their variability.

While useful to assess the reliability of the force solution estimated with the QSM or the CDM, a deeper and more accurate characterisation of force indeterminacy does not solve the problem. To reduce the influence of force indeterminacy, the length scale associated with contact deformation is re-introduced in both methods. In the context of the application to ideal experiments (MD simulations), this simply consists in estimating normal forces from the measurement of a particle interpenetration. Using this as an initial guess for the iterative solver turns out to be enough, for the QSM, to almost eliminate the non-uniqueness issue, in that a lower error is found, independently of the degree of force indeterminacy of the assembly. For the CDM, the simple use of the elastic solution in normal forces as an initial guess for the Gauss-Seidel iterator is not sufficient:

however, by fixing normal forces to constant values – and estimating only tangential ones – the targeted solution can always be retrieved.

After this validation phase, the methods have been applied to real experiments (Chapter 4) on a 2D-analogue granular material composed of rods with a circular section, equivalent to the disks used in the simulations that are object of the validation phase.

The CEM proves unable to provide a realistic estimation of forces from experiments. In the first place, a difficulty is encountered in the definition of measurable quantities that can describe contact deflection and be injected into appropriate force laws. In fact, the typical MD-DEM model of rigid particles that can overlap due to compliant contacts does not apply well to this case: while the assumption of undeformed particles seems appropriate, the definition of a quantity equivalent to particle interpenetration in simulations is not easy. This model is then replaced by the adoption of an incremental force law also for normal forces, based on the computation of contact relative displacements from particle rigid body motions. However, a rough quantification of the expected error, simply coming from measurement inaccuracy, returns a too large uncertainty, in the order of the average normal force; the obtained solution, therefore, cannot be considered reliable. This is confirmed by several results that show a fair agreement with experimentally-measured quantities only in qualitative terms, while being inconsistent from a quantitative point of view. It should also be recalled that this technique has two more main disadvantages, *i.e.*, the impossibility of estimating forces in already loaded states, and the fact of never accounting for mechanical equilibrium.

The other two methods are more suitable to experimental applications, because of their main features highlighted in the validation phase; among them, the fact of requiring fewer input data – only the geometry of the packing and boundary conditions – and, consequently, the possibility of obtaining an estimate of forces without knowing the previous history of the packing. Related to this, also the higher robustness of the methods is an important aspect: the main source of inaccuracy to be considered is the error in contact detection; however, the validation phase shows that the influence of this error is rather limited, *i.e.*, the obtained solution is only slightly affected by the error that is expected in experimental measurements.

The results of the application of both methods to experimental data confirms their better suitability for the estimation of forces, with respect to the CEM. The homogenised stress computed from estimated forces shows a good agreement with the stress applied and measured by the experimental device, not only qualitatively but also quantitatively. Focusing on single states, the visualisation of maps of normal contact forces shows the typical features of force organisation in granular materials, *i.e.*, the appearance of force

chains, mainly along the direction of maximum compression of the system, and of ring-like structures. The distribution of the obtained normal forces also shows a good agreement with common features of granular materials, such as the relatively high width of the range of values covered by normal forces, and the almost exponential tail for strong (above-average) forces. This is important because it can be deduced that, even in case the exact values of individual forces could not be retrieved, knowing their distribution is already sufficient to define the range of values they cover and the probability associated to each value in this range. Finally, estimated forces are compared between consecutive states of the tests, showing a satisfactory persistence of the whole network: despite the non-uniqueness of the solution, already discussed in the validation phase, similar sets of forces are retrieved for similar conditions (in terms of contact network and applied load).

The non-uniqueness of forces, however, remains an important constraint: the estimated solution, though plausible and consistent with the boundary conditions, is only one of the possible solutions. Therefore, some strategies are implemented for the reduction of force variability. In the application to numerical data, a unique solution can be retrieved by exploiting measurements of contact deformation, thanks to the simple adopted model for particle interaction; in the experimental application, on the other hand, a good approximation of normal forces cannot be easily obtained, as explained with respect to the CEM's results. In order to improve the quality of force estimation by reducing the variability of forces, a possible strategy is to use the solution obtained from previous states as initial guess to the current state. This is done for the CDM; however, this procedure does not change dramatically the result.

Some additional remarks are necessary when it comes to identifying the most suitable of either method to force estimation in experiments. Though a quantitative evaluation of the obtained solution in experiments is not easy, some observations show that the solution provided by the CDM is more reliable: the distribution of CDM's normal forces shows a better agreement than the QSM's one with typical features of force distribution in granular media; in general, the ability of the CDM to treat particle rearrangements makes it more suitable to deal with measurement error resulting in a bad detection of the contact list.

The main novelty of this work lies in the simplicity of the proposed methods, which require fewer input information with respect to other methods of contact force measurement that were developed in the past. A second objective was to enlarge the range of applicability: since no measurement of particle internal deformation is needed, all the three methods – in particular the QSM and the CDM – can be applied to assemblies of

very stiff particles. More generally, while other methods are only applicable to systems with "soft" particles (with respect to the resolution of the system), this would no longer represent a limitation with the approach we propose. Force estimation could be extended also to systems with smaller particles, that means, at the same time, a larger number of particles – and so a specimen that is more representative of material properties –, for a given size of the system. The ability to deal with stiff particles, for which measurable intra-particle deformations cannot be easily accessed, is especially valuable in the perspective of an application to the materials of geomechanical interest, since quartz and other minerals composing the most common granular materials in geomechanics, *i.e.*, sand, typically have a high stiffness in comparison with the relatively low stresses that they undergo in the most common engineering applications.

## 5.2 Future work and perspectives

Due to the exploratory character of this work, there is still room for several future advances and improvements for each of the proposed methods, including the CEM. In fact, despite turning out to be unable to provide a realistic estimate of forces in this case study, this method can still prove very useful in a future perspective. First, the reliability of CEM-estimated forces can be improved by increasing the accuracy of experimental measurements: this requires an increase in either the deformability of the particles or the resolution of measurements (or both at the same time). Another enhancement of the method might come from the adoption of a more advanced, non-linear force law, that may better describe the complex contact behaviour observed during the single contact compression test. However, the inaccuracy coming from measurement error is expected to be predominant; moreover, the influence of the choice of a contact model is not easy to be assessed as it cannot be easily decoupled from other sources of error.

Despite its limitations, the CEM may still prove useful in combination with the other methods: in particular, the estimation of normal forces from measurements of contact deformation could provide a first approximation to be used in the QSM or the CDM. This can be intended as a way of re-introducing the length scale associated with contact deformation, that is neglected in the CDM; in general, for both methods, it would also represent a way of partially accounting for the history of the packing, and, in doing so, overcoming the issue of non-uniqueness of the solution through a reduction of the variability of forces.

Some additional remarks can be made, in general, on the challenges associated with the application of the three methods to more complex situations. Both the validation

phase and the experimental application described in this work are carried out on model specimens, consisting of 2D (or 2D-analogue) granular packings made of circular particles. It is important to underline that, despite this, all the three methods, in principle, can be applied to non-idealised materials, allowing 3D application and the use of particles with any shape. In fact, none of them poses conceptual limitations in this regard: the main principles of the three methods are directly taken from the DEM approaches they are inspired from, all of which allow this kind of extension.

As to the mathematical formulation of the methods, moving from 2D to 3D would only result in an increase of the number of variables of the problem. Particle shape would not generally introduce any complexity in terms of contact laws; only the relations between particle-based and contact-based quantities, which characterise both the QSM and the CDM, would be slightly more complex.

An improvement of the QSM might be achieved by studying the stability of equilibrium and taking it into account in the formulation of the method. A stability criterion, such as the one expressed by the second-order work, can give more information on the nature of the equilibrium states, and possibly help reducing the variability of forces by separating all possible equilibrium states with respect to their stability.

In terms of more technical challenges, the application to real cases would only introduce some further complexity in contact detection and, more generally, measurement accuracy. For example, the high resolution provided by camera devices in 2D photographs is generally not reproducible with 3D imaging devices. In particular, contact detection is a major issue in these cases, with a systematic problem of overestimation of the number of contacts (Wiebicke et al., 2017). Both the QSM and the CDM, anyway, show a certain robustness with respect to such inaccuracies. Non-idealised shapes would also require more advanced procedures for contact detection (as, *e.g.*, in Kawamoto et al. (2018)).

What is still missing in the application of the proposed methods is a metric allowing the quantification of the accuracy with which forces are determined. A way of validating the estimated forces can be represented by the comparison with those obtained with any of the methods that were developed in the previous years. In particular, it would be interesting to see if methods that exploit measurements of particle deformations can get to a similar solution as methods that do not rely on these measurements, such as those proposed here.

Moreover, it is demonstrated that the combination of some of the proposed methods (QSM, CDM) with part of other methods results – in particular, with normal forces estimated through contact deformation measurements – seems a promising way of improving the accuracy of force estimation. With the same principle already discussed for

the combination with the CEM – which, on the other hand, cannot provide a reliable estimation of normal forces yet –, any other method can be used to get a first approximation of normal forces. Then, by injecting it in the QSM, it is expected that it can get to a solution that reproduces very well the full set of forces. Of course, this approach can be adopted also for the CDM, although the QSM proves more suitable for finding a solution (in terms of both normal and tangential forces) when starting from an approximated one as initial guess, provided that a contact network capable of supporting the applied load is given.

A better understanding of the proposed methods, and of their applicability to real cases, might come from applications on different materials (*e.g.*, aluminium, polyurethane). This was already discussed regarding the CEM, for which, in particular, a lower contact stiffness might help reduce the error in the determination of force increments; however, it could be also useful to test the applicability of the other two methods to specimens that show different properties, due to different material deformability and interparticle friction coefficient. These differences can cause a change in the coordination of the assembly, and, so, in the degree of force indeterminacy, whose influence on force estimation with the QSM and the CDM was previously shown. Some effects of the change in the deformability of the particles (and so in the contact stiffness) were already predicted in the application to numerical data, for which different cases were tested; in the same way, it would be appropriate to reproduce the same analysis in experiments. In particular, for lower stiffnesses it can be expected that the specimen, for given loading conditions, shows a higher coordination and force indeterminacy; at the same time, however, the higher deformability would make contact detection easier, and so the contact network more reliable, due to larger intra-particle deformations. The opposite can be expected for stiffer materials, which are supposed to be more suitable especially for the application of the CDM, that bases all its formulation on the assumption of contact rigidity.

In addition to all these observations, it should be recalled that the three methods are all based on advanced measurements that are part of the grain-scale characterisation of granular materials; any foreseeable technological advance in this field is something that all methods would certainly benefit from.

# Bibliography


Allersma, H. G. B. (1982). Determination of the stress distribution in assemblies of photoelastic particles. *Experimental Mechanics*, 22(9):336–341.

Andò, E., Hall, S., Viggiani, G., and Desrues, J. (2012). Experimental micromechanics : grain-scale observation of sand deformation. *Géotechnique Letters*, 2(3):107–112.

Andrade, J. E. and Avila, C. F. (2012). Granular element method (GEM): Linking interparticle forces with macroscopic loading. *Granular Matter*, 14(1):51–61.

Andrade, J. E., Avila, C. F., Hall, S. A., Lenoir, N., and Viggiani, G. (2011). Multiscale modeling and characterization of granular matter: From grain kinematics to continuum mechanics. *Journal of the Mechanics and Physics of Solids*, 59(2):237–250.

Blair, D. L., Mueggenburg, N. W., Marshall, A. H., Jaeger, H. M., and Nagel, S. R. (2001). Force distributions in three-dimensional granular assemblies : Effects of packing order and interparticle friction. *Physical Review E*, 63(4):1–8.

Calvetti, F., Combe, G., and Lanier, J. (1997). Experimental micromechanical analysis of a 2D granular material: Relation between structure evolution and loading path. *Mechanics of Cohesive-Frictional Materials*, 2(2):121–163.

Chu, T. C., Ranson, W. F., and Sutton, M. A. (1985). Applications of digital-image-correlation techniques to experimental mechanics. *Experimental Mechanics*, 25(3):232–244.

Ciamarra, M. P., Lara, A. H., Lee, A. T., Goldman, D. I., Vishik, I., and Swinney, H. L. (2004). Dynamics of drag and force distributions for projectile impact in a granular medium. *Physical Review Letters*, 92(19):1–4.

Combe, G. and Richefeu, V. (2013). TRACKER: A particle image tracking (PIT) technique dedicated to nonsmooth motions involved in granular packings. *AIP Conference Proceedings*, 1542:461–464.

Combe, G., Richefeu, V., Stasiak, M., and Atman, A. P. F. (2015). Experimental Validation of a Nonextensive Scaling Law in Confined Granular Media. *Physical Review Letters*, 115(23):1–5.

Combe, G. and Roux, J.-N. (2011). Construction of granular assemblies under static loading. In *Discrete-element Modeling of Granular Materials*, chapter 6, pages 171–201. Wiley-ISTE.

Coppersmith, S. N., Liu, C.-H., Majumdar, S. N., Narayan, O., and Witten, T. A. (1996). Model for Force Fluctuations in Bead Packs. *Physical Review E*, 53(5):4673–4685.

Cundall, P. A. and Strack, O. D. L. (1979). A discrete numerical model for granular assemblies. *Géotechnique*, 29:47–65.

Da Cruz, F., Emam, S., Prochnow, M., Roux, J. N., and Chevoir, F. (2005). Rheophysics of dense granular materials: Discrete simulation of plane shear flows. *Physical Review E - Statistical, Nonlinear, and Soft Matter Physics*, 72(2):1–17.

Daniels, K. E., Kollmer, J. E., and Puckett, J. G. (2017). Photoelastic force measurements in granular materials. *Review of Scientific Instruments*, 88(5):051808.

Dantu, P. (1957). Contribution à l'étude mécanique et géométrique des milieux pulvérulents. In *Proceedings of the 4th International Conference on Soil Mechanics and Foundation Engineering*. Butterworth Scientific, London.

Doreau-Malioche, J., Combe, G., Viggiani, G., and Toni, J. B. (2018). Shaft friction changes for cyclically loaded displacement piles: an X-ray investigation. *Géotechnique Letters*, 8(1):1–7.

Hall, S. A., Wright, J., Pirling, T., Andò, E., Hughes, D. J., and Viggiani, G. (2011). Can intergranular force transmission be identified in sand? First results of spatially-resolved neutron and X-ray diffraction. *Granular Matter*, 13(3):251–254.

Hasan, A. and Alshibli, K. A. (2012). Three dimensional fabric evolution of sheared sand. *Granular Matter*, 14(4):469–482.

Hurley, R. C., Hall, S. A., Andrade, J. E., and Wright, J. (2016a). Quantifying Interparticle Forces and Heterogeneity in 3D Granular Materials. *Physical Review Letters*, 117(9):1–5.

Hurley, R. C., Lim, K. W., Ravichandran, G., and Andrade, J. E. (2016b). Dynamic Inter-Particle Force Inference in Granular Materials: Method and Application. *Experimental Mechanics*, 56(2):217–229.

Jean, M. and Moreau, J.-J. (1992). Unilaterality and granular friction in the dynamics of rigid body collections. In Curnier, A., editor, *Proceedings of the Contacy Mechanics International Symposium*. Presses Polytechniques Universitaires Romandes, Lausanne.

Joer, H., Lanier, J., Desrues, J., and Flavigny, E. (1992). $1\gamma2\varepsilon$: A new shear apparatus to study the behavior of granular materials. *Geotechnical Testing Journal*, 15:129.

Karanjgaokar, N. (2017). Evaluation of energy contributions using inter-particle forces in granular materials under impact loading. *Granular Matter*, 19(2):1–20.

Karatza, Z., Andò, E., Papanicolopulos, S.-A., Ooi, J. Y., and Viggiani, G. (2018). Evolution of deformation and breakage in sand studied using X-ray tomography. *Géotechnique*, 68(2):107–117.

Kawamoto, R., Andò, E., Viggiani, G., and Andrade, J. E. (2018). All you need is shape: Predicting shear banding in sand with LS-DEM. *Journal of the Mechanics and Physics of Solids*, 111:375–392.

Lecompte, D., Bossuyt, S., Cooreman, S., Sol, H., and Vantomme, J. (2007). Study and generation of optimal speckle patterns for DIC. In *Proceedings of the annual conference and exposition on experimental and applied mechanics.*, pages 1643–9.

Liu, C.-H., Nagel, S. R., Schecter, D. A., Coppersmith, S. N., Majumdar, S. N., Narayan, O., and Witten, T. A. (1995). Force fluctuations in bead packs. *Science*, 269:513.

Mac Donald, K. and Ravichandran, G. (2018). Towards Measuring Intergranular Force Transmission Using Confocal Microscopy and Digital Volume Correlation. In Lamberti, L., Lin, M., Furlong, C., and Sciammarella, C., editors, *Advancement of Optical Methods in Experimental Mechanics*, volume 3 of *Conference Proceedings of the Society for Experimental Mechanics Series*. Springer, Cham.

Majmudar, T. S. and Behringer, R. P. (2005). Contact force measurements and stress-induced anisotropy in granular materials. *Nature*, 435(7045):1079–1082.

Marteau, E. and Andrade, J. E. (2017). A novel experimental device for investigating the multiscale behavior of granular materials under shear. *Granular Matter*, 19(4):1–12.

McNamara, S. C., García-Rojo, R., and Herrmann, H. J. (2005). Indeterminacy and the onset of motion in a simple granular packing. *Physical Review E*, 72(2):1–12.

McNamara, S. C. and Herrmann, H. (2004). Measurement of indeterminacy in packings of perfectly rigid disks. *Physical Review E - Statistical, Nonlinear, and Soft Matter Physics*, 70(6):1–12.

Moreau, J. J. (1977). Evolution problem associated with a moving convex set in a hilbert space. *Journal of Differential Equations*, 13:347374.

Moreau, J. J. (1983). Liasons unilatérales sans frottement et chocs inélastiques. *Comptes Rendus de l'Académie des Sciences*, 296:14731476.

Moreau, J. J. (1988a). Bounded variation in time. In Panagiotopoulos, P. and Strang, G., editors, *Topics in Nonsmooth Mechanics.*, page 174. Bikhäuser, Basel.

Moreau, J. J. (1988b). Unilateral contact and dry friction in finite freedom dynamics. In *International Centre for Mechanical Sciences, Courses and Lectures.*, volume 302. Springer, Vienna.

Moreau, J. J. (1994). Some numerical methods in multibody dynamics: Application to granular materials. *European Journal of Mechanics - A/Solids*, 13(4):93–114.

Moreau, J. J. (1997). Numerical investigation of shear zones in granular materials. In Wolf, D. and Grassberger, P., editors, *Friction Arching Contact Dynamics.*, page 233247. World Scientific, Singapore.

Moreau, J. J. (2004). An introduction to unilateral dynamics. In Frémond, M. and Maceri, F., editors, *Novel approaches in civil engineering*, pages 1–46. Springer-Verlag.

Mueggenburg, N. W., Jaeger, H. M., and Nagel, S. R. (2002). Stress transmission through three-dimensional ordered granular arrays. *Physical Review E*, 66(April):1–9.

Mueth, D. M., Jaeger, H. M., and Nagel, S. R. (1998). Force distribution in a granular medium. *Physical Review E*, 57(3):3164–3169.

Muir Wood, D. and Leśniewska, D. (2011). Stresses in granular materials. *Granular Matter*, 13(4):395–415.

Pan, B., Qian, K., Xie, H., and Asundi, A. (2009). Two-dimensional digital image correlation for in-plane displacement and strain measurement: A review. *Measurement Science and Technology*, 20(6).

Radjai, F., Brendel, L., and Roux, S. (1996a). Nonsmoothness, indeterminacy, and friction in two-dimensional arrays of rigid particles. *Physical review E*, 54(1):861–873.

Radjai, F., Jean, M., Moreau, J.-J., and Roux, S. (1996b). Force Distributions in Dense Two-Dimensional Granular Systems. *Physical Review Letters*, 77(2):274–277.

Radjai, F. and Richefeu, V. (2009). Contact dynamics as a nonsmooth discrete element method. *Mechanics of Materials*, 41(6):715–728.

Radjai, F., Roux, J.-N., and Daouadji, A. (2017). Modeling Granular Materials: Century-Long Research across Scales. *J. Eng. Mech.*, 143(4):04017002.

Radjai, F. and Roux, S. (2002). Turbulentlike fluctuations in quasistatic flow of granular media. *Physical Review Letters*, 89(6):064302/1–064302/4.

Radjai, F., Roux, S., and Moreau, J. J. (1999). Contact forces in a granular packing. *Chaos*, 9(3):544–550.

Richefeu, V., Combe, G., and Maurin, R. (2013). An Attempt in Assessing Contact Forces From a Kinematic Field. *AIP Conference Proceedings*, 1542:429.

Richefeu, V., Combe, G., and Viggiani, G. (2012). An experimental assessment of displacement fluctuations in a 2D granular material subjected to shear. *Géotechnique Letters*, 2(July):113–118.

Rothenburg, L. and Bathurst, R. J. (1989). Analytical study of induced anisotropy in idealized granular materials. *Géotechnique*, 39(4):601–614.

Roux, J.-N. (2000). Geometric origin of mechanical properties of granular materials. *Physical Review E*, 61(6):6802–6836.

Roux, J.-N. and Chevoir, F. (2011). Dimensional Analysis and Control Parameters. In *Discrete-element Modeling of Granular Materials*, chapter 8, pages 83–116. Wiley-ISTE.

Roux, J.-N. and Combe, G. (2011). Quasistatic methods. In *Discrete-element Modeling of Granular Materials*, chapter 3, pages 83–116. Wiley-ISTE.

Saadatfar, M., Sheppard, A. P., Senden, T. J., and Kabla, A. J. (2012). Mapping forces in a 3D elastic assembly of grains. *Journal of the Mechanics and Physics of Solids*, 60(1):55–66.

Schneebeli, G. (1956). Une analogie mécanique pour les terres sans cohésion. *Comptes Rendus de l'Academie des Sciences*, 243(1):125–126.

Schneebeli, G. (1957). Une analogie mécanique pour l'étude de la stabilité des ouvrages en terre à deux dimensions. In *Proceedings of the 4th International Conference on Soil Mechanics and Foundation Engineering*. Butterworth Scientific, London.

Stasiak, M., Combe, G., Desrues, J., Richefeu, V., Villard, P., and Armand, G. (2017). Experimental investigation of mode I fracture for brittle tube-shaped particles. *EPJ Web of Conferences. Powders and grains*, 07015:4–7.

Terzaghi, K. (1920). Old Earth Pressure Theories and New Test Results. *Engineering News-Record*, 85:632–637.

Tordesillas, A. and Muthuswamy, M. (2009). On the modelling of confined buckling of force chains. *Journal of the Mechanics and Physics of Solids*, 57:706727.

Tordesillas, A., Zhang, J., and Behringer, R. P. (2009). Buckling force chains in dense granular assemblies: physical and numerical experiments. *Geomechanics and Geoengineering*, 4:316.

Unger, T. and Kertesz, J. (2003). Frictional indeterminancy of forces in hard-disk packings. *International Journal of Modern Physics B*, 17(29):5623–5630.

Unger, T., Kertesz, J., and Wolf, D. E. (2005). Force indeterminacy in the Jammed state of hard disks. *Physical Review Letters*, 94(17):1–4.

Vacher, P., Dumoulin, S., Morestin, F., and S., M.-T. (1999). Bidimensional strain measurement using digital images. *Proceedings of the Institution of Mechanical Engineers, Part C: Journal of Mechanical Engineering Science*, 213(8):811–817.

Weber, J. (1966). Recherches concernant les contraintes intergranulaires dans les milieux pulvérulents. *Bulletin de liaison des ponts et chaussées*, 20:3.1–3.20.

Wiebicke, M., Andò, E., Herle, I., and Viggiani, G. (2017). On the metrology of interparticle contacts in sand from x-ray tomography images. *Measurement Science and Technology*, 28(12).

# List of Figures


1.1 Sketch of the experimental apparatus used by Mueth et al. (1998). . . . . 15
1.2 Typical stress paths highlighted with photoelasticity (Majmudar and Behringer, 2005). . . . . 17
1.3 Contact forces inferred with GEM superimposed on difference of principal stresses $\sigma_1 - \sigma_2$ for a simple shear test (Marteau and Andrade, 2017). . . . 19
1.4 Contact forces obtained in a 3D, frictional, stiff material by Hurley et al. (2016a), for a uniaxial compression test on quartz grains. . . . . 19

2.1 Typical MD-DEM force laws adopted for the CEM. . . . . 27
2.2 Typical CD-DEM contact laws adopted for the CDM. . . . . 31
2.3 Single contact parameters. . . . . 33
2.4 Solution of the local Signorini-Coulomb problem. . . . . 35
2.5 Solution of the local Signorini-Coulomb problem. . . . . 37
2.6 Projector $\mathcal{P}$ onto the Coulomb cone, for the case of non-associated flow rule. . . . . 44
2.7 Maps of normal contact forces in an isotropically-loaded packing of about 100 particles at different stages of the Gauss-Seidel iterative procedure. . . 47
2.8 Maps of normal contact forces in an isotropically-loaded packing of about 100 particles at different stages of the QSM double projection iterative procedure. . . . . 47
2.9 Probability Distribution of normal forces estimated with the CDM and QSM, for an isotropically loaded assembly of 1850 particles, during the iterations of the two methods. . . . . 48
2.10 Maps of normal contact forces estimated with the CDM and QSM on an isotropically-loaded system of $\approx$ 1800 particles. . . . . 48
2.11 Sketch of a simple system used to introduce the three numerical methods for force estimation. . . . . 50

2.12 Sketch of the contact $1 \rightarrow 3$, with indication of the range of admissibility of the force $\vec{f}_{1\rightarrow 3}$. . . . . 51
2.13 Evolution of the mobilised friction $\mathfrak{m}$ in the MD simulation for different initial conditions, represented by the perturbation $F_{\text{noise}}$ applied at the first time step. . . . . 52
2.14 Evolution of the normal and tangential components of the contact force $\vec{f}_{1\rightarrow 3}$, in the MD simulation, for five different cases, each corresponding to a different initial condition and resulting in a different final solution. . . . 53
2.15 Results of the force estimation with the CEM, for different solutions (different mobilised friction $\mathfrak{m}$) of a system with 1 DOF. . . . . 55
2.16 Characterisation of the range of variability of the solutions found with the CDM for the system in Figure 2.11. . . . . 58
2.17 Percentage of solutions that mobilise the whole friction ($\mathfrak{m} = \pm 1$), for different values of the interparticle friction coefficient $\mu$, in the application of the CDM to the system in Figure 2.11. . . . . 59
2.18 Evolution of the normal and tangential components of the contact force $\vec{f}_{1\rightarrow 3}$, in the CDM application, from the initial values of normal and tangential contact forces to the final values. . . . . 60
2.19 Convergence towards admissible solutions obtained with the CDM when starting from three different initial conditions. . . . . 61
2.20 Characterisation of the convergence for a set of 1000 solutions obtained with the CDM for different initial conditions. . . . . 62
2.21 Velocity of convergence for a set of 1000 solutions obtained with the CDM for different initial conditions. . . . . 63
2.22 Percentage of solutions that mobilise the whole friction, for different values of the interparticle friction coefficient $\mu$, in the application of the QSM to the system in Figure 2.11. . . . . 66
2.23 Comparison of the solutions obtained, for the same initial conditions, with the CDM and the QSM. . . . . 67
2.24 Characterisation of the range of variability of the solutions found with the QSM for the system in Figure 2.11. . . . . 67
2.25 Evolution of the normal and tangential components of the contact force $\vec{f}_{1\rightarrow 3}$, in the QSM application, from the initial values of normal and tangential contact forces to the final values. . . . . 69

2.26 Evolution of the normal and tangential components of the contact force $\vec{f}_{1\to3}$, in the application of the step-wise quasi-static approach, from the initial values of normal and tangential contact forces to the final values. . 70
2.27 Convergence towards admissible solutions obtained with the QSM when starting from different initial conditions, in terms of the distance from equilibrium. . . . . 71
2.28 Characterisation of the convergence for a set of 1000 solutions obtained with the QSM for different initial conditions. . . . . 72
2.29 Velocity of convergence for a set of 1000 solutions obtained with the CDM for different initial conditions. . . . . 73

3.1 Stress-strain curves for the three biaxial vertical MD simulations. . . . . 79
3.2 Evolution of the volumetric deformation for the three DEM simulations. . . 79
3.3 Distance of CDM- (left) and QSM-estimated forces (right) from a reference one, plotted with the distance of randomly-assigned initial conditions they start from. . . . . 83
3.4 Maps of normal forces for different solutions obtained with the CDM for a single state of one MD simulation ($\kappa = 100$). . . . . 85
3.5 Evolution of Pearson's $r$ of tangential forces, estimated with the CEM on numerical data (MD simulation with $\kappa = 1000$) for different frequencies of data acquisition, when previously accumulated tangential forces are taken into account (left) and when they are neglected (right). . . . . 89
3.6 Evolution of the difference, for Pearson's $r$ of tangential forces estimated with the CEM on numerical data (MD simulation with $\kappa = 100$), between two cases: accounting for previously accumulated tangential forces, and neglecting them. . . . . 90
3.7 Comparison between the homogenised stresses computed, respectively, from original contact forces and from CEM-estimated forces, with four different frequencies of data acquisition. . . . . 91
3.8 Evolution of Pearson's $r$ of normal forces, as estimated with the CEM on numerical data (MD simulation with $\kappa = 100$), in two cases: when previously accumulated forces are taken into account and when they are not. . . . . 92
3.9 Sketch of the evolution of a contact between two states $s-1$ and $s$. . . . . 93

3.10 (Left) Ratio of normal relative displacement with increment of overlap, plotted with the unsigned change in orientation of the normal unit vector for all persisting contacts, between two consecutive states of the MD simulation with $\kappa = 100$. (Right) Corresponding error in the determination of normal force increments. . . . . 95
3.11 Evolution of Pearson's $r$ of normal forces for different frequencies of data acquisition, as estimated with the CEM on numerical data (MD simulation with $\kappa = 100$). . . . . 95
3.12 Evolution of the correlation of normal and tangential forces, estimated via the QSM, for two different MD simulations. . . . . 97
3.13 Evolution of Pearson's $r$ for normal (left) and tangential (right) contact forces in the three MD simulations (for $\kappa = 100, 1000, 10000$ respectively), between the solution estimated via the QSM and the real one. . . . . 98
3.14 Evolution of Pearson's $r$ for normal and tangential forces, between the original ones and those estimated via the QSM for an MD simulation with $\kappa = 100$, for different initial conditions. . . . . 99
3.15 Evolution of the correlation of normal and tangential forces, estimated via the QSM, for one MD simulation, with indication of states for which the method could not converge. . . . . 100
3.16 Evolution of the error of the QSM during the iterative procedure, for a single state of an MD simulation with $\kappa = 100$, before and after the assembly is let to relax under constant stress. . . . . 101
3.17 Evolution of Pearson's $r$ for normal (left) and tangential (right) contact forces, between the real values and the ones estimated via the QSM, as the contact network is perturbed by modifying grain radii. . . . . 103
3.18 Comparison of maps of normal forces: original forces vs forces estimated via QSM with 5% fewer contacts and 9% more contacts. . . . . 103
3.19 Evolution of Pearson's $r$ for normal (left) and tangential (right) contact forces, between the real values and the ones estimated via the QSM, as the contact network is perturbed by modifying grain positions. . . . . 104
3.20 Comparison of maps of normal forces: original forces vs forces estimated via QSM with 4% and 7% error on contacts, due to perturbation on grain positions. . . . . 105
3.21 Evolution of Pearson's $r$ for normal and tangential contact forces in the three MD simulations (for $\kappa = 100, 1000, 10000$ respectively), between the solution estimated via the CDM and the real one. . . . . 107

3.22 Cumulative Distribution Function of normal force error for all contacts in the application of CDM to a state at the early stage of the three MD simulations. . . . . 107
3.23 Evolution of Pearson's $r$ for normal and tangential forces, between the original ones and those estimated via the CDM for an MD simulation with $\kappa = 100$, when forces are initialised to null values and when they are initialised to the values from the previous state. . . . . 108
3.24 Evolution of the homogenised stress tensor components from reference (MD) contact forces and forces estimated via the CDM, for a simulation with $\kappa = 100$, when forces are initialised to null values and when they are initialised to the values from the previous state. . . . . 109
3.25 Evaluation of the normal and tangential forces estimated via the CDM, simultaneously or separately (by alternatively fixing either of them), for an MD simulation with $\kappa = 1000$. . . . . 111
3.26 Evaluation of the normal and tangential forces estimated via the CDM, when normal forces are initialised to their original values and when they are not, for an MD simulation with $\kappa = 1000$. . . . . 112
3.27 Evolution of Pearson's $r$ for normal and tangential forces, between the original forces and those estimated via the CDM for an MD simulation with $\kappa = 100$, with indication of admissible and non-admissible solutions. . 114
3.28 Evolution of the mean normal relative velocity during the Gauss-Seidel iterations of an application of the CDM, to a single state of an MD simulation with $\kappa = 100$, when forces are initialised to zero and when they are retrieved from the previous step. . . . . 115
3.29 Evaluation of the normal forces estimated via the CDM as the number of contacts is artificially increased (left) or decreased (right), for a state in the early stage of the MD simulation with $\kappa = 100, 1000, 10000$. . . . . 117
3.30 Comparison of maps of normal forces: original forces vs forces estimated via CDM with 10% fewer contacts and 10% more contacts, due to error on grain radii. . . . . 117
3.31 Cumulative Distribution Function of normal forces carried by the additional 10% contacts for the same state as in Figure 3.30. . . . . 118
3.32 Evolution of Pearson's $r$ for normal and tangential contact forces, between the real values and the ones estimated via the CDM, as the contact network is perturbed by modifying grain positions. . . . . 119

3.33 Comparison of maps of normal forces: original forces vs forces estimated via CDM with 7% and 11% error on contacts, due to perturbation on grain positions. . . . . 119
3.34 Evolution of one indicator of force variability ($\eta$), compared with the evolution of Pearson's $r$ between normal (tangential) forces estimated through the CDM and real ones, for an MD simulation of a small system (12 particles, $\kappa = 100$). . . . . 123
3.35 Evolution of one indicator of force variability ($\theta$), compared with the evolution of Pearson's $r$ between normal (tangential) forces estimated through the CDM and real ones, for an MD simulation of a small system (12 particles, $\kappa = 100$). . . . . 123
3.36 Evolution of the degree of force indeterminacy $h$ with Pearson's $r$ on CDM-estimated normal and tangential forces, for the three MD simulations with 1850 particles. . . . . 124
3.37 Evolution of the degree of force indeterminacy $h$ with Pearson's $r$ on QSM-estimated normal and tangential forces, for the three MD simulations with 1850 particles. . . . . 125
3.38 Evolution of the degree of force indeterminacy $h$, compared with the evolution of Pearson's $r$ between normal (tangential) forces estimated through the CDM and real ones, for an MD simulation with 1850 particles and $\kappa = 100$. . . . . 125
3.39 Evolution of Pearson's $r$ for normal and tangential forces, between the original set of forces and, respectively, the CDM solution and the QSM one, when (almost) null normal forces are used as an initial guess for both methods. . . . . 127
3.40 Evolution of Pearson's $r$ of CDM-estimated normal forces for the MD-DEM simulation with $\kappa = 100$. $r$ is separately computed for the strong and weak force network. . . . . 129

4.1 Image of an isotropically compressed specimen in the $1\gamma2\varepsilon$ device. . . . . 133
4.2 Image of the loading system for the compression test on a pair of grains in contact (left), with plot of the force-displacement response (right). . . . 134
4.3 Map of the vertical strain $\varepsilon_{yy}$ obtained from the software 7D (Vacher et al., 1999) for the compression test on a pair of grains. . . . . 135
4.4 Image of the $1\gamma2\varepsilon$ device (left), with a sketch to illustrate the main components (right). . . . . 136

4.5 Working principle of the apparatus with definition of the geometrical constraints. . . . 137
4.6 Evolution with time of pressure, in one of the isotropic compression tests. 139
4.7 (a) Evolution with time of the vertical and horizontal strains ($\varepsilon_{yy}$ and $\varepsilon_{xx}$, respectively), in one of the isotropic compression tests. (b) Stress-strain plot for the third cycle of the test. . . . 140
4.8 Plot of the stress-strain curve and evolution of the volumetric deformation for the biaxial vertical compression test. . . . 141
4.9 Plot of the evolution of the main geometric properties during the biaxial vertical compression test: void ratio $e$, coordination number $z$ (left) and degree of force indeterminacy $h$ (right). . . . 141
4.10 Plot of the stress-strain curve (black) and evolution of the volumetric deformation (gray) for the biaxial horizontal compression test. . . . 143
4.11 Plot of the evolution of the main geometric properties during the biaxial horizontal compression test: void ratio $e$, coordination number $z$ and degree of force indeterminacy $h$. . . . 143
4.12 Plot of the stress-strain curve (black) and evolution of the volumetric deformation (gray) for the simple shear test. . . . 144
4.13 Plot of the evolution of the main geometric properties during the simple shear test: void ratio $e$, coordination number $z$ (a) and degree of force indeterminacy $h$ (b). . . . 145
4.14 Vertical and horizontal normal stresses in the oedometer compression test. 145
4.15 Oedometric curve for the loading branch of the first cycle of the oedometer compression test. . . . 146
4.16 Example of a gray level histogram from an image of a $1\gamma2\varepsilon$ specimen. . . . 147
4.17 Zoom on two grains to show the black-and-white dots on their visible face. 150
4.18 Sketch of two grains in contact, with definition of the convention for the local reference. . . . 153
4.19 Sketch of the applied loading conditions in three different tests. . . . 153
4.20 Polar histogram of contact orientations for three different tests . . . . 154
4.21 Polar histogram of contacts undergoing negative relative displacement. . . 155
4.22 Comparison between the $1\gamma2\varepsilon$ macroscopic stress components and the Weber stress components computed from contact forces estimated via the CEM for an oedometer compression test. . . . 160

4.23 Comparison between the $1\gamma2\varepsilon$ macroscopic stress components and the Weber stress components computed from contact forces estimated via the CEM for an isotropic compression test. . . . . 161
4.24 Distribution of normal stress magnitude acting on planes with different orientations, from contact forces estimated via the CEM, at the end of the biaxial vertical (a) and horizontal (b) compression tests. . . . . 162
4.25 Comparison between the $1\gamma2\varepsilon$ macroscopic stress components and the Weber stress components computed from contact forces estimated via the CEM for biaxial vertical and horizontal compression tests. . . . . 162
4.26 Comparison between the $1\gamma2\varepsilon$ macroscopic stress components and the Weber stress components computed from contact forces estimated via the QSM to an oedometer compression test. . . . . 165
4.27 Map of normal contact forces obtained via the QSM at the end of the first loading cycle of the oedometer compression test. . . . . 166
4.28 Evolution of Pearson's $r$ for normal and tangential forces estimated via the QSM in consecutive states of an oedometer compression test. . . . . 167
4.29 Probability distribution of normalised normal forces, estimated via the QSM at the end of the first loading cycle of an oedometer compression test. 168
4.30 Comparison between the $1\gamma2\varepsilon$ pressure $p$ and the Weber pressure computed from contact forces estimated via the QSM in an isotropic compression test. . . . . 169
4.31 Comparison between the $1\gamma2\varepsilon$ macroscopic stress components and the Weber stress components computed from contact forces estimated via the QSM in biaxial vertical (a) and horizontal (b) compression tests. . . . . 169
4.32 Comparison between the $1\gamma2\varepsilon$ macroscopic stress components and the Weber stress components computed from contact forces estimated via the CDM to an oedometer compression test. . . . . 172
4.33 Map of normal contact forces obtained via Contact Dynamics at the end of the first loading cycle of the oedometer compression test. . . . . 173
4.34 Probability Distribution of normalised normal forces, estimated via the CDM at the end of the first loading cycle of an oedometer compression test.174
4.35 Evolution of Pearson's $r$ for normal and tangential forces estimated via the CDM in consecutive states of an oedometer compression test. . . . . 175
4.36 Comparison between the $1\gamma2\varepsilon$ macroscopic stress components and the Weber stress components computed from contact forces estimated via the CDM to an isotropic compression test. . . . . 176

4.37 Comparison between the $1\gamma 2\varepsilon$ macroscopic stress components and the Weber stress components computed from contact forces estimated via the CDM to a biaxial vertical compression test. . . . . 176
4.38 Evolution of Pearson's $r$ for normal and tangential forces estimated via the CDM in consecutive states of a biaxial vertical compression test, with and without using previously computed forces as initial guess for the next state. 177
4.39 Comparison between the $1\gamma 2\varepsilon$ macroscopic stress components and the Weber stress components computed from contact forces estimated via the CDM to a biaxial horizontal compression test. . . . . 178
4.40 Map of normal contact forces obtained with the three methods at the end of the first loading cycle of the oedometer compression test: zoom on a part of the specimen. . . . . 180
4.41 Cumulative distribution function of the distance from equilibrium for all particles, at the end of the first loading cycle of the oedometer compression test, in the solutions obtained with the three methods. . . . . 181

B.1 Sketch of the set-up for the measurement of the interparticle friction angle $\mu$. . . . . 210

# List of Tables

2.1 Summary and comparison of the main governing equations of the three methods (CEM, CDM, QSM). . . . . 46

3.1 Main characteristics of the initial states of MD simulations prepared with different stiffness level $\kappa$. . . . . 78

4.1 Distribution of the number of rods for each category of grain diameter. . . 131
4.2 Accuracy for particle tracking in a $1\gamma 2\varepsilon$ test. . . . . 151

# Appendices

# Appendix

## A Matrix form of the single-contact problem in the CDM

The solution of a single-contact problem within CDM loops can be expressed using a matrix formulation. This formulation, which is not given in a matrix form in the manuscript, is quickly outlined here so that some parallels can be drawn with the QSM, which is naturally formulated by means of matrix relations. Focusing on a contact noted $c$ – or equivalently $(ij)$, when the involved particles need to be identified – the relative velocities in the contact frame are

$$\underline{\dot{\boldsymbol{u}}}^c = \underline{\dot{\boldsymbol{u}}}^{(ij)} = (\dot{u}_n^c \ \dot{u}_t^c)^T$$

A third component may be added if a rolling resistance is considered. In the 2D case with 3 DOFs per particle, the velocities of the two particles $i$ and $j$ in contact express

$$\underline{\dot{\boldsymbol{U}}}^{(ij)} = \left(\dot{U}_x^i \ \dot{U}_y^i \ \dot{\theta}^i \ \dot{U}_x^j \ \dot{U}_y^j \ \dot{\theta}^j\right)^T$$

The associated contact forces and the actions on particles $i$ and $j$ are given accordingly

$$\underline{\boldsymbol{f}}^c = (f_n^c \ f_t^c)^T \quad \text{and} \quad \underline{\boldsymbol{F}}^{(ij)} = \left(\mathcal{F}_x^i \ \mathcal{F}_y^i \ \mathcal{M}^i \ \mathcal{F}_x^j \ \mathcal{F}_y^j \ \mathcal{M}^j\right)^T$$

A matrix $\underline{\underline{\boldsymbol{G}}}^c$ can be introduced so that

$$\underline{\dot{\boldsymbol{u}}}^c = \underline{\underline{\boldsymbol{G}}}^c \cdot \underline{\dot{\boldsymbol{U}}}^c \quad \text{and} \quad \underline{\boldsymbol{F}}^c = \left(\underline{\underline{\boldsymbol{G}}}^c\right)^T \cdot \underline{\boldsymbol{f}}^c \tag{A.1}$$

with

$$\underline{\underline{\boldsymbol{G}}}^c = \begin{pmatrix} -n_x^c & -n_y^c & 0 & n_x^c & n_y^c & 0 \\ -t_x^c & -t_y^c & -R_i & t_x^c & t_y^c & -R_j \end{pmatrix} \tag{A.2}$$

In this relation the contact normal $\vec{n} = (n_x, n_y)^T$ is oriented from particle $i$ to particle $j$, but the local velocities in Equation A.1 are those of particle $j$ relative to particle $i$; in

this way, the normal relative velocity $\dot{u}_n$ is negative when the particles are getting closer. We may notice that this convention is different from the one employed in the QSM (see Equation 2.37), mainly for sign convenience.

Assuming a mean acceleration over a time increment $\delta t$, Newton-Euler relations of dynamic motion can be summarised in a single relation (for each contact $c \equiv (ij)$) thanks to the gathering of variables into matrices:

$$\underline{\underline{\boldsymbol{M}}}^c \cdot \frac{1}{\delta t} \Delta \underline{\dot{\boldsymbol{U}}}^c = \underline{\boldsymbol{F}}^c \tag{A.3}$$

where $\underline{\underline{\boldsymbol{M}}}^c$ is a matrix of inertia holding, in the diagonal, the masses and inertia of the two particles $i$ and $j$. In the NSCD approach, which ignores contact elasticity and thus relies on the non-smooth mechanics, this relation is given in terms of particle velocities at the beginning and at the end of a time increment $\delta t$, respectively $\underline{\dot{\boldsymbol{U}}}^{c-}$ and $\underline{\dot{\boldsymbol{U}}}^{c+}$:

$$\underline{\underline{\boldsymbol{M}}}^c \cdot (\underline{\dot{\boldsymbol{U}}}^{c+} - \underline{\dot{\boldsymbol{U}}}^{c-}) = \underline{\boldsymbol{F}}^c \delta t \tag{A.4}$$

where we may remark that the second member hold the force and moment *impulses* $\underline{\boldsymbol{F}}^c \delta t$.

By linking the contact forces with the resultant actions using $\left(\underline{\underline{\boldsymbol{G}}}^c\right)^T$, and since the matrix of inertia is invertible (positive values in the diagonal), the equations of dynamics can read:

$$\left(\underline{\underline{\boldsymbol{M}}}^c\right)^{-1} \cdot \left(\underline{\underline{\boldsymbol{G}}}^c\right)^T \cdot \underline{\boldsymbol{f}}^c \delta t = \underline{\dot{\boldsymbol{U}}}^{c+} - \underline{\dot{\boldsymbol{U}}}^{c-} \tag{A.5}$$

which leads, by multiplying both sides by $\underline{\underline{\boldsymbol{G}}}^c$:

$$\underline{\underline{\boldsymbol{G}}}^c \cdot \left(\underline{\underline{\boldsymbol{M}}}^c\right)^{-1} \cdot \left(\underline{\underline{\boldsymbol{G}}}^c\right)^T \cdot \underline{\boldsymbol{f}}^c \delta t = \underline{\underline{\boldsymbol{G}}}^c \cdot (\underline{\dot{\boldsymbol{U}}}^{c+} - \underline{\dot{\boldsymbol{U}}}^{c-}) \tag{A.6}$$

$$\underline{\underline{\boldsymbol{W}}}^c \cdot \underline{\boldsymbol{f}}^c \delta t = (\underline{\dot{\boldsymbol{u}}}^{c+} - \underline{\dot{\boldsymbol{u}}}^{c-}) \tag{A.7}$$

This relation introduces the Delassus operator $\underline{\underline{\boldsymbol{W}}}^c$. In this form, the equations of dynamics if expressed locally, at the contact level, by an affine relation between the contact forces $\underline{\boldsymbol{f}}^c$ and the right-limit relative velocities $\underline{\dot{\boldsymbol{u}}}^{c+}$ ($\underline{\dot{\boldsymbol{u}}}^{c-}$ is known in the problem).

In order to be able to model shocks by accounting for normal and tangential coefficients of restitution, a formal relative velocity is introduced. It corresponds to a weighted average of the left-limit and right-limit relative velocities:

$$(\mathbb{I} + \underline{\underline{\boldsymbol{e}}}) \cdot \underline{\dot{\boldsymbol{u}}}^c = \underline{\dot{\boldsymbol{u}}}^{c+} + \underline{\underline{\boldsymbol{e}}} \cdot \underline{\dot{\boldsymbol{u}}}^{c-} \quad \text{where} \quad \underline{\underline{\boldsymbol{e}}} = \begin{pmatrix} e_n & 0 \\ 0 & e_t \end{pmatrix} = \begin{pmatrix} -\dot{u}_n^{c+}/\dot{u}_n^{c-} & 0 \\ 0 & \dot{u}_t^{c+}/\dot{u}_t^{c-} \end{pmatrix} \tag{A.8}$$

This allows the expression of the locally transferred equation of dynamics as an affine relation linking contact forces with formal relative velocities:

$$\underline{\underline{\boldsymbol{W}}}^c \cdot \underline{\boldsymbol{f}}^c = \frac{1}{\delta t}\left((\mathbb{I} + \underline{\underline{\boldsymbol{e}}}) \cdot \underline{\dot{\boldsymbol{u}}}^c - (\mathbb{I} + \underline{\underline{\boldsymbol{e}}}) \cdot \underline{\dot{\boldsymbol{u}}}^{c-}\right) \tag{A.9}$$

and the force corrections involved in the Gauss-Seidel iterations can be applied by considering both the complementary relations (Signorini-Coulomb conditions) and the slopes of the locally transferred equations of dynamics:

$$\frac{\Delta \underline{\boldsymbol{f}}^c}{\Delta \underline{\dot{\boldsymbol{u}}}^c} = \underline{\underline{\boldsymbol{W}}}^c \cdot \underline{\boldsymbol{f}}^c = \frac{1}{\delta t}(\underline{\underline{\boldsymbol{W}}}^c)^{-1} \cdot (\mathbb{I} + \underline{\underline{\boldsymbol{e}}}) \tag{A.10}$$

# B Determination of the interparticle friction coefficient

An estimation of the interparticle friction angle is carried out by an appropriate test that makes use of the experimental set-up described in Figure B.1, as in Calvetti et al. (1997).

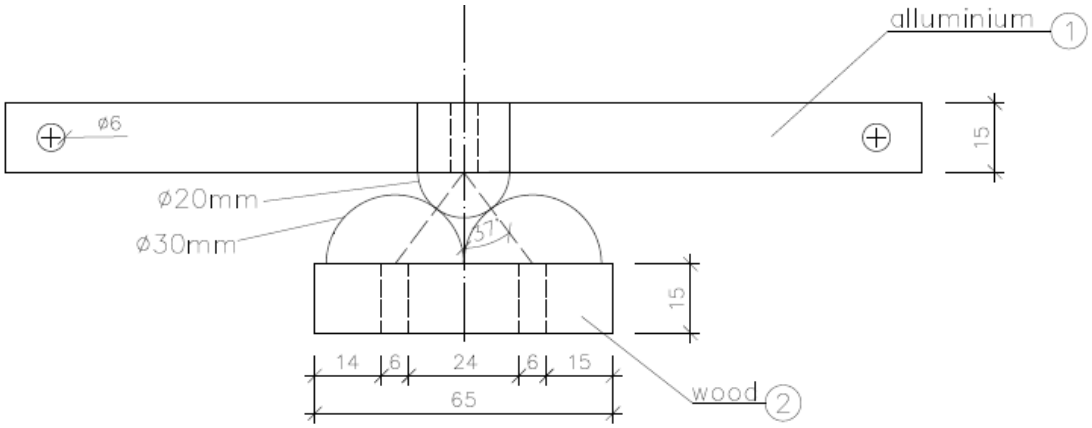


Figure B.1 – Sketch of the set-up for the measurement of the interparticle friction angle $\mu$.

The three particles in the system are wooden rods with smooth surfaces, as those composing the granular material described in Section 4.1.1. The two particles A and B have a radius of 3 cm and are fixed on the wooden base; they both support a smaller particle C ($r = 2$ cm), which is loaded by two weights – $P_1$ and $P_2$ – applied at the same distance from the mass centre of C. $P_1$ and $P_2$ are initially equal and particle C is in static equilibrium. By increasing $P_2$, a limit equilibrium is reached and rod C rotates and slides at contact points with rods A and B.

In normal conditions, the problem of static equilibrium of this system is undetermined, since the number of unknowns (4, *i.e.*, the normal and tangential force components for both contacts) is higher than the number of equations (the 3 equations corresponding to the DOFs of particle C). At sliding, normal and tangential forces are related, as $f_t = \mu f_n$, and the unknowns of the system are reduced to 3: the normal forces at the two contacts, and the friction coefficient $\mu = \tan\phi$. In these conditions, the equilibrium equation gives the following relation:

$$\sin 2\phi = 2\,\frac{P_2 - P_1}{P_2 + P_1}\,\frac{L}{R}\,\cos\alpha \quad . \tag{B.1}$$

This relation is valid only if $\alpha > \phi$ and both contacts are maintained when the sliding condition is reached. Several tests are performed with different values for $\alpha$ and $P_1$; based on them, the interparticle friction angle is found to be $\phi = 28^\circ(\pm 2^\circ)$ for our

wooden rollers with smooth surfaces.